Force Measurement Techniques in Short Duration Hypersonic Facilities

Andrew M. Hyslop

Supervisor: Prof. M. McGilvray
Dr. L. J. Doherty

Department of Engineering Science
University of Oxford

This dissertation is submitted for the degree of
Doctor of Philosophy

Wolfson College

June 2023

Acknowledgements

First and foremost, I would like to thank my supervisors Matthew McGilvray and Luke Doherty for their exhaustive support and guidance throughout this DPhil. Matt – you inspired me as my tutor to embark on this journey and I'm forever thankful for that. Luke – I will always be grateful for the time you put aside to give me advice, no matter how busy you were. Your knowledge and skills as a researcher, teacher and mentor have been invaluable to me and this work.

Thank you to everyone at DSTL for enabling the research within this thesis. Most notably to Trevor, your advice and guidance that kept this work relevant is highly appreciated.

I would also like to express my gratitude towards the whole of the Oxford hypersonics group and the endless support everyone provided. In particular I'd like to thank Hassan for the frequent tea breaks providing endless entertainment and inspiration for work – I know you'll go far in your academic career. Will, we've come a long way since our days at St Hilda's, thanks for being an awesome friend and for all the help over the years. Marc – thanks for always being there to talk to, you are great friend and hiking partner! Joe, thank you for the many moments of entertainment – I'll miss our daily pilgrimage to JCT. I can't forget my desk buddy Alex, thanks for always managing to brighten my day, hope the interviews for my replacement go well! Jack – your willingness to talk through problems and lend a hand is highly appreciated. Chris, Tobi, Maïlys, Max and Tristan – thanks for operating HDT, your support during the challenging times of testing is highly appreciated. To the rest of the hypersonics group, you are all amazing people – thank you for all of the good times.

I'd also like to extend my thanks to the multiple support staff and technicians in the Osney Thermofluids Institute. Greg, Dave, Harry, Leo – your support and advice with machining and instrumentation has made the work in this thesis possible and I will always be grateful. Anna – thanks for always being willing to deal with my last minute admin requests and providing great advice for hiking in the Welsh mountains.

To my old housemates at Marlborough Road; Ryan, Tom and Jon. There was never a dull moment in our house and I'm grateful to all of you for keeping me sane during the Covid lockdowns. Grigore, Liam, David, Chris, Y.C – you are all amazing friends. Chloe, thank

you for support and encouragement in getting me over the line, I'm looking forward to many more happy years together in the future.

To my parents, Beverley and Michael, thank you for always being there for me and your continuous love and support throughout my life. You've given me the best possible start to life and without your support I would not have made it to this milestone. Finally, Alison, you are an amazing and supportive sister. Thank you for reading every page of this thesis and editing my many grammatical errors.

List of Publications

First-authored journal articles included in this thesis:

1. Hyslop, A., Doherty, L.J., McGilvray, M., Neely, A., McQuellin, L.P., Barth, J. and Mullen, G., 2021. Free-Flight Aerodynamic Testing of the Skylon Space Plane. *Journal of Spacecraft and Rockets*, 58(5), pp.1487-1497.

2. Hyslop, A., Doherty, L.J. and McGilvray, M., 2022. The Measurement of Static Aerodynamic Force Coefficients in a Hypersonic Ludwieg Tube using the Free-Flight Technique *Experiments in Fluids* (under Review)

3. Hyslop, A., Doherty, L.J. and McGilvray, M., 2022. Comparison of Hypersonic Force Measurement Techniques in a Short Duration Hypersonic Facility *Experiments in Fluids* (under Review)

4. Hyslop, A., Doherty, L.J. and McGilvray, M., 2022. The Measurement of Static Aerodynamic Coefficients of a Complex Body Using the Free-Flight Technique in Short Duration Hypersonic Flow *Journal of Spacecraft and Rockets* (under Review)

First-authored conference papers relevant to this thesis but not included herein:

1. Hyslop, A., McGilvray, M., Doherty, L., Neely, A., McQuellin, L., Barth, J. and Mullen, G., 2019. Aerodynamic Testing of the Skylon Spaceplane. *International Conference on Flight vehicles, Aerothermodynamics and Re-entry Missions and Engineering, Monopoli, Italy.*

2. Hyslop, A.M., McGilvray, M. and Doherty, L.J., 2022. Free-Flight Aerodynamic Testing of a 7 Degree Half-Angle Cone. *In AIAA SCITECH 2022 Forum* (p. 1324).

Co-authored conference papers during the tenure of the author's DPhil candidacy (not included herein):

1. Subiah, S., Collen, P., Doherty, L., Penty Geraets, R., Hyslop, A. and McGilvray, M., 2019. Condition Development and Commissioning of the Oxford T6 Stalker Tunnel in Reflected Shock Tunnel Mode. *International Conference on Flight Vehicles, Aerothermodynamics and Re-entry Missions and Engineering, Monopoli, Italy.*

2. Collen, P., Doherty, L., Subiah, S., Hyslop, A. and McGilvray, M., 2019. Performance Capability Experiments in T6: A Hypervelocity, Transient and Multi-Mode Ground Test Facility for High-Enthalpy Aerothermodynamics Research. *International Conference on Flight Vehicles, Aerothermodynamics and Re-entry Missions and Engineering, Monopoli, Italy.*

3. Wheeler, C., Hyslop, A., Vieira, J., Le Page, L., Quinn, M., Chowdhury, N. and Doherty, J. 2022. Surface Pressure Measurements on a Free-Flying Cone at Mach 7 using Pressure Sensitive Paint. *HiSST: 2nd International Conference on High-Speed Vehicle Science Technology, Bruges, Belgium*

Abstract

In this thesis, the free-flight force measurement technique is commissioned, validated and implemented with increasing complexity in geometries within the University of Oxford High Density Tunnel, a short-duration, heated Ludwieg Tube. The motivation of the work was to improve the current capability of force measurement techniques through the free-flight methodology, allowing for the measurement of high quality, flight representative forces with lower uncertainties than established force measurement techniques. Rather than rigidly mount a sub-scale model through a sting and measure forces through a load cell, the free-flight technique allows the model to move in six degrees of freedom during the test time. This allows for forces and moments to be measured that are not impacted by the mounting structure but require non-intrusive methods to measure the model's kinematics. In this work, kinematics are measured through a 3 degree of freedom image tracking algorithm with sub-pixel accuracy and through accelerometers mounted internally to the model on an on-board data acquisition system.

This thesis introduces the static free-flight technique, whereby the aerodynamic pitching moment is minimised by matching the location of centre of gravity to centre of pressure, reducing the static margin of the model. This technique limits the dynamic influence on the measured aerodynamic coefficients and allows for only the static derivatives to be measured. This technique was conducted with a 7 degree half-angle cone, a simple geometry in which the measured coefficients can be validated against a numerical panel method code, giving confidence in the methodology. The tests were conducted at a Mach 7 condition representative of a hypersonic vehicle's trajectory at 35 km altitude. Non-intrusive image tracking and on-board inertial measurement units were used to determine accelerations to calculate the aerodynamic forces acting on the cone. Results for lift, drag and pitching moment coefficients were obtained over a range of angles of attack and compared with predictions from a hypersonic panel method code. The experimental and numerical data sets agreed well over the range of angles of attack with the experimental uncertainties remaining below 3.1 % for all coefficients.

Following validation of the static free-flight technique, tests were conducted to directly compare free-flight against force balance techniques. The force balance was calibrated

using two methods; a static calibration and by dynamically calibrating the balance by generating a global impulse response function of the model and using the stress wave deconvolution methodology. The experimental model was a blunted 7 degree half-angle cone and experiments were conducted at a Mach 5 test condition which provided sufficient dynamic pressure to generate aerodynamic forces suitable for the measurement range of the force balance. Results for lift, drag and pitching moment coefficients were obtained over a range of angles of attack and compared with predictions from a hypersonic panel method code. Agreement between the independent force techniques and numerical data sets was good over the range of angles of attack. Maximum uncertainties were shown to be ± 0.56 N and ± 0.44 N for free-flight for lift and drag respectively and ± 1.59 N and ± 1.27 N for the dynamically calibrated force balance.

Finally, after showing that the free-flight methodology in the High Density Tunnel resulted in lower uncertainties than other force measurement techniques, it was applied to a 7 degree half-angle cone with fins, at a flight-representative Mach 7 condition. The fins resulted in a centre of pressure that was a function of angle of attack. Longitudinal static force and moment coefficients were measured at the Mach 7 condition with the experimental data agreeing well with numerical predictions. Forces were obtained using both image tracking at 76,000 fps as well as the direct measurement of accelerations using an on-board inertial measurement unit. Uncertainties remained below $\pm$ 0.0075 for lift coefficient and $\pm$ 0.0051 for drag coefficient. The fins were also angled to allow the model to roll in free-flight so that roll coefficient could also be determined.

Table of contents

List of figures

List of tables

Nomenclature

Acronyms

AGARD	Advisory Group for Aerospace Research and Development
AIAA	American Institute of Aeronautics and Astronautics
BOS	Background Orientated Schlieren
CFD	Computational Fluid Dynamics
CoG	Centre of Gravity
CoP	Centre of Pressure
DAQ	Data Acquisition System
DARPA	Defense Advanced Research Projects Agency
DLR	German Aerospace Center
ESA	European Space Agency
GIRF	Global Impulse Response Function
HDT	High Density Tunnel
HTV	Hypersonic Technology Vehicle
IMU	Inertial Measurement Unit
IRF	Impulse Response Function
ISL	Institute of Research of Saint Louis
ISS	International Space Station

JAXA	Japan Aerospace Exploration Agency
LDT	Low Density Tunnel
LED	Light-Emitting Diode
LICH	Light Piston Compression Heating
MGBS	Magnetic Suspension and Balance Systems
NASA	National Aeronautics and Space Administration
PID	Proportional, Integral, Differential
RAE	Royal Aircraft Establishment
REST	Rectangular-to-Elliptical Shape Transition
TTL	Transistor–Transistor Logic
UCAV	Unmanned Combat Aerial Vehicle
UNSW	University of New South Wales
USQ	University of Southern Queensland
VKI	Von Karman Institute

Greek Letters

α	Angle of attack ($^\circ$)
$\dot{\alpha}$	Rate of change in angle of attack ($^\circ/s$)
β	Side slip angle ($^\circ$)
δt	Sampling rate ($/s$)
δ	Control surface deflection ($^\circ$)
$\hat{\delta}$	Panel inclination angle
δ_e	Elevator position ($^\circ$)
γ	Adiabatic constant
μ	Dynamic Viscosity ($Pa.s$)

Ω	Angular rate $(^\circ/s)$
ω	Frequency of oscillation $(/s)$
$\dot{\Omega}$	Angular acceleration $(^\circ/s^2)$
ϕ, θ, ψ	Euler angles $(^\circ)$
$\dot{\phi}, \dot{\theta}, \dot{\psi}$	Euler rates $(^\circ/s)$
π	Number of dimensionless groups
ρ	Density (kg/m^3)

Roman Letters

a	Velocity of sound (m/s)
c	Reference length (m)
C_D	Drag coefficient
C_L	Lift coefficient
C_l	Roll moment coefficient
C_M	Pitching moment coefficient
C_p	Pressure coefficient
C_{p0}	Stagnation pressure coefficient
D	Drag (N)
E	Young's modulus (Pa)
EI'	Bending stiffness $(N.m^2)$
F	Force (m)
$\mathbf{F}$	Force matrix (N)
Fr	Froude number
$g(t)$	Impulse resonponse function (V/N)
G	Shear modulus of elasticity (Pa)

g	Acceleration of gravity (m/s^2)
$\mathbf{G}$	Global impulse resonponse function (V/N)
GJ'	Torsional stiffness ($N.m^2$)
I'	Second bending moment of area (m^4)
I	Moment of inertia ($kg.m^2$)
i_h	Horizontal stabiliser position ($^\circ$)
I_yy	Moment of inertia about pitch axis ($kg.m^2$)
I_{xx}	Moment of inertia about roll axis
J'	Second torsional moment of area (m^4)
$\mathbf{K}$	Cross-coupling matrix (V/N)
L	Lift (N)
l	Length (m)
M	Pitching moment ($N.m$)
m	Mass (kg)
M_∞	Mach number
M_n	Mach number normal to the shock
n	Geometric scaling factor
$\hat{N}$	Panel normal vector
N_b	Number of base units
N_q	Number of quantities
P	Static pressure (Pa)
p	Roll rate ($^\circ/s$)
P_0	Total pressure (Pa)
q	Pitch rate ($^\circ/s$)

$\bar{q}$	Dynamic pressure (Pa)
R	Gas constant for air ($J/kg.K$)
r	Yaw rate ($^\circ/s$)
Re	Reynolds number
Re_u	Unit Reynolds number ($/m$)
S	Reference area (m^2)
St	Strouhal Number
T	Static temperature (K)
t	Time (s)
T_0	Total temperature (K)
$u(t)$	Applied load (N)
V	Velocity (m/s)
v	Pertubation in freestream velocity (m/s)
$\dot{V}$	Acceleration (m/s^2)
$\hat{V}$	Panel velocity vector
$\mathbf{V}$	Voltage matrix (V)
W	Weight (N)
$\ddot{x}, \ddot{y}, \ddot{z}$	Acceleration in Cartesian co-ordinates (m/s^2)
$y(t)$	Strain response (V)

Subscripts and Superscripts

A	Axial impulse hit
B	Body frame of reference
E	Earth frame of reference
f	Fluid property

m	Model property
N	Normal impulse hit
v	Vehicle property

Chapter 1

Introduction

1.1 Overview

In the development phase of any aircraft, whether the target flight regime is subsonic, supersonic or hypersonic, it is important to characterise the aerodynamic forces and moments acting upon the vehicle during flight as it determines the resulting motion of the vehicle. This relationship between aerodynamic forces and vehicle motion is classified as flight dynamics [109]. The aerodynamic forces in flight arise from pressure and shear stress variations acting on a body as a result of an incident flow. Typically, these forces are resolved into three orthogonal components for six degrees of freedom motion; lift, drag and side force, as well as resulting pitching, roll and yaw moments. For longitudinal motion this simplifies to lift, drag and pitching moment. Accurate predictions of these three components are essential in understanding a vehicle's baseline performance and predicting its response to disturbances in such a way that an appropriate control strategy can be implemented.

The final frontier of flight which remains unconquered is that of sustained hypersonic atmospheric flight, often defined by exceeding a Mach number of 5 but more realistically the appearance of certain flow phenomena such as extreme heating of the vehicle and surrounding flow [2]. Due to the complexities of the flow when moving at hypersonic speeds, there lies a lot of uncertainties and difficulties when predicting the forces that act on a body in these flight conditions. These characteristics make numerical simulations much more complex and ground facilities often compromise on one of these flow features to match another, for example Reynolds number at the expense of flow enthalpy. When developing a vehicle, there are four methods that can assess the aerodynamic performance of a vehicle:

- Full-scale atmospheric flight tests
- Sub-scale atmospheric flight tests

- Ground based (sub-scale) experiments
- Analytical and numerical simulations

The optimal method of assessing the aerodynamic performance of a vehicle is through full-scale flight testing. However, this is very costly and usually will only be performed in the final stages of the design cycle (the NASA space-shuttle programme cost $1.5 billion per launch [80]). Before this point is reached, it is likely that the design of the vehicle will have been optimised through ground based experiments and numerical simulations, both of which are a fraction of the cost of performing flight testing.

As hypersonic vehicles tend to be highly integrated designs, often with many competing criteria to be accounted for, the optimisation process is initially achieved almost exclusively computationally [7]. With ever increasing computational power available to researchers and the improving ability of programmes to comprehensively predict the performance of vehicles, it is still important that the experimental tools are available to validate this data. While often this computational optimisation is the first stage of the design process, experimental methods are still a necessary part of the design process as demonstrated by the HEXAFLY-INT project [90], a hypersonic glider. Throughout the years, engineers have created many tools; analytical, experimental and numerical to help understand these forces in the hypersonic regime. Analytical techniques such as Modified Newtonian Theory and local inclination methods [2] provide estimations of surface pressures, however they are inviscid approximations which limit their usefulness to a limited number of situations. Numerical simulations, which involve dividing a fluid domain into finite divisions and solving the fundamental equations of fluid flow (Navier-Stokes) iteratively across each cell, can provide estimations of a vehicle's performance. However, a full nose-to-tail vehicle high-fidelity simulation is computationally demanding and may still be a function of the domain mesh or approximations used in the simulation (the number of chemical species present or viscosity model, for example) [107].

Usually numerical simulations need experiments for validation, typically with tests of sub-scale models conducted in hypersonic facilities. Testing in ground based facilities, however, does have its own limitations too. Most facilities that produce flight representative conditions are of short duration in nature and have flow times in the order of milliseconds to tens of milliseconds and have large uncertainties in flow conditions. The limitation on steady test time and the high sampling rate required to acquire data can make it difficult to obtain meaningful results. In the field of force measurements, this has led to the development of many force measurement techniques to overcome these limitations [6]. Although hypersonic force measurement techniques have been around for many years, there have still been many

issues taking the leap from ground based experiments and numerical simulations to flight testing.

1.2 Research Motivation

The practice of conducting experiments and numerical simulations prior to expensive flight testing is well established. However, issues occur when the experimental and numerical data is not of sufficient quality or not valid for the design flight conditions.

On the 2nd June, 2001, the NASA X-43A was released from a modified B-52 bomber to demonstrate the technologies required for air-breathing hypersonic flight. The flight only lasted for 13.5 seconds before the right elevon was overstressed and suffered structural failure resulting in complete loss of the vehicle. This failure occurred because the control system was unable to maintain vehicle stability during flight. Investigations found that the predicted aerodynamic forces were very different to reality as the test flight was conducted at 20,000 feet but the experimental and numerical data was obtained for 40,000 feet [77].

On the 22nd April, 2010, DARPA conducted the first flight of the Hypersonic Technology Vehicle 2 (HTV-2), an unmanned boost-glide vehicle, which ended in failure after 9 minutes due to higher than predicted yaw coupled with roll which exceeded the available control capability of the vehicle [87]. The second test successfully demonstrated aerodynamically stable flight but this time failed due to thermal degradation of the aeroshell.

In both cases, there were discrepancies in the aerodynamic data taken from wind tunnels and numerical predictions to the flight data which in some cases lead to failure of the vehicles. From these case studies, it is clear that there is a need for improved capability of ground testing facilities for hypersonic flows to reduce the risk of failures due to inaccurate predictions of aerodynamic forces and moments. To quote Bernstein and Pankhurst [6]:

"But when, for example, the results have to be extrapolated to different Reynolds numbers from those of tests, one may be forced to accept inaccuracies in the extrapolated results, and may not be justified in pursuing very high accuracy measurements in themselves"

This demonstrates that care which must be taken when data is taken from wind tunnel facilities that the freestream conditions are also representative of the flight flow regime of interest if the data is to be considered high accuracy. The University of Oxford High Density Tunnel (HDT) offers the opportunity to achieve flight representative test conditions and sufficient test time to measure quasi-static forces. This compounded with improvements

in force measurement techniques such as free-flight offers an opportunity to make these necessary advancements identified by Bernstein.

1.3 The Free-Flight Force Measurement Technique

The free-flight technique is by no means a new idea. Implemented for the first time in the early 1960s [86, 23], it is a different approach to traditional force measurement techniques that typically involve a sting mounted force balance. The methodology of a free-flight technique is as follows; a model is released into the tunnel core flow and is free to move in six degrees of freedom. The forces are calculated by measuring the acceleration of the model, either directly through on-board accelerometers or through differentiating displacements obtained by image tracking [39].

There are two major advantages of this methodology over conventional sting-mounted force balance experiments. The first is that as the model has no mounting structure, the flow is realistic of flight and there are no shock waves from mounts. Stings have been shown to interfere with the base pressure of models when mounted at angles of attack [79], ultimately influencing the measured force. The second advantage is that the internal vibrations within the model structure generated from the impulsive aerodynamic forces from hypersonic facilities need to be considered to a lesser degree than for a force balance model. A sting mounted model suffers from vibrations upon flow initiation from the aerodynamic forces which do not necessarily damp out during the test time [62] and the vibrations are superimposed on the strain gauge signals. As the free-flight model is not rigidly held, the acceleration signal tends to suffer a lot less from oscillations.

Whilst these advantages have been known for a long time, the uncertainties of free-flight experiments have historically been high due to limitations in technology of the era [6]. With the advances in miniaturised electronics, accelerometers can be installed internally within the model, improving the uncertainties associated with the technique [67]. Furthermore, the capability of high-speed cameras has improved, both in resolution and recording speed, allowing for more accurate image tracking capabilities to be utilised [45]. Both of these improvements make free-flight a very attractive method of measuring forces.

With these advances in mind, the opportunity to further improve the capability of free-flight force measurement within the University of Oxford High Density Tunnel is possible. This thesis aims to reduce the uncertainties associated with the technique and compare the results to other established force measurement techniques.

1.4 Thesis Aims

The aim of this thesis is to develop the capability of force measurement techniques suited for short duration hypersonic facilities to provide high quality aerodynamic force data that is representative of flight. The following contributions are made in this thesis towards achieving this aim:

1. **Understand how the application of scaling laws to free-flying models influences the measured aerodynamic coefficients, in particular, the influence of Reynolds number and the inertial properties of the model.**

   Unlike with traditional force measurement techniques, free-flight allows the model to move freely in the flow and relies on the measurement of model kinematics. Therefore, as well as the requirements of scaling Reynolds number and Mach number, the influence of other criteria such as mass, centre of gravity and inertia will need to be understood.

2. **To separate the static and the dynamic derivates from the overall aerodynamic coefficient measured during free-flight tests, thereby providing higher quality data in a single free-flight test.**

   This thesis presents the development of the static free-flight technique. A methodology where the pitching motion of a free-flight model is limited so that the resultant forces that are measured are solely those related to the static behaviour - similar to the forces measured by a force balance.

3. **Validation of the static free-flight technique using a simple geometry in which aerodynamic coefficients can be easily predicted by numerical codes.**

   Before moving to complex hypersonic geometries, it is necessary to validate a technique to gain confidence in its ability to measure aerodynamic forces and moments and understand its potential uncertainties. Applying the static free-flight technique to a blunted 7 degree half-angle cone allows for the methodology to be validated against a numerical panel method code.

4. **Provide a qualitative and quantitative comparison of established force measurement techniques with free-flight within the same facility.**

   For a force measurement technique to become established, a comparison must be made to similar techniques to show its advantages and disadvantages. The more established force measurement technique is by using a force balance, either by a static or dynamic

calibration. Free-flight and force balance experiments are conducted at the same freestream conditions and their experimental uncertainties are quantified.

5. **Validate the static free-flight technique for a complex geometry - one in which the centre of pressure is not constant with angle of attack**

   The final step of developing a methodology is to apply and validate it with a complex geometry. By doing so, it confirms that the technique is applicable to any slender geometries which an experimenter decides to investigate.

1.5 Thesis Structure

The core work of this thesis is divided into six chapters. This is a hybrid thesis where three of the chapters are each a stand-alone journal paper. A summary of each chapter is provided below:

1. **Chapter 2**: This chapter provides a literature review of force measurement techniques which have been used previously in hypersonic facilities. After reviewing the relevance of the techniques and their suitability to the University of Oxford High Density Tunnel (HDT), previous work undertaken using the free-flight technique is reviewed in detail.

2. **Chapter 3**: The scaling of freestream conditions and model parameters is vital if the forces measured in wind tunnel facilities are to be representative of flight. This chapter discusses the pertinent parameters behind scaling for aerodynamic experiments and their relation to obtaining flight representative aerodynamic coefficients. A discussion of static and dynamic aerodynamic derivatives is also included. These scaling parameters are then applied in the context of free-flight and finally how the HDT is suitable for this form of aerodynamic testing.

3. **Chapter 4**: Validation of the free-flight technique is explored in this chapter by measuring the forces and moments of a 7 degree half-angle cone in free-flight. The measured aerodynamic coefficients are validated against a numerical panel method code. This chapter comprises a journal paper currently under review in Experiments in Fluids.

4. **Chapter 5**: This chapter provides a direct comparison of the force data provided by the free-flight technique against a force balance (both static and dynamic calibration) within the same facility and provides information on their respective experimental

uncertainties. This chapter comprises a journal paper currently under review in Experiments in Fluids.

5. **Chapter 6**: The static free-flight technique is applied to a finned 7 degree half-angle cone, a complex geometry in which the centre of pressure is a function of angle of attack. The experimental data is validated against a panel method code. Roll coefficients are also derived for the first time in this chapter. This chapter comprises a journal paper currently under review in the Journal of Spacecraft and Rockets.

6. **Chapter 7**: A final conclusion of the whole series of work presented in this thesis is drawn. Recommendations for future work are also provided.

Chapter 2

Literature Review

The need for engineers to accurately determine aerodynamic coefficients of vehicles in flight has led to the development of many force and moment measurement experimental techniques within wind tunnel facilities to provide flight representative data, all with their advantages and disadvantages. This section discusses the different techniques available to aerodynamicists working in the hypersonic regime for the measurement of flight representative forces and gives a brief overview of the development of techniques and any relevant work. This is by no means a complete review of the literature due to the sheer number of experiments conducted in this area, but the key literature and experimental methods are detailed here.

2.1 Overview of Ground Techniques for Aerodynamic Force and Moment Measurement

This section provides an overview of existing techniques that measure aerodynamic forces and moments in ground-based facilities. This section will firstly discuss the typical force measurement techniques used in subsonic facilities and why this methodology is not always suited for hypersonic facilities. Following this, the different techniques used for measuring forces in hypersonic facilities are reviewed cumulating in a discussion of their suitability for use in a short duration Ludwieg tube facility with a test time of 50 ms.

2.1.1 Force Balances

The measurement of forces in facilities that are subsonic, transonic and supersonic is a well established field. Flow durations in these facilities typically range from seconds to hours and hence there is sufficient test time for the applied external aerodynamic forces

and internal stress waves passing within a model upon flow onset to reach an equilibrium and allow for a steady static force to be measured. Typically within these flow regimes, forces are measured with a multicomponent force balance with orthogonal force and moment components resolved relative to a Cartesian co-ordinate system [6].

A force balance is a system that is connected to a model either internally within the model or externally with a supporting structure [20]. When flow from the wind tunnel establishes over the model, the aerodynamic forces are transferred to the force balance through stress waves within the model and small deflections within the force balance are measured by appropriately located strain gauges. In its most simplistic form, a strain-gauge load cell is located within the supporting structure and used to directly measure the forces at the point of equilibrium providing high-quality aerodynamic data which is representative of the full-scale vehicle. This can range from single-component drag measurements to six-component force and moment measurements. Frequently, the attitude of the model will be controlled by the operator between tests to characterise the vehicle at a range of orientations.

For traditional force balances, calibration is achieved through applying a static load to the force balance to each axis independently and measuring the strain gauge signal response of all the channels. It cannot be assumed that the response of each axis is independent of off-axis channels. Therefore, this process is repeated for all of the components of the force balance so that a cross-coupling matrix can be formed which transforms the vector of voltage strain gauge signals to forces and moments.

There are many examples of force balance experiments in the subsonic and transonic regime in the open literature for a range of vehicle geometries. An example of such was conducted at the NASA Langley Research centre for a sting-mounted 2.7 % scale Boeing 777 (Fig. 2.1) at high Reynolds numbers in the transonic regime [76, 10]. Five components of force (lift, drag and side) and moment (pitch and yaw) were measured during the tests at a range of angles of attack and freestream conditions. A big advantage of force balance experiments is that wiring for instrumentation can run down the sting which allows for extra sensors in the confines of the model. For these experiments, 6 rows of pressure taps were placed on the wings.

A further example of subsonic balance experiments was conducted by McParlin et al. [58] in the QinetiQ 5 metre pressurized low-speed wind tunnel for a model of a lambda wing planform UCAV concept as seen in figure 2.2. The model was limited to 5 foot due to the loading range of the 6 component force balance and attitude was measured using an internal accelerometer. Pressure measurements were made near the wing leading edge at seven stations spanwise with the objective of the wind tunnel tests being to examine the onset and development of the flow separation near the wing leading edge and its sensitivity to

Fig. 2.1 Sting mounted Boeing 777 in the National Transonic Facility, NASA [10]

leading edge radius and Reynolds number. Force and pressure data was obtained at a range of angles of attack up until stall and was ultimately used to validate against CFD data.

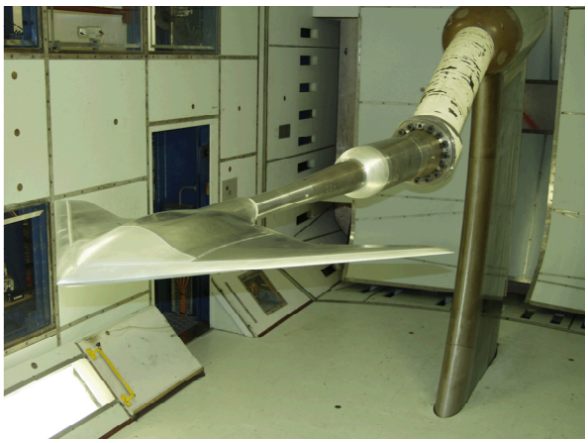

Fig. 2.2 UCAV model in the QinetiQ 5 m tunnel [58]

More examples of subsonic/transonic force measurements range from validations of a six component force balance with the AGARD-B geometry [72], measurement of Reynolds effects on the lift/drag on various wing geometries [44], six-axis force measurement of a quadcopter drone [4] to half model flying-Vs [75]. For all of these cases, the test time is sufficient that a force balance is an appropriate way of determining forces. When moving to the hypersonic regime of testing, the cost of continuous flow facilities is high due to the large amounts of energy required to produce hypersonic flow. Therefore, many hypersonic facilities are of much shorter duration and the standard ways of measuring forces become much more difficult to use, resulting in large uncertainties [6].

Static Force Balances

Static force balance techniques used in continuous flow subsonic facilities are difficult to transfer into short duration hypersonic facilities. Before discussing historic experimental work, it is useful to consider the underlying mechanisms behind sting mounted force balance measurements [14]. Consider an aerodynamic body in a wind tunnel facility. As the facility starts up, the test gas arrives first at the leading edge and then sweeps over the body. At every instance in time, the gas imparts transient forces over the body of the model determined by variations in surface pressure and skin friction. This in turn imparts stress waves which propagate through the models structure and which are transmitted and reflected at model interfaces, leading to a complex formation of super-imposed waves within the model. These waves will eventually damp out to reach a qausi-steady equilibrium with the applied forces. Therefore the quality of the force data measured by the load cell is often influenced by the amount of test time available to the experimenter. Many hypersonic facilities that produce flight representative conditions are short duration in nature and it can often be the case that the stress waves do not reach equilibrium within the test time.

There are a lot more difficulties associated with force balance experiments in the hypersonic regime. In blow-down facilities, the test time is sufficiently large that the stress-waves within the model reach an equilibrium in that time and steady-state forces can be measured. This is not always the case for all hypersonic facilities where the test times may range from a single millisecond to tens of milliseconds. Bernstein and Pankhurst [6] summarises the main difficulties experimenters have with the design and use of traditional force balances in short duration facilities:

1. An ideal multi-component force balance is one in which each axis is independent of signals from other axes. This is often not the case with calibration required to determine the degree of cross-coupling.

2. The attachments to the model and the support transmit stress-waves through the structure. If these are not designed well it can affect the dynamic behaviour of the system.

3. The dynamic behaviour of the whole system is an important consideration. If the natural frequency of the system corresponds to the test time, the force signals will not reach an equilibrium making it difficult to determine the steady state force.

4. Strain gauges are often sensitive to temperature fluctuations. A well designed force balance will have methods of reducing temperature changes, minimising the impact of thermal drift.

For force balance tests to be successful in short duration hypersonic facilities Jessen and Grönig [35] suggested that the criterion for the minimum natural frequency of the model sting setup was at least five cycles of the lowest natural frequency of the model- balance-sting system that must appear during the test time to be able to measure steady state forces and moments. This criterion can be very difficult to reach due to the fundamental physics behind how force balances work. Strain gauges measure deflections and the larger the deflection the easier it is to measure. The deflection of a system upon applying a load is a function of its stiffness with a greater stiffness resulting in a smaller deflection for a given load. The criteria for the minimum natural frequency requires a very stiff model but in practice this would result in deflections that are difficult to measure.

However, static force balance measurements have been successfully applied by Juhany and Darji [38] in which six-component force balance experiments were conducted in the KAU-AT0 Ludwieg tube with a tangent-ogive cylinder at Mach 3. Prior to testing, it was shown that the natural frequency of the system was outside the critical range of interest, allowing for force and moment measurements in the 100 ms of test time duration. A moving average filter of 20 ms was applied to the presented force data so it is difficult to see the raw response of the force balance. However, test-time averaged normal and axial force data both showed good agreement to experimental data by DLR.

Other examples of force measurements with a force balance in hypersonic facilities is the work conducted by Wang et al. [100] in the JF12 shock tunnel located in China. Due to the size of the facility (265 m long, nozzle 2.5 m exit diameter), the shock tunnel generates 100 ms of test flow which is enough time for statically calibrated force balances to be used. Axial and normal forces are measured for a 1.5 metre long cone and good agreement is achieved with previously published NASA Langley data. Two sting balances (a three and six component) were created to measure forces which were machined for the facility with example voltage traces seen in Figure 2.3. The raw voltage traces show large degrees of oscillations, particularly in the normal force which has slow frequency oscillations. These physical vibrations show that even in 100 ms of test time, it is difficult to get clean force signals from statically calibrated force balances.

Another big disadvantage of force balances is that the mounting sting can interfere with the flow if not designed appropriately. Pick [79] showed that the base pressure of a sharp cone became highly non-uniform and sensitive to angle of attack above 15 $^{\circ}$ and greater. Consequently, the base pressure values of the sting mounted model deviated from the free-flight model. For a condition at Mach 9.9, the base pressure for the sting mounted model was 70 % above the free-flight model. This unwanted flow interference would have an influence

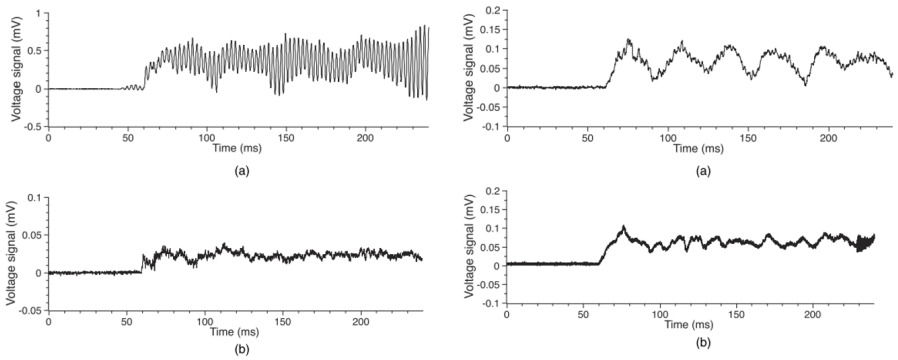

Fig. 2.3 Raw voltage signals from force balances which show structural vibrations superimposed on the force data [100], left - 3 component balance, right - 6 component balance, a - axial signal, b - normal signal)

on the measured forces in a sting mounted experiment if large angles of attack are being investigated.

Stress-Wave Force Balance

The examples from literature for statically calibrated force balances were all for facilities of test times of greater than 100 ms. Sanderson and Simmons [84] concludes that stiffness-dominated balances are only suitable for test times > 200 ms and inertia-dominated accelerometer balances can lower the acceptable test time to only 10 ms. For facilities of test times less than 100 ms such as gun tunnels, Ludwieg tubes, shock tunnels for example, the internal vibrations within the model will not necessarily reach an equilibrium due to the difficulty of designing a sting of sufficiently high natural frequency for the magnitude of the vibrations to decay. Experimentalists, however, have developed two methods which overcome this limitation, stress-wave force measurement and accelerometer-compensated force measurement. A brief explanation of the stress-wave technique is provided in this review, for a detailed discussion see Doherty [14].

The stress-wave technique, first presented by Sanderson and Simmons [84], requires a dynamic calibration of the model force-balance structure to determine aerodynamic forces. Knowledge of the impulse response function of the model and sufficient characterisation of the stress wave pattern allows the experimenter to deconvolve the measured strain signals to determine the net aerodynamic load. Sanderson and Simmons [84] resolved the drag force acting on an axisymmetric body in flow duration of 1 ms using the stress-wave deconvolution method. The dynamic calibration was achieved through suspending weights to the model and cutting them to provide an instantaneous step in force. Figure 2.4 shows the strain gauge measured drag and the deconvolved drag. The deconvolved drag agrees very well with the

predicted theory and uncertainties were around 10 %. Sanderson recommends the use of non-metallic materials such as nylon to allow for shorter response times, improving the response of the balance. This is due to the high damping properties nylon has on sound waves transmitted through it, reducing the oscillation superimposed on the strain gauges.

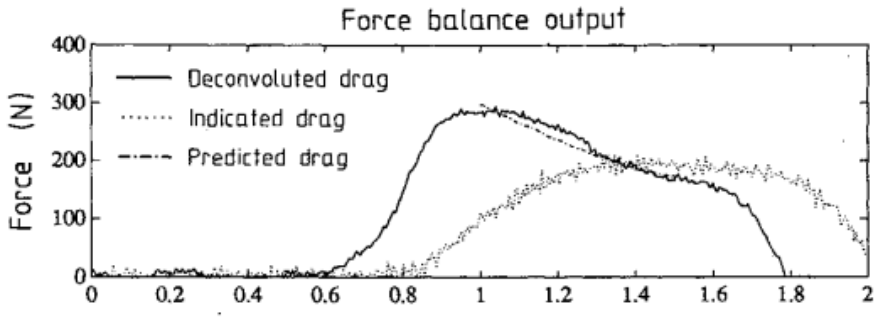

Fig. 2.4 Drag measurement from load cell and deconvolved force (x axis is time (ms)) [84]

Mee et al. [62] used a combination of finite-element analysis and experiments to demonstrate that the stress-wave technique can be used to recover normal, axial and pitching moment for a sharp cone. Again, step loading of cutting weights was used to dynamically calibrate the balance. The experiments showed for the first time that three-component measurements could be taken in shock facilities and obtain reasonable results with experimental uncertainties around 13 %.

In 2003, Mee [61] revisited the stress-wave force balance methodology in the T4 free-piston facility with a 15 degree sharp cone of 182 mm in length measuring only the drag component. This paper presents multiple calibration methods but introduces the determination of an impulse response function from a pulse test using an instrumented piezo-electric impulse force hammer for the first time. This methodology reduced the uncertainty in force measurement down to 3 %.

Following this work, researchers have applied the impulse hammer calibration to force balances to obtain flight representative data, including Robinson et al. [81] in the HEG shock tunnel for a 303 mm long 10 degree blunted cone shown in Figure 2.5. To characterise the global impulse response function required to deconvolve the forces from the measured strains, Robinson set up numerous calibration locations across the surface of the cone and combined the impulse responses to form the global matrix. Force coefficients were measured during experiments that showed good agreement with CFD. Robinson determines that the uncertainty of force measurement is between 4 - 5 %.

Extending this concept of multiple hammer hits further, Doherty et al. [14, 16] applied the stress wave force balance technique to the REST scramjet in the T4 shock tunnel. The

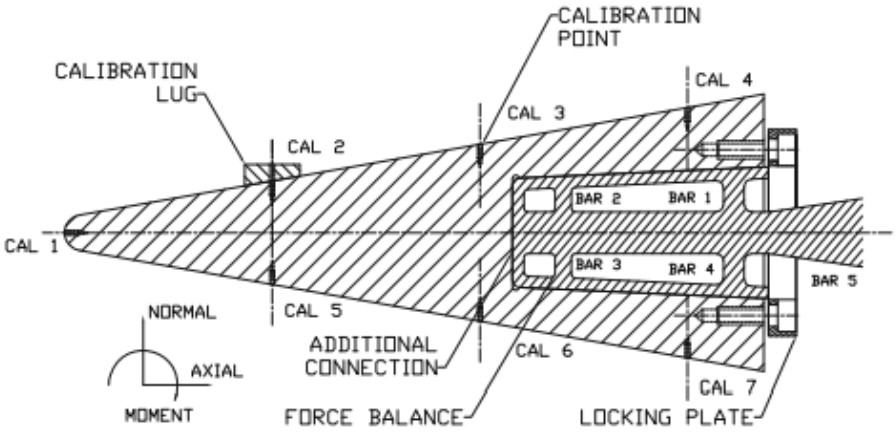

Fig. 2.5 Calibration locations used for the blunted cone experiments [81]

work represents the first measured force data for a hydrogen fuelled scramjet at a Mach 10 flight condition. Figure 2.6 shows the location of the hammer hits used to obtain the global impulse response function, weighted appropriately using data from CFD. The drag coefficient was shown to have uncertainties of 10 %. Net positive thrust was not achieved in the testing due to a low performing three-dimensional nozzle, small engine scale and relatively large leading edge bluntness.

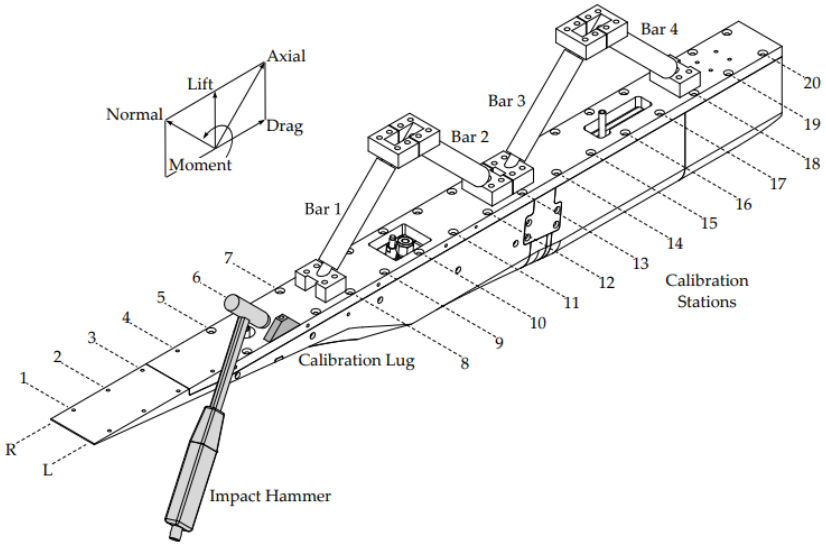

Fig. 2.6 Calibration locations used for the REST scramjet [16]

Accelerometer Compensated Force Balance

An approach to resolving the restrictions on dynamic behaviour of force balances and their mounting structures is to fix an accelerometer into the force balance structure and measure the inertial forces generated by the sting oscillating, first introduced by Martin and Stevenson in 1962 [55]. More recently, Storkmann et al. [92] used the technique in both the TH2 shock facility and VKI Longshot. Whilst the design of Storkmann's strain-gauge balance was optimised for use without compensation, during real use it was shown to oscillate between 80 -200 Hz which was too low for a steady state reading of forces and moments and hence compensation was necessary. To compensate using accelerometers, the oscillating mass of the balances must be determined to form the inertial forces from the data. This was achieved through using an impulse hammer to characterise the model in situ. The balance in these experiments was equipped with six-accelerometers to allow for measurement on all six force balance axes. Three models were tested on this balance; a pointed cone, Apollo capsule and the ELAC I delta wing. Figure 2.7 shows an example shot with the cone model for which raw data and accelerometer compensated data is shown. The addition of the accelerometer removes the oscillatory behaviour of the sting-model from the force data allowing cleaner forces to be obtained during the test time. However, the large scatter in the experimental data was greater than the effect of air chemistry. This prevented the authors from identifying clear trends about the effect of hypersonic gas chemistry and gas composition on the force and moment coefficients for the capsule geometry. The ELAC model was unable to be compensated with accelerometers due to the low resonant frequency of the model balance system which shows that careful model design is still required for models using this approach for measuring forces.

The technique was also applied by Marineau et al. [53, 54] for a 6 inch Apollo capsule model in the Large Energy National Shock Tunnel providing up to 40 ms of test time. The experimental force and moment was within 3.5 % of the numerical predictions, representing the first time the effects of thermodynamic and chemical nonequilibrium on the force and moment coefficients was accurately measured on a reentry capsule in a reflected-shock tunnel using the accelerometer compensated technique.

2.1.2 Ballistic Range

Moving away from rigidly mounted models, ballistic testing allows for the determination of aerodynamic coefficients of vehicles without the interference of stings. It involves launching a sub-scale model from a cannon at very high speeds so that it can move freely in six-degrees of freedom over the length of the ballistic range. There are two variations on this method; an

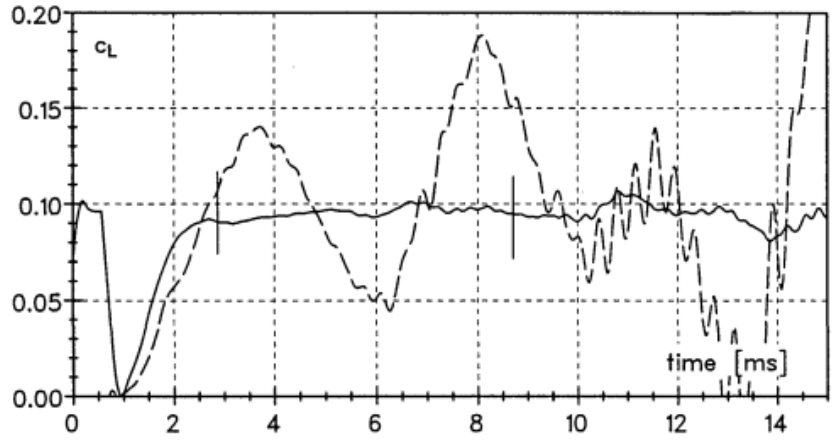

Fig. 2.7 Lift coefficient for cone model, dashed line - uncompensated data, solid line - accelerometer compensated data [92]

outdoor range tests models in air at atmospheric pressure whereas an indoor enclosed range can change the test gas composition and pressure. As the pressures in an evacuated tube are lower, it makes higher Mach numbers more achievable but this is at the expense of the costs of producing such a large facility that can provide enough model flight test time at these very high speeds. To be able to track the model optically in free-flight, multiple optical sensors are required along the length of the range. Strawa et al. [93] discusses the expense of performing such optical tracking as the speed of the model passing by dictates sub-microsecond exposure times to eliminate the effects of motion blur, and extremely powerful light sources, faster optics, and more sensitive sensors are required. Wilder et al. [103] discussed the capability of the NASA Ames ballistic ranges and the challenges in designing models suitable for testing the ballistic ranges. Models need to be able to withstand the high heating loads upon launch as well as accelerations up to 100,000 g. The extreme initial accelerations are not suitable for small on-board accelerometers which usually have thresholds an order of magnitude lower. If this threshold is exceeded, the internal mechanics of the sensors can be permanently damaged, therefore measurement techniques in ballistic ranges are limited to optical techniques only.

An early example of this form of testing was conducted by Bailey and Hiatt [3] who tested spheres at the Hyperballistic Range of the von Karman Gas Dynamics Facility over a large range of Mach numbers (0.1-6.0) and Reynolds numbers to determine drag coefficients. Six shadowgraph stations were used to track the sphere's displacements and hence differentiated to determine acceleration. This double differentiation is a noisy process and leads to increased uncertainties (2 %). Measurements were accurately taken for drag coefficient over the map of Reynolds numbers and Mach numbers.

More recently Schoenenberger et al. [85] conducted ballistic range tests for the flight profile of the Mars 2020 entry capsule for a 2 % model. As well as using shadowgraph images at 15 locations down the range of the TEF facility, the model was instrumented with on-board pressure sensors to measure the aftbody pressures. Aerodynamic coefficients were determined by fitting 6-DOF trajectories through shadowgraph position/orientation data.

2.1.3 Electromagnetic Suspension

Magnetic suspension and balance systems (MGBS) are an attractive method of measuring forces in hypersonic facilities offering the main benefit of sting-free interaction with the flow. A MGBS is designed to suspend a model within the core flow of a wind tunnel facility using a series of electromagnets which generate a magnetic field. By creating a gradient of flux density within the core of a facility, control of the model and measurement of forces can be obtained. With clever design of the magnetic coils, up to six degrees of freedom in force and moments can be measured. It is important that an appropriate control system is in place to control the model's position and attitude within the tunnel.

Since the early 1970s, magnetic suspension systems have been used at the University of Oxford within the Low Density Tunnel (LDT), a free-jet, open circuit, continuous flow facility capable of providing hypersonic flows within the slip and transition regimes. A thorough review of work within the University of Oxford is provided in Doherty et al. [15]. Owen and Owen [73, 74] conducted magnetic suspension experiments with simple re-entry geometries in rarefied flow, this included:

1. The measurement of drag coefficient for sharp cones.
2. Drag measurements of an Aerobreak geometry
3. A feasibility study of the NASA Hyper-X flight separation manoeuvre

For this work, the magnetic fields were controlled by Proportional, Integral, Differential (PID) analogue electrics with feedback provided by optical detection of model position. The models were controlled in 3 degrees of freedom pitch, lift and drag and aerodynamic forces measured by the magnetic force required to suspend the model being taken. Initial experiments were undertaken with a 6 degree half-angle cone with a series of afterbody geometries. Owen clearly demonstrated that increasing the afterbody sting length had a notable effect on the drag measurements of up to 18 %. Following the cone model experiments, the complex Hyper-X was tested within the facility. Unfortunately, no aerodynamic data was published from these experiments due to the sensitive nature of the work.

Fig. 2.8 Hyper-X seperation in LDT [69]

It must be noted that the above experiments for magnetic suspension facilities are typically within the facilities with low density or low speed flows with small un-instrumented models resulting in forces that are low in magnitude when compared to facilities simulating flow in the continuum regime. This type of setup is yet to be implemented within an impulsive Ludwieg tube type facility likely due to the difficulty of balancing the larger magnitude of aerodynamic forces generated within these facilities, particularly in the transient start up period.

2.1.4 Weakly Restrained Model

A weakly restrained model is one in which the supporting system is designed so that the forces imposed by them are negligible compared to the aerodynamic forces. Often, the model is allowed to move in a controlled manner with low friction brushes or bearings guiding the path. The mounting structure will often allow for wires to pass through to the model, allowing for instrumentation of the model. There will often be a mechanical limit to the motion of the model to prevent damage to the mounting structure, model or cables.

An example of the weakly restrained model testing was conducted by Joshi and Reddy [37] in the IISc shock tunnel at Mach 5.5 with four different missile geometries. For these tests, three fast response accelerometers were rigidly attached to the inside wall of a hollow model and the model was attached to a central sting by two rubber springs. Although the model motion was limited by the springs, it was shown that the extent of dampening on the model is insignificant and so the model can be seen to be 'free-flying' during the test time. The values of lift and drag coefficient agreed well with theory with uncertainties around 10 %. However, pitching moment coefficient data was in poor agreement with the numerical predictions. Joshi cites that this is due to the pitching moment data being measured by the difference of two accelerometers which amplifies any inaccuracies in the measured value.

Sahoo et al. [83] compared the weakly restrained technique to a stress-wave force balance in the HST2 shock tunnel at Mach 5.75. In this case for the weakly restrained tests, the 30 °

semi-apex-angle blunt cone model was suspended by strings and allowed to displace by 0.1 mm in the 1 ms test time. Only the drag component was measured and the uncertainties for the stress wave balance and accelerometer balance were found to be 6 % and 5 % respectively.

Overall, the weakly restrained methodology has been show to be effective at measuring forces in short duration facilities, however, in more recent times it has been replaced with the free-flight methodology due to the lack of sting interference, as seen in the next section.

2.1.5 Free-Flight

A variation of sting-free aerodynamic testing is known as the free-flight technique [10]. Rather than the sub-scale model moving at high speeds as in the ballistic range, in the free-flight technique the model is released into the core of a wind tunnel and is allowed to move in 6 degrees of freedom in the oncoming tunnel freestream. Therefore, as the model is unconstrained, non-intrusive methods of determining forces are required by measuring the kinematics of the model motion.

The earliest free-flight tests to the author's knowledge were conducted under Seigel [86] at the US Naval Ordnance Laboratory and Geiger [23] at the General Electric Space Sciences Laboratory, both in shock tunnel facilities. Due to the lack of sophisticated technologies of the era, measurements were limited to optical tracking and schlieren photography of the models. Whilst technology has become more advanced in recent years, the general principles of the free-flight methodology have remained the same. A typical methodology of a free-flight test in short duration facilities is as follows: the model is released prior to arrival of the test flow, the flow is initiated over the model which allows it to move as it would in flight. Consequently, there is no external interference on the flow around the model, thus, it is more representative of real flight. This technique requires non-intrusive methods to measure accelerations, from which the aerodynamic forces may be derived.

As a consequence of this methodology, there are a number of areas a researcher must consider when conducting free-flight experiments. These include:

1. Model scaling - it is important that a number of features of the model are scaled appropriately to achieve kinematic and dynamic similitude with flight, these include geometric scaling, inertial scaling (mass and moment of inertia) and scaling of centre of gravity. This is summarised in Chapter 3 and by Wolowicz et al. [105]. Furthermore, the scale must be chosen such that the wind tunnel model is appropriately sized for the core flow of the facility.

2. Freestream scaling - the freestream conditions produced by the wind tunnel facility must be scaled to correctly represent flight. In the hypersonic regime, this involves the matching of Reynolds and Mach number. This is discussed further in Chapter 3.

3. Release mechanism - a suitable method of releasing the model into the core flow prior to testing is required. It is imperative that the model is correctly positioned within the tunnel upon flow onset to prevent interaction of the model with the edge of the core flow.

4. Catching mechanism - unlike conventional tests where models are held rigidly in place, free-flight models are allowed to move freely. Therefore, a mechanism is required to catch the model after a test to mitigate the chance of damage after a test.

5. Non-intrusive measurements - a methodology is required in free-flight that can measure the kinematics of a model. Frequently this is optical tracking and the measurement of linear and angular displacements or on-board inertial measurement units (IMU) measuring linear accelerations and angular velocities.

Before going in depth into the literature for free-flight experiments, the pros and cons of the force measurement techniques presented in this section are discussed.

2.1.6 Review of Hypersonic Force Measurement Techniques

In this section, relevant literature for different force measurement techniques have been reviewed. Table 2.1 discusses the key advantages and disadvantages of each method and their relevance for short duration testing in a Ludwieg tube facility with test duration of 50 ms.

The force balance is the most common form of testing for aerodynamic force measurements but difficulties arise in short duration facilities with regard to the dynamic response time of the supporting structure and model in determining quasi-steady state forces with minimum acceptable test times of 100 ms quoted in the literature. The stress wave force balance and accelerometer compensated force balances seek to overcome this issue and reduce the effective measurement time to 1 ms. However, difficulties arise with complex geometries when calibrating the model to obtain a global impulse response functions and the complexities required to write a matrix deconvolution algorithm to back out the forces from the strains. Even with these improvements, there still lies the fundamental issue of sting interference with the flow that can result in parasitic drag on the measurements and unwanted shocks.

Ballistic range force measurements have been shown to acquire useful force data at flight representative conditions. However, the cost of building such a facility is high and requires

multiple sets of optical equipment down the length of the range to measure the trajectory. Furthermore, accelerometers are unable to survive the extreme accelerations the models are subject to in the range.

Weakly restrained models offer the benefit of removing the rigid mounting structure and hence increase the natural frequency of the system to allow for forces to be measured through the displacement of a model or measuring accelerations with accelerometers. However, similar to a force balance, the 'weak restraints' must be carefully designed so they do not interact with the flow and affect the flow physics and hence aerodynamic forces.

The methodology of using a magnetic suspension and balance system offers a form of aerodynamic testing that is truly independent of flow disruptions such as stings. The presence of a strong magnetic field, however, will make it difficult to instrument a model with on-board electrical sensors without sufficient shielding. Furthermore, the cost of building and implementing such a system is very high. To date, a MSBS system has yet to be used in an impulsive system such as a Ludwieg tube as the forces imparted on a model are much higher than typical tunnels these are used in for rarefied flow. This leads to questions if it is possible to design a system for use in these tunnels.

The free-flight methodology offers sting-free testing in wind tunnel facilities. Forces can be acquired both through on board inertial measurement units and image tracking. The technique can be complex to setup as model scaling needs to be considered and appropriate ballasting to position the centre of gravity is required but it overcomes all of the limitations of the other techniques for acquiring force measurements in short duration hypersonic facilities as well as offering the chance to measure dynamic behaviour of models.

Overall, all of the techniques above have been shown to measure forces with various advantages and disadvantages in hypersonic facilities. The choice of technique used is often influenced by the availability of a particular facility, adding convenience. For testing in a Ludwieg tube, the free-flight methodology and the stress-wave force balance are the most viable options with the benefit of free-flight being sting-free. The historic work in the area of free-flight will be discussed further in the next section.

Table 2.1 Summary of force measurement techniques in the literature

Technique	Free of Sting Interference	Suitable for Ludwieg Tube	Direct Force Measurements	Optical Measurements	Static Measurements	Dynamic Measurements
Force Balance	No	No	Yes	No	Yes	No
Stress Wave Force Balance	No	Yes	Yes	No	Yes	No
Accelerometer Compensated Force Balance	No	Yes	Yes	No	Yes	No
Ballistic Range	Yes	No	No	Yes	Maybe	Yes
Weakly Restrained	No	Yes	Yes	Yes	Yes	Maybe
Magnetic Suspension	Yes	No	Yes	Yes	Yes	Yes
Free-Flight	Yes	Yes	Yes	Yes	Yes	Yes

2.2 Hypersonic Free-Flight Literature

After reviewing the relevant literature on the many different force measurement techniques in hypersonic facilities, a case has been made to pursue in depth the literature for free-flight experiments. This section reviews the most recent advances in the free-flight force measurement technique separated by institution, including all the advancements each author has made to the literature.

2.2.1 University of New South Wales (UNSW) Canberra and University of Southern Queensland (USQ)

Free-flight has been conducted for over a decade at UNSW Canberra with the experiments increasing in complexity over time. The first true free-flight experiment that utilised modern high speed image tracking technology was conducted by Neely et al. [69] in 2008 to determine the drag coefficient of a sphere in a shock tunnel facility, a force measurement well documented in previous work. The free-flight experiments used lightweight polystyrene spheres of 37.5 mm diameter in the T-ADFA shock tunnel, a facility that produces Mach 10 for test time of between 0.5 - 1.5 ms. The model was released using electromagnets and model displacements determined using optical tracking at 32,000 fps for 103 frames. The displacement of the sphere was determined by fitting a circle to the outline using an edge detection algorithm and scaling the image based from the sphere diameter.

The calculated drag coefficient agreed well with previously established data, albeit with high uncertainties of approximately 14 % as seen in Figure 2.9. Neely cites the main contributors to the uncertainty of force measurement with this technique as the uncertainty of freestream conditions in shock facilities and the spatial resolution of the images. It is optimal to have as much as the model filling the field of view as possible so that the errors are not within the individual pixels of the image. It is also optimal to have high quality lighting to increase the contrast between the background of the facility and the edge of the model.

Following on from the work of Neely, it was noted that having on-board accelerometers and gyroscopes to directly measure accelerations would reduce the uncertainty of the free-flight technique. A breakthrough in free-flight research was achieved by Mudford et al. [67] who used miniaturised on-board accelerometers and gyroscopes to directly measure linear accelerations and angular velocities. The advantage this has over optical tracking is that the double differentiation required to calculate accelerations from displacement data when using optical tracking introduced large uncertainties into the measurement of aerodynamic coefficients. Measuring the accelerations through IMUs (Inertial measurement unit) directly removes this issue.

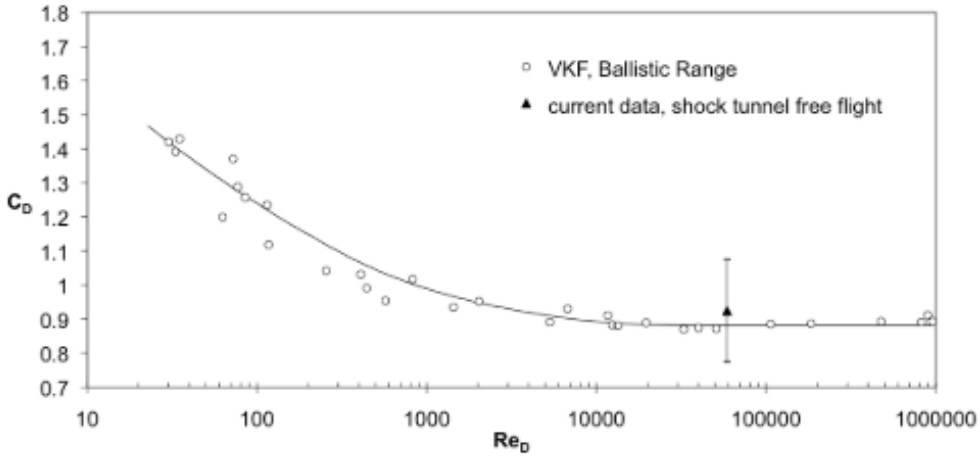

Fig. 2.9 Drag Coefficient of spheres in high Mach number flow [69]

These experiments were conducted in the University of Southern Queensland's medium duration TUSQ facility providing 200 ms of steady test time of Mach 6 flow. The model was a hollow steel hemispherical-nosed cylinder of 110 mm in length with IMU instrumentation onboard. The accelerometer was an Analog Devices ADXL326 sampled at 100 Hz. Optical tracking was also performed at 2000 fps and combined with schlieren imagery. The release mechanism consisted of a string sling holding the model in place which was cut by a push knife solenoid prior to flow onset (as seen in Figure 2.10). The results indicated that the onboard IMU data produces more reliable, robust and detailed results but Mudford concludes that the ideal is to have both systems in tandem as independent validation of the technique. Large variation was seen on the pitching moment coefficient data between shots with the data 30 % greater than numerical predictions. Of particular interest was the non zero value of pitching moment at zero degrees angle of attack for all shots - an unphysical result for an axisymmetric body. Mudford accounts two reasons for this uncertainty in angle of attack; the first is that the reference datum of an angle of the image had an offset or secondly, the flow is not exactly parallel to the nozzle.

Continuing on from the work of Mudford, Kennell et al. [40, 39] conducted free-flight tests of a 1 : 13 sub-scale model of ESA's HEXAFLY-INT EFTV glider geometry of 253 mm in length at the TUSQ facility at Mach 5.85 which represents the first free-flight tests conducted with a complex lifting geometry instrumented with an IMU. As this model represented a real flight geometry, the model inertial properties and freestream conditions were scaled as such that the measured coefficients were representative of the flight vehicle.

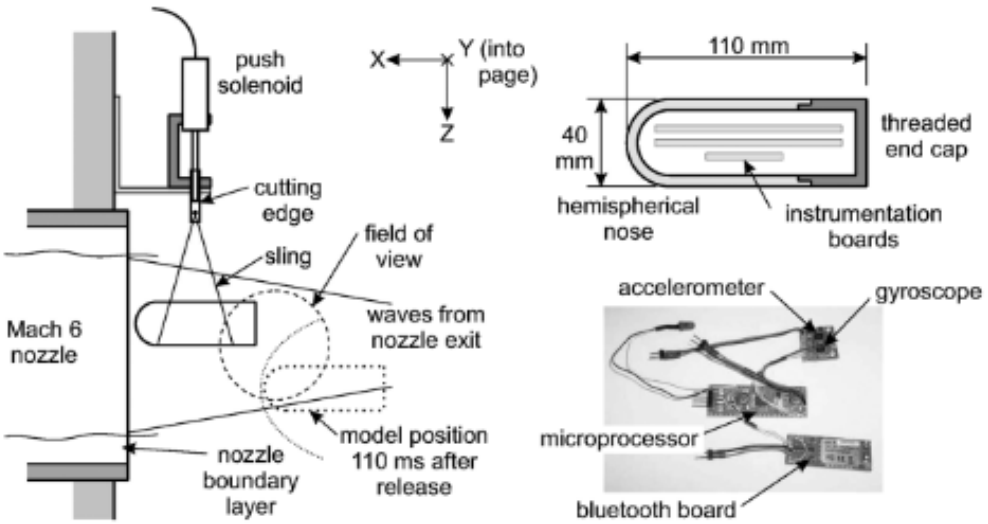

Fig. 2.10 Mudford's [67] free-flight experimental setup

However, the facility was unable to match the required Reynolds number for complete similitude of that trajectory point which means the simulated altitude is no longer matched.

Both high-speed image tracking and on-board electronics are used to determine the aerodynamic coefficients. Image tracking was achieved by tracking registration marks on the side of the model; providing both translation and rotational motion. The release mechanism used was a mechanical arm with a conformal to the model rubber fitting that allowed the angle of attack to be set. The model was released when a knife edge cuts the string. The tests show good agreement in lift coefficient and pitching moment coefficient although there were large degrees of scatter between runs. The drag coefficient shows no correlation of the expected quadratic shape. Kennell suggests this is due to the roll experienced throughout the experiment which reaches a maximum of 30 degrees. Static stability is also determined and found to be stable – denoted by a negative gradient on a Cm vs alpha graph. Uncertainties were shown to be of 15.9 % in magnitude with the main source of error propagating from the uncertainties in the freestream conditions. Overall, the experiments showed that longitudinal force coefficients can be obtained through free-flight with complex geometries, however, dynamic motion such as roll, pitch and yaw may influence the instantaneous measured coefficient.

Increasing the complexity of the free-flight experiments further, Kennell et al. [41] conducted free-flight separation experiments with the HEXAFLY geometry and its attitude control module. These experiments represent the first free-flight separation experiments in which both models were instrumented with onboard inertial measurement units. Image tracking for both modules was also conducted. The models had their mass and moment of

inertia scaled from flight vehicle values to match the dynamic scaling requirements. However, there was a large mismatch in the mass of the glider for the low pressure condition which resulted in different separation mechanics to flight. The justification of these experiments was that whilst the inertia and separation dynamics would not represent flight, numerical simulations can be conducted to match these inertias providing validation. The experiments were simulated with DLR TAU CFD and showed reasonable agreement with the experimental data. These experiments ultimately showed that whilst it is possible to conduct separation experiments with reasonable results, it is difficult to scale the inertia of the models to reach true flight conditions.

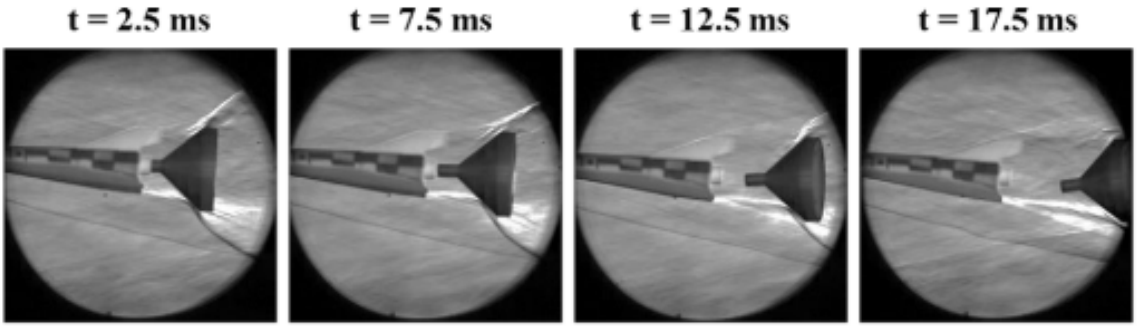

Fig. 2.11 Kennell's [41] experimental HEXAFLY and separation module experiments

2.2.2 Japan Aerospace Exploration Agency

Experiments have been conducted at the Japan Aerospace Exploration Agency (JAXA) with various geometries in the HIEST shock tunnel. Unlike the experiments at UNSW, the facility at JAXA is a high enthalpy facility and hence can replicate real gas effects with the downside of shorter test time, approximately 1-10 ms. In 2010, Tanno et al. [27] conducted the precursor experiments for true free-flight. Models were weakly suspended with thin wires in the HIEST shock tunnel and force measurements were taken with accelerometers during the test time. Three component force measurements were taken for a blunted cone model and HB-2 model which were instrumented with 4 accelerometers. The model was calibrated with an instrumented impact hammer and a deconvolution process was undertaken to characterises the impulse response function of the suspended model. This response function could then be deconvolved with the accelerometer data to obtain the frequency removed accelerations. Results were compared with experiments undertaken in a blow-down facility with a force balance with good agreement giving confidence in the short duration methodology in a shock tunnel with uncertainties in coefficients remaining below 4 %.

Following on from the weakly suspended experiments, Tanno et al. [95, 96, 28, 97] has conducted multiple free-flight campaigns with various geometries, ranging from reentry capsules to lifting bodies, in high enthalpy conditions. The models were between 195 - 440 mm in length and weighed between 16.78 - 20.13 kg. Due to the weight of the models and short test time, model displacement and pitching were very small during the test time and as a result these experiments can be seen as 'static' aerodynamic tests. Models were released into the flow using high powered electromagnets and all on board sensors were sufficiently shielded from the electromagnet. In all of the models, piezoelectric accelerometers with a sampling time of 500 kHz were used. Without the use of gyroscopes, a minimum of six accelerometers are required - two on each axis - to obtain six degrees of freedom linear and angular accelerations. Gyroscopes are not used to obtain angular rates because they have lower sampling rates than accelerometers. Pressure transducers were also included on the models to obtain a measurement of pitot pressure to normalise the aerodynamic forces.

In 2014, Tanno et al. [95] experiments in free-flight with a blunted cone were undertaken in HIEST at a high enthalpy condition (16 MJ/kg) to produce real gas effects in the flow and at a low enthalpy condition (4 MJ/kg) in which perfect gas conditions can be assumed. This same cone was also tested in the JAXA HWT2 blow-down facility to allow direct comparison with the assumed perfect gas conditions in HIEST. This work represented the first free-flight experiments to investigate the influence of real gas effects on aerodynamic coefficients. For all three cases, axial and normal forces were within experimental uncertainty when compared to the numerical predictions but for the pitching moment coefficient, there was an offset in the coefficient for the real gas effect conditions resulting in a higher trim angle of attack (as seen in Figure 2.12). As this trend was only noted in the pitching moment, not the axial and normal force coefficient, Tanno concluded that this change is a result of the centre of pressure shifting forward due to the real gas effects.

In 2018, Tanno et al. [97] conducted free-flight experiments at the low and high enthalpy conditions for more complex geometries; a re-entry capsule and a lifting body, HYFLEX. For the re-entry capsule, the trim angle for the low enthalpy condition was 29 degrees and for the high enthalpy condition was 32 degrees. However, after the uncertainty bands are applied to the data set, the PI-bands overlapped so Tanno concluded that there was no significant difference between the two conditions. The longitudinal forces measured were the same between the two cases. The impacts of real gas effects were much more pronounced for the HYFLEX lifting body where the trim angle of attack was 45 degrees and 55 degrees respectively for the low and high enthalpy conditions. Therefore, this work showed that the effects of real gas effects on centre of pressure and pitching moment are significant, particularly for lifting bodies.

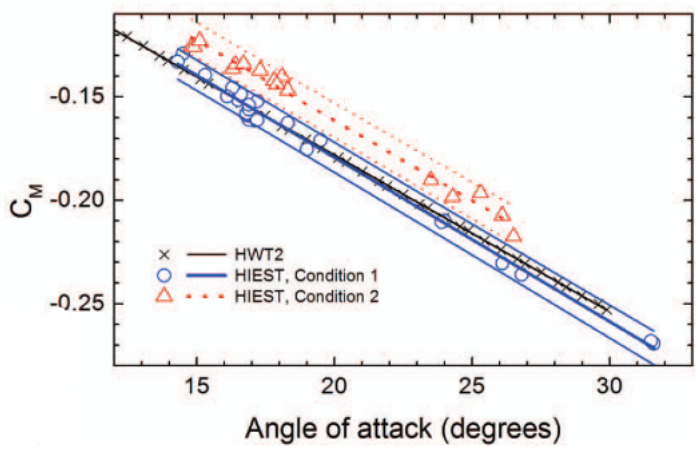

Fig. 2.12 Pitching moment coefficient for blunted cone demonstrating higher trim angle due to real gas effects [95]

Fig. 2.13 HYFLEX in free-flight in JAXA HIEST [97]

Tanno et al. [98] also conducted free-flight experiments with the Model of Demonstrator Kakuda Initiative (MoDKI), a fully integrated scramjet vehicle measuring 1.1 m long. The model contained the fuel injection system but was only tested in the fuel off orientation. In this model, more accelerometers were used than required resulting in an overdetermined system, improving the uncertainties originating from the measurement variability of each acceleration. Experiments were conducted at angles of attack from 0.7 to 3.4 degrees at a Mach 8 condition. Figure 2.14 shows the MoDKI vehicle suspended on electromagnets

in HIEST. This work represents the first time a redundant accelerometer system has been used to obtain force coefficients, however, this may have limited use due to the fact that the models tested in HIEST are very large and have the volume to contain a large quantity of onboard sensors.

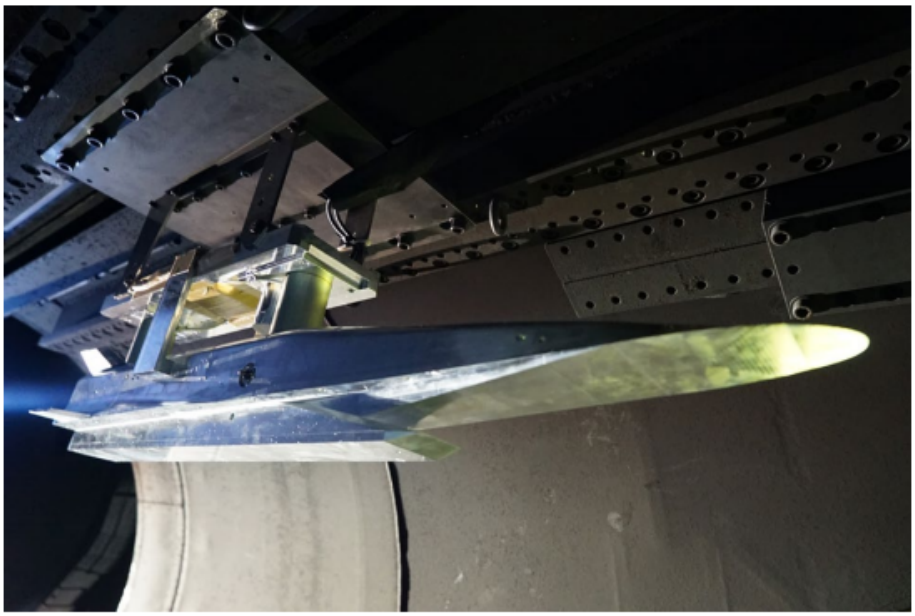

Fig. 2.14 MoDKI model suspended on electromagnets in JAXA HIEST [98]

2.2.3 California Institute of Technology

Laurence has been at the forefront over the years of improving the optical techniques used to measure displacements (linear and angular) during free-flight experiments and as such become standard for other free-flight researchers to employ similar techniques. A series of improvements to the algorithm have been made over the years, in 2009 Laurence and Hornung [45] published work which presented the measurement of displacements using linear and non-linear image tracking techniques. The linear technique was implemented on a sphere and was used to fit a circle to the outline of the shape using an edge detecting Sobel filter followed by a liner regression on the equation of a circle to the detected locus of edge points. This method provided information about the centre of the circle and the radius providing a scaling factor for the image. The algorithm was found to have a standard deviation on displacement of 6 μm resulting in a uncertainty of 7 % of the drag force. The non-linear technique requires an analytical solution of the cross section of the model in the form of model radius and internal angle, with the origin taken as the centre of mass. Edge

detection finds the locus of the model outline and from this Newton's method is used to fit the x,y co-ordinates, centre of gravity co-ordinates, angle of attack and scaling factor. This algorithm was applied to the Orion capsule in semi-constrained free-flight, instrumented with accelerometers within the T5 hypervelocity shock tunnel with standard deviations of 60 - 90 μm in displacement and 0.04 $^\circ$ in angle of attack. Whilst this is worse than the linear technique, this was attributed to the quality of the images obtained with a spark-gap source rather than the algorithm. The experimental results, shown in Figure 2.15 shows large degree of scatter in both lift and drag, attributed to the high luminosity of the flow in shock facilities, making it harder to detect the edge of the model. The data for pitching moment coefficient was not presented as the measured values were inseparable from the uncertainty.

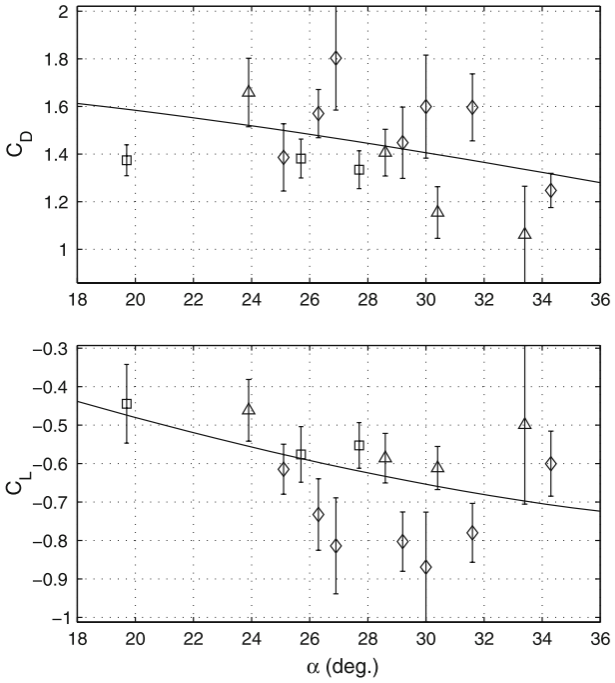

Fig. 2.15 Lift and drag coefficient for the Orion capsule measured through Image tracking. Circle - low enthalpy, triangle -high enthalpy, solid line - Newtonian profiles [45]

Revisiting the images in 2010, Laurence and Karl [46] revisited the Orion data and applied a new highly accurate least-squares tracking algorithm to the outline of the capsule. Changes from the previous algorithm included, a switch to the Canny edge-detection filter and the implementation of a sub-pixel algorithm on the detected edge pixels. Through this new implementation, the precision in linear displacements were reduced to 1 μm and angular displacements to 0.001 $^\circ$. This in turn reduced the uncertainty in accelerations to just 1 %.

2.2.4 University of Maryland

The University of Maryland (Starshak and Laurence) [88, 89] have developed an advanced GPU-accelerated optical tracking algorithm for free-flight experiments and represents the first set of experiments to track free-flight experiments in 5/6 degrees of freedom with a single camera. The work extends on the optical tracking developed by Laurence et al. [45, 46], by edge fitting arbitrary geometries using outlines constructed from a 3D model of the test article generated from CAD programmes. In theory, this allows any geometry that has been designed with computer aided design software to be tracked in 5 or 6 degrees of freedom depending on the geometry. For an 100 mm model Starshak reports an accuracy of 1 μm and pitch angle accuracy of 0.001 $^{\circ}$. The algorithm was tested in the University of Maryland HyperTERP shock tunnel facility at a Mach 6.4 condition with a test time of 1-3 ms. Both a plastic sphere and 3D printed lifting body, HL-20, were tested. The results for lift coefficient of the HL-20 body were significantly lower than numerical predictions. This was due to the unknown angularity of the flow relative to the free-flying model which would require pressure transducers to resolve. The downside of this algorithm is that it takes approximately 20 seconds to analyse a single frame so is very computationally expensive.

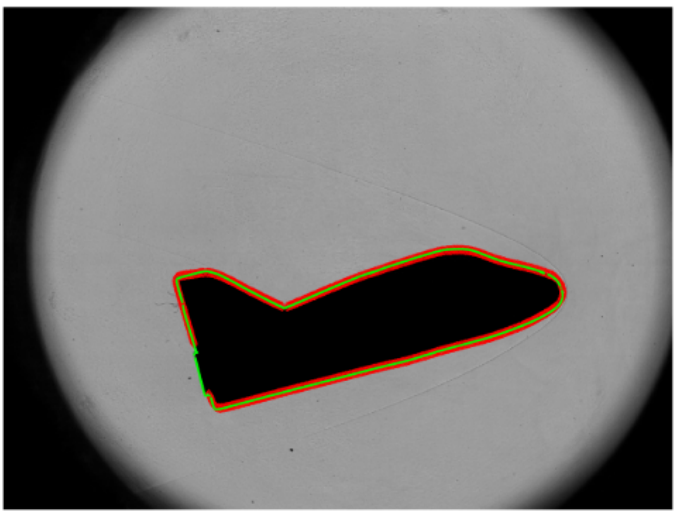

Fig. 2.16 HL-20 model in free-flight with optical tracking algorithm overlaid [88]

2.2.5 DLR

Following this work, Friedl et al. [22] developed an optical tracking algorithm from high-speed imagery for use in the Göttengen shock tunnel for reentry capsules. The main steps of

the image tracking algorithm are as follows (based from the previous work of Laurence and Karl [46]):

1. Compute gradients of schlieren image
2. Mark pixels of high intensity
3. Sub-pixel refinement of edge points
4. Compare analytic model description with edge points
5. Iterative optimization of fit and removal of outlier pixels

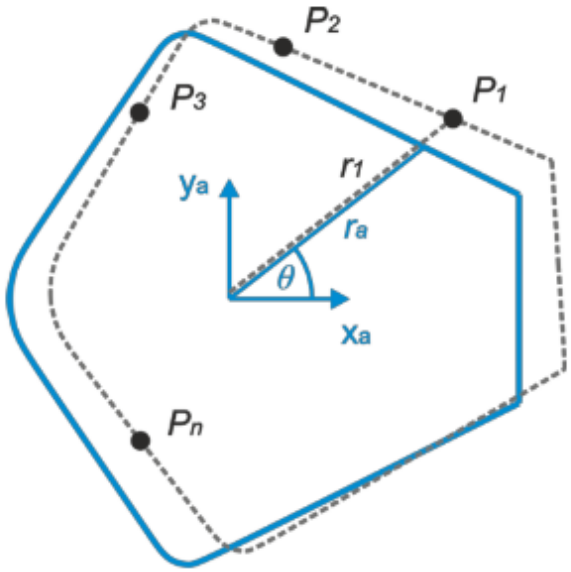

Fig. 2.17 Schematic of image tracking algorithm used by Friedl et al. [22]

A Phantom v1210 high-speed camera was used to acquire schlieren imagery at a frame rate of 32,000 fps and these frames were used for the image tracking. Drag coefficients was obtained for the capsule with an uncertainty of 0.34 %.

Following this study, DLR have used the free-flight technique to measure the net aerodynamic force generated by a scramjet intake, both with fuel on and fuel off [25], the first active fuel-on scramjet experiments in free-flight. The tests were conducted on the LAPCAT II inlet for which the model was 1.5 m long and weighed 85 kg. Similar to the JAXA testing discussed, model displacement is in the order if 0.1 mm so again can be considered a sting-free static test. The tests are conducted in the High Enthalpy Shock Tunnel Göttengen which generates Mach 7.4 flow for 3-7 ms. Upon onset of flow, Kevlar strings suspending

the model are cut and on-board pressure transducers are triggered to measure flow properties. Optical tracking was used to derive model motion and forces derived from the displacement history. However, as the model was larger than the field of view of the window, only a small trapezoidal shape at the top of the scramjet was tracked. Due to the mass of the model, the displacement was very small during the test resulting in an uncertainty of approximately 7%. Ultimately, the experiments showed that the scramjet generated thrust when the fuel was injected and that the numerical simulations under predicted the measured forces by 7.6-16 %.

2.2.6 von Karman Institute

The free-flight work at the von Karman Institute has primarily focused on geometries representative of space debris, aiming at determining their lift, drag and pitching moment coefficients using optical methods. Grossir et al. [24] conducted free-flight experiments in the VKI Longshot facility providing a test time of 20 ms with Mach 11 flow. Pure nitrogen is used as the test gas to prevent flow dissociation effects at the high enthalpy conditions whilst providing flow that wss representative of Earth reentry. Two models were tested; a hemisphere of 50 mm diameter and an annular ring of 60 mm diameter. The image tracking algorithm is of similar form to Laurence et al. [45] in which the edge of the geometry is detected in schlieren imagery frames. Grossir notes issues with the attached shocks to the bodies within the schlieren imagery that make it difficult to detect the true edge of the object with this methodology. Results are presented for lift, drag and pitching moment coefficient which are all in good agreement with numerical predictions over a wide range of angles of attack.

2.2.7 University of Manchester

Fisher et al. [21] conducted free-flight experiments to examine the shock-shock interactions between a fixed sphere and a sphere in free-flight at a Mach 5 condition. The flow field was visualised using both schlieren and background orientated schlieren (BOS). Six Edney shock interactions were identified. Overall, it was concluded that the spatial resolution of conventional schlieren was much superior to BOS in determining shock patterns. The model release for these experiments consisted of a compressed spring released by the movement of a yoke plate. Due to a sphere's symmetry, the release did not need to take into account angular control such as pitch, roll and yaw.

2.2.8 French-German Institute of Research of Saint Louis (ISL)

ISL's shock tunnel facility has been used to conduct free-flight experiments of missile-type geometries with flow durations of approximately 10 ms at Mach numbers of 3 and 4.5 . Wey et al. [101] conducted experiments with a 12.8 mm calibre Explosively Formed Penetrator (EFP) model. The model drop mechanism consists of thin paper and string which breaks up upon flow initiation. This event takes approximately 1 ms and does have an influence on the initial conditions of the model motion. Aerodynamic data is extracted exclusively using optical tracking of three reference points on the model. Drag and pitching moment coefficient data agreed well with the reference data with max discrepancy at 11 %. Martinez et al. [56] conducted more free-flight experiments with the Guided Supersonic Projectile (GSP) using the same methodology as Wey. The tracking methodology was improved by increasing the number of markings on the model and using these points to derive both rolling and yaw motion from a single camera. The results for out-of-plane motion were not validated against a separate method so accuracy of the methodology was difficult to determine.

2.2.9 University of Stuttgart

Leiser et al. [47] conducted free-flight experiments replicating the break-up scenario of the International Space Station (ISS) during re-entry. The work marks the first approach at measuring internal joint stress with complex geometries during separation. The experiments were conducted in the TUSQ facility at the University of Southern Queensland. The ISS model was comprised of three individual cylindrical modules that were 3D printed and tested in 3 different orientations as seen in Figure 2.18. The drop mechanism for this work was a Chebychev lambda linkage release platform which in its mechanical design, guarantees that no forces are applied to the model during release. Forces were determined during the test by tracking the individual modules and calculating the relative motion between the modules, hence inferring the forces in the joints. The frame rate of the optical setup was 2 kHz which resulted in large uncertainties in the measured joint force between repeats, in one orientation the uncertainty is 50 %.

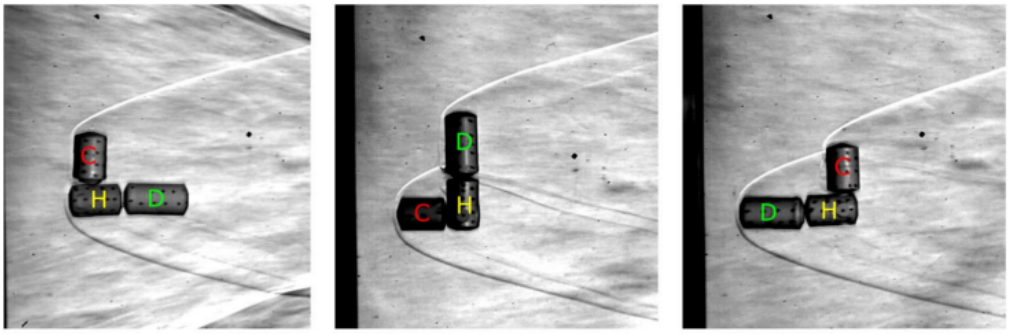

a) Normal b) Vertical c) Reverse

Fig. 2.18 Orientations of the ISS modules tested in free-flight [47]

2.2.10 University of Southampton

Whilst not as recent as the other experiments discussed in this section, Lewis and East [48] conducted free-flight experiments in the University of Southampton gun tunnel with 10 ° half-angle cones with a focus on measuring dynamic stability derivatives. A 42 mm low inertia cone model was free-flown and designed so that it would oscillate in the test time of the flow. High-speed passive tracking was used to measure the model's displacements, with lasers projecting the shadow of the model onto photo-sensitive diodes. The coefficients were calculated by curve fitting the measured data and the accuracy of dynamic derivatives was determined by how many full oscillations in pitch were seen during the test time. The derivative can be determined from the decay of the amplitude of oscillations. The measurement of dynamic derivatives showed significant scatter which was attributed to the yaw oscillation the model would undergo if it was not perfectly aligned with the freestream. There is also a fair degree of scatter in the static force coefficients, in particularly the normal force coefficient which is influenced by the initial angle of attack the model begins oscillations at. The experiments ultimately showed that dynamic derivates can be measured in free-flight if there is sufficient test time for the model to oscillate.

2.2.11 Summary

The previous section has reviewed all recent notable free-flight experiments within hypersonic facilities and presented their significance to the literature. In this section, some of the important aspects of free-flight are summarised and the approaches taken by different researchers highlighted.

Drop Mechanism

Common to all free-flight experiments is a method of releasing a model into the facility core flow prior to a test. An ideal release exerts no forces or moments on the model that results in unwanted pitching from the initial release angle. Furthermore, it is highly desirable that the mechanism allows for high precision adjustment when setting the initial angle of attack. There have been four main avenues taken to achieve a clean release:

1. String cut by knife edge [40, 39, 67] - a solenoid triggers a knife to cut string to release the model to the core flow. Blocks conformal to the model are used to set the initial angle of attack. Authors note that this system can be time consuming to set-up before an experiment but achieves high accuracy in the initial angle of attack. Care must be taken that the string does not interfere with the flow when cut.

2. String cut by flow initiation [45, 46, 88, 89, 25, 22] - the most popular method of releasing a model due to its simplicity. However, its simplicity means it is very difficult to set the initial angle of attack accurately and the method requires high enthalpy flow to cut the string.

3. Release by electromagnet [95, 96, 28, 97] - electrical triggers are used to release a model via electromagnet. Allows for clean release of model but requires the model to contain material that can be attracted by a magnet. Difficulties can also arise if the geometries tested does not have a flat surface for the electromagnet to attach to.

4. Chebychev lambda linkage [47] - its design guarantees that no forces are applied to the model during release. Complex to design and challenging to change angle of attack of model.

Inertial Measurement Unit

In the literature, the choice of IMU used by researchers is dictated by the internal volume of the model used. The size of model is often limited by the core flow size of the facility. If the model is sufficiently large enough, PCB piezoelectric accelerometers can be used which have high sampling rates of up to 500 kHz. Tanno et al. [98] required a model length of between 0.5 m and 1.1 m to have sufficient internal volume to use these accelerometers but they allow for very high sensitivities and sampling rates.

For smaller models (0.5 m or less), MEMS based accelerometers have been used which have sampling rates of up to 8 kHz [41, 59]. Their sensitivity tends to be lower than PCB accelerometers but their small size and ease of packaging them on an on-board DAQ makes them highly suitable for free-flight experiments.

Optical Tracking

There are two main approaches used by researchers in the creation of image tracking algorithms; the first is tracking shapes and features on the surface of the model as used by Kennell et al. [41], Leisner et al. [47] and Hanneman et al. [25]. The main benefit of these methods is that the algorithm is fairly straight forward to implement due to large amounts of publications in the open literature and it can obtain 3 degrees of freedom motion with high accuracy.

The second approach, originally championed by Laurence and Karl [46], is to track the outline of the model and relate the outline to the attitude and centre of gravity of the model from numerical or analytical equations. This method tends to detect more points than the first so can have greater accuracy in tracking, however can run into difficulties if the outline of the model is not clear against the background of the test section or if there are any close lying shock waves in the image. Starshak et al. [88] extended this method out to track for 6 degrees of freedom, but the methodology is very computationally expensive.

2.2.12 Conclusions

This section has reviewed the relevant literature relating to free-flight experiments. A wide range of facilities are presented in Table 2.2 and a variety of model sizes, weights and geometries used in free-flight experiments are summarised in Table 2.3 . A large amount of work has been conducted in free-flight improving the accuracy of both on-board measurements using IMUs and image tracking with the improvements in both miniaturisation of sensors and improvements to optical high-speed cameras. The uncertainties for the measurements of forces and moments in the literature are also presented in Table 2.4.

After reviewing the literature, the following gaps in the literature have been identified as areas of study:

1. Many authors discuss the benefits of free-flight in the literature as being sting-free and free of support based oscillations. However, a direct comparison of the force balance technique (including stress-wave balance) and free-flight in the same facility at the same freestream conditions has not been conducted. This research would most importantly provide a quantitative comparison in terms of force measurement uncertainties with all other variables controlled.

2. Very little free-flight research has been conducted within Ludwieg Tube facilities that can provide true scaled flight conditions, matching both Reynolds and Mach number. The University of Oxford High Density Tunnel offers the opportunity to provide this.

3. Aerodynamic coefficients are comprised of both static and dynamic components. For a force balance, there is no pitching motion so only static derivatives are measured. In the free-flight experiments reviewed, the models are allowed to freely pitch and so the measured coefficients are a combination of both statics and dynamics. A non-pitching free-flight model will allow for purely static coefficients to be measured.

4. With the question of unknown measurements in terms of statics and dynamics. A static free-flight campaign requires a first validation case to be conducted with simplistic geometry allowing confidence in the free-flight technique for complex geometries.

Table 2.2 Freestream conditions for free-flight experiments from the literature.

Facility	Type	Mach Number	Total Pressure (MPa)	Total Temperature (K)	Dynamic Pressure (kPa)	Reynolds Number (x10^6\ m)	Enthalpy (MJ/kg)	Test Time (ms)	Model length (mm)
T-ADFA [69]	Free-piston shock	9.1-10.3	8.8-15	10500-3732	20	0.3-1.2	13.4-4.0	0.5-1.5	37.5
TUSQ [67, 40, 39, 41, 47]	Free-piston Ludwieg	5.85	0.95	550	16.4	7.15	-	200	110-253
HIEST [95, 96, 98, 28, 97]	Shock	7.6-6.2	13-15	3000-7600	47.3-57.6	2-0.45	3.8-16	2	316
HWT2 [95, 96]	Blowdown	9.7	6.1	1100	12.4	0.87	-	60000	316
HEG [22, 25]	Shock	7.36	17.7	2700	74.7	-	3.24	3	1500
T5 [45, 46]	Shock	4.5	21-60	7817	405	-	9-25	2.5	140
HyperTerp [88, 89]	Reflected shock	6.4	1.3	735	16.3	5.3	-	1-3	100
Longshot [24]	Gun	11-11.8	31.3	1837	30.7	6.0-9.6	1.2-2.5	10	50
HSST [21]	Blowdown	5	0.8	300-900	27.6-29.7	4.2-23.7	-	7500	30
ISL [101, 56]	Shock	3-4.5	11-47	1400	400	1.6	-	3	77-185

Table 2.3 Model properties for free-flight experiments from the literature.

Author	**Model**	**Mass (kg)**	**Inertia (kgmm^2)**	**Model Length (mm)**	**Release Mechanism**	**Angle of Attack Range (°)**	**Amount of Pitch in a test (°)**
Neely [69]	Sphere	0.04	N/A	37.5	Electromagnet	N/A	N/A
Mudford [67]	Hemispherical-nosed cylinder	0.33	410	110	String-cut (knife)	0.2-2.5	2.2
Kennell [40, 39, 41]	HEXAFLY	0.288	3500	252.7	String-cut (knife)	-8 - 3	7
Tanno [97]	Cone, Capsule, HYFLEX	16.78	0.13 - 0.226 x10^6	15.6-440	Electromagnet	15-55	0.1
Tanno [98]	MoDKI scramjet	18.96	1.21 x10^6	1100	Electromagnet	0-4	-
Laurence [45, 46]	Sphere, Orion capsule	-	-	140	String-cut (by flow)	20-36	0.8
Starshak [88, 89]	HL-20	0.043	-	100	String-cut (by flow)	15	0.3
Friedl [22]	Capsule	0.515	-	-	String-cut (by flow)	0	-
Hanneman [25]	SSFE	85	-	1500	String-cut (by flow)	-2	-
Grossir [24]	Space debris	-	20	50	String-cut by flow)	-90-90	-
Fisher [21]	Sphere	-	-	30	Solenoid-yoke plate	N/A	N/A
Wey [101]	EFP	0.09	4810	77.32	Sheet holder	0-6	18
Martinez [56]	GSP	0.036	-	185	-	0-2	1.4
Leiser [47]	ISS modules	0.005	-	5	Chebychev lambda linkage	-	-

Table 2.4 Summary of free-flight in literature (for multiple papers by authors, most recent work is taken).

Paper	Image Tracking	Frame Rate (kFPS)	Light Source	Uncertainty	IMU	Sampling Rate (Hz)	Uncertainty
Neely [69]	Yes	5	LED	14 %	No	-	-
Mudford [67]	Yes	2	LED	Unspecified	Yes	100	Unspecified
Kennell [39]	Yes	2	LED	Unspecified	Yes	8000	2 %
Tanno [97]	No	-	-	-	Yes	500 k	8 %
Laurence [46]	Yes	14	Continuous white light	2-3 %	No	-	-
Starshak [89]	Yes	43-52k	LED	Unspecified	No	-	-
Friedl [22]	Yes	32	Laser	Unspecified	No	-	-
Grossir [24]	Yes	4.796	LED	2 %	No	-	-
Martinez [56]	Yes	12.5	LED	11 %	No	-	-
Leiser [47]	Yes	2	LED	Unspecified	No	-	-

Chapter 3

Scaling for Aerodynamic Experiments

In general, experimental sub-scale models are used to determine the aerodynamic characteristics of full-scale flight vehicles and provide validation for theoretical and numerical models, often used to develop said flight vehicles. In order to allow for comparisons between experimental work and flight conditions to be valid, the experimenter must have confidence that certain similitude parameters are met and of course, understand the limitations of the data derived from sub-scale experimental work.

The degree of similitude that is required between flight and experiments often depends on the test objectives. In a perfect scenario, all of the similitude criteria will be met but in most experimental cases this is not possible and there will be a need for compromise due to the limitations of ground facilities. For example, in the compressible flow regime, it is of upmost importance that Mach number and Reynolds number similitude is conserved. This, as seen later in the chapter, has the consequence of leaving Froude number unmatched.

The following chapter will discuss the parameters involved in achieving similitude between flight and experimental conditions, and through the use of the Lord Rayleigh method of dimensional analysis, present the key dimensionless groups that are pivotal in achieving similitude for aerodynamic wind tunnel experiments. Following this, the dimensionless groups will be used in context of scaling for sting-based and free-flight aerodynamic experiments with the limitations of the methods presented. Before going into the details of scaling, the key parameters of this thesis, aerodynamic coefficients, will be discussed in depth.

3.1 Aerodynamic Coefficients

3.1.1 Aerodynamic Forces and Moments

Before discussing the concept of aerodynamic coefficients, it is important to understand the origin of forces in flight and the parameters that influence them at any given time. The first force which must be considered is the vehicle's weight. For a vehicle to stay indefinitely in flight, this force must be overcome. Thrust, which will not be present for gliding vehicles, is the force which propels the vehicle forward. Finally, it is conventional to define the aerodynamic forces acting on a vehicle in flight as two orthogonal components (in 3 degrees of freedom), lift and drag. Lift is the force that overcomes the weight of a vehicle and drag acts to reduce the kinetic energy of the body (although can be advantageous in re-entry vehicles for example). The instantaneous aerodynamic forces and moments are comprised of the integration of pressure and shear components exerted on the body by the fluid passing over it. The position where the total sum of the pressure field acts on a body is known as the centre of pressure. This is the point where the aerodynamic forces can be assumed to act if the body is assumed to be a point mass. The distance between the centre of pressure and centre of gravity determines the magnitude of pitching moment that acts in flight and whether a vehicle is stable or unstable.

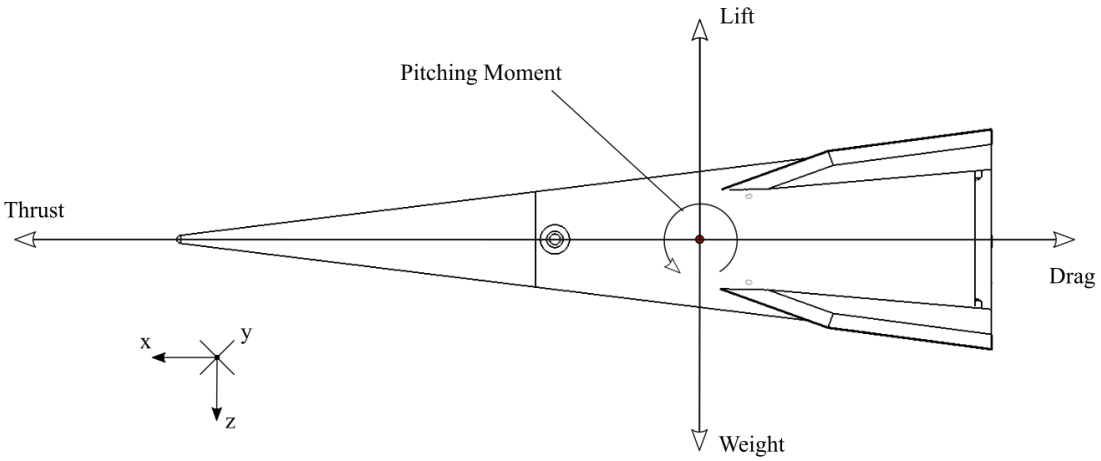

Fig. 3.1 Free body diagram of longitudinal forces acting on a vehicle in flight

The generation of aerodynamic forces in flight is a transient process and this means that there are many elements that determine what these instantaneous forces/moments are, some static and some dynamic in nature. These include:

1. The overall vehicle geometry. This determines the path the fluid takes around the vehicle and therefore one of the big contributors to the overall force. Usually the geometry is defined by a reference area (S) and a reference length, c.

2. The orientation (angle of attack, α, and side-slip, β) of the body relative to the freestream velocity vector.

3. The density of the fluid medium, ρ.

4. The relative velocity between the fluid and the vehicle, V.

5. The Reynolds number of the flow which gives an indication of features such as boundary layer effects and viscosity.

6. The freestream Mach number determines the compressibility effects of the flow such as shock angles.

7. The history of the vehicle's trajectory through the fluid - this impacts upon the propagation of upstream wake disturbances, the hysteresis of flow separation and other unsteady, dynamic effects.

Unless full scale experiments are conducted with a flight vehicle, the measured forces in flight are likely to be different in magnitude to those measured by a sub-scale model within a wind tunnel. To allow for comparison between ground testing and flight, it is conventional to non-dimensionalise forces and moments into aerodynamic coefficients. The derivation of aerodynamic coefficients can be undertaken by a dimensionless analysis of pertinent parameters as described in the next section.

3.1.2 Dimensionless Analysis of Force and Moment Coefficients

For similitude of aerodynamic characteristics and kinematics of a model relative to a full-scale vehicle, the dependence of one physical quantity must be the same for the model as the vehicle. This is achieved through the use of non-dimensional quantities obtained through dimensional analysis of the parameters defining the forces and moments of flight. Wolowicz et al. [105] states that there are 18 quantities that define the forces, moments, kinematics and aerodynamics of an aircraft for 3 degrees of freedom longitudinal motion. These quantities can be summarised as (defined in Table 3.1):

$$F = f\left(\rho_f, \mu, a, l, \alpha, V, \dot{V}, \delta, \Omega, \dot{\Omega}, \omega, g, t, m, I, EI', GJ'\right) \tag{3.1}$$

$$M = f\left(\rho_f, \mu, a, l, \alpha, V, \dot{V}, \delta, \Omega, \dot{\Omega}, \omega, g, t, m, I, EI', GJ'\right) \tag{3.2}$$

The forces and moments which act on an aircraft that moves through a fluid are dependent on the properties of the aircraft and the fluid, but also the aircraft's displacement, velocity and acceleration, both linear and angular. The 18 quantities chosen contain three base units: mass, length and time. For any given dimensional analysis, if the number of quantities is given by, N_q, and number of base units is given by N_b, then the number of dimensionless groups, π is given by:

$$\pi = N_q - N_b \tag{3.3}$$

Therefore, for this work there are 15 dimensionless groups which represent the requirements for complete static and dynamic similitude of a model relative to the vehicle. The full dimensionless analysis, using the Lord Rayleigh method can be found in Wolowicz et al. [105]. The outcome of the analysis is as follows:

$$C_L, C_D, C_M = f\left(\alpha, \delta, \frac{\Omega l}{V}, \frac{\dot{\Omega} l^2}{V^2}, \frac{\dot{V} l^2}{V^2}, \frac{\omega l}{V}, \frac{\rho_f V l}{\mu}, \frac{V^2}{lg}, \frac{V}{a}, \frac{m}{\rho_f l^3}, \frac{I}{\rho_f l^5}, \frac{EI'}{\rho_f V^2 l^4}, \frac{GJ'}{\rho_f V^2 l^4}, \frac{tV}{l}\right) \tag{3.4}$$

Table 3.2 defines the dimensionless groups found in Eq. (3.4). It can be seen that through the Lord Rayleigh method, commonly recognised dimensionless groups for aerodynamic testing are formed and importantly, the aerodynamic moments and forces are non-dimensionalised to give force and moment coefficients.

It can be seen that this analysis does not include parameters with the base units of temperature, for example, total temperature, enthalpy, thermal conductivity etc. These parameters are ignored as aerodynamic wind tunnel facilities which generate medium duration flows require the flow to be cold in order to match Reynolds number between flight and experimental tests. This has the consequence on features such as heat transfer, real gas effects and skin friction for the model not being matched for flight.

Table 3.1 Nomenclature for scaling

Variable	**Definition**	Units
α	Angle of attack	$^\circ$
δ	Control surface deflection	$^\circ$
μ	Dynamic viscosity	$Pa.s$
Ω	Angular rate	$^\circ/s$
$\dot{\Omega}$	Angular acceleration	$^\circ/s^2$
ω	Frequency of oscillation	$/s$
ρ_f	Fluid density	kg/m^3c
a	Velocity of sound	m/s
EI'	Bending stiffness	$N.m^2$
F	Force	N
GJ'	Torsional stiffness	$N.m^2$
g	Acceleration of gravity	m/s^2
I	Moment of inertia	$kg.m^2$
l	Length	m
M	Moment	$N.m$
m	Mass	kg
t	Time	s
V	Velocity	m/s
$\dot{V}$	Acceleration	m/s^2

Table 3.2 Dimensionless Groups

Dimensionless Group	**Definition**
Angle of attack	α
Control surface deflection	δ
Aerodynamic force coefficient	$\frac{F}{\frac{1}{2}\rho_f V^2 l^2}$
Aerodynamic moment coefficient	$\frac{M}{\frac{1}{2}\rho_f V^2 l^3}$
Reduced angular velocity	$\frac{\Omega l}{V}$
Reduced angular acceleration	$\frac{\dot{\Omega} l^2}{V^2}$
Reduced linear velocity	$\frac{\dot{V} l^2}{V^2}$
Strouhal number	$\frac{\omega l}{V}$
Reynolds number	$\frac{\rho_f V l}{\mu}$
Froude number	$\frac{V^2}{lg}$
Mach number	$\frac{V}{a}$
Relative density factor	$\frac{m}{\rho_f l^3}$
Relative moment of inertia	$\frac{I}{\rho_f l^5}$
Aero-elastic bending parameter	$\frac{EI'}{\rho_f V^2 l^4}$
Aero-elastic torsion parameter	$\frac{GJ'}{\rho_f V^2 l^4}$
Reduced time parameter	$\frac{tV}{L}$

3.1.3 Aerodynamic Coefficients

Aerodynamic Coefficients are defined by forces and moments non-dimensionalised by the dynamic pressure and a reference area (and additional reference length for moment) as shown in the equations below:

$$C_L = \frac{L}{\frac{1}{2}\rho_f V^2 S} \tag{3.5}$$

$$C_D = \frac{D}{\frac{1}{2}\rho_f V^2 S} \tag{3.6}$$

$$C_M = \frac{M}{\frac{1}{2}\rho_f V^2 S c} \tag{3.7}$$

In this form, the dependency on the magnitude of forces and moments is removed and provided the pertinent parameters for the freestream and model properties are scaled appropriately for the experiments being undertaken, are representative of the flight aerodynamic coefficients. If the scaling is undertaken correctly, the value of aerodynamic coefficients measured in the wind tunnel will be the same as that in flight.

However, it can be seen in Eq. 3.1 and 3.2 and as discussed in Section 3.1.1 that aerodynamic force and moment coefficients are influenced by both static and dynamic phenomena. Therefore, equations 3.5 - 3.7 are a summation of both static and dynamic derivatives and care must be taken in experiments that the right phenomena is being measured and not being influenced by other factors. By completing a Taylor series expansion for the aerodynamic coefficients of the parameters of interest, the following equations are obtained (higher order terms discounted):

$$C_L = C_{L_0} + C_{L_\alpha}\alpha + C_{L_{\delta_e}}\delta_e + C_{L_{i_h}} i_h + C_{L_v}\frac{v}{V} + C_{L_q}\frac{qc}{2V} + C_{L_{\dot{\alpha}}}\frac{\dot{\alpha}c}{2V} \tag{3.8}$$

$$C_D = C_{D_0} + C_{D_\alpha}\alpha + C_{D_{\delta_e}}\delta_e + C_{D_{i_h}} i_h + C_{D_v}\frac{v}{V} + C_{D_q}\frac{qc}{2V} + C_{D_{\dot{\alpha}}}\frac{\dot{\alpha}c}{2V} \tag{3.9}$$

$$C_M = C_{M_0} + C_{M_\alpha}\alpha + C_{M_{\delta_e}}\delta_e + C_{M_{i_h}} i_h + C_{M_v}\frac{v}{V} + C_{M_q}\frac{qc}{2V} + C_{M_{\dot{\alpha}}}\frac{\dot{\alpha}c}{2V} \tag{3.10}$$

where C_{x_0} (where x can be substituted for L,D or M) is the value of C_x when all other derivates are equal to zero, C_{x_α} the change in the coefficient with angle of attack, $C_{x_{\delta_e}}$ and

$C_{x_{i_h}}$ are the influence on the coefficients with specific control surface deflections. These four derivatives are known as the static derivatives as they are not functions of transient flow variables. The rest are dynamic derivatives; C_{x_v} is the derivative that results in changes of relative velocity (between body and freestream), $C_{x_{\dot{\alpha}}}$ results from a lag in the development of downwash resulting from a rate of change of angle of attack and C_{x_q} is the result of changes due to the vehicle pitching.

Before expanding on these coefficients further, in particular the pitching moment coefficient, the concept of stability in relation to flight vehicles will be explored first.

3.1.4 Stability

Stability is a key characteristic in determining the performance of a vehicle, having a direct impact on characteristics such as manoeuvrability and control. Stability can be separated into two parts; static and dynamic. Yechout [109] defines static stability as the initial tendency of a vehicle following a perturbation from a steady-state flight condition to induce aerodynamic moments and forces to return the vehicle to the equilibrium position. The classic example of illustrating this definition is shown in Figure 3.2.

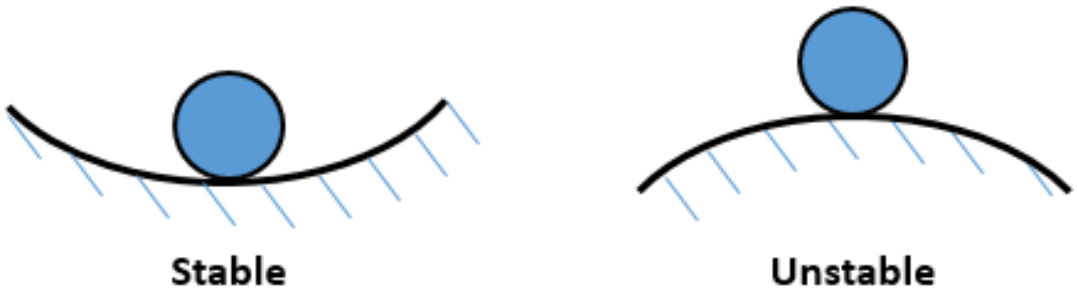

Fig. 3.2 Demonstration of Static stability .

In the first case, if the ball is displaced, the ball will initially seek the equilibrium position so is statically stable. In the second case, if the ball is displaced, it will be driven away from the equilibrium position and therefore is statically unstable. For the context of aircraft dynamics, the equilibrium position is defined as the trim angle of attack, the angle at which it experiences no moment about its centre of gravity. This trim angle of attack, can be changed on an aircraft, typically through the use of control surface deflections. Static stability also relates to how a vehicle handles, for example, a vehicle which is highly statically stable will be sluggish to handle. Therefore, a vehicle made for manoeuvring may be made to be statically unstable with advanced computational control systems to correct for flight.

Dynamic stability is defined as the temporal response of a vehicle after the aircraft is disturbed from a trim condition. Dynamic instability is when a disturbed system accelerates towards the equilibrium position, overshoots it and the amplitude of these oscillations increases with time. A dynamically stable system will have oscillations which decay over time, which is the desirable case. A vehicle can be statically stable but dynamically unstable. The stability of a vehicle can be different on all axes, a vehicle stable on the longitudinal axis is not necessarily stable on the yaw and roll axes.

3.1.5 Pitching Moment Coefficient

As derived in Equations 3.8 - 3.10, the aerodynamic coefficients are summations of many derivatives that are functions of both static and dynamic behaviour. The individual derivatives are discussed in more detail here for the pitching moment coefficient, but their origins and applications can easily be transferred to the lift and drag coefficients too.

Stability Derivative

C_{M_α} is often referred to as the stability derivative. The coefficient represents a change in the applicable moment coefficient with respect to a change in direction of the freestream. It is referred to as the stability derivative as a perturbation in angle of attack from an equilibrium position (or trim angle of attack) will dictate if the body is stable or not as described in Section 3.1.4. Aerodynamic coefficients are often plotted against angle of attack and therefore this derivative is the gradient of that plot. Therefore, for a vehicle to be classified as statically stable:

$$C_{m_\alpha} < 0 \tag{3.11}$$

This can be seen in Figure 3.3 where the plots have negative gradient implying static stability. The plot on the left shows static stability for fixed control surface deflections whereas the plot on the right shows how control surface deflections change the trim angle of attack (whilst maintaining static stability).

Primary Control Derivatives

Also known as the control powers, the primary control derivatives, $C_{M_{\delta_e}}$ and $C_{M_{i_h}}$, result from deflections in control surfaces (where δ_e is the elevator and i_h is the horizontal stabiliser). Effectively the control surfaces act to change the position of the centre of pressure thereby

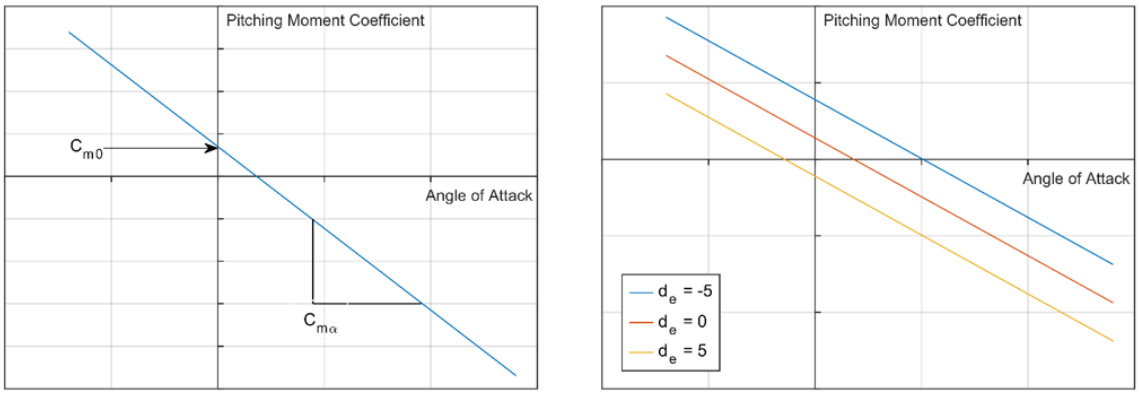

Fig. 3.3 Demonstration of the static pitching moment coefficients. Left – pitching moment coefficient for a statically stable vehicle. Right - the effect of control surfaces

changing the trim angle of attack. This is very effective for controlling small changes in the aircraft's trajectory.

Mach Tuck Derivative

The Mach tuck derivative, C_{M_v}, results from changes in C_{M_0} and the centre of pressure location with changes in forward speed, V. This effect is most notable in the transonic region where the aerodynamic centre tends to move aft which can result in a nose-down pitching moment. As a consequence the Mach tuck derivative would become more negative.

Quasi-Steady Derivative

The quasi-steady derivative, $C_{M_{\dot{\alpha}}}$, occurs if there is a rate of change in angle of attack. To help understand this derivative, consider an aircraft with a horizontal tail. As the angle of attack changes, there is a lag in the development of downwash at this downstream horizontal tail. The C_{M_α} derivative assumes that the downwash is fully developed so the $C_{M_{\dot{\alpha}}}$ derivative provides a correction factor for when the aircraft is undergoing a rate of change in angle of attack.

Pitch Damping Derivative

At first glance, the pitch rate derivative, C_{M_q}, may appear the same as the quasi-steady derivative but there is a subtle difference. Again consider the horizontal tail of an aircraft. If the flight vehicle has a pitch rate about the centre of gravity, downstream of the vehicle, the relative velocity vector is different as compared to the CoG. Therefore, it results in a change in the nominal flight angle of attack at this point which will result in a damping effect in

the pitching moment. The diagram in Figure 3.4 shows the origin of this derivative with the relative velocity triangles shown. The change in relative angle of attack applies to all points along the body of the vehicle, not just the lifting surfaces.

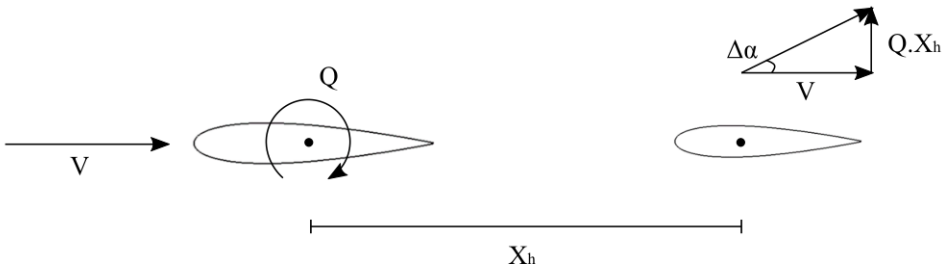

Fig. 3.4 Origin of the pitch damping derivative, C_{M_q}. Pitch rate (about centre of gravity) of aircraft causes a change in angle of attack at the horizontal tail

Frequently, when determining aerodynamic derivatives, $C_{M_{\dot{\alpha}}}$ and C_{M_q} are measured together as they are difficult to differentiate between.

3.2 Dimensionless Groups for Aerodynamic Scaling

In an ideal wind tunnel experiment, all dimensionless groups in Table 3.2 would be matched between flight and the experiments for full similitude to be reached for a free-flight test. However, many of the dimensionless groups are related to each other making it difficult to obtain full similitude. A good example of this is the relationship between Froude number, Reynolds number and Mach number. Before discussing the various methodologies typically used to scale models for use in wind tunnel facilities, the important dimensionless numbers presented in Table 3.2 will be discussed.

3.2.1 Reynolds Number

Reynolds number is defined as the ratio of inertial to viscous forces, as seen in the following equation:

$$Re = \frac{\rho V l}{\mu} \tag{3.12}$$

This dimensionless number determines the dominant forces present in a certain flight regime, for example in high Reynolds flight it will be the inertial forces that are dominating. Therefore, in relation to wind tunnel experiments, Reynolds number determines the dynamic similarity of the flow around the model or vehicle. As Reynolds number is a function of length, to match Reynolds number between flight and a sub-scale model, the flow properties must be manipulated to allow for similitude which is normally achieved by increasing the tunnel flow density.

Reynolds number is one of the driving components on the transition of flow from laminar to turbulent and the location it occurs. This can influence the measured forces as there is a large difference in skin friction depending on if the flow regime is laminar or turbulent which influences the determined drag coefficient. This effect is more pronounced on long, slender vehicles such as space planes, where viscous forces become substantial.

As Reynolds number can be seen as a measure of the flows inertia, it can also determine the angle of attack at which flow separation occurs and hence the maximum lift-to-drag ratio a body can achieve. With these factors in mind, the importance of matching Reynolds number between flight and tunnel can be seen.

3.2.2 Mach Number

Mach number is defined as the ratio of the vehicle velocity to the velocity of sound in a compressible fluid medium:

$$M_\infty = \frac{V}{a} \tag{3.13}$$

Mach number is important in the preservation of compressibility effects for a geometrically similar body. Therefore, it is highly influential in fluid properties behind shocks and also the angularity of the shocks produced by a body. The effects of compressibility can be shown to be important above Mach numbers of 0.2 where flow can no longer be assumed to be incompressible.

At high Mach numbers (5 and above), the effects of compressibility have a severe effect on flow stagnation temperature. When the stagnation temperatures get above a certain threshold, effects such as dissociation, ionisation and changes to the adiabatic constant, γ, can occur. This is only applicable for certain flight trajectories, however.

Another consequence of high Mach numbers is the strong coupling effects between Mach number and viscous effects. As the Mach number increases, the proximity of a shock wave to a body and hence the boundary layer decreases. The shock waves interact with the boundary layer, changing its properties and hence the viscous drag acting on the body.

At sufficiently high Mach numbers, certain aerodynamic quantities such as pressure coefficient, lift coefficient and wave-drag coefficients become independent of Mach number [2]. This phenomena is known as the Mach-number independence principle. The Mach number threshold this occurs at is geometry dependent. As the value of this threshold can never be guaranteed, Mach number is always matched in aerodynamic experiments.

With all these factors, there is high importance that Mach number is matched between flight and wind tunnel testing in the hypersonic regime.

3.2.3 Froude Number

Froude number defines the ratio of inertial forces to gravitational forces acting on a vehicle for a given trajectory point. Similitude is important so that vehicle manoeuvres are preserved for geometrically similar bodies. It is defined as:

$$Fr = \frac{V^2}{lg} \tag{3.14}$$

Froude number was originally used to describe the buoyancy effects for boats but can also be used to describe flight manoeuvres such as banking, pitching up and level flight in planes. Considering the equation for the value of lift coefficient for steady level flight, the lift must be equal to the vehicle's weight, therefore:

$$C_L = \frac{W}{\frac{1}{2}\rho V^2 S} = \frac{2mg}{\rho M_\infty^2 a^2 S} = \frac{2m}{\rho Sc} \cdot \frac{gc}{M_\infty^2 a^2} = f\left(\frac{m}{\rho l^3}, M_\infty, \frac{V^2}{lG}\right) \tag{3.15}$$

Equation 3.15 shows that the lift coefficient for level flight is a function of Froude number, relative density factor and Mach number. This implies that if Froude number is not matched, the value of lift coefficient may be different at a given angle of attack between flight and tunnel. This implies that the angle of attack similitude may not be preserved if Froude number is left unmatched.

3.2.4 Strouhal Number and Reduced Angular Velocity

Also known as the reduced frequency parameter, Strouhal number is defined by:

$$St = \frac{\omega l}{V} \tag{3.16}$$

Strouhal number is important for similitude in features that are unsteady in nature as a result of oscillatory behaviour, for example, the derivation of damping derivatives from pitching data. Other factors it can influence include flow separation, boundary layer

establishment and the time required for flow to adjust to perturbations [105]. Therefore, this parameter is important to consider if work is being conducted on dynamic behaviour.

Reduced angular velocity in definition is very similar in form to Strouhal number:

$$Reduced\ angular\ velocity = \frac{\Omega l}{V} \tag{3.17}$$

However, this parameter applies to vehicle manoeuvres where the body exhibits angular rates or pitching rates of control surfaces.

3.2.5 Relative Density Factor and Relative Mass Moment of Inertia

Relative density factor is an important group in the consideration of force coefficients for angle of attack similitude in manoeuvres in flight to be achieved. In the analysis of level flight seen in Equation 3.15, relative density factor can be seen in the derivation. A similar derivation can be undertaken for pitching moment coefficients in which the relative mass moment of inertia is obtained.

It must be noted that these dimensionless groups are very important for the measurement of dynamic phenomena as it preserves angle of attack similitude.

3.2.6 Aeroelastic Bending and Torsion Parameter

If the aerodynamic characteristics of a body are influenced by the flexibility of any component, then it is necessary to scale the elastic similitude of those components, both in bending and torsion. For most aerodynamic experiments where full body force measurements are required, the model is usually made sufficiently rigid that these parameters need not be considered. For example, this would be important for similitude testing of a subsonic, unpowered glider where the wings are flexible.

3.2.7 Reduced Parameters

The reduced time, velocity, angular velocity and angular acceleration dimensionless groups relate the full-scale vehicle motion to the motion that would be seen by a wind tunnel model provided the scaling laws are followed. They can be considered if it is necessary to a certain maneuvre to occur within a certain time period, such as the test time of a facility.

3.3 Methodologies for Aerodynamic Scaling

For general full-body aerodynamic force measurement experiments (in free-flight), there are two methods used to achieve similitude between flight and wind tunnel testing. They are Froude scaling and Mach scaling. The determining factor over which methodology is most applicable is dictated by whether the flow can be considered compressible or incompressible. The following section discusses the scaling methodologies in detail and any limitations which they may have. In the following analysis, subscript v relates to full-scale vehicle properties and m to wind tunnel model properties and the geometric scaling factor is defined by:

$$n = \frac{l_m}{l_v} \tag{3.18}$$

3.3.1 Froude Scaling

Froude scaling is used in incompressible flow regimes to match flight conditions to flow properties in tunnel testing. The two underlying assumptions behind this methodology is that both Froude number and Reynolds number is matched between flight:

$$Fr_v = Fr_m \tag{3.19}$$

$$\left(\frac{V^2}{gl}\right)_v = \left(\frac{V^2}{gl}\right)_m \tag{3.20}$$

Assuming that the gravitational field in the wind tunnel is the same as in flight, an equation for the ratio of velocity can be found (substituting in Equation 3.18):

$$\frac{V_m}{V_v} = \sqrt{n} \tag{3.21}$$

Now for Reynolds number:

$$Re_v = Re_m \tag{3.22}$$

$$\left(\frac{\rho V l}{\mu}\right)_v = \left(\frac{\rho V l}{\mu}\right)_m \tag{3.23}$$

$$\frac{\rho_v}{\rho_m} = \frac{V_m}{V_v} \cdot \frac{l_m}{l_v} \cdot \frac{\mu_v}{\mu_m} \tag{3.24}$$

Substituting in equations 3.21 and 3.18:

$$\frac{\rho_v}{\rho_m} = n^{\frac{3}{2}} . \frac{\mu_v}{\mu_m} \tag{3.25}$$

This equation describes the bounds that a facility needs to achieve in terms of freestream density to achieve similitude between flight and test flow if Reynolds and Froude number are to be matched. However, Froude scaling is not suitable for the hypersonic regime as it leaves Mach number unmatched except for a specific scaling factor:

$$M_{\infty,v} = M_{\infty,m} \tag{3.26}$$

$$\left(\frac{V}{a}\right)_v = \left(\frac{V}{a}\right)_m \tag{3.27}$$

$$\frac{V_m}{V_v} = \frac{a_m}{a_v} \tag{3.28}$$

Substituting in equation 3.21:

$$n = \left(\frac{a_m}{a_v}\right)^2 \tag{3.29}$$

This scaling factor is often impossible to achieve in practice which makes Froude scaling impracticable for hypersonic free-flight testing. If the assumption made in Equation 3.21 that the gravitational field ratio of unity is removed, the experimenter could manipulate the gravitational field in the wind tunnel to match Froude number, however, this would likely be very costly to achieve. The consequences of mismatching Froude number will be discussed later.

3.3.2 Mach Scaling

Mach scaling has the overarching assumptions that both Mach number and Reynolds number are matched between flight and tunnel conditions. The consequences of this are that shock angles and compressibility effects are matched as well as viscous effects. To derive the equation required to describe a facilities freestream conditions, consider the ratio of Mach numbers being matched:

$$M_{\infty,v} = M_{\infty,m} \tag{3.30}$$

$$\frac{V_m}{V_v} = \frac{a_m}{a_v} \tag{3.31}$$

The equation for speed of sound in a fluid for a mixture of thermally perfect gases is given by:

$$a = \sqrt{\gamma RT} \tag{3.32}$$

Substituting Equation 3.32 into 3.31:

$$\frac{V_m}{V_v} = \frac{(\sqrt{\gamma RT})_m}{(\sqrt{\gamma RT})_v} \tag{3.33}$$

For the flight conditions used in this thesis, it can be shown that the ratio of the square root of specific heats is 3 % maximum from unity. Therefore, the equation can be reduced to:

$$\frac{V_m}{V_v} = \frac{\sqrt{T_m}}{\sqrt{T_v}} \tag{3.34}$$

At greater Mach numbers and lower altitudes than this thesis, the assumption of the ratio of specific heats being unity would not be valid. Now equating flight and tunnel Reynolds number, starting with Equation 3.24:

$$\frac{\rho_v}{\rho_m} = \frac{V_m}{V_v}.\frac{l_m}{l_v}.\frac{\mu_v}{\mu_m} \tag{3.35}$$

Substituting in Equations 3.18 and 3.34:

$$\frac{\rho_v}{\rho_m} = \frac{\sqrt{T_m}}{\sqrt{T_v}}.n.\frac{\mu_v}{\mu_m} \tag{3.36}$$

If isentropic flow is assumed, then the ratio of static temperatures is equal to the ratio of total temperatures, again, this assumes that the ratio of specific heats is close to unity. Further more if the ideal gas law is assumed in the flight regime of interest:

$$\rho = \frac{p}{RT} \tag{3.37}$$

Then the ratio of Reynolds number becomes:

$$\frac{P_v}{P_m}.\frac{T_m}{T_v} = \frac{\sqrt{T_{0,m}}}{\sqrt{T_{0,v}}}.n.\frac{\mu_v}{\mu_m} \tag{3.38}$$

Again, assuming the ratio of static to total variables is the same between flight and tunnel testing:

$$\frac{P_{0,m}}{P_{0,v}} = \frac{\sqrt{T_{0,m}}}{\sqrt{T_{0,v}}}.\frac{1}{n}.\frac{\mu_m(T_0, gas)}{\mu_v(T_0, gas)} \tag{3.39}$$

This equation shows that the ratio of total pressure between flight and tunnel for similitude is entirely a function of total temperature, as viscosity is usually defined using numerical correlations that are functions of temperature. When testing a specific flight geometry, it is likely that the flight trajectory would be known as well as a scaling factor appropriate for a given testing facility. Therefore, Equation 3.39 defines a map of conditions a facility must achieve in order to satisfy Mach scaling similitude. With the scaling factor and the trajectory defined, the degree of similitude a facility can reach is dependent on the total pressure and temperature capability of the facility.

As shown in equation 3.29, if Reynolds and Mach number is matched, Froude number can only be matched for one specific scale which in practice will be very difficult to achieve (due to limitations on core flow size, hence models in wind tunnels). The consequence of mismatching Froude number can be seen if the equation for lift coefficient is examined more closely and steady, level flight is considered (where weight is equal to lift):

$$C_L = \frac{W.cos(\alpha)}{\frac{1}{2}\rho V^2 S} = \frac{2mg.cos(\alpha)}{\rho V^2 S}.\frac{l}{l} \tag{3.40}$$

Grouping into dimensionless groups:

$$C_L = 2.\left(\frac{m}{\rho S l}\right).\left(\frac{gl}{V^2}\right).cos(\alpha) \tag{3.41}$$

Lift coefficient for level flight results in two dimensionless groups being formed, Froude number and relative density factor. This is not to say that the measured lift coefficient will be different at a given angle of attack if Froude number is mismatched. The result is that for steady level flight, the angle of attack required in the tunnel compared to in flight will be different as the buoyancy forces are not matched between our two cases. This has bigger implications on studies in which vehicle manoeuvres are of interest.

3.3.3 Static and Dynamic Hypersonic Testing

For experimental testing where only static derivatives are of interest and the dynamic behaviour of a vehicle does not need to be replicated, only some of the dimensionless groups are required to be matched. For a force balance experiment where a model is semi-rigidly held in position on a sting, Equation 3.4 reduces to:

$$C_L, C_D, C_M = f\left(\alpha, \delta, \frac{\rho_f V l}{\mu}, \frac{V^2}{lg}, \frac{V}{a}, \frac{EI'}{\rho_f V^2 l^4}, \frac{GJ'}{\rho_f V^2 l^4}\right) \tag{3.42}$$

The need to scale the body's mass and inertia is removed as the model is rigidly held in position and therefore the dimensionless groups that relate to the trajectory are removed too. If an analogous experiment is considered for a model in free-flight, where the model remains at constant angle of attack for the duration of the experiment to measure static coefficients, it is true that the same dimensionless groups above need to be considered. Therefore, only the scaling laws considered to this point in the thesis for Mach scaling need to be matched for similitude for static derivatives.

For dynamic experiments, the trajectory history and temporal phenomena are important to achieve similitude. Dimensionless groups such as relative density factor and relative mass moment of inertia must be considered when scaling:

$$\left(\frac{m}{\rho_f l^3}\right)_m = \left(\frac{m}{\rho_f l^3}\right)_m \tag{3.43}$$

$$\frac{m_m}{m_v} = n^3 \frac{\rho_{f_m}}{\rho_{f_v}} \tag{3.44}$$

$$\left(\frac{I}{\rho_f l^5}\right)_m = \left(\frac{I}{\rho_f l^5}\right)_m \tag{3.45}$$

$$\frac{I_m}{I_v} = n^5 \frac{\rho_{f_m}}{\rho_{f_v}} \tag{3.46}$$

These equations dictate the wind tunnel model's mass and inertial properties for dynamic similitude to be achieved in free-flight. Following the calculation of these parameters, the reduced time parameter can be calculated which gives an idea of the difference in time period between flight and tunnel dynamic phenomena. Matching the reduced time parameter between flight and tunnel:

$$\left(\frac{tV}{l}\right)_m = \left(\frac{tV}{l}\right)_m \tag{3.47}$$

$$\left(\frac{tM_\infty a}{l}\right)_m = \left(\frac{tM_\infty a}{l}\right)_m \tag{3.48}$$

Introducing the equation for speed of sound (Equations 3.32) and assume Mach number similitude simplifies the equation to:

$$\frac{t_m}{t_v} = n\sqrt{\frac{T_{0_v}}{T_{0_m}}} \tag{3.49}$$

Through this equation, if the time scale of a dynamic phenomena in flight is known, the corresponding time scale in the tunnel can be calculated. For example, if the experiments are measuring the aerodynamic damping derivatives, the time period of oscillations will scale by this factor. This parameter is useful as it can be used to check if a facility has sufficient test time to measure dynamic phenomena for a given scale.

3.3.4 Summary of Mach Scaling for Aerodynamic Experiments

To summarise, to obtain similitude for aerodynamic experiments in hypersonic facilities with Mach scaling, the following steps must be taken:

1. From the flight geometry of interest, determine a trajectory point and its mass/inertial properties at that position. Calculate the flight total pressure and total temperature.

2. Determine the desired size of the model suitable for the core flow of the facility and calculate the scaling factor, n.

3. Using Equation 3.39, determine the facility freestream conditions for Mach and Reynolds number similitude. If the total temperature of the facility can be varied, there will be a choice of total pressures that can be used.

   (At this point, if sting based testing or static free-flight is the methodology of force measurement, no more scaling rules need to be followed. Continue with the steps if dynamic scaling is also required)

4. Use Equations 3.44 and 3.46 to determine the inertial properties required for the model to have dynamic similitude. The centre of gravity of the flight vehicle will also need to be geometrically scaled for the model.

3.4 Hypersonic Wind Tunnels

Wind tunnel facilities allow experimenters to conduct ground based tests at flight-representative conditions at a significantly lower cost when compared with conducting a full flight test programme. Ground-based facilities also allow measurements to be taken using instrumentation and optics that would not be possible to use in flight. The trade off for ground based facilities, however, is that no single hypersonic facility can capture all the conditions that are experienced by a vehicle within flight. Therefore it is critical that the experimenter chooses the appropriate facility that is suitable for the phenomena that is being studied and understands the limitations of it.

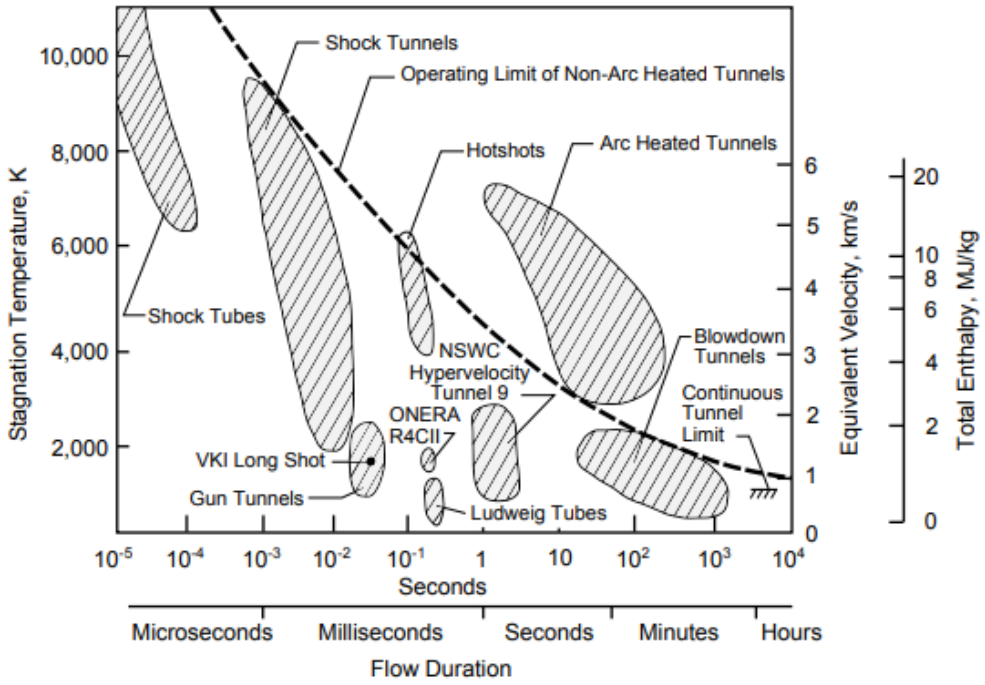

Fig. 3.5 Comparison of Test-Time Production of various Hypersonic Ground Facilities, taken from Wise [104]

The choice of hypersonic facility for force measurement studies is dictated by the parameters above and also the available test time. Continuous wind tunnels can achieve test times of hours but are limited by the pressure differential and mass flow that can be maintained by the compressor systems. Therefore, only modest densities and Reynolds numbers can be achieved at low Mach numbers. This can make it difficult to hit flight representative conditions in the hypersonic regime. Blow-down tunnels operate on a high pressure differential using stored gas that is separated from the test section via a valve or diaphragm. The test gas is expanded through a nozzle to reach the desired Mach number. The gas is also required to be heated to avoid liquefaction in the test section post the nozzle expansion. Test-times for these facilities range from seconds to minutes. Ludwieg tubes operate on similar principles but allow for higher pressure hence Reynolds number flows to be created. This is at the expensive of test times reduced to being in the tens of milliseconds. Blow down and Ludwieg tube facilities are suited for aerodynamic experiments as Reynolds number and viscous effect simulation are important to replicate.

Shock tunnel facilities use a shock wave moving through a high-pressure reservoir to create high temperature and pressure flows allowing for high-temperature effects to be

replicated. However, these facilities only have available test times of a couple of milliseconds which make force measurements in these facilities very difficult.

A comprehensive overview of hypersonic wind tunnel facilities can be found in the following references [52, 51]. Figure 3.5, taken from Wise [104], shows what the flow conditions and test times different facilities can achieve.

3.5 The University of Oxford High Density Tunnel (HDT)

The Oxford HDT is a heated Ludwieg tube facility that is capable of generating long duration flows at high Reynolds numbers that makes it particularly suited for aerodynamic testing of hypersonic geometries. All tests conducted in this work were undertaken in this facility. The following section discusses the history and the operation of the HDT. The Chapters containing experimental work present the freestream conditions used in those experiments.

3.5.1 History of the High Density Tunnel

The HDT was originally commissioned and built by Royal Aircraft Establishment (RAE) in the UK during the 1960's and operated as a cold hydrogen driven shock tube [36]. In the mid 1980's, the facility was converted into a Ludwieg Tube with the ability to add light piston compression heating, also known as LICH mode. In the early 1990's, external electrical heating and a fast acting plug valve was added to the facility. In 2012, the tunnel was acquired by the University of Oxford Thermo-Fluids Institute from Qinetiq and was commissioned in June 2016 [57] [108] to extend the portfolio of hypersonic ground-test facilities at the University of Oxford. At the time of writing this thesis, over 2500 shots have been fired in Ludwieg tube mode.

3.5.2 Details of Tunnel Operation

The Oxford High Density Tunnel was operated in its Ludwieg tube mode for the entirety of this research. Figure 3.6 shows a schematic of the tunnel which can be used as a reference for the following description of how the facility is operated. Before firing the facility, the tunnel barrels are filled with a test gas (air for this work) to a desired fill pressure. The facility is typically operated at total pressures up to 50 bar but is rated for fill pressures of 275 bar. External heaters on the barrels heat the test gas to increase the total temperature so that it does not liquefy through the expansion process in the nozzle. The Ludwieg tube is connected to a bespoke fast-acting plug valve which upon opening feeds the stagnation plenum of a contoured converging/diverging nozzle. At the time of writing, nozzle geometries exist that

provide Mach numbers of integers between 4 to 7. The test time is initiated when the plug valve opens which allows the test gas to exhaust into the test section (of diameter 760 mm and length 940 mm), through to a vacuum dump tank of volume 28 m^3. The facility nozzles are 1395 mm in length with exit diameter 350 mm, producing a core flow of 280 mm at nozzle exit.

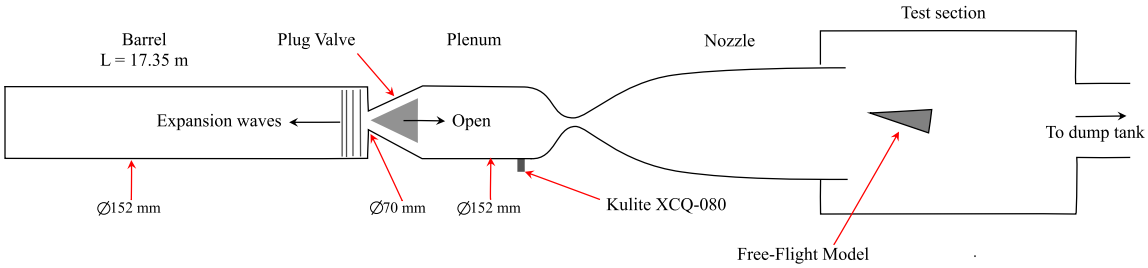

Fig. 3.6 Schematic of the University of Oxford High Density Tunnel (adapted from Hillyer et al. [29].)

When the plug valve is opened, expansion waves propagate down the barrel of the tunnel. These rarefaction waves are reflected at the far end of the barrel wall and pass back down along the tube. Therefore, the useful test time is defined by the time it takes for the waves to travel back and forth down the barrel and pass through the nozzle. These repeated reflections result in multiple quasi-steady flow periods (henceforth referred to as plateaus), resulting in a range of conditions for an individual shot. The plug valve opening and closing timings can be modified to dictate the number of steady test time plateaus required and hence the amount of flow that passes through the facility. For free-flight experiments, it is beneficial to terminate the flow as soon as possible after the first plateau as it is likely that the model is no longer within the core flow and subsequent flow may force the model into undesirable locations. Figure 3.7 demonstrates the ability of the experimenter to vary the plug valve timings. Shot 1671 shows a free-flight shot where the plug valve is closed quickly to minimise the flow the model experiences. Shot 1678 shows an alignment shot with a static model where it is no longer important to control the duration of the flow. More details about the plug valve can be found in McGilvray et al. [57].

A schematic of the Oxford HDT is provided in Figure 3.8 and a photo of the tunnel is provided in Figure 3.9,

3.5.3 Suitability of HDT for Aerodynamic Experiments

The suitability of a tunnel in terms of freestream test conditions in relation to aerodynamic experiments is determined by the ability of the facility to replicate both Reynolds and Mach

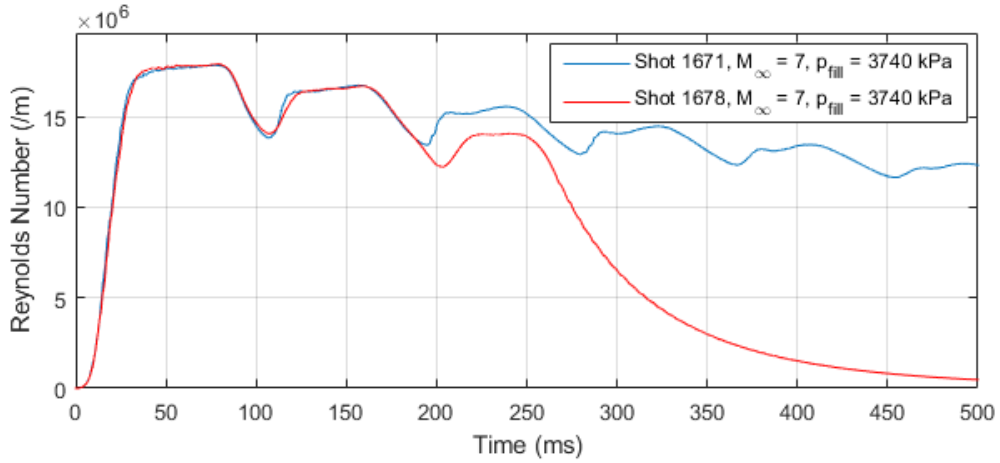

Fig. 3.7 Comparison of HDT shots with two different plug valve timings for the same fill conditions

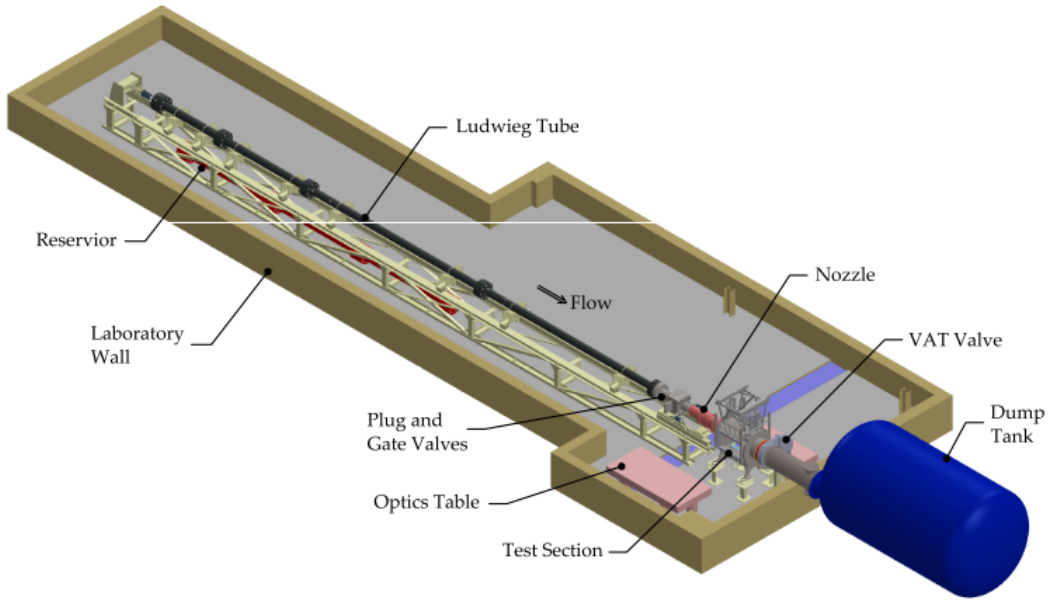

Fig. 3.8 An annotated schematic of the Oxford High Density Tunnel [57]

number for a given model scale (Mach scaling). Figure 3.10 presents the flight freestream conditions as Mach number against altitude for different vehicle trajectories. Using Equation 3.39, a facility map can be created for the freestream conditions that can be reached for a given model scale. Using the bounds of fill pressures (10 - 50 bar) and total temperatures (320-600 K), bands can be created for a given model scale for what flight freestream conditions can be achieved. Using US standard atmosphere [71], the equivalent flight conditions are converted

Fig. 3.9 Photo of the University of Oxford High Density Tunnel, test section can be seen at the far end of the facility

to trajectory points on the Figure so that bands of achievable altitudes at different Mach numbers for a given model scale are shown.

The Figure shows that air-breathing trajectories are achievable through the range of Mach numbers at modest 1:10 vehicle scales. The boost-glide trajectory (the Mach 7 data point is the one used in the majority of work in this thesis), is achievable at Mach 6 and Mach 7 for low model scales. This demonstrates that the University of Oxford High Density Tunnel is a suitable facility to conduct aerodynamic experiments, both in terms of providing sufficient test time and providing freestream conditions that are representative of flight.

3.6 Summary

This Chapter has laid down the criteria required for aerodynamic scaling with facilities in different flight regimes. The Mach scaling laws have been presented with their suitability demonstrated for the hypersonic regime. The application of Mach scaling has also been shown for both static and dynamic experiments demonstrating the importance of different dimensionless groups being replicated between flight and tunnel conditions, most importantly Mach and Reynolds number similitude.

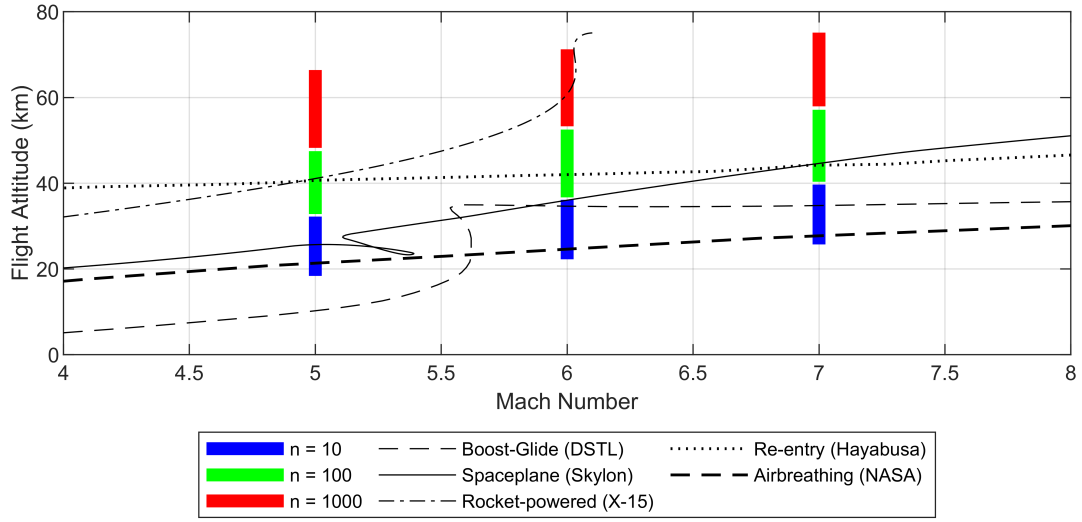

Fig. 3.10 HDT facility map with vehicle trajectories overlaid. 1:n is the vehicle to model scale. [32, 63, 64, 31]

The Oxford HDT has also been discussed demonstrating its capability to match flight conditions that have been Mach scaled to tunnel conditions.

Chapter 4

The Measurement of Static Aerodynamic Force Coefficients in a Hypersonic Ludwieg Tube using the Free-Flight Technique

Preamble

A research aim of the thesis was to obtain high quality aerodynamic coefficients using the free-flight technique and separate the static derivates of force from the aerodynamic coefficients. In this chapter, the static free-flight technique is validated by obtaining the static aerodynamic coefficients of a 7 degree half angle cone with low uncertainties and compared to a numerical panel method simulation. The pre-requisite work in commissioning the free-flight infrastructure with the Skylon Spaceplane is presented in Appendix A (a published journal paper in the AIAA Journal of Spacecraft and Rockets). For this work, the model was allowed to freely pitch and can be seen as the motivation to conduct static free-flight experiments. This Chapter consists of a journal paper currently under review in Experiments in Fluids. The content and structure of this chapter represent 100 % of the main body of the original paper.

Authors of the original paper:

Hyslop, A., Doherty, L.J., McGilvray, M.

Author contribution:

- **Hyslop, A.** : Lead author, conceptualisation, data curation, formal analysis, and writing.
- Doherty, L.J. : Supervision as Senior Research Associate.
- McGilvray, M. : Supervision as Principal Investigator.

Associated Appendices:

Appendix A - Free-Flight Aerodynamics of the Skylon Spaceplane
Appendix B - Mach 6 supplementary data

Abstract

Free-flight experiments have been conducted in the University of Oxford High Density tunnel, a heated Ludwieg tube, with a 7 degree half angle cone. The purpose of the investigation was two-fold; firstly to show that high quality static aerodynamic force coefficients can be measured using the free-flight technique, independent from influence of dynamic derivatives, and secondly to provide a validation case for the free-flight technique with a simple geometry for the measurement of force coefficients. To achieve a quasi-static free-flight test, the experiments were undertaken in a novel way in such that the centre of gravity of the model could be fine-tuned to be at the same position as the centre of pressure, hence minimising the static margin of the model. This resulted in a model that exhibited minimal pitch during a test and therefore limited influence of longitudinal dynamic derivatives, thus providing high-quality static aerodynamic data for an unconstrained model. The tests were conducted at a Mach 7 condition representative of a hypersonic vehicle's trajectory at 35 km altitude. Non-intrusive image tracking and on-board inertial measurement units were used to determine accelerations to calculate the aerodynamic forces acting on the cone. Results for lift, drag and pitching moment coefficients were obtained over a range of angles of attack and compared with predictions from a hypersonic panel method code. The experimental and numerical data sets agreed well over the range of angles of attack with the experimental uncertainties remaining below 3.1% for all coefficients.

4.1 Introduction

The knowledge of a vehicle's aerodynamic force coefficients over its flight map is essential for evaluating its performance. The definition of an aircraft's performance often varies depending on its classification, for example; it is highly desirable that a hypersonic boost-glide vehicle has a high lift-to-drag ratio over the extent of its trajectory to maximise its range. Therefore in the design phase, pre-requisite predictions of an aircraft's force coefficients are required before going ahead with costly flight testing. Often these force coefficients are initially predicted using numerical simulations, however, experimental validation is still

required to gain confidence in the simulations. In general, the creation of a high-fidelity, nose-to-tail numerical simulation of hypersonic vehicles is difficult and computationally expensive [107] [91]. Validation of such simulations requires high-quality experimental data, however, the measurement of forces in short duration hypersonic facilities at flight representative conditions still poses many challenges to researchers.

Further, the measurement of aerodynamic force coefficients is complicated as the instantaneous measured coefficient is a summation of both static and dynamic components if the experiment is not designed correctly. The dynamic components for longitudinal motion are caused by vehicle manoeuvres (such as pitching) or perturbations in freestream variables. By eliminating this behaviour, it is possible to measure purely static components of force with low levels of uncertainty. The most common method of determining static aerodynamic coefficients in wind tunnel facilities is to mount a model on a semi-rigid sting and measure forces and moments using a force balance. Complexities can occur with multi-component balances due to the often coupled nature of the force signals across the different axes. Furthermore, in short duration hypersonic facilities with test of times in the order of milliseconds to tens of milliseconds, stress waves within the model and supporting structure do not reach equilibrium making it difficult to measure quasi-static aerodynamic forces. Therefore, it is important that the dynamic response of the sting-model system is shorter than the available test time which is often difficult to achieve in hypersonic facilities [38]. Mee et al. [62] developed a rigid 3 component force balance for measurements in shock tunnels using the stress wave technique but accurate forces were still difficult to obtain, even when using advanced deconvolution techniques. The presence of the sting also results in undesirable drag and also produces unrealistic flow fields downstream of the model. Pick [79] showed that the interference effects of a sting is very influential at angles of attack of 15 degrees or greater for sharp cones in hypersonic flow.

Removing the sting and allowing the model to move unconstrained in the flow in six degrees of freedom is known as the free-flight technique. A typical methodology of a free-flight test in short duration facilities is as follows: the model is released prior to arrival of the test flow, the flow is initiated over the model which moves as it would in flight. As the model is not constrained, non-intrusive methods of measuring accelerations, rather than forces, are required. Using this technique removes the complex structural dynamic considerations that must be taken into account for sting based experiments as well as the undesirable sting-flow-field effects. Free-flight has been successfully demonstrated by Kennell et al. [40, 39] with ESA's HEXAFLY INT EFTV geometry and Hyslop et al. [33] for Reaction Engines' Skylon spaceplane. For these experiments, low inertia models were used which allowed the model to freely pitch over a wide range of angles of attack during a test and hence providing

large sweeps of aerodynamic coefficient data in a single run. With the large amounts of pitching during the test, the aerodynamic coefficients may include dynamic influence in the measurement. Lewis and East [48] conducted free-flight experiments for a low inertia cone which was designed to exhibit oscillations in pitch which damped in amplitude during the test time. From this damped pitching data they were able to measure the dynamic derivatives but at the sacrifice of scatter in both the static and dynamic derivatives measurements due to the curve fitting procedure used to determine forces. Therefore, to remove this dynamic component, the current work uses high inertia models with minimal static margin to reduce the magnitude of pitching seen during a test. This results in a purely static free-flight test analogous to a static force balance experiment without the sting.

This paper presents the methodology for obtaining static aerodynamic force coefficients using the free-flight experimental technique in the University of Oxford High Density Tunnel (HDT) applied to a 7 degree half-angle cone model. Data was acquired both using high speed video and an on-board IMU (Inertial Measurement Unit). Novel to this work is the ability to fine tune and measure (to 0.1 mm accuracy) the model's centre of gravity to minimise the static margin so that the model stays at constant angle of attack for the duration of the test time. Furthermore, by using a simple 7 degree cone, this work has lead to the validation of the free-flight technique for the determination of static aerodynamic coefficients against standard analytical models. This gives confidence in the technique for testing more complex geometries in the future.

4.2 Aerodynamic Force Coefficients

Aerodynamic coefficients for any vehicle in flight in six degrees of freedom can be defined by 3 orthogonal force coefficients and 3 orthogonal moment coefficients. If only longitudinal motion is considered, this reduces the coefficients to 2 force coefficients, lift (C_L) and drag (C_D), and a pitching moment coefficient (C_M). Ultimately, the instantaneous force and moments that act on a vehicle in flight are found through the integration of shear and pressure components acting over the body. These forces and moments can then be non-dimensionalised by the freestream dynamic pressure, $\bar{q}$, and a reference area, S, to give the force coefficients and an additional length, c, for the moment coefficient. The factors that influence the magnitude of the pressure and shear components are as follow:

1. The geometry of the vehicle - usually defined in terms of its mean chord length (c) and a ,reference area.

2. The orientation of the vehicle with respect to the freestream velocity vector, defined by angle of attack (α) and side-slip (β).

3. The velocity of the vehicle with respect to the fluid (V).

4. The density of the fluid (ρ).

5. The compressibility of the fluid, defined by the Mach number (M_∞).

6. The Reynolds number of the fluid - this characterises features such as viscous drag and boundary layer effects.

7. The history of the vehicle's trajectory through the fluid - this impacts upon the propagation of upstream wake disturbances, the hysteresis of flow separation and other unsteady, dynamic effects.

Therefore, to formally express the longitudinal aerodynamic force coefficients of a vehicle in flight at any time, t, as a function, it must be dependent on the Mach number, Reynolds number, attitude history and angular rate history of the vehicle:

$$C_L(t), C_D(t), C_M(t) = F\left[M(t), Re(t), \alpha(\tau), \beta(\tau), p(\tau), q(\tau), r(\tau)\right] \forall -\infty \leqq \tau \leq t. \quad (4.1)$$

Where p, q, r are roll, pitch and yaw rates respectively and τ denotes a point in time prior to time t. Equation 4.1 can be simplified with the assumptions of symmetric (3 degree of freedom) flight conditions, removing the dependency of side-slip, yaw rates and roll rates.

From the factors that make up the instantaneous forces and moments in flight, it can be seen that there is a dependency on the previous flight history. If the vehicle has undertaken a manoeuvre in roll, pitch or yaw, the history of that manoeuvre will manifest itself in the imparted forces and moments through transient features such as flow separation and propagation of shocks upstream. This introduces a dynamic dependency on the aerodynamic forces as time progresses. Therefore, to formally write the equations for aerodynamic coefficients as a sum of their parts, both static (stiffness) and dynamic (damping) components must be introduced. The equations of motion for a body in flight, written in their dimensionless form yield the equation for the aerodynamic coefficients as (discounting higher order derivatives) [105]:

$$C_L = C_{L_0} + C_{L_\alpha}\alpha + C_{L_{\delta_e}}\delta_e + C_{L_v}\frac{v}{V} + C_{L_q}\frac{qc}{2V} + C_{L_{\dot{\alpha}}}\frac{\dot{\alpha}c}{2V} + \ldots \quad (4.2)$$

$$C_D = C_{D_0} + C_{D_\alpha}\alpha + C_{D_{\delta_e}}\delta_e + C_{D_v}\frac{v}{V} + C_{D_q}\frac{qc}{2V} + C_{D_{\dot{\alpha}}}\frac{\dot{\alpha}c}{2V} + ... \tag{4.3}$$

$$C_M = C_{M_0} + C_{M_\alpha}\alpha + C_{M_{\delta_e}}\delta_e + C_{M_v}\frac{v}{V} + C_{M_q}\frac{qc}{2V} + C_{M_{\dot{\alpha}}}\frac{\dot{\alpha}c}{2V} + ... \tag{4.4}$$

where subscript 0 denotes the zero angle of attack coefficient, δ_e a control surface deflection, u a perturbation in freestream velocity and $\dot{\alpha}$ the rate of change of angle of attack. Equations 4.2 - 4.4 can be split into two categories, where the first 3 terms are the static derivatives (C_{X_0} - the zero degree angle of attack coefficient, C_{X_α} - the dependency of the coefficient with angle of attack and C_{X_δ} - the dependency of the coefficient with the deflection of a control surface deflection) which are independent of previous flight behaviour and the last 3 terms are dynamic derivates (C_{X_v} - the dependency on fluctuation in relative velocity, C_{X_q} - the dependency on the pitch rate of the aircraft and $C_{X_{\dot{\alpha}}}$ - the dependency on the rate of change of angle of attack of the vehicle).

To be able to measure purely static derivatives in wind tunnel facilities, the experimenter must remove the ability of the model to exhibit any dynamic behaviour with time. From equations 4.2 - 4.4 it can be seen that to remove any dynamic influence on the coefficients, two criteria must be fulfilled; the model must not be allowed to pitch and there must be minimal perturbations in the freestream flow. In wind tunnel facilities, it is assumed that during the test time, the perturbation of freestream velocity is small which removes the dependency on C_{X_u}. Furthermore, if the model is not allowed to pitch during the test and the freestream angularity of the flow is uniform with model position in the tunnel, the effects of C_{X_q} and $C_{X_{\dot{\alpha}}}$ are negated during the test. By fulfilling these conditions, a purely static condition is achieved and only the static coefficients are measured. This reduces Eq. 4.1 to :

$$C_L, C_D, C_M = F\left[M_\infty, Re, \alpha\right] \tag{4.5}$$

For sting-based experiments combined with a load cell or force balance, this static test condition is easy to reach by holding the model rigid whilst flow is initiated over the model. In free-flight, this is harder to achieve as the model is free to move in six degrees of freedom. The next section discusses how this static free-flight condition is achieved. It must be noted that static coefficients can be estimated using dynamic techniques, but as discussed by Rodden et al. [82] and Newman [70], are best measured through use of static techniques to minimise uncertainties in the measured coefficients.

4.3 Static Free-Flight Technique

Section 4.2 presented the criteria required to achieve static force measurements for wind tunnel experiments by removing the influence of dynamic phenomena during a test. For free-flight testing, the scaled model is free to move in six degrees of freedom so it is not possible to constrain the model from pitching through the use of rigid mounts. This section discusses how a free-flight model can be designed so that the nature of the test is static and also how the freestream flow is calculated to achieve similitude with flight.

4.3.1 Static Model Design

For this study, the primary purpose was to measure static aerodynamic coefficients and hence the model was designed to optimise this condition. In typical aerodynamic force measurement experiments, the model is rigidly mounted using a sting so that it is fixed at a single angle of attack for the entire test. A comparable test in free-flight is one in which the model exhibits minimal pitching and remains at a constant angle of attack. There are two approaches which could be taken to achieve this. The first is to design a model that has very large inertia so that during a test, the forces acting on the model result in very small angular (and linear) accelerations. The main difficulty with this approach is that as the accelerations are small, they are difficult to measure and uncertainties in the resulting force coefficients are large.

The second approach and the one used in this work is to ballast the model so that the net pitching moment acting on the model in flight is zero. Consider the aerodynamic forces acting on a free body in free-flight; as the fluid passes over the body during a test, pressure and shear components are exerted on the surface of the body. Integrating the shear and pressure components over the body results in the overall aerodynamic force acting on the body. This integrated force can be considered to be a single force vector at the average integrated location, often referred to as the centre of pressure (CoP). The force vector is usually split into two orthogonal forces referred to as lift and drag. The final force that needs to be considered is the model's weight which can be considered to act as a single vector through the centre of gravity (CoG). The position of the CoG relative to the CoP determines the stability of the body in flight. If the CoG is fore of the CoP, the body is statically stable and will tend to pitch towards an equilibrium position if perturbed. If the CoG is aft of the CoP, the body is statically unstable and will pitch away from an equilibrium position which is often undesirable as it makes the body difficult to control. In both of these instances, the body will exhibit increasing pitch rates as the distance between the CoP and CoG is increased.

If a model is designed so that the CoP is at the same position of the CoG, there will be no aerodynamic pitching moment and hence can be considered as a static free-flight test.

In practice, this requires: (1) a method of predicting the CoP location, (2) a model design that allows for fine tuning of the CoG location and (3) a setup that can accurately measure the CoG location before a test. It should be noted that in this methodology, the model design is independent of mass and moment of inertia and so the experimenter is not limited by material choice as they would be if scaling for dynamic experiments which require strict similitude criteria to be matched for mass and inertia to obtain flight representative dynamic derivatives.

4.3.2 Freestream Scaling

To achieve similitude for flight conditions between the subscale free-flight model and flight vehicle, two criteria must be matched. The first is that for hypersonic flows, the Mach number between flight and the tunnel flow must be matched. This preserves flow features such as compressibility effects and shock angles. The second criteria is that Reynolds number is matched between flight and tunnel so that features such as viscous effects and boundary layer transition are preserved. As a consequence of this, it can be shown that matching these features causes a mismatch in Froude number [105] (ratio of inertial to buoyancy forces). As matching the Froude number preserves gravitational effects, the mismatch means that angle of attack similitude may not be preserved.

If both Reynolds and Mach number are matched, the following equation can be derived by taking ratios of Reynolds number (where subscript m denotes the model, subscript v the full-scale vehicle and ρ_f is the fluid density, n is the geometric scaling factor, T is static temperature and μ is dynamic viscosity):

$$\left(\frac{\rho_f T^{\frac{1}{2}}}{\mu}\right)_m = n\left(\frac{\rho_f T^{\frac{1}{2}}}{\mu}\right)_v \tag{4.6}$$

With knowledge of the model scale and flight trajectory point of interest, all flow properties on the right hand side of Eq. 4.6 are fixed. Therefore, the left hand side describes a test envelope that the test facility must achieve in order to achieve similitude. For the series of experiments in this work, a trajectory was used that is representative of vehicles in the hypersonic regime [32]. A condition at Mach 7 at a representative altitude of 35 km was used. Section 4.4.2 discusses the scaling applied to this trajectory point and Table 4.1 present both the in flight and scaled free-stream conditions.

4.4 Experimental Setup

4.4.1 Facility and Test Infrastructure

The experiments were conducted in the University of Oxford High Density Tunnel located within the Oxford Thermofluids Institute. The facility was operated as a heated Ludwieg tube with the Mach 7 contoured nozzle of exit diameter 350 mm, producing a core flow of 280 mm at nozzle exit. The facility is typically operated at total pressures up to 50 bar but is rated for fill pressures of 275 bar. For further details on the HDT operation and measurement of freestream conditions, see McGilvray et al. [57] and Wylie et al. [108]. This facility was selected for these experiments because it offers sufficient steady flow duration ($\sim$ 50 ms) to allow for the measurement of quasi-static forces in free-flight at flight representative conditions.

Shown in Fig. 4.1, a catcher net and model drop mechanism were designed for the HDT. The catcher mechanism consists of two aluminium rings which are interwoven through 32 uniformly spaced holes with 1.5 mm diameter Dyneema cord to form a net. The upstream ring is held at a 30 ° inclination which is designed to deflect the model towards the tunnel floor upon contact which is lined with multi-layer foam. The purpose of the catcher rings is two-fold, firstly to reduce the amount of damage taken by the model by providing a soft impact surface, and secondly to prevent the model entering the facility dump tank where it would be difficult to retrieve.

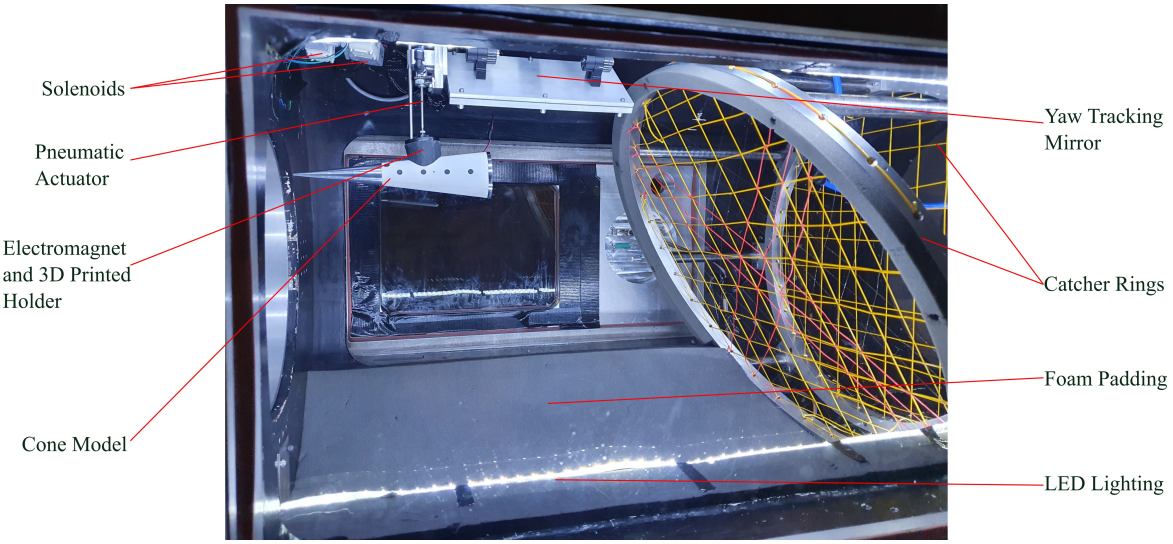

Fig. 4.1 Free-flight drop mechanism and catcher rings in the HDT test section.

The drop mechanism was designed to release the model into the core flow prior to the arrival of test flow. The system consisted of a 25 mm electromagnet connected to a 50

mm stroke length SMC pneumatic actuator which removes the electromagnet from the core flow once the model is released. The actuator and electromagnet were controlled by a bespoke electrical control unit which upon receiving a TTL pulse from the tunnel, triggers the electromagnet to release the model and powers two solenoids to retract the actuator, removing the magnet from the oncoming flow. The entire drop mechanism is mounted on a linear rail so that the axial position of the drop can be changed if required. A 3D printed holder was used to house the electromagnet and was shaped to be conformal to the cone model, allowing for repeatable alignment in roll and axial position of the model prior to the test. Different holders were printed to allow for the initial angle of attack to be set in two degree increments. A steel rod is inserted into a tightly tolerance hole in the holder which fixes the initial position in yaw. The printed holder is shaped to position the electromagnet directly above the centre of gravity of the model to minimise any exerted rotational inertia on the model when it is released and hence provided a consistent and repeatable model release.

Attached to the top plates of the drop mechanism through angled bracket mounts is a mirror which allows for optical tracking on the yaw axis of the model. To improve optical visibility of the model during the test, four 400 lumen LED strips were attached internal to the test section.

4.4.2 Test Conditions

To determine the scaled tunnel freestream conditions, a model scale and flight trajectory must be chosen so that flow conditions for similitude can be determined using Eq. 4.6. For this work, the model scale was dictated by the requirement that the entire model remain within the core flow diamond (biconic) of the HDT nozzles throughout the duration of steady test flow. This resulted in a model that was geometrically scaled to 1:12th of the design scale; the total length of the model was 250 mm (with the assumption that a full scale vehicle is on order of length 3 m) [1]. A trajectory point replicating a hypersonic vehicle at Mach 7 at an altitude of 35 km was used. The conditions obtained during a test were surveyed prior to the experiments using a rake instrumented with pressure transducers and thermocouples, providing freestream total pressure, pitot pressure and total temperature traces. From these measurements, the pitot-to-stag ratio was used to calculate Mach number, Keyes' Law to calculate dynamic viscosity [43] and isentropic relations to calculate the rest of the tunnel conditions. Equivalent flight conditions were calculated through US Standard Atmosphere [71] and viscosity using Sutherland's Law [94]. The uniformity of the core flow with respect to axial position was also measured with the rake. The core flow was determined to be of 280 mm diameter at nozzle exit reducing to 240 mm at 300 mm downstream. Uncertainties in the calculated freestream variables are determined using the Taylor Series Method through the

propagation of uncertainties from the measured properties. The flight freestream conditions and scaled tunnel conditions are shown in Table 4.1. Computation fluid dynamic (CFD) simulations of the nozzle conducted in Eilmer4 show agreement with the measured core flow diameter at nozzle exit and predict the angularity of the flow to remain within +/- 0.12° within the core flow.

Table 4.1 Mach 7 Flight vs scaled tunnel condition.

Measured Freestream Properties	**HDT Test Flow**	**Flight**
Total Pressure (kPa)	3348 ± 7	2313
Pitot Pressure (kPa)	49.9 ± 0.7	35.5
Total Temperature (K)	555 ± 15	2560
Calculated Freestream Properties		
Altitude (km)	35	35
Mach Number	7.05 ± 0.02	7
Velocity (ms^{-1})	1006 ± 14	2160
Density (kgm^{-3})	0.0532 ± 0.0018	0.0082
Static Pressure (Pa)	774 ± 15.8	559
Static Temperature (K)	50.8 ± 1.4	242
Dynamic Viscosity (μPas)	3.64 ± 0.10	15.2
Dynamic Pressure (kPa)	26.9 ± 0.6	19.1
Unit Reynolds Number ($10^6 m^{-1}$)	14.7 ± 0.7	1.16
Reynolds Number (10^6)	3.68 ± 0.16	3.48

4.4.3 Experimental Model

The experimental model, seen in Figures 4.1 and 4.2, was geometrically scaled to be representative of a full-scale hypersonic vehicle, resulting in a 1:12th scale model. The model was designed to be modular to allow for easy instrumentation and ballasting. Therefore, it was manufactured so that it could be split into two halves for ease of access. The two halves form a male thread near the front when joined together so that nose tips of different materials (for ballasting purposes) and nose radii (1.25, 2.5 and 5 mm) could be used. For these sets of experiments, the cone halves and rear were machined from steel and the nose tips were aluminium.

The most important aspect of the experimental model was the ability to change the centre of gravity location. As the model was made of steel, the ballasting was achieved through tungsten disks whose position could be adjusted internally in the model using threaded steel rods. The CoP of the model was predicted prior to testing using Modified-Newtonian Theory to be 83.6 mm from the base. The tungsten ballast allowed for the CoG to be shifted between 80.1 mm to 85.7 mm. Table 3 presents the inertial and geometric properties of the cone model. The centre of gravity was measured using a moment balance, whereby the model was suspended using two strings. The tension in the upstream string was measured using a load cell. This setup allowed the CoG to be determined to +/- 0.1 mm. The moment of inertia was not measured directly but determined through the Computer Aided Design software Solidworks. As these were static aerodynamic tests, an accurate measurement of moment of inertia is not required as the model exhibits minimal pitch.

Internal to the model was an on-board Data Acquisition system (DAQ) which contained a six degree-of-freedom inertial measurement unit (IMU) consisting of accelerometers and gyroscopes. The board was mounted on a 3D printed holder which fitted conformal to the internal shape of the cone halves, fixing it rigidly in place.

For the exterior, the model was painted white and a laser-cut stencil was used to airbrush black dots on the model with a tolerance in centre point location of +/- 0.2 mm for the purpose of image tracking. The black and white paint created a high contrast finish enabling the image tracking algorithm to work more effectively in post-processing. Also painted on the model were two 'T' shapes to mark the point where the electromagnet attaches to the model. It is important for the drop mechanism that the release point was at the CoG of the model to prevent pitching during the drop free-fall period.

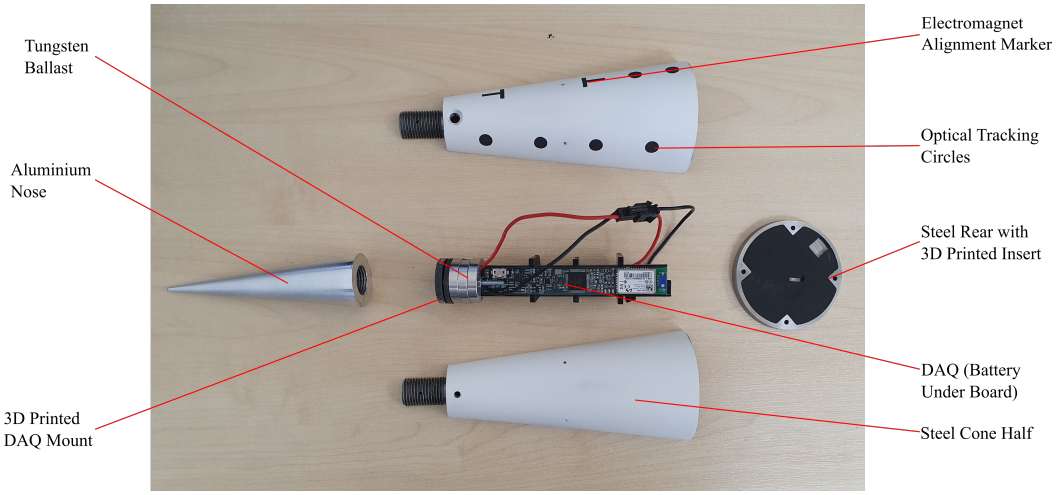

Fig. 4.2 Constituent components of the 7 degree cone model.

Table 4.2 Model inertial and geometric properties

Length (mm)	250 ± 0.2
Cone Half-Angle (°)	7 ± 0.03
Nominal Nose Radius (mm)	1.25 ± 0.1
Base Area (m^2)	$3.2\ \text{x}10^{-3} \pm 0.01$
Centre of gravity (mm)	84.3 ± 0.1
Mass (g)	669.73 ± 0.01
Moment of Inertia (kgm^2)	$2.15\ \text{x}10^{-3}$

4.4.4 On-board Data Acquisition System

The on-board inertial measurement instrument (hereby referred to as the DAQ) were designed and built by UNSW Canberra. They consisted of an integrated 3-axis accelerometer and 3-axis gyroscope, non-volatile memory, a Bluetooth radio module and a microcontroller. These components were integrated on a single printed circuit board with planform dimensions of $\sim$ 114 mm x 12 mm. This measurement system has successfully demonstrated the ability to collect accurate acceleration and angular velocity data necessary for hypersonic wind tunnel model aerodynamics [39, 59]. The IMU was a single chip device with an accelerometer full scale range of +/- 16 g and a data output rate of 4 kHz. The full scale range of the gyroscope was +/-2000 deg/s with a data output rate of 8 kHz. Non-linearity of the accelerometer and gyroscope axis is reported to be 0.1% and 0.5% respectively. For this work a sample rate of 8 kHz was used which allowed for $\sim$ 320 samples over the 40 ms duration of the experiment. Triggering of the instrument was achieved by detection of sustained free-fall upon model release.

4.4.5 Optical Setup

For this work, image tracking was conducted on both the yaw and longitudinal axis. The longitudinal axis was imaged by a FASTCAM AX200 high-speed camera set to a frame rate of 6400 fps with 1,024 x 1,024 pixel resolution at a focal length of 50 mm at f 2.8. The camera faced directly through the test section windows, imaging the longitudinal plane of motion of the model. To fully capture the free-fall of the model, a pre-trigger of 500 frames was used and a total of 2180 frames recorded, activated by a TTL pulse from the facility prior to the test. A FASTCAM UX100 high-speed camera was used to track the yaw axis with a frame rate 1000 fps resulting in a resolution of 1,280 x 1,024 pixels. The yaw axis was imaged through a reflection of a mirror on the roof of the test section and was mainly used to confirm the model was exhibiting minimal yaw during a test. Six 1000 lumen torches were used to front light the model, providing adequate spacial uniformity of light. The two cameras were positioned as such that both systems could operate concurrently during a test with neither system obstructing the field of view of the cameras. A few experiments were conducted with schlieren imaging to confirm that the model was in the core flow during the course of a test. In order to achieve this, both of the optical tracking cameras were removed. For the schlieren, a conventional Z-type setup with horizontal knife edge was used to visualise the density gradients in flow field around the cone model. The light was emitted continuously from a Luminous PT-120-TE green LED as the camera's detector is particularly sensitive to this wavelength region. The flow was imaged with the FASTCAM AX200 high-speed camera at 6400 fps.

4.5 Numerical Study

For this work, a panel method aerodynamics code was created to determine the aerodynamic coefficients of the cone geometry. This builds upon the work of Donaldson and Ireland [17], expanding on the functionality and creating an aerodynamic tool in the MATLAB language domain. The purpose of the code was twofold; the experimental work validates the aerodynamics code so that it can be used in future for more complex geometries and secondly, the rapid nature of the code means it can be tied to trajectory calculations. The aerodynamics code is written entirely in MATLAB and best simulates trajectories that are in the continuum regime. The code requires an input of the freestream conditions to begin the analysis. This is either calculated by inputting a trajectory point (altitude) and Mach number so that freestream conditions can be calculated through 'US Standard Atmosphere 1976' [71] or utilizing a condition calculator that outputs HDT test conditions. Following this, the attitude (roll, pitch and yaw) of the geometry of interest are inputted.

This section discusses the principles on which the code operates and the methods it uses for deriving key values for calculations.

4.5.1 Geometry

Geometry is processed in the form of a tessellated triangular mesh with the individual faces referred to as 'panels'. For simplicity and speed, meshes are input using the STL format due to the wide availability of meshing preprocessing tools. Figure 4.3 shows an example of the 7 degree cone mesh used in the processing. The preprocessing closely follows the methods used by Donaldson [17]. Upon importing the geometry into MATLAB, the mesh panels are processed so that the surface area, geometric centre and unit normal are calculated. The user also manually inputs a reference length, overall surface area and location of centre of gravity for later calculations.

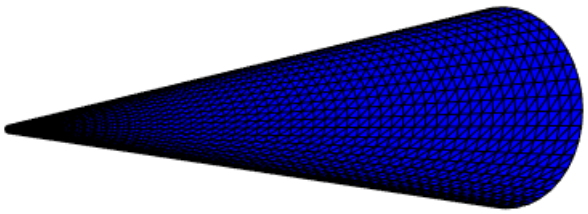

Fig. 4.3 Triangulated mesh of a 7 degree cone

To determine the surface pressures of each of the panels, the panels are first processed to determine their orientation relative to the freestream velocity vector. This angle, denoted δ, is subsequently used for the calculation of pressure coefficient. The equation for panel orientation to freestream is given by (where $\hat{N}$ is a panel normal and $\hat{V}$ is the velocity vector):

$$\delta = \cos^{-1}\left(\frac{\hat{N}.\hat{V}}{|\,\hat{N}\,|\,.\,|\,\hat{V}\,|}\right) = \cos^{-1}\left(\hat{N}.\hat{V}\right) \tag{4.7}$$

4.5.2 Aerodynamics

To determine the pressure coefficient, C_p, on each of the panels, the code uses widely established panel inclination methods which relate the inclination angle $\hat{\delta}$ and freestream properties to the pressure coefficient. Firstly, using the value of δ, a panel is determined to be either windward (exposed to the flow) or leeward (hidden from the flow). If $\mid \delta \mid < 90$ the panel is treated as windward, otherwise it is assigned to be leeward. The user has different options to calculate the pressure coefficient. The windward methods are given by:

1. Modified Newtonian Flow – the pressure exerted on a vehicle is due to the loss of momentum of the fluid normal to the vehicle's surface. The modified version includes the stagnation pressure coefficient of the freestream, C_{P0}, as a correction factor.

$$C_p = C_{P0} \sin^2 \hat{\delta} \tag{4.8}$$

2. Tangent Cone – a semi-empirical method based on a three-dimensional flow field determined by constructing an equivalent cone tangent to the centroid of a panel and then calculating the surface pressures behind a conical shock. This code uses an empirical method derived from Cruz and Sova [12] (where M_n is the Mach number normal to the shock) and is suited towards slender bodies of revolution:

$$C_p = \frac{48 M_n^2 \sin^2 \hat{\delta}}{23 M_n^2 - 5} \tag{4.9}$$

The leeward methods are given by:

1. Newtonian - all leeward panels have the same surface pressure as the freestream pressure, resulting in a pressure coefficient of zero.

$$C_p = 0 \tag{4.10}$$

2. High Mach base pressure (full vacuum) - a total vacuum is formed in the wake region of the model, γ is the ratio of specific heats.

$$C_p = \frac{-2}{\gamma M^2} \tag{4.11}$$

3. High Mach base pressure (70%) - recirculation and expansion in the wake region dive the surface pressures above a full vacuum.

$$C_p = \frac{-1}{M_\infty^2} \tag{4.12}$$

The user can select which methods to use to calculate the surface pressure coefficients for a given model. For blunt bodies, Modified-Newtonian theory is often more suitable than Tangent-Cone due to the nature of the flow and shock patterns around a blunt body. For this work, Tangent-Cone is used with a toggle which switches to Modified-Newtonian for blunt areas such as the blunted nose. 70% base pressure is selected for the leeward panels due to its good agreement with experimental data.

4.5.3 Viscous Effects

At hypersonic Mach numbers, the interaction between the outer inviscid flow and viscous boundary layer become significant and cannot be discounted. It has been shown in previous studies that viscous shear stresses can account for more than 25% on hypersonic vehicles [2]. The method in this study accounts for viscous effects by determining the path of streamlines across the surface of a vehicle. These streamlines can then be used to determine the local Reynolds number of a panel and hence correlations can be used to determine local skin friction coefficients, similar to the method applied by Wuilbercq et al. in HyFlow [106].

In order to generate surface streamlines, the surface velocity field is calculated based on Newtonian impact theory in which particles upon collision to a surface, retain their tangential velocity. Streamlines are tracked from the rear of the vehicle and propagated from panel to panel using a 4th order Runge-Kutta numerical method. A streamline is ultimately terminated at a stagnation point which can be determined by setting a bound on the dot product between the surface normal and streamline shear vector; these will be tangential at a stagnation point. After a suitable number of streamlines are detected which give good coverage of the vehicle's surface, the running length of each streamline is calculated. This is then interpolated over the mesh so that each panel has a running length value. Figure 4.4 presents streamlines as calculated for the cone model at 4 degrees angle of attack.

The streamline running length is ultimately used to calculate the local Reynolds number on each of the panels. However, difficulties arise when calculating the temperature of the flow at the surface of a panel due to the large temperature gradient across the thickness of the hypersonic boundary layer. To correct for this, the code uses the Smart-Meador method [60] to calculate a reference boundary layer temperature. These expressions are then used to calculate the local skin friction coefficients using Eckert's procedure [18] which are derived from experimental skin friction coefficients on a flat plate. It is down to the user to decide whether the flow is laminar or turbulent in the current version of the code. With knowledge of

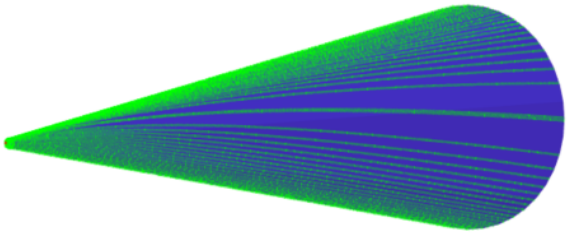

Fig. 4.4 Calculated streamlines for cone at 4 degrees angle of attack

both the inviscid pressure coefficient and skin friction coefficients, the overall aerodynamic coefficients can be calculated.

4.6 Data Processing

Two non-intrusive independent methods of deriving aerodynamic force coefficients were used in this work. Both methods ultimately measure the model's acceleration to determine the instantaneous forces acting on the model during the test time using the model's mass, m, and moment of inertia, I_{yy} (Table 4.2). The forces are then non-dimensionalised by the freestream dynamic pressure (Table 4.1) and a reference area, which in this work was taken to be the cone base area (S = 3.2x10^{-3} m^2). The reference length, c, used in the calculation of pitching moment was the model length (0.25m).

$$C_L = \frac{m\ddot{z}}{\overline{q}S}, \quad C_D = \frac{m\ddot{x}}{\overline{q}S}, \quad C_M = \frac{I_{yy}\ddot{\theta}}{\overline{q}Sc} \tag{4.13}$$

4.6.1 IMU Data Processing

Before discussing the details of processing IMU accelerations and angular velocities, it is first necessary to define the co-ordinate systems used in the processing. There are two frames of references used in this work; the first is known as the Inertial/Earth coordinate system which is defined as having the +z axis towards the ground, +x axis pointing upstream towards the facility nozzle and the +y axis orthogonal to both to form a right-hand coordinate system. This frame of reference is what all global force coefficients are defined relative to.

The second co-ordinate system is referred to as the body frame of reference. This is defined relative to the model as +x towards the nose of the vehicle, +z towards the bottom

of the vehicle with +y completing the orthogonal system. The IMU located on the model measures accelerations and angular velocities in the body frame of reference and hence during a test, this frame of reference is moving relative to the Inertial frame. To process the raw gyroscopic and accelerometer IMU data, it is filtered with a 6^{th} order low pass Butterworth filter with a cut off frequency of 500 Hz to remove high frequency noise. The body angular rates are then transformed to Euler angular rates, using Eq. 4.14, allowing the Euler angles to be determined via numerical integration of Euler-rates. Using the Euler angles, the linear accelerations measured by the IMU are transformed to the inertial frame of reference according to Eq. 4.15. Finally the aerodynamic coefficients can be obtained using Eq. 4.13.

The rotation matrix for the angular rates and accelerations (subscript E for Earth coordinates and B for body coordinates) are as follows (where c, s and t are cosine, sine and tangent functions respectively, p, q and r are body roll, pitch and yaw rates respectively and ϕ, θ and ψ are Euler angles):

$$\begin{bmatrix} \dot{\phi} \\ \dot{\theta} \\ \dot{\psi} \end{bmatrix} = \begin{bmatrix} 1 & s(\phi)t(\theta) & c(\phi)t(\theta) \\ 0 & c(\phi) & -s(\phi) \\ 0 & \dfrac{s(\phi)}{c(\theta)} & \dfrac{c(\phi)}{c(\theta)} \end{bmatrix} \begin{bmatrix} p \\ q \\ r \end{bmatrix} \tag{4.14}$$

$$\begin{bmatrix} \ddot{X} \\ \ddot{Y} \\ \ddot{Z} \end{bmatrix}_E = \begin{bmatrix} c(\psi)c(\theta) & c(\psi)s(\phi)s(\theta) - c(\phi)s(\psi) & s(\phi)s(\psi) + c(\phi)c(\psi)s(\theta) \\ c(\theta)s(\psi) & c(\phi)c(\psi) + s(\phi)s(\psi)s(\theta) & c(\phi)s(\psi)s(\theta) - c(\psi)s(\phi) \\ -s(\theta) & c(\theta)s(\phi) & c(\phi)c(\theta) \end{bmatrix} \begin{bmatrix} \ddot{X} \\ \ddot{Y} \\ \ddot{Z} \end{bmatrix}_B \tag{4.15}$$

Figure 4.5 presents a plot of filtered IMU accelerations with freestream total pressure for a typical free-flight test. As seen in the figure, the model free-falls for approximately 120 ms before the onset of flow. During this time the model falls into the centre of the core flow of the tunnel. The tunnel takes 30 ms to start up before the steady plateau in free stream conditions are reached. It is during this steady plateau that the test time is taken. The filtered accelerations in the direction of lift and drag mimic the plateau in free stream stagnation pressure. The accelerations stay constant during the steady test time due to the minimal pitching exhibited by the model during a test. In Fig. 4.5 it can be seen that there is a non-negligible acceleration in the out of plane axis. This exists as a consequence of the inability to accurately align the model with respect to the freestream on the yaw axis in the current tunnel arrangement due to lack of optical access. These accelerations will cause the measured drag coefficient to be slightly increased.

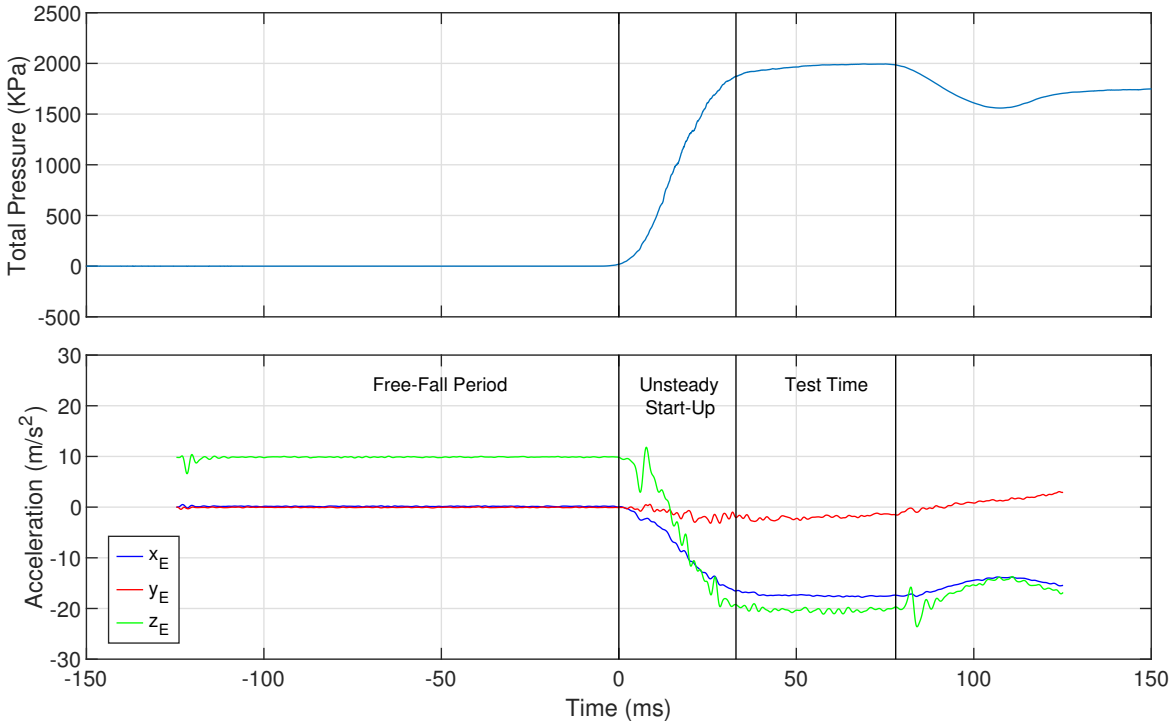

Fig. 4.5 Example filtered accelerometer accelerations in the Earth frame of reference with HDT total pressure.

4.6.2 Image Processing

Optical tracking was used to measure the model's displacement about the centre of gravity of the model. The technique used in this work uses a methodology which finds the centre point of high contrast circles painted on the surface of the model. As seen in Figure 4.6, for longitudinal tracking (about pitch axis), four black circles are painted on the side of the model which are at known locations relative to the model. Only two circles are required by the algorithm; the additional two circles are added for redundancy in the case of damage or non-uniform lighting. The methodology for image tracking is the same as in the work of Hyslop et al. [33] but the steps are briefly summarised as follows:

1. Apply Gaussian filter to image and subtract from original (High pass filter).
2. Apply Canny filter to image so that only pixels detected as an edge are shown [9].
3. Apply Hough transform to find circles in the image after narrowing the search radius [30].
4. Detect pixels in the proximity of the circle located by the Hough transform.

5. Use sub-pixel detection on the original image using the methodology set out in von Gioi and Randall [99] at the location where pixels were detected by the Hough transform.

6. Fit a circle to the pixels using linear regression as set out in Laurence et al. [45] and use this equation to find the centre point of the circle.

Following the detection of the centre point of two circles, a line is fitted between these two points. For the current model, the centre of gravity lies on this line at a known distance relative to the upstream circle. This process is repeated for each frame giving a time history of centre of gravity displacement. Knowledge of the physical distance between the detected circles allows each image to be scaled from pixels to metres. For the current setup, the image scaling factor was 0.69 mm/pixel. Figure 4.6 presents a composite image of a typical free-flight experiment with the image tracking algorithm detection points overlaid. The red line in Figure 4.6 shows the location of the CoG of the model for the duration of the test time, confirming that the model remains in the core flow for the duration of the test. Prior to testing, the spatial uniformity of the lens was measured and corrected for through the use of a uniform grid inserted into the tunnel using the Matlab camera calibrator algorithm.

Angle of attack is determined by detecting the edge of the cone and using this to find the relative angle to the horizontal. This angle is then corrected as explained in Section 4.6.3 to give the true angle of attack of the model. Painting the model white gave strong contrast between the background and the boundary of the cone surface. The boundary is detected by using a Canny filter to isolate the edges followed by sub-pixel detection to find the true edge. These points are then fitted with a straight line and the gradient is calculated to determine the angle of attack. The model edge is the preferred method of detecting angle of attack (over the circles) as it is unaffected by model roll during a test as the conical model is axisymmetric.

To determine the aerodynamics coefficients, the displacement data is differentiated twice to give the accelerations and hence aerodynamic coefficients using Eq. 4.13. The intermediate velocity data required numerical smoothing using a Gaussian filter before being differentiated into accelerations.

The accuracy of the algorithm was analysed by calculating the position of centre of gravity for 500 frames where the model was held stationary. The standard deviation of centre of gravity position for this test was calculated to be 4 μm. Given that the pixel resolution was 0.69 mm/pixel, and the radius of the detected circles was approximately 5 pixels out of a frame size of 1024 x 1024, this very small standard deviation for the detected CoG when the model is held stationary indicates that centre of gravity can be determined with a high degree of accuracy. This analysis does not take into account errors which result from misalignment

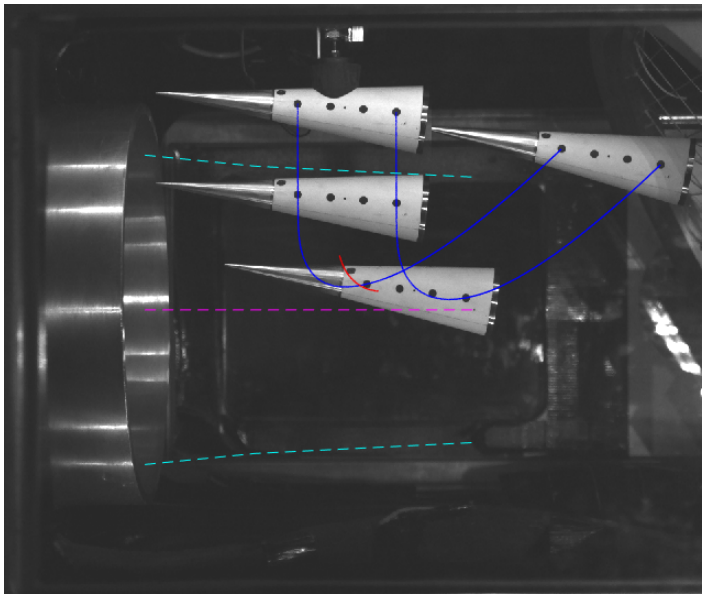

Fig. 4.6 Montage photo of image processing (Blue - detected circle centre points, Red - calculated centre of gravity, shown for test time, cyan - core flow location as acquired by a pitot survey, pink - nozzle centreline).

of the optical equipment but gives an approximation of the uncertainty associated with the numerical algorithm.

Yaw tracking has further complications when compared with longitudinal tracking because as the model falls, the distance between the yaw plane and the camera is not constant. To overcome this, the model was imaged with a smaller aperture of f8 to increase the depth of field. At this smaller aperture, it was necessary to decrease the frame rate to 1000 fps to expose the image correctly. Yaw tracking was implemented to confirm that the yaw of the model stayed within acceptable bounds of +/- 0.5 deg for the duration of the test as model yaw can highly influence the measured drag coefficient.

4.6.3 Angle of Attack Correction

One consideration with free-flight experiments to be accounted for is the relative angle of attack of the model to the free-stream flow from the facility. The initial angle of attack for these experiments is determined from optical tracking. This however, could potentially result in a systematic error in angle of attack for all data points due to the unknown relative angle between the camera horizontal and freestream flow. For rigidly mounted, sting-based experiments, the experimenter will often use pressure transducers to measure the true zero degree angle of attack and use this subsequent position as a datum. This methodology becomes more difficult for free-flying models as on-board pressure sensors would be required.

To overcome this alignment issue, an alignment probe (four radial pressure transducers, north, east, south and west) was sting mounted to a two axis traverse and experiments were conducted to find the true zero angle of attack. This is at the point where the north and south pressure transducer read the same static pressure value. The optical cameras were used to calculate the angle of attack from their reference point and this offset was subsequently applied to all of the experimental data. The offset in angle of attack at Mach 7 was found to be -0.57 $\pm$ 0.05 $^\circ$ for this test campaign. The camera set up remained fixed between free-flight tests and alignment test. In an ideal setup with sufficient optical access, this process would be conducted on the yaw plane too to guarantee full alignment with the freestream.

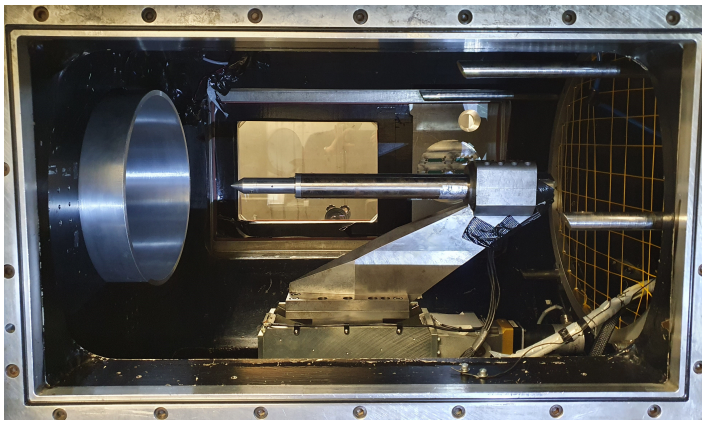

Fig. 4.7 Alignment probe installed in the Oxford High Density Tunnel

4.7 Experimental Results

The results from the free-flight experiments are presented in this section. Lift, drag and pitching moment data are shown, as well as centre of pressure variation at the Mach 7 conditions. The experimental results are shown for both the IMU data and optical tracking and presented against viscous tangent cone predictions from the numerical panel method simulations. Uncertainties are shown as error bands around the data points as calculated using the Moffat's error propagation method [66] for freestream parameters, model properties, IMU and image tracking.

4.7.1 Aerodynamic Coefficients

In total, 14 independent tests were conducted at a Mach 7 test condition in Table 4.1. Figure 4.8 presents the measured variation in lift coefficient with angle-of-attack, including a comparison with viscous tangent-cone calculations. The general trend of data is linear

and agrees well with the numerical tangent-cone predictions. The linear trend gives a zero value for lift coefficient at 0 ° angle of attack as expected for a axisymmetric body. The overall agreement between the image tracking and IMU data is also good for lift coefficient. Figure 4.9 presents the drag coefficient against angle of attack for the Mach 7 condition. The non-viscous and viscous numerical predictions are plotted for comparison with the experimental data. The experimental data agrees well with the viscous numerical prediction and exhibits the expected parabolic shape. The inviscid case is only plotted for the drag coefficient as at the angles of attack tested, the viscous effects make minimal difference to the other coefficients. Figure 4.10 shows the variation in lift-to-drag ratio with angle-of-attack. The numerical predictions have good agreement with the experimental data with a slight offset at the extremities of the data range. The maximum uncertainties for lift and drag coefficient occur at the high angle of attack tests for both the IMU and image tracking data. For lift coefficient, the maximum uncertainty is $\pm$ 0.0058 corresponding to a force of $\pm$ 0.49 N with a percentage uncertainty of 2.2 % in the overall measurement and for drag coefficient, the maximum uncertainty is $\pm$ 0.0040 corresponding to a force of $\pm$ 0.34 N with a percentage uncertainty of 3.1 %.

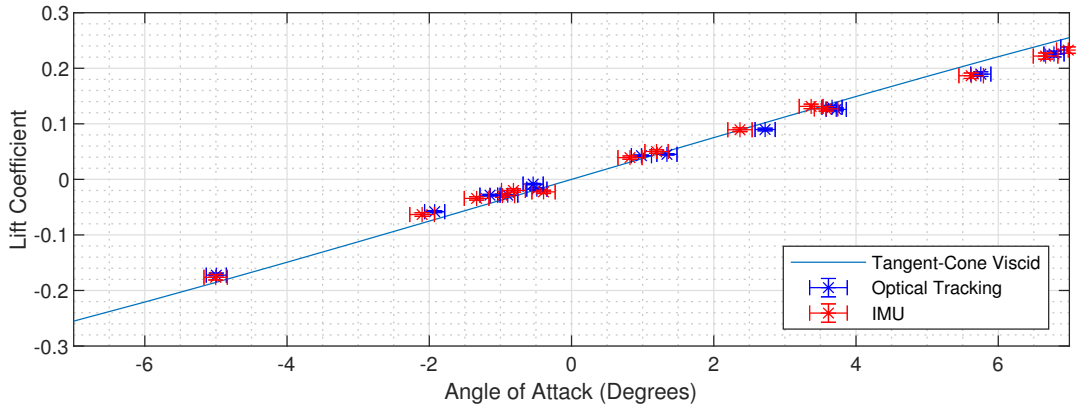

Fig. 4.8 Lift coefficient at Mach 7 condition. Individual tests plotted against tangent-cone numerical prediction

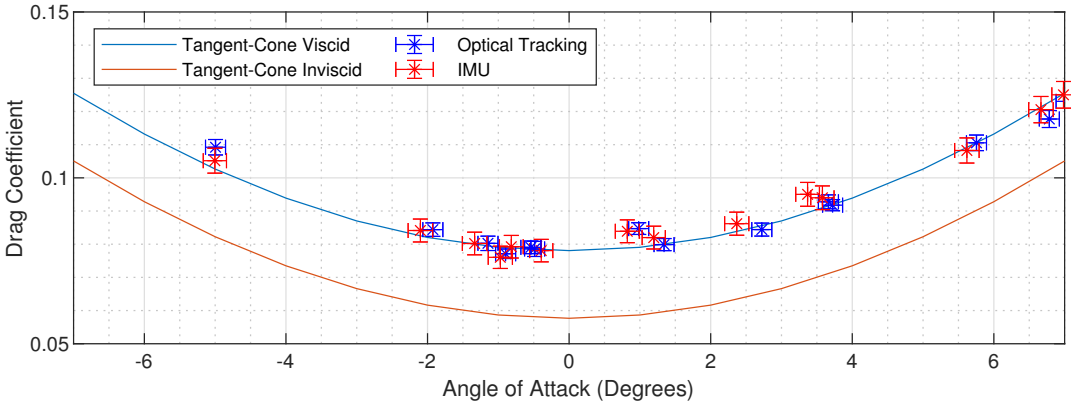

Fig. 4.9 Drag coefficient at Mach 7 condition. Individual tests plotted against tangent-cone numerical prediction

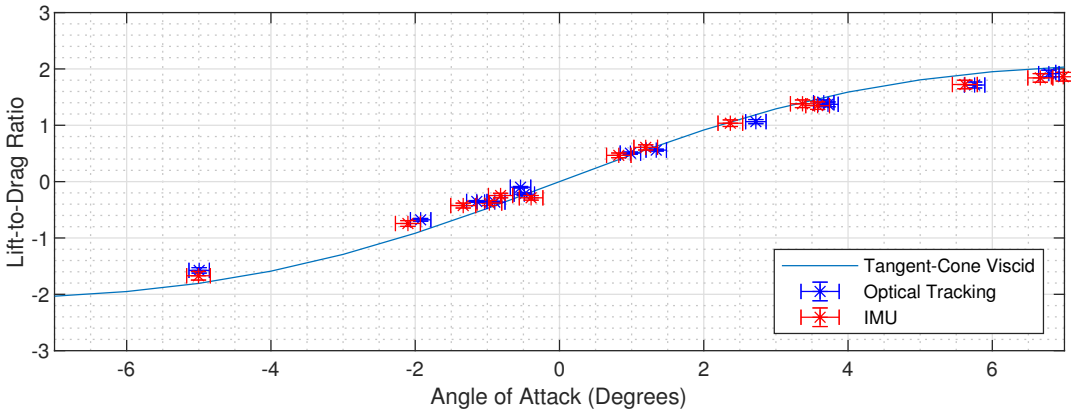

Fig. 4.10 Lift to drag ratio at Mach 7 condition. Individual tests plotted against tangent-cone numerical prediction

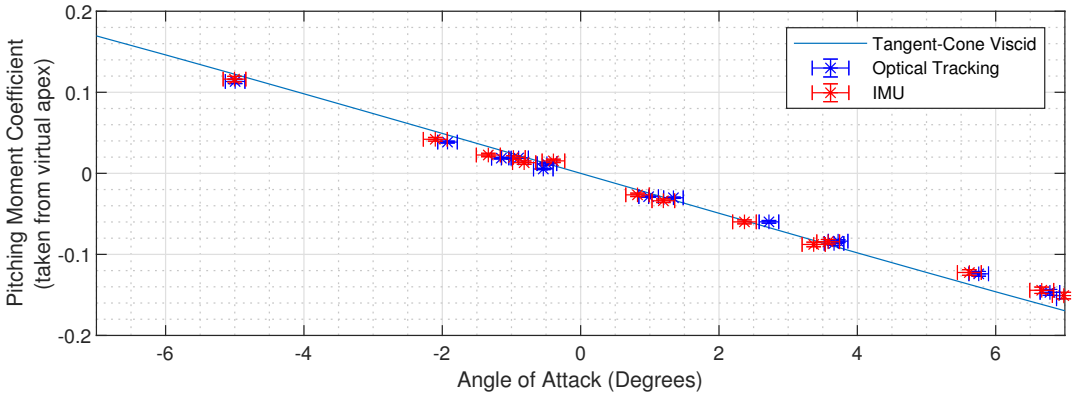

Fig. 4.11 Pitching moment coefficient at Mach 7 condition. Individual tests plotted against tangent-cone numerical prediction

The pitching moment coefficient presented in Figure 4.11 exhibits the static stability when referenced from the nose and the agreement between experimental and numerical data is good. The numerical data begins to over predict at the extremities of the data. The trim angle of attack is found to be 0 ° angle of attack as expected and centre of pressure, shown in Figure 4.12, is invariant with angle of attack. As all tests were conducted at angles of attack below the half angle of the cone, there was no separation on the leeward surface and so centre of pressure remains constant with angle of attack. The uncertainty in centre of pressure increases as the angle of attack approaches zero degrees. This occurs as the equation for calculating centre of pressure is asymptotic due to C_L and C_M approaching zero as the angle of attack reaches zero.

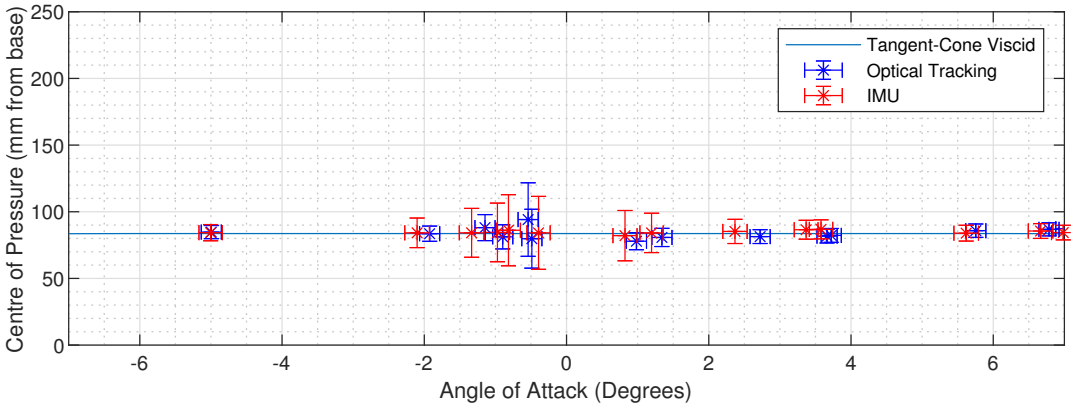

Fig. 4.12 Centre of pressure at Mach 7 condition. Individual tests plotted against tangent-cone numerical prediction

4.7.2 IMU versus Image Tracking

Figure 4.13 compares the longitudinal trajectories of the cone model by both the on-board IMU and image tracking. The IMU measures acceleration and angular velocities directly so the data must be integrated to find velocities and displacements. The opposite is true of the image tracking which directly measures displacements and angular displacements and therefore must be differentiated to find velocities and accelerations. For the plots shown in Figure 4.13, the agreement between the two independent methodologies is excellent, demonstrating the either method can reliably be used to accurately measure static aerodynamic coefficients in free-flight experiments.

For the acceleration data, small ripples can be seen in the IMU data, particularly in the vertical (z) axis. This is attributed to vibrations in the model and DAQ supporting structure that are caused by the impulsive nature of the aerodynamic forces acting on the model.

These small vibrations superimpose themselves on the acceleration signals increasing the noise levels on the measured signals. This demonstrates that similar to stress-wave force measurement experiments [62, 16] where careful consideration must be given to the location of strain gauges and the frequency response of the entire model, free-flight experiments require that the DAQ supporting structure provides sufficient damping with respect to model vibrations. The supporting structure for the IMU for these experiments, seen in Figure 4.2, has a low natural frequency in the vertical plane which as a consequence results in vibrations on the vertical acceleration signal. The agreement between the velocity and displacement data on both axes is very good for the entire duration of the experiment. The final plot of angle of attack comparison shows good agreement. The image tracking deviates from the IMU data, particularly at time = -70 ms. As the model moves through the test section, the background of the image changes and in some areas the contrast between the edge of the cone and the background was not as strong. This effect can cause the detection of the edge of the model to become more difficult leading to deviations of around $\pm$ 0.2 $^\circ$ from the IMU data. This shows the importance of ensuring a consistent, high contrast between the features to be detected (in this case the model edge) and the background.

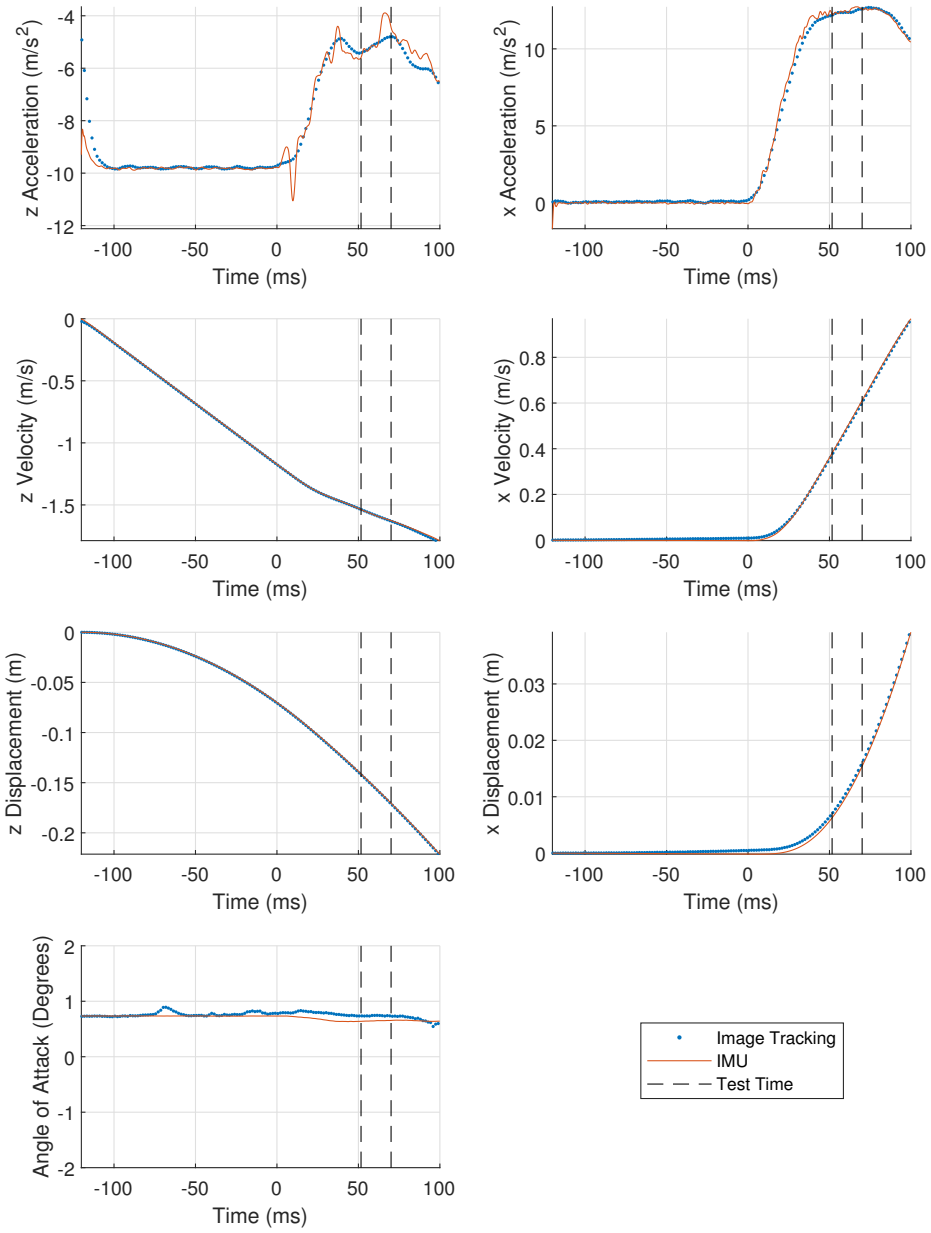

Fig. 4.13 Comparison of longitudinal motion as measured by image tracking and IMU data. Image tracking has been downsampled (by factor of 10) to make comparison plots clearer. Time = 0 is the point of flow initiation

4.7.3 Trajectory Prediction

A trajectory model was created that predicts the model's path through the test section for given initial conditions (centre of gravity, angle of attack, dynamic pressure trace, Mach number and free-fall time). The code is a 3 degree of freedom solver that uses the panel code discussed in section 4.5 to provide the aerodynamic coefficients for a calculated angle of attack which are converted to forces through the input of a transient dynamic pressure trace, replicating a free-flight experiment. The panel code also calculates the centre of pressure of the model so that the pitching moment can be calculated for a pre-determined centre of gravity.

Figure 4.14 shows a comparison between a free-flight experiment and the predicted trajectory from the code. The code has bounds which are based on the uncertainty of the release time being approximately +/-4 ms. Whilst this release uncertainty has a large effect on the trajectory, it does not effect the measured aerodynamic coefficients. The numerical trajectory is only calculated up until the point of end of test time. After this point, the trajectory becomes more difficult to predict as the model passes out of the core flow through the expansion wave of the nozzle. From the figure it can be seen that the agreement between the numerical and experimental trajectory is very good which acts as a validation for the code when predicting the trajectory of more complex geometries. This gives capability to numerically simulate a free-flight experiment which is needed in order to safely fly more complex geometries (that generate more lift).

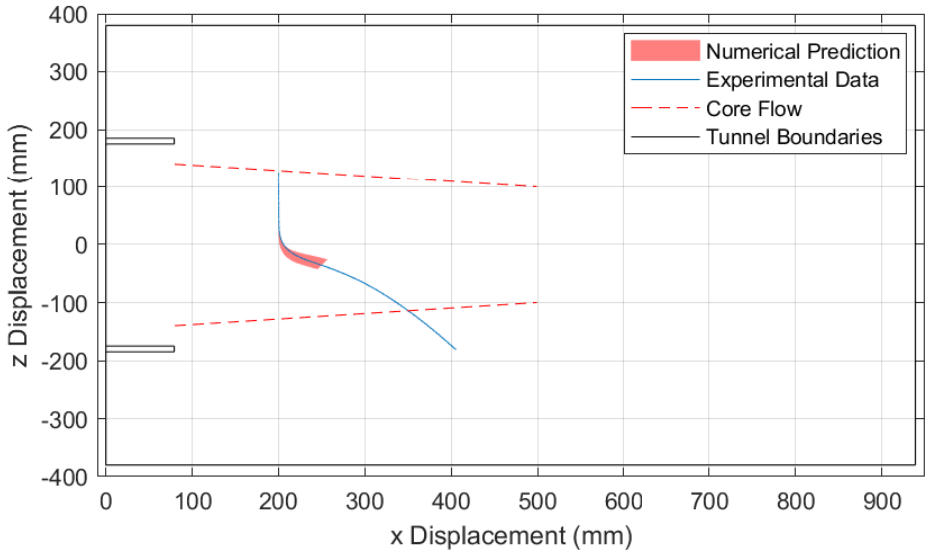

Fig. 4.14 Comparison of trajectory as calculated by the numerical code and experimental data for shot 1648

4.7.4 Pitching Cone Experiments

These tests were conducted to see if the influence of model dynamics can be seen in the measured force data when the model is allowed to pitch. Three tests were conducted at an initial release of 6 degrees angle of attack with the model ballasted so that it was statically stable and therefore allowed to pitch during the test. The pitching model weighed 775.525 g and had a CoG position of 96.6 mm from the base. Figure 4.15 presents the angle of attack variation for both the pitching experiments and some example static experiments. Figures 4.16 - 4.18 show a comparison between the pitching cone data and the individual non-pitching (static) cone shots (overlaid with the numerical predictions). Uncertainty bands for the pitching cone are presented on the figures which were calculated using the Taylor Series Method of propagating uncertainties. Good agreement between the data sets can be seen for the lift and pitching moment coefficient data. There is divergence between the data sets for the drag coefficient data for the pitching cone test, including from the numerical predictions.

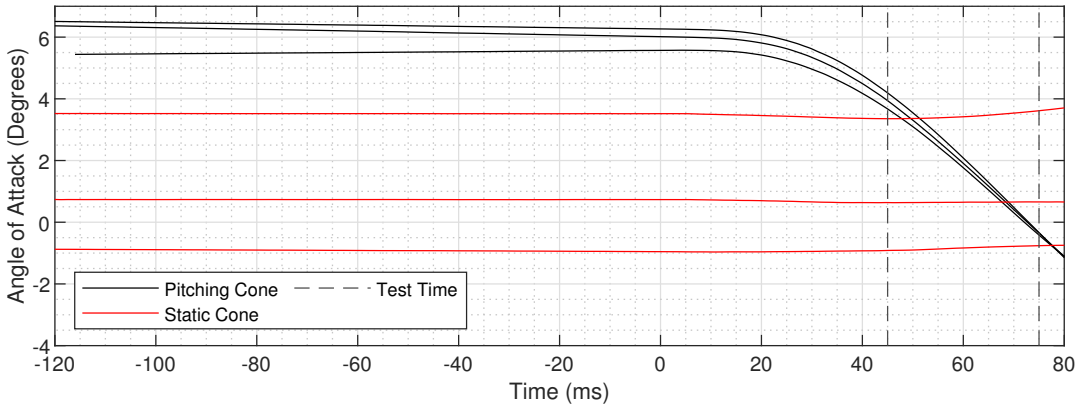

Fig. 4.15 Angle of attack variation for pitching and static free-flight shots

The measurement of drag coefficient is particularly sensitive to yaw and therefore yawing motion would result in a change in measured drag coefficient for a given angle of attack. This is unlikely as yawing motion would increase the measured drag and the data sees a reduction in drag below the numerical predictions. An alternative explanation is that this deviation in drag coefficient can be explained by the influence of dynamic phenomena. As the model pitches, the expansion fan from the base of the cone changes angle. As a consequence, there will be a delay in the base pressure re-establishing itself from the changing magnitude of flow expansion, leading to a lag in the force coefficient reaching its true static value.

For all three figures, there is some degree of oscillatory behaviour in the measured force coefficient when the cone is allowed to pitch. This is likely due to the model internal

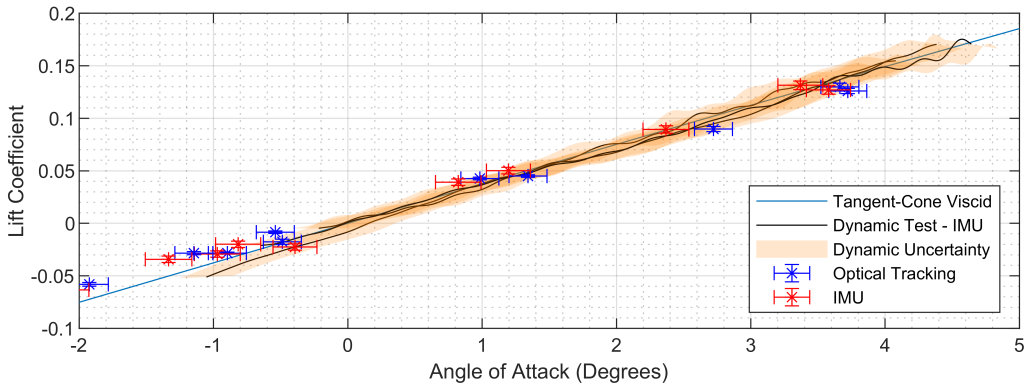

Fig. 4.16 Lift coefficient at Mach 7 condition. Individual tests plotted against tangent-cone numerical prediction

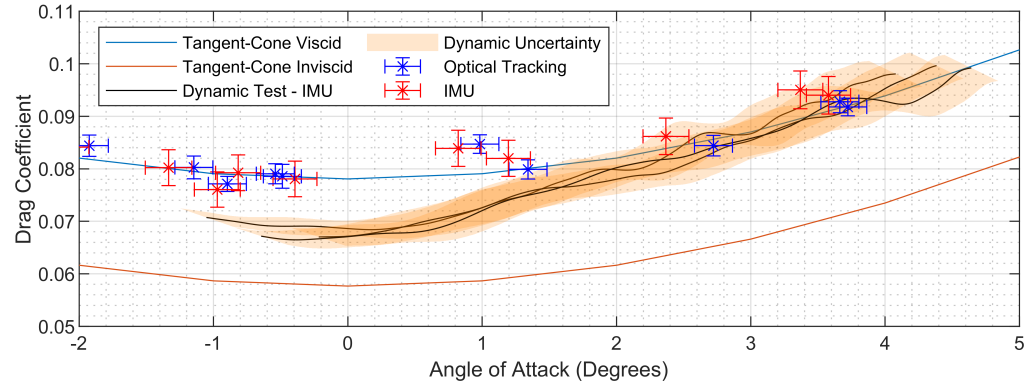

Fig. 4.17 Drag coefficient at Mach 7 condition. Individual tests plotted against tangent-cone numerical prediction

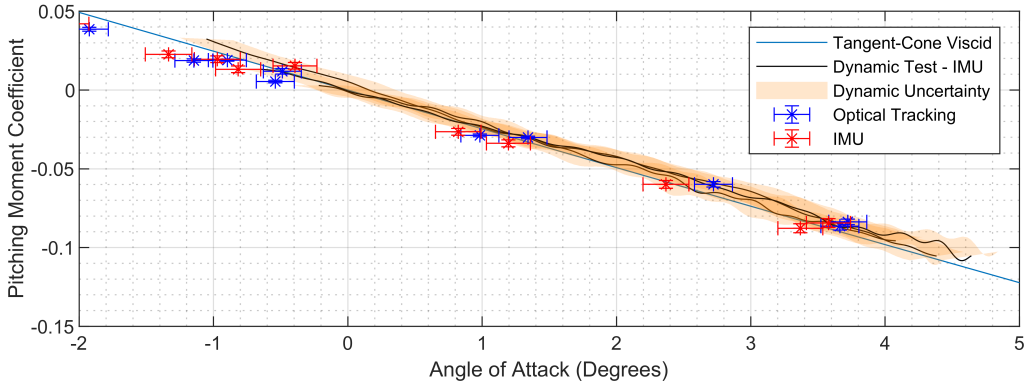

Fig. 4.18 Pitching moment coefficient at Mach 7 condition. Individual tests plotted against tangent-cone numerical prediction

dynamics and the transmission of stress waves within the internal supporting structure which houses the accelerometers. As the magnitude of force is non-constant during the test, unlike for the non-pitching static tests, the oscillations are seen on the force data as the internal vibrations do not damp out. The oscillations are particularly pronounced at the start of the test (when the model is at high degrees of angle of attack).

Overall, it can be seen that there are advantages and disadvantages to both methodologies. The pitching cone experiments give a sweep of coefficients in a single experiment at the sacrifice of higher uncertainties due to internal vibrations and a slight mismatch in the agreement with the static data for drag coefficient. It is inconclusive if the source of this mismatch is due to the dynamic influence or other factors such as yaw. However, static free-flight measurements result in lower uncertainties but require more experimental time to build a data base of aerodynamic coefficients with respect to angle of attack.

4.7.5 Flow Visualisation

Schlieren imagery was used to visualise the flow around the cone model for 2 independent shots. To achieve this, the image tracking system was removed due to the limitation of optical access to the test section. The purpose of using schlieren imagery was two-fold; firstly it confirmed that the model was in the core flow of the nozzle for the duration of the tests and secondly, it confirmed that no unusual flow phenomena were present that would affect the force coefficients. Unfortunately, the whole cone model cannot be seen in one frame due to a limitation of mirror size and consequent elliptical field of view. Figure 4.19 shows a series of images from free-flight test. The first image is prior to flow arrival with the model in free-fall and the subsequent three images are with flow on. As expected, the images show a bow shock from the nose tip and expansion fans over the model base. The images also confirm that the model remains in the core flow for the duration of the test.

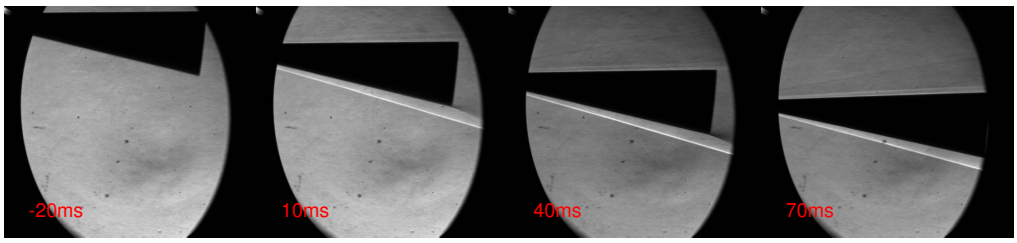

Fig. 4.19 Schlieren imagery of cone model in free-flight at Mach 7. Time at 0 ms refers to flow arrival.

4.8 Summary and Conclusions

The experimental measurement of static lift, drag and pitching moment coefficients have been presented for a 7 degree half angle cone at a Mach 7 test condition representative of an altitude of 35 km. The use of a model with minimal static margin has been shown to be effective at determining static aerodynamic coefficients with very low uncertainties that have been validated against numerical simulations. Lift and drag coefficient exhibited the expected shapes with respect to angle of attack with drag coefficient being notably influenced by viscous effects. Furthermore, the two independent methods of measuring accelerations, image tracking and an on-board IMU, show very good agreement in the experimental data, adding redundancy to the overall free-flight methodology. Centre of pressure was also shown to be invariant with angle of attack and in good agreement with the panel code. The static method of measuring forces when compared to pitching tests gives less oscillations in the measured force data and therefore a more accurate measurement of the coefficient. Furthermore, it can be seen that the measured drag coefficient when the model is allowed to pitch diverges from the static values, hence justifying the use of the static free-flight methodology to obtain static coefficients. More research is required to determine if this divergence to be accounted for by the effects of dynamics. In particular, the point at which the pitch rate of the model begins to result in dynamic influence. Overall, the quasi-static free-flight technique has been validated for a simple 7 degree half-angle cone which gives a high degree of confidence for obtaining static aerodynamic coefficients for more complex hypersonic vehicles.

4.9 Acknowledgments

The authors would like to acknowledge the exhaustive work of Mailys Buquet for operating the HDT during testing. We would also like to thank Greg King for his precise work painting the cone model. We would also like to thank Prof. Andrew Neely and Mr Liam McQuellin from UNSW Canberra for supplying the free-flight DAQs. Finally, we would like to thank Trevor Birch of DSTL for his advice and support during the project. Further thanks go to Tamara Sopek for setting up the nozzle CFD simulations.

Chapter 5

Comparison of Force Measurement Techniques in a Short Duration Hypersonic Facility

Preamble

A research aim of the thesis was to directly compare the established force balance force measurement technique to free-flight at the same conditions within the same facility to provide direct quantitative and qualitative analysis of the techniques. In this chapter, the static free-flight technique and force balance technique (static and stress-wave deconvolution calibration) are applied to a 7 degree half-angle cone. An understanding of the relative uncertainties and difficulties with each technique is discussed. This Chapter consists of a journal paper currently under review in Experiments in Fluids. The content and structure of this chapter represent 100 % of the main body of the original paper.

Authors of the original paper:

Hyslop, A., Doherty, L.J., McGilvray, M.

Author contribution:

- **Hyslop, A.** : Lead author, conceptualisation, data curation, formal analysis, and writing.
- Doherty, L.J. : Supervision as Senior Research Associate.
- McGilvray, M. : Supervision as Principal Investigator.

Associated Appendices:

N/A

Abstract

Force measurement experiments have been conducted within the University of Oxford's High Density Tunnel (HDT) with a 7 degree half-angle cone. The purpose of the study was to provide a direct comparison between two independent force techniques in the same facility at the same freestream conditions to provide a quantitative and qualitative discussion of the advantages and disadvantages of both techniques. The first force measurement technique used a conventional 4-axis sting-mounted force balance which was calibrated both statically and through the stress wave deconvolution method, whilst the second technique used the less established static free-flight methodology. Experiments were conducted at a Mach 5 test condition which provided sufficient dynamic pressure to generate aerodynamic forces suitable for the measurement range of the force balance. Results for lift, drag and pitching moment coefficients were obtained over a range of angles of attack and compared with predictions from a hypersonic panel method code. Agreement between the independent force techniques and numerical data sets was good over the range of angles of attack. Maximum uncertainties were shown to be ± 0.56 N and ± 0.44 N for free-flight for lift and drag respectively and ± 1.59 N and ± 1.27 N for the dynamically calibrated force balance which demonstrates the superiority of free-flight.

5.1 Introduction

The ability to obtain high quality force measurement data with low uncertainties is vital when developing new vehicles in all flight regimes, subsonic to hypersonic. For subsonic to supersonic flows, the methodology of force measurements is well established as blow-down facilities can replicate flight conditions for long, steady test times (minutes to hours) which allows for strain gauge force balances to be used. In the field of hypersonics, facilities that are able to replicate scaled flight Reynolds numbers, such as Ludwieg tubes, produce very short duration flow in the order of milliseconds to tens of milliseconds due to the amount of energy required to produce these flows. Due to the limited test time available to experimenters, the temporal response of models and supporting structures must be considered which can make it

difficult to obtain high quality force data. Furthermore, numerical nose-to-tail simulations of hypersonic vehicles are difficult and computationally expensive as features such as boundary layer transition is challenging to predict [107, 91] which motivates efforts to obtain accurate force data from experiments.

There have been two major approaches over the years in attempts to obtain high quality force data in the area of hypersonics that are discussed in detail in Bernstein and Pankhurst [6], the first of which is to use a sting-mounted force balance. This is the most common method of determining aerodynamic forces and moment in wind tunnels facilities, particularly in the subsonic regime. In its most simplistic form, a strain-gauge load cell is located within the supporting structure and used to directly measure the forces at the point of equilibrium providing aerodynamic data which is representative of the full-scale vehicle. This can range from single-component drag measurements to six-component force and moment measurements. Frequently, the attitude of the model will be controlled by the operator between tests to characterise the model at a range of orientations. This methodology works well for blow-down facilities or hypersonic facilities with sufficient test time [8, 65]. However, in short duration facilities with test times in the order of milliseconds to tens of milliseconds, the impulsive start of the facilities results in stress waves within the model-mounting structure that do not reach equilibrium within the test time and hence makes it difficult to obtain quasi-static aerodynamic forces. To overcome these issues, the stress-wave technique was developed by Sanderson and Simmons [84] resolving the drag force acting on a axisymmetric body in flow duration of 1 ms. This technique requires a dynamic calibration of the model force-balance structure to determine aerodynamic forces. Knowledge of the impulse response function of the model and sufficient characterisation of the stress wave patterns allows the experimenter to deconvolve the measured strain signals to determine the net aerodynamic load. The calibration is achieved through a series of instrumented impulse hammer hits as described by Mee [61] for a single-component balance and Doherty et al. [16] for a three-component balance. Another well documented issue with force balance measurements is the interference of the sting that can result in undesirable effects in drag [79].

The other approach to force measurement experiments in hypersonic facilities is known as the free-flight technique. This removes the sting and allows the model to move freely in 6 degrees of freedom. A typical methodology of a free-flight test in short duration facilities is as follows: the model is released prior to arrival of the test flow, the flow is initiated over the model which allows it to move as it would in flight. As the model is not constrained, non-intrusive methods of measuring accelerations, rather than forces, are required. Low inertia models in free-flight have been successfully demonstrated by Kennell et al. [39, 41]

with ESA's HEXAFLY INT EFTV geometry, McQuellin et al. [59] with an axisymmetric flyer and sustainer, and Hyslop et al. [33] for Reaction Engines' Skylon spaceplane. For these experiments, low inertia models were used which allowed the model to freely pitch over a wide range of angles of attack during a test and hence providing large sweeps of aerodynamic coefficient data in a single run. With the large amounts of pitching during the test, the aerodynamic coefficients will include some dynamic influence in the measurement. This paper presents a direct comparison of force measurement of two independent techniques in the University of Oxford High Density Tunnel (HDT) applied to a 7 degree half angle cone. Both free-flight, previously used by Hyslop et al. [34], and force balance with stress-wave deconvolution are used to determine the aerodynamic coefficients at a Mach 5 test condition. The advantages and disadvantages of both techniques will be discussed in detail in this paper.

5.2 Experimental Facility

5.2.1 University of Oxford High Density Tunnel

The experiments were conducted in the University of Oxford High Density Tunnel (HDT), located within the Oxford Thermofluids Institute. Whilst the facility has multiple modes of operation, for these tests it was operated as a heated Ludwieg tube which provides ~50 ms of steady flow duration during which force measurements are taken. The facility was fitted with a Mach 5 contoured nozzle of exit diameter of 350 mm that produces a core flow of 280 mm at nozzle exit. The facility is typically operated at total pressures up to 50 bar but is rated for fill pressures of 275 bar. For further details on the HDT operation and measurement of freestream conditions, see McGilvray et al. [57] and Wylie et al. [108]. Figure 5.1 shows typical total pressure and temperature traces at the test conditions used in these experiments. Only the first plateau was used as the test time in which forces were measured, as after this time, the free-flight model is no longer in the core flow. For the total temperature trace, a spike can be seen in the data before the test time which is due to the unsteady filling of the tunnel plenum prior to flow passing through the nozzle. It has settled before the test time so a constant Reynolds number can be assumed in the subsequent plateaus.

5.2.2 Test Conditions

For this work, a test condition was chosen that provided sufficient dynamic pressure such that the aerodynamic forces acting on the model were suitably in the range of the 0.7 inch force balance discussed in Section 5.4. The condition used was a Mach 5 flow with a total pressure of 13.8 bar. The free-stream conditions were determined using an instrumented twin probe

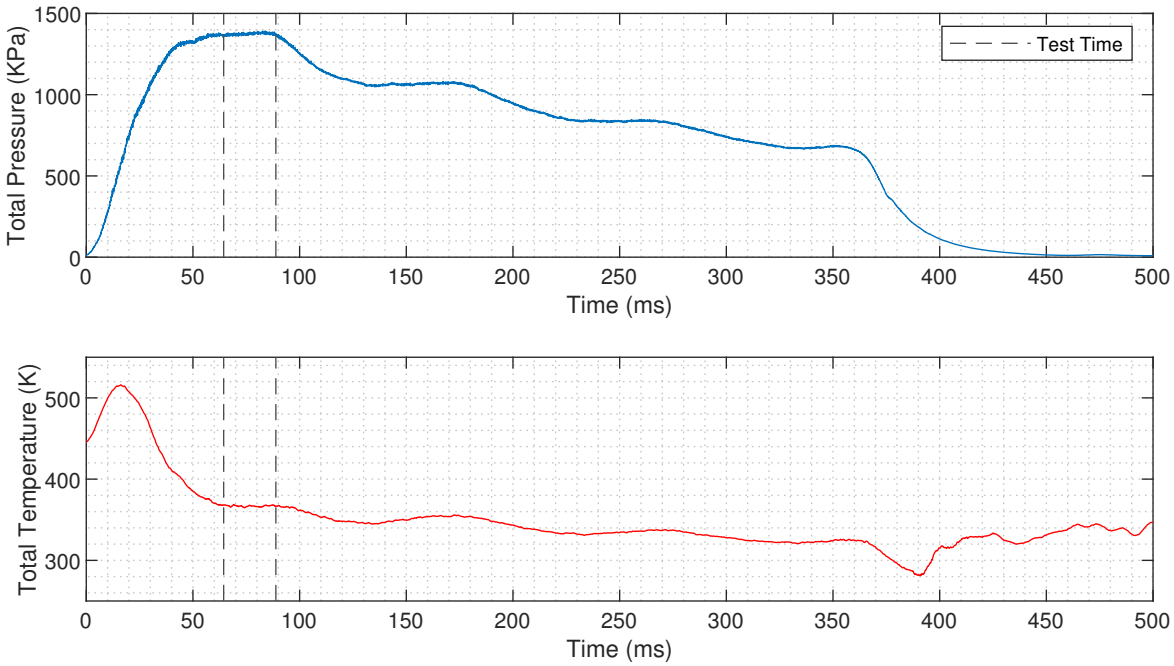

Fig. 5.1 Example total pressure and temperature traces for the HDT

during the force balance experiments. This consisted of a Pitot probe, which allowed for the measurement of freestream Mach number using the ratio of pitot to stagnation pressure, and an aspirated thermocouple allowing for the measurement of freestream total temperature. Dynamic viscosity was calculated using Keyes' Law [43] and static pressure and temperature through isentropic relations with an assumed ratio of specific heats of 1.4.

Prior to the force experiments, the diameter of the core flow was measured using a rake instrumented with pressure sensors. At nozzle exit, the core flow was determined to be 280 mm reducing to 240 mm at 300 mm downstream. A full summary of the test conditions is given in Table 5.1. Flow angularity was predicted using Eilmer4 CFD to remain within $\pm$ 0.12° within the core flow.

5.3 Static Free Flight

The methodology used for these experiments uses the same set up as in Hyslop et al. [34] and therefore only an overall summary is provided. A free-flight experiment is conducted in the HDT as follows, the model is released from an electromagnet and allowed to fall freely. When the model has reached a suitable height relative to the core flow of the tunnel, the tunnel fires and the model is allowed to move freely in 6 degrees of freedom. As the model is not restrained, non-intrusive methods of measuring the model's kinematics are required. For

Table 5.1 HDT conditions during test time.

	HDT Test Flow
Measured Freestream Properties	
Total Pressure (kPa)	$1375 \pm 7\,2$
Pitot Pressure (kPa)	88.3 ± 0.7
Total Temperature (K)	369 ± 15
Calculated Freestream Properties	
Altitude (km)	45.7
Mach Number	4.95 ± 0.01
Velocity (ms^{-1})	785 ± 16
Density (kgm^{-3})	0.153 ± 0.007
Static Pressure (Pa)	2759 ± 41
Static Temperature (K)	62.7 ± 2.6
Dynamic Viscosity (μPas)	4.50 ± 0.18
Dynamic Pressure (kPa)	47.3 ± 0.7
Unit Reynolds Number ($10^6 m^{-1}$)	26.8 ± 1.7

this work, linear and angular displacements are measured directly using image tracking and linear accelerations and angular velocities are measured via an onboard inertial measurement unit (IMU). To achieve the static free-flight condition, where the amount of pitching exhibited by the model is minimised, the model is ballasted so that the centre of gravity (CoG) location is as close to the centre of pressure (CoP) as possible, hence minimising the aerodynamic pitching moment.

5.3.1 Infrastructure

The test infrastructure used to conduct free-flight experiments in the HDT is shown in Figure 5.2 and consists of protective nets, foam padding and a drop mechanism. The drop mechanism consists of a 25 mm electromagnet that is connected to a 50 mm SMC pneumatic actuator that retracts to remove the electromagnet from the core flow after model release to prevent any undesirable shocks from the flow field. The mechanism is controlled by a bespoke electrical unit that upon receiving a TTL pulse, de-energises the electromagnet and powers two solenoids to retract the actuator. The electromagnet is contained within a 3D printed holder that fits conformal to the model surface, allowing for repeatable alignment in roll and axial position. Different holders were printed to allow the initial angle of attack of the model to be set at 0, 3 and 6 degrees. A steel rod is inserted into the holder prior to a test to fix the model yaw.

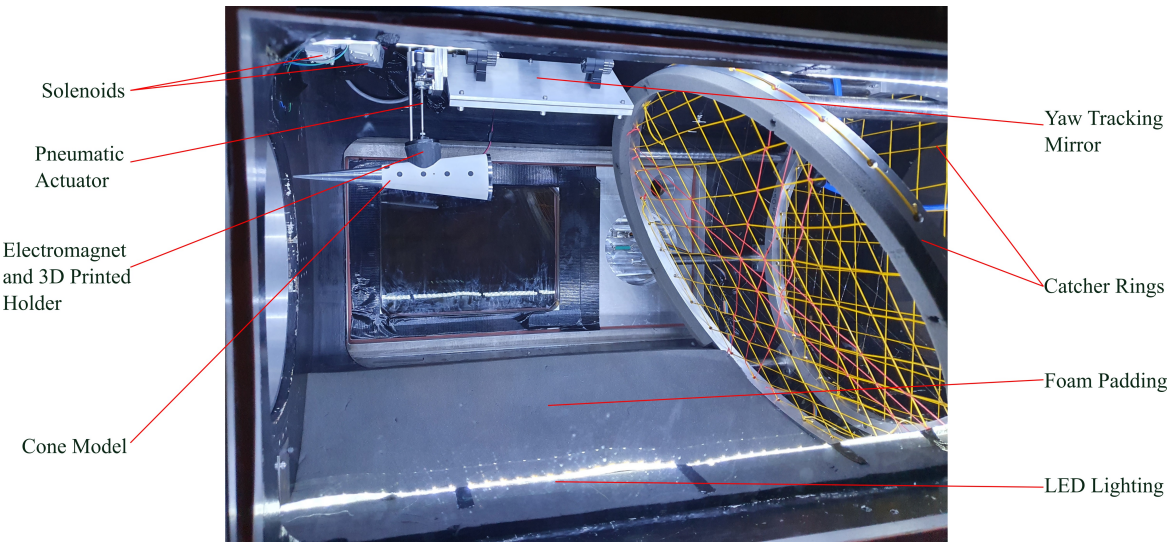

Fig. 5.2 Free-flight drop mechanism and catcher rings in the HDT test section.

To protect the model after a test, a catcher mechanism consisting of two aluminium rings interwoven with Dyneema string was implemented. The upstream ring was held at a 30 ° inclination with the purpose of deflecting the model to the tunnel floor which is padded with foam providing a soft impact surface. The second downstream ring is a redundancy that prevents the model exiting the test section into the dump tank where it would be difficult to retrieve.

5.3.2 Model

The experimental model was a 7 degree half angle cone of length 250 mm with a nose bluntness of 1.25 mm in radius. The model was manufactured in two halves so that it was modular for ease of instrumentation and ballasting. The main body of the cone was made from steel and the nose tips aluminium. An exploded view of the cone model is shown in Figure 5.3.

The most important aspect of this model was the ability to accurately ballast and locate the position of the centre of gravity of the model so that the model does not pitch during the test, thereby creating the static condition. The model was ballasted using tungsten disks that could have their axial position adjusted through the use of threaded steel rods. The tungsten ballast allowed for the CoG to be shifted between the ranges of 80.1 mm to 85.7 mm from the cone base. The CoP location was predicted to be 84.2 mm (from the cone base) prior to testing using Modified-Newtonian theory and the CoG set to this position for the experiments. The centre of gravity was measured using a moment balance, whereby the

model was suspended using two strings. The tension in the upstream string was measured using a load cell. This setup allowed the CoG to be determined to +/- 0.1 mm. The inertial properties of the model are shown in Table 5.2.

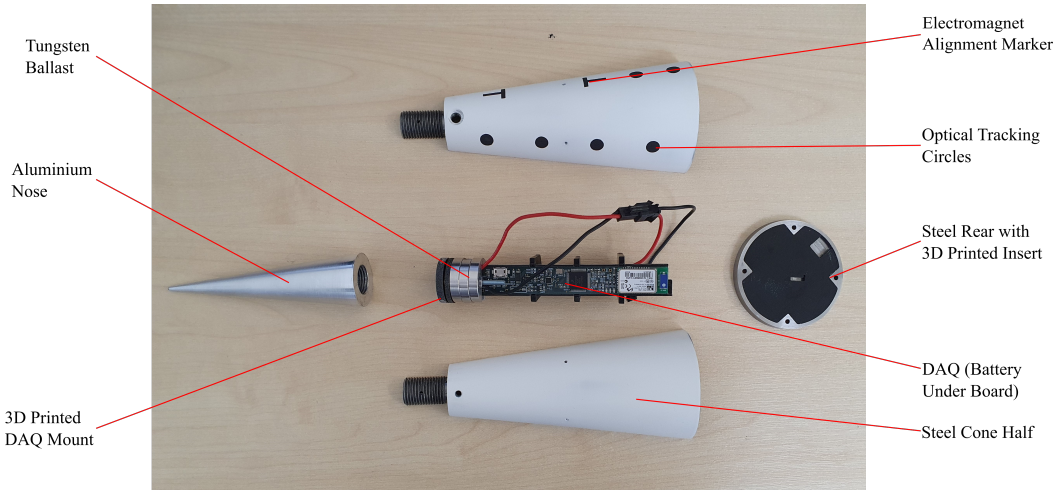

Fig. 5.3 Constituent components of the free-flight 7 degree cone model.

Table 5.2 Model inertial and geometric properties

Length (mm)	250 ± 0.2
Cone Half-Angle (°)	7 ± 0.03
Nominal Nose Radius (mm)	1.25 ± 0.1
Base Area (m^2)	$3.2\ \text{x}10^{-3} \pm 0.01$
Centre of gravity (mm)	84.2 ± 0.1
Mass (g)	671.261 ± 0.001
Moment of Inertia (kgm^2)	$2.17\ \text{x}10^{-3}$

Located internally within the model was a onboard DAQ that consisted of an IMU containing a 3 axis accelerometer (+/- 16 g) and gyroscope (+/-2000 deg/s) which were designed and built by UNSW Canberra. The IMU had a sample rate of 8 KHz and could be armed via an external terminal through Bluetooth. Triggering of the instrument was achieved by detection of sustained free-fall upon model release. For the exterior, a laser-cut stencil was designed to airbrush black dots on the model for the purpose of image tracking. Two "T" shapes were also painted on the model to locate the release point of the model for the desired CoG location to minimise pitching during model free-fall.

5.3.3 Data Reduction

Aerodynamic force coefficients were derived using two independent methodologies. Both methods ultimately measure the model's acceleration to determine the instantaneous forces acting on the model during the test time using the model's mass and moment of inertia (Table 5.2). The forces are then non-dimensionalised by the freestream dynamic pressure (Table 5.1) and a reference area, which for this model was taken to be the cone base area (S = 3.2x10^{-3} m^2). The reference length used in the calculation of pitching moment was the model length. The aerodynamic coefficients can be calculated as follows:

$$C_L = \frac{m\ddot{z}}{\overline{q}S}, \quad C_D = \frac{m\ddot{x}}{\overline{q}S}, \quad C_M = \frac{I_{yy}\ddot{\theta}}{\overline{q}Sc} \tag{5.1}$$

Inertial Measurement Unit

When using inertial measurement units that are free to move in space, it is important that co-ordinate systems of interest are well defined so that accelerations and angular placement are referenced to the correct frame before calculating the forces acting on the body. There are two frames of references used in free-flight experiments; the first is known as the Inertial/Earth coordinate system which is defined as having the +z axis towards the ground, +x axis pointing upstream towards the facility nozzle and the +y axis orthogonal to both to form a right-hand coordinate system. This frame of reference is what all global force coefficients are defined relative to. The second co-ordinate system is referred to as the body frame of reference. This is defined relative to the model as +x towards the nose of the vehicle, +z towards the bottom of the vehicle with +y completing the orthogonal system. The IMU located on the model measures accelerations and angular velocities in the body frame of reference and hence during a test, this frame of reference is moving relative to the Inertial frame.

To process the raw IMU data, the data is filtered with a 6^{th} order low pass Butterworth filter with a cut off frequency of 500 Hz to remove high frequency noise. The body angular rates are then transformed to Euler angular rates, using Eq. 5.2, allowing the Euler angles to be determined via numerical integration of Euler-rates. Using the Euler angles, the linear accelerations measured by the IMU are transformed to the inertial frame of reference according to Eq. 5.4. A gyroscope is unable to measure its attitude relative to the freestream and so initial conditions must be set before the angular velocities are differentiated. For this work, the initial angle of attack is calculated using image tracking of the external edge of the cone. Finally the aerodynamic coefficients can be obtained using Eq. 5.1.

The rotation matrix for the angular rates and accelerations are as follows (where c, s and t are cosine, sine and tangent functions respectively):

$$\begin{bmatrix} \dot{\phi} \\ \dot{\theta} \\ \dot{\psi} \end{bmatrix} = \begin{bmatrix} 1 & s(\phi)t(\theta) & c(\phi)t(\theta) \\ 0 & c(\phi) & -s(\phi) \\ 0 & \frac{s(\phi)}{c(\theta)} & \frac{c(\phi)}{c(\theta)} \end{bmatrix} \begin{bmatrix} p \\ q \\ r \end{bmatrix} \tag{5.2}$$

$$\begin{bmatrix} \ddot{X} \\ \ddot{Y} \\ \ddot{Z} \end{bmatrix}_E = \begin{bmatrix} c(\psi)c(\theta) & c(\psi)s(\phi)s(\theta) - c(\phi)s(\psi) & s(\phi)s(\psi) + c(\phi)c(\psi)s(\theta) \\ c(\theta)s(\psi) & c(\phi)c(\psi) + s(\phi)s(\psi)s(\theta) & c(\phi)s(\psi)s(\theta) - c(\psi)s(\phi) \\ -s(\theta) & c(\theta)s(\phi) & c(\phi)c(\theta) \end{bmatrix} \begin{bmatrix} \ddot{X} \\ \ddot{Y} \\ \ddot{Z} \end{bmatrix}_B \tag{5.3}$$

Image Tracking

Optical tracking was used for free-flight to directly measure the model's displacement about the centre of gravity and track the angle of attack with respect to the test time. After determining the displacement history of the model, the data can be differentiated twice to obtain the accelerations acting on the model and hence forces. The model was imaged using a Photron FASTCAM AX200 high-speed camera set to a frame rate of 6400 fps with 1,024 x 1,024 pixel resolution at a focal length of 50 mm at f 2.8. The camera faced directly through the test section windows, imaging the longitudinal plane of motion of the model. To fully capture the free-fall of the model, a pre-trigger of 500 frames was used and a total of 2180 frames recorded, activated by a TTL pulse from the facility prior to the test. Six 1000 lumen torches were used to front light the model, providing adequate spacial uniformity of light. The spatial uniformity and distortion of the lens was corrected in post-processing using the MATLAB camera calibrator app through the use of a uniform grid inserted into the tunnel.

The method used to measure the model's longitudinal displacement in free-flight consisted of tracking high-contrast, black circles painted with a location accuracy of +/- 0.1 mm on the model as seen in Figure 5.2. As seen in the Figure, there are four circles painted on the model but only two are required for the algorithm to locate the position of the centre of gravity. This added redundancy exists in case one of the circles is damaged. The methodology for image tracking is the same as in the work of Hyslop et al. [33] but the steps can be summarised as follows:

1. Apply Gaussian filter to image and subtract from original (High pass filter).
2. Apply Canny filter to image so that only pixels detected as an edge are shown [9].
3. Apply Hough transform to find circles in the image after narrowing the search radius [30].

4. Detect pixels in the proximity of the circle located by the Hough transform.

5. Use sub-pixel detection on the original image, at the location pixels were detected. Sub-pixel methodology set out in von Gioi and Randall [99].

6. Fit a circle to the pixels using linear regression as set out in Laurence et al. [45] and use this equation to find the centre point of the circle.

Once the centre points of two circles has been detected, a line can be fitted between the two points and linear interpolation can be used to find the CoG. This process is repeated for each frame giving a time history of centre of gravity displacement and angle of attack. As the distance between the centre points is also a known quantity, the scale of the image can be calculated. For this optical setup, the scaling factor was 0.69 mm/pixel. Figure 5.4 presents a composite image of a typical free-flight experiment with the image tracking algorithm detection points overlaid as well as the extent of the nozzle core flow.

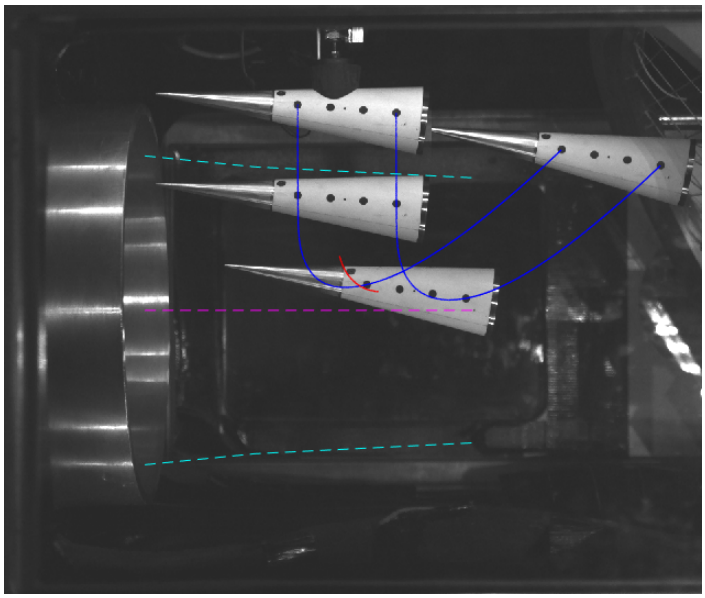

Fig. 5.4 Montage photo of image processing (Blue - detected circle centre points, Red - calculated centre of gravity, shown for test time, cyan lines show core flow location as acquired by a pitot survey).

In theory, angle of attack can be calculated using the circles on the model, however it has been found that this methodology is very sensitive to perspective and model yaw. This could be overcome with a second optical camera tracking on the yaw plane. However, this is challenging to implement within the current HDT test section due to lack of optical access. Angle of attack is detected by finding the relative angle between the edge of the cone and the

horizontal. As the model was painted white, there is strong contrast between the background of the image and the cone which allows for the edge to be detected with a Canny filter followed by sub-pixel detection to find the true edge. Fitting these points with a straight line and calculating the gradient allows for the angle of attack to be determined.

To determine the aerodynamic coefficients, the displacement data is differentiated twice to give the accelerations and hence aerodynamic coefficients using Eq. 5.1. The intermediate velocity data required numerical smoothing using a Gaussian filter before being differentiated into accelerations.

5.4 Force Balance

This section will discuss the methodology and data reduction used to obtain aerodynamic force coefficients from a 0.7 inch 4-axis force balance used in the HDT with the 7 degree half-angle cone as the test model. Two conical models were used for the force balance experiments, a steel cone that could be instrumented with pressure transducers to allow alignment with the freestream, and a nylon cone designed to optimise the stress wave transmission for force measurement.

5.4.1 0.7 Inch Force Balance

The 0.7 inch force balance is an internal balance that can measure forces on 3 orthogonal axes (axial, normal and side) and the pitching moment. The rated forces and moments are shown in Table 5.3. The sensing strain elements are at the end of a supporting sting structure and arranged as a double bending beam balance type design [20]. The main advantage of this setup is that the balance body is fabricated from a single piece of material which helps to avoid any hysteresis caused by screws or joints in the structure.

Table 5.3 0.7 inch force balance rated loads.

Axis	Rated Loading
Axial Force	60 N
Normal Force	360 N
Side Force	360 N
Pitching Moment	10.16 Nm

The principle of the bending beam balance is demonstrated by Figure 5.5. The model is represented by the shell surrounding the sensing elements and the mounting sting is represented by the earth symbol. The strain gauges of interest for the force or moment

represented are shown in red and relevant strain diagrams are also given. The forces and moments are measured relative to a reference centre which is located in the centre of the beam and is 46 mm from the tip of the balance for the 0.7 inch balance used in these experiments.

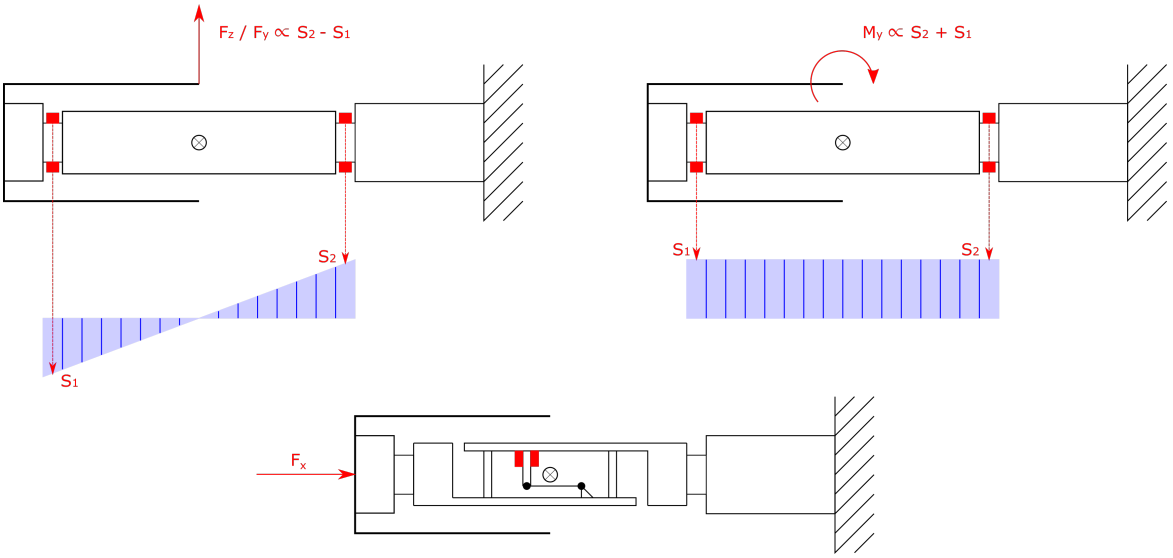

Fig. 5.5 Principle of beam bending force balance operation (adapted from Ewald [20]). The shell represents the model, earth symbol the sting and red elements strain gauges of interest. Shear stress diagrams are shown for the normal and pure moment loading cases.

The principle of measuring normal (Fz) or side (Fy) forces for these balances is identical. Upon application of a pure normal force (shown on the left in Fig. 5.5), bending strains of equal magnitude but opposite sign are imparted at the strain gauge locations. Therefore subtraction of the strains results in a signal proportional to the normal force. The right hand side of Figure 5.5 shows the balance response to a loading case of pure pitching moment. This results in a constant bending strain along the beam and therefore the addition of the stresses at the strain gauge position results in a signal proportional to the pitching moment. From the diagram, it can be seen how coupling between channels can be problematic as the same strain gauge sensors are used for different force/ moment axes.

The measurement of axial force component in these balances is more complex. There are two reasons for this; firstly it is typical for aerodynamic tests that the axial force is of much lower magnitude than the other force components. Secondly, this force results in only longitudinal stresses in the beam which are much smaller than the bending stresses. To compensate for these two factors, an incline cut is made in the balance that separates the model side to the sting fixed part as shown at the bottom of Figure 5.5. The two parts are connected by four parallelogram flexures that allow the balance parts to move against each other in the axial direction. The movement is transferred to the force sensing flexure which

is equipped with strain gauges. Ultimately this setup transforms the axial force into bending stresses that can be measured with high sensitivity.

5.4.2 Infrastructure

The infrastructure used to conduct force balance experiments in the Oxford HDT is shown in Figure 5.6. As seen in the figure, the force balance is supported using a model mounting arm which is designed to provide minimal flow interference with the model. Dowel pins were used to connect the model to the mounting setup ensuring that the force balance strain gauges are aligned to the freestream in roll. The mounting arm is connected to a two degrees-of-freedom traverse that allows the user to set pitch between +/- 15 ° and yaw between +/- 5 °.

Mounted to the wall of the test section was a probe that is inserted towards the base of the nozzle. The twin probe contained an aspirated thermocouple and a pitot pressure probe to allow for full characterisation of the free-stream flow. Schlieren imagery was used during testing to confirm that the bow shock from the probe did not impinge on the model and impacting the measured forces.

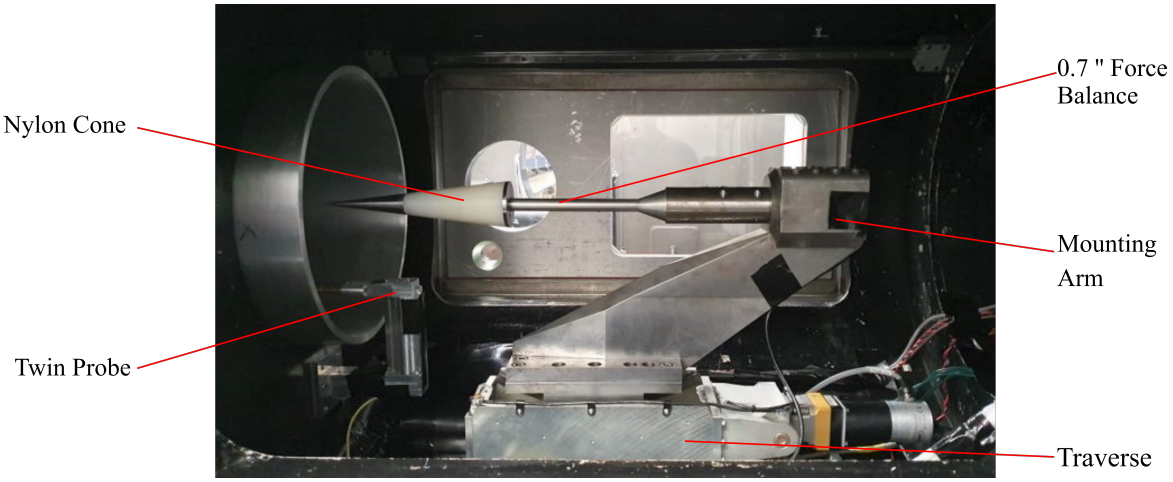

Fig. 5.6 Force balance infrastructure in the Oxford HDT.

5.4.3 Cone Model

For the force balance work, two 7 degree half-angle conical models were used that could be easily interchanged. The first utilises the same model used in free-flight (Section 5.3.2) by exchanging the rear piece for a mounting adapter. Whilst this model was not optimised for force measurements due to its hollow nature, it could be instrumented with 6 Honeywell pressure transducers (4 radially at 90 degree intervals and 2 in the base) embedded on a

single PCB board at the base of the model to allow for alignment with the freestream flow and measurement of base pressure. The sensors were connected to the pressure tappings using 0.5 mm inner diameter flexible tube. A Molex Picoblade connector was inserted into the base of the model to transfer data from the boards to an external DAQ. A thread at the front of the model allowed for different nose bluntnesses to be tested. The steel cone model is shown in exploded view in Figure 5.7.

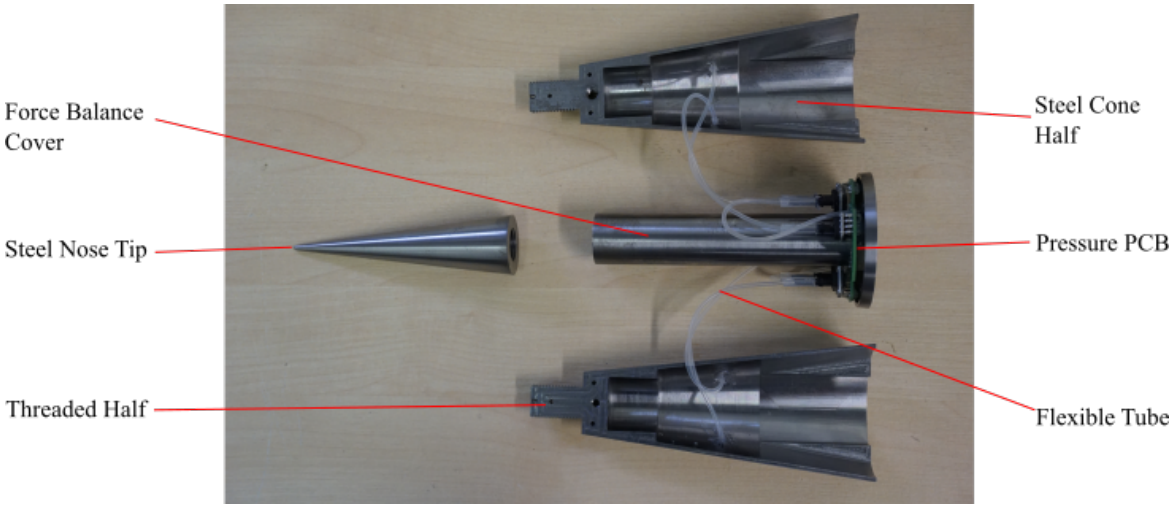

Fig. 5.7 Steel cone used for alignment in force balance experiments

The second model, seen in Figure 5.6, was a nylon cone of the same dimensions as the steel cone and can be attached to the same base plate. Unlike the steel model, the nylon model was solid apart from a bore in which the force balance can be inserted into. A solid model reduces the time it takes for the internal vibrations to damp down when the model is excited with an impulse. At the bottom of the bore, a copper crush washer is used to connect the live end of the force balance with the model. All contact surfaces were also greased. These improved connections allow for the stress waves to propagate through boundaries with reduced reflections between the contact surfaces, reducing the interference of reflected waves. Furthermore, as presented in Sanderson and Simmons [84], nylon exhibits greater damping of internal vibrations than steel (more energy absorbed per cycle) which results in a much faster time constant for decay in vibrational amplitude. In the context of wind tunnel experiments, vibrations within the model dampen faster during the test time, allowing for less noisy force signal to be measured.

Figure 5.8 shows the pressure traces from a test with the model aligned to the freestream. The four radial pressure transducers measure equal static pressure, showing that the cone is aligned. The base pressure shows a degree of transience over the first 100 ms of time post the facility firing which is due to the establishment of flow over the base of the cone. It

takes approximately 50 ms for the expansion fan over the base of the cone to fully establish and begin to equalise the base pressure. The static pressures seen in Figure 5.8 are not representative of the flow in Table 5.1 as alignment was conducted at a lower total pressure so that the vibrations of the steel model did not damage the force balance.

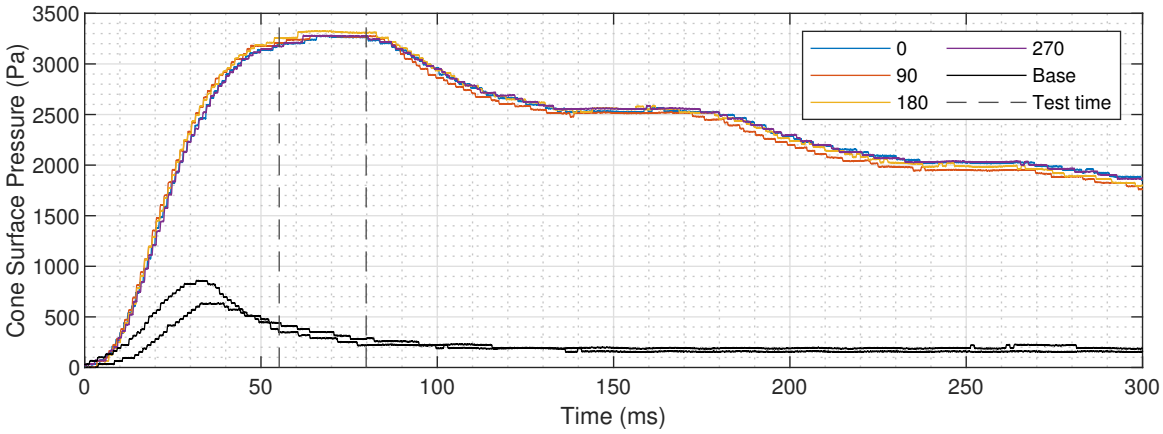

Fig. 5.8 Cone surface pressures for the steel model aligned with the freestream

5.4.4 Data Reduction

There are two ways of obtaining force data from the balance which is dependent on the method of calibration. The first method is using a static calibration and the second is a dynamic calibration using an impulse hammer. Regardless of the calibration used, the resultant forces can be resolved into orthogonal lift and drag components that can then be used to determine their corresponding aerodynamic coefficients:

$$C_L = \frac{L}{\overline{q}S}, \quad C_D = \frac{D}{\overline{q}S}, \quad C_M = \frac{M}{\overline{q}Sc} \tag{5.4}$$

Static Calibration

For an ideal multi-axis force balance, the application of a load that is purely a single component aligned with one of the measurement axis will result in a single voltage signal from the associated strain gauge. However, due to the complexity of the systems, often off-axis voltage signals will also be measured - a phenomena known as cross-coupling. The conversion of measured voltage strains to forces for the 0.7 inch load cell is given by:

$$\begin{bmatrix} V_x \\ V_y \\ V_z \\ V_{My} \end{bmatrix} = \begin{bmatrix} k_{x,x} & k_{x,y} & k_{x,z} & k_{x,My} \\ k_{y,x} & k_{y,y} & k_{y,z} & k_{y,My} \\ k_{z,x} & k_{z,y} & k_{z,z} & k_{z,My} \\ k_{My,x} & k_{My,y} & k_{My,z} & k_{My,My} \end{bmatrix} \begin{bmatrix} F_x \\ F_y \\ F_z \\ M_y \end{bmatrix} \tag{5.5}$$

Where the co-ordinate system for this balance is as follows; +x towards the nose of the model, +z towards the bottom of the model with +y completing the orthogonal system. Or in matrix notation:

$$\mathbf{V} = \mathbf{KF} \tag{5.6}$$

For a well designed force balance the cross-coupling coefficient matrix, **K**, will be diagonally dominant meaning that there is minimal cross-coupling between the force balance channels. However, in practice this is often not the case and so careful calibration of the force balance is required. To statically calibrate a multi-axis force balance, known loads are applied individually to each of the orthogonal axes within the measurement range of the balance and the corresponding output is measured. The balance was statically calibrated externally by Novatech prior to the experiments. For each of the axes loaded, a row of the cross-coupling matrix, **K**, can be determined. After determining the cross-coupling matrix from the calibrations, the matrix can be inverted to determine the transfer function between output strain voltage and the applied forces:

$$\mathbf{F} = \mathbf{K}^{-1}\mathbf{V} \tag{5.7}$$

Dynamic Calibration

During short duration experiments in hypersonic facilities, the aerodynamic forces around the model may obtain quasi-static equilibrium but the internal stress waves between the model and support structure may not achieve equilibrium in the test time. As a consequence, a static calibration method that assumes steady-state internal forces may not be a suitable technique for measuring forces. Therefore, a dynamic calibration may be more suitable methodology for obtaining steady-state aerodynamic forces.

The dynamic calibration used for this force balance is known as the stress wave force measurement technique [16]. The technique is based on the assumption that the system is casual, time-invariant and linear, and that the time-evolution of strain within the combined force-balance, model, and supporting structure assembly is uniquely defined by the time-evolution of the aerodynamic load acting on the surface of the model. For a single component

system, a convolution between the applied load, $u(t)$ and a system impulse response function (IRF), $g(t)$, yields the measured strain response, $y(t)$, as follows:

$$y(t) = \int_0^t g(t-\tau)u(\tau)d\tau \tag{5.8}$$

The IRF is obtained through a calibration either prior or post the experiments. For discretised data, $u(t)$, $y(t)$, and $g(t)$ can be rewritten as:

$$y_r = \sum_{s=0}^{r} g_{r-s}u_s\delta t \tag{5.9}$$

where $r \in (0,1,2,..,k)$ and δt is the sampling rate. Rewriting this equation in matrix form yields:

$$\mathbf{y} = G\mathbf{u}\delta t \tag{5.10}$$

If this analysis is generalised to a four component system, Eq. 5.10 becomes:

$$\begin{bmatrix} \mathbf{y}_x \\ \mathbf{y}_y \\ \mathbf{y}_z \\ \mathbf{y}_{My} \end{bmatrix} = \begin{bmatrix} G_{x.x} & G_{x.y} & G_{x.z} & G_{x.My} \\ G_{y.x} & G_{y.y} & G_{y.z} & G_{y.My} \\ G_{z.x} & G_{z.y} & G_{z.z} & G_{z.My} \\ G_{My.x} & G_{My.y} & G_{My.z} & G_{My.My} \end{bmatrix} \begin{bmatrix} \mathbf{u}_x \\ \mathbf{u}_y \\ \mathbf{u}_z \\ \mathbf{u}_{My} \end{bmatrix} \delta t \tag{5.11}$$

where G_{nm} is the IRF that relates output $\mathbf{y}_n$ to input $\mathbf{u}_m$. The matrix containing all of the individual IRFs is known as the global impulse response function (GIRF) and can only be found through careful dynamic calibration. For an ideal force balance, the GIRF would be diagonally dominant with all values off the diagonal being null matrices, i.e. the input applied to an orthogonal axis only results in an output on the same axis. In this work, if the relative strain output of an off-axis term was less than 1% of the on-axis strain (for a unit normal load), the off-axis IRF was discounted. For this force balance, cross-coupling was only significant for the axial force upon the application of a normal force. This was applied to save computational time and reduced Eq. 5.11 to:

$$\begin{bmatrix} \mathbf{y}_x \\ \mathbf{y}_y \\ \mathbf{y}_z \\ \mathbf{y}_{My} \end{bmatrix} = \begin{bmatrix} G_{x.x} & 0 & G_{x.z} & 0 \\ 0 & G_{y.y} & 0 & 0 \\ 0 & 0 & G_{z.z} & 0 \\ 0 & 0 & 0 & G_{My.My} \end{bmatrix} \begin{bmatrix} \mathbf{u}_x \\ \mathbf{u}_y \\ \mathbf{u}_z \\ \mathbf{u}_{My} \end{bmatrix} \delta t \tag{5.12}$$

If the calibration process sufficiently characterises the GIRF, equation 5.12 can be used to find the applied aerodynamic load, $\mathbf{u}$, through a deconvolution process with the measured

strains ($\mathbf{y}$) and GIRF. For this work the deconvolution process was undertaken in Matlab solving Equation 5.12.

The calibration process to characterise the GIRF for this experiments was conducted with the model in situ within the wind tunnel prior to the experiments taking place. The calibration was achieved using an instrumented impact hammer (PCB Piezotronics 086C01) through application of impulsive forces at discrete model locations in orthogonal directions. Figure 5.9 shows the position of the impulse hits used to characterise the cone model, where *A* and *N* correspond to normal and axial impulses respectively. As depicted in the figure, hits to characterise the axial force were conducted at the base at the four cardinal points and the nose. Characterisation of the normal component were conducted along the length of the cone at 3 positions equally spaced out (the same is true for the side force which is not depicted in the figure). By using multiple locations for impulse hammer hits and combining the individual IRFs, the stress wave patterns for the whole model was characterised more completely. The IRFs for axial, normal (and side) were formed as shown in Equation 5.13 - 5.15 with weighting factors for each impulse. For axial force, the same overall weightings were given to the nose hit and the four combined cardinal base hits (noting the flip in polarity due to the direction of the hit). For normal and side force, equal weighting was given along the length of the cone and for the pitching moment, the two normal impulses at the extremity of the cone were combined to form the IRF.

$$G_{x,x} = \frac{1}{2}(G_{A_{nose}} - \frac{1}{4}(G_{A_N} + G_{A_W} + G_{A_E} + G_{A_S})) \tag{5.13}$$

$$G_{z,z} = \frac{1}{3}(G_{N_A} + G_{N_B} + G_{N_C}) \tag{5.14}$$

$$G_{My,My} = \frac{1}{2}(G_{N_A} - G_{N_C}) \tag{5.15}$$

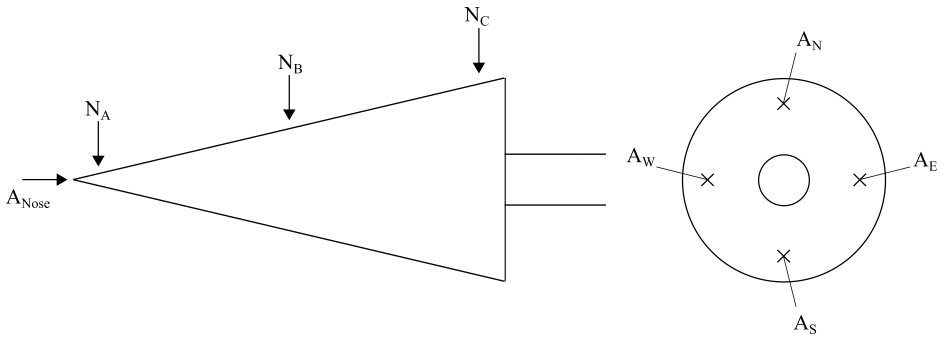

Fig. 5.9 Location of axial and normal impulse hits used to generate the GIRF

For each hammer hit location, three independent hammer hits were conducted. The first two hammer hits are used to generate a mean IRF at that location by deconvolving the impulse with the measured strains. The third is used as a validation, the mean IRF generated is deconvolved with the strain signal to see if the impulse for the third hit is recovered, thereby giving confidence that the IRF is valid and insensitive to small changes in component strains. This is completed for all hammer hit locations.

5.5 Results

The following section presents the experimental results for both force measurement techniques in the form of raw force signals and aerodynamic coefficients. Comparisons are made between the free-flight methodology and the force balance setup used for these experiments. It must be noted that uncertainties are specific to the University of Oxford 0.7 inch force balance and may be improved with a different force balance design.

5.5.1 Raw Force Signals

The first useful comparison to consider are the raw unfiltered force data. Ultimately, the cleaner the raw force signal, the lower the overall uncertainty in forces and hence coefficients. Figure 5.10 presents the measured unfiltered forces from both the force balance (static and dynamic calibration) and in free-flight at zero degrees angle of attack. The image tracking forces are not presented here as it is not a direct force measurement (displacements are measured) unlike the other methodologies. It can be seen from the static force balance data that vibrations within the model - support structure do not damp out in the test time and heavily superimpose themselves on the measured strain signals. This results in large oscillations within the force data. For steady signals to be measured, the aerodynamic forces must reach equilibrium with the resultant stresses applied to the load cells of the force balance. With application of the dynamic calibration, the magnitude of the vibrations is heavily reduced and results in a much cleaner force signal with respect to time, however, the oscillations are not completely removed.

However, the raw signal with the least oscillatory behaviour is the free-flight IMU data. By removing the rigid mount, internal vibrations decay much faster within the model and are not imposed on the IMU resulting in clean accelerations (hence forces) measured in the test time. Therefore, the free-flight technique will have the lowest statistical uncertainties when the force is averaged over the test time. This is shown in Table 5.4 where the standard deviation for free-flight is 1.4 % of the mean value compared to 22.1 % for the statically

calibrated force balance data. The unfiltered normal force signals also exhibit oscillatory behaviour for the force balance albeit at a slower frequency. This is expected as the balance acts as a oscillating cantilever for this force measurement axis due to the sting. The IMU data for the normal axis is more oscillatory than for the drag data reflected in the higher standard deviation of the mean for this axis (in Table 5.4). This result is unsurprising as due to the design of the DAQ mount, it is less rigid on the normal axis than on the axial axis so oscillations will not damp out as quickly. Regardless, the standard deviation of the IMU data is still lower for all components than the force balance techniques.

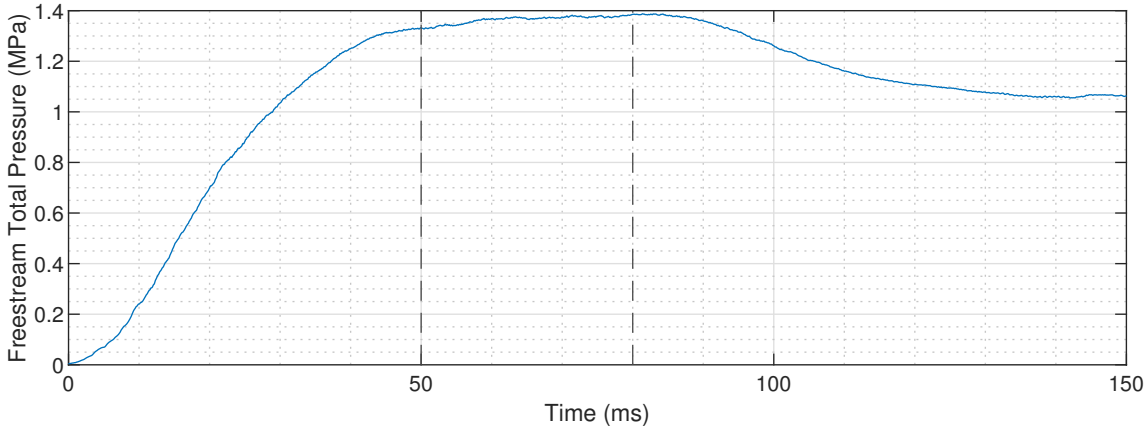

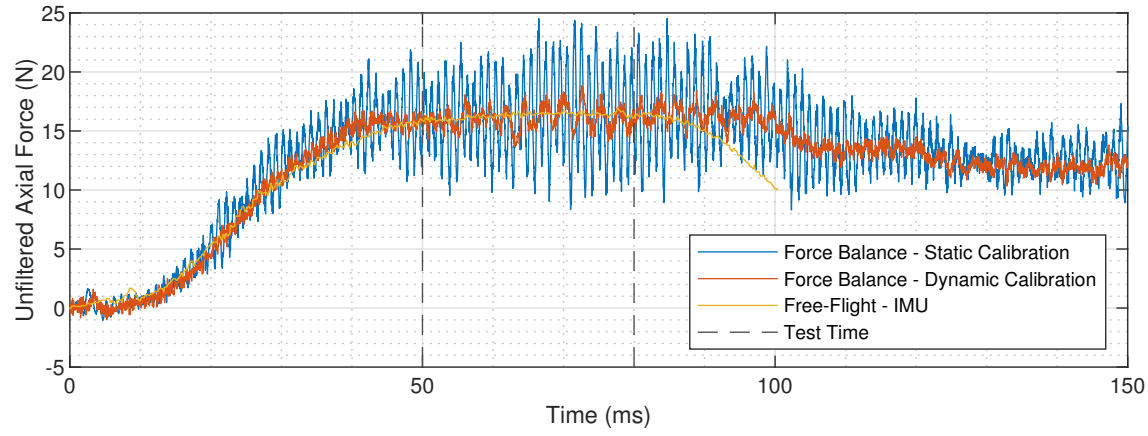

Table 5.4 Force technique statistical properties for unfiltered forces at zero Angle of attack

Technique	F_x **Mean**	F_x **Standard Deviation**	F_z **Mean**	F_z **Standard Deviation**
F.B. Static	16.45 N	$\pm$ 3.64 N	-1.25 N	$\pm$ 3.15 N
F.B. Dynamic	16.14 N	$\pm$ 0.91 N	-1.22 N	$\pm$ 1.53 N
Free-Flight	16.30 N	$\pm$ 0.23 N	0.61 N	$\pm$ 0.68 N

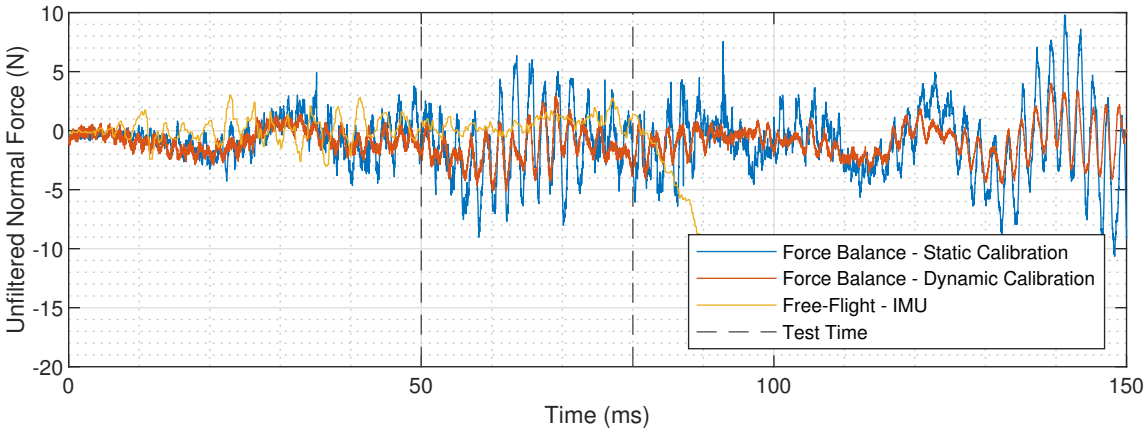

Fig. 5.10 Freestream total pressure (top), unfiltered axial forces (middle) and unfiltered normal force (bottom) for the different force measurement techniques at zero degree angle of attack

5.5.2 Aerodynamic Coefficients

For these experiments, tests were conducted using each methodology at 0, 3 and 6 degrees angle of attack; 3 in free-flight and 5 tests with the force balance giving data for both static and dynamic calibrations. The data is compared with numerical results from a hypersonic panel method code which includes a viscous streamline correction at the Mach 5 condition. For more details on the panel code, see Hyslop et al. [34]. Uncertainties presented for the free-flight and force balance data are presented as error bars on the figures and were calculated using Moffat's error propagation method [66] for freestream parameters, model properties and through the force derivation. For all experimental data, the uncertainties are highest for the static force balance calibration and lowest for the free-flight data. The uncertainty in angle of attack, however, is higher than for the free-flight as it relies on an image tracking rather than the direct measurement of freestream alignment using pressure transducers as for the force balance.

Figure 5.11 shows the variation of lift coefficient with angle of attack which shows a positive linear trend with a zero degree lift coefficient value of zero, reflecting the symmetric shape of the cone. All experimental data points agree within the experimental uncertainty and are in good agreement with the numerical predictions. At 6 degrees angles of attack, the dynamic calibration differs from the static calibration by 12.7 % with the static calibration over predicting. This is likely due to the method of calibrating the force balance for the static tests as only 5 data points were taken over the range of the balance for the calibration which could result in error if there is some degree of non-linearity or hysteresis in the system.

The variation of drag coefficient with angle of attack is shown in Figure 5.12. For this figure, both the viscid and inviscid numerical results are plotted. The inviscid cases are not shown on the other figures as at these low angles of attack, the effects of viscosity are minimal on lift and pitching moment. All of the data points lie slightly above the viscid numerical predictions. One reason for this could be explained in the calculation of base pressure in the panel method code. As seen in Figure 5.8, the base pressure is not quite at equilibrium for the duration of the first plateau of test time which would result in an offset in drag coefficient. Whilst force balance data is acquired for all plateaus during a test, in free-flight the model is no longer in the core flow so data can not be obtained. Lift-to-drag ratio is shown in figure 5.13 and shows good agreement with the numerical and experimental data.

Pitching moment coefficient with angle of attack is shown in Figure 5.14 and is referenced from the virtual apex of the cone. The gradient of pitching moment with angle of attack is negative, as would be expected from this reference point, as it would show static stability if the CoG was hypothetically in this location. Agreement between all methodologies lie within the uncertainties.

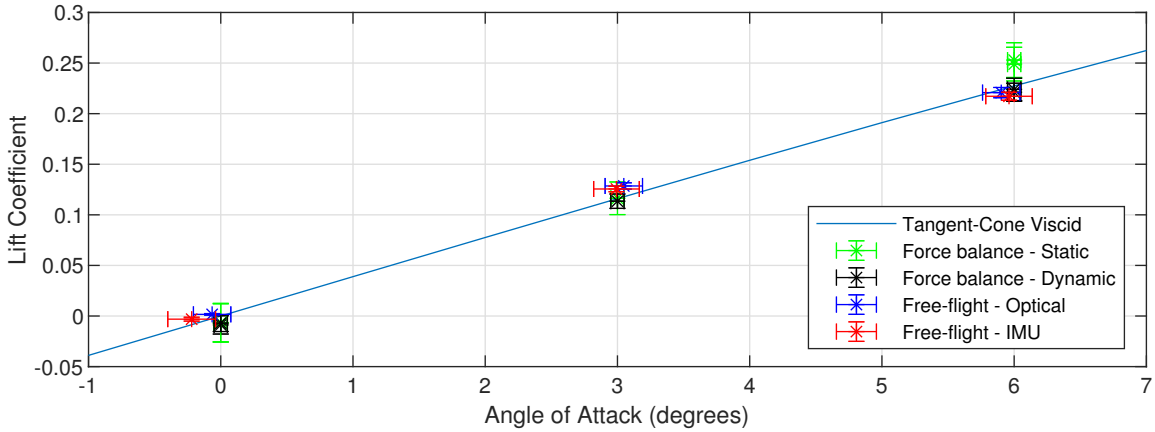

Fig. 5.11 Lift coefficient at Mach 5 condition. Individual tests plotted against tangent-cone numerical prediction

5.5.3 Comparison of Methodologies

In a comparison of the methodologies, one of the most important factors to take into account are the experimental uncertainties for the techniques. The maximum uncertainties for each of the measurement axis of interest are shown in Table 5.5 for the different experimental methods. They are presented in the form of raw force/moment so that the uncertainties can be seen without the influence of the freestream uncertainties as well as in coefficient form which

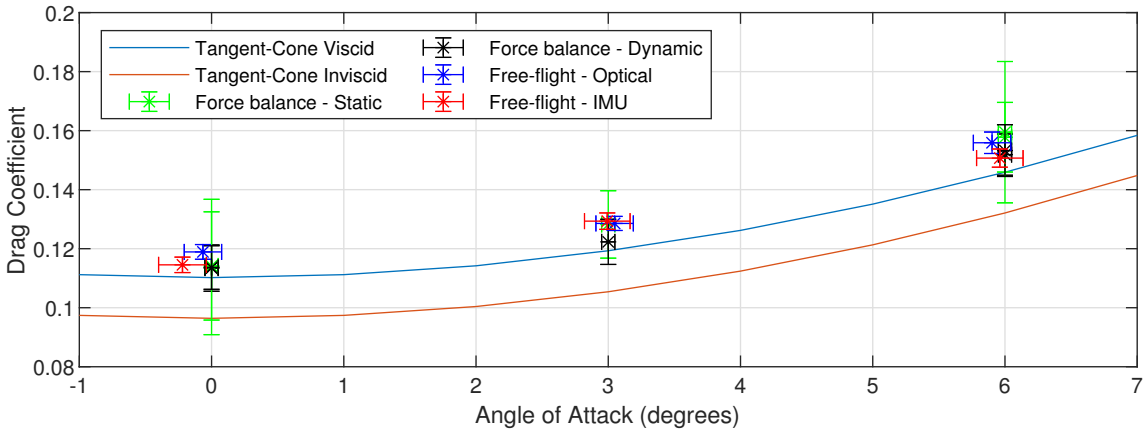

Fig. 5.12 Drag coefficient at Mach 5 condition. Individual tests plotted against tangent-cone numerical prediction

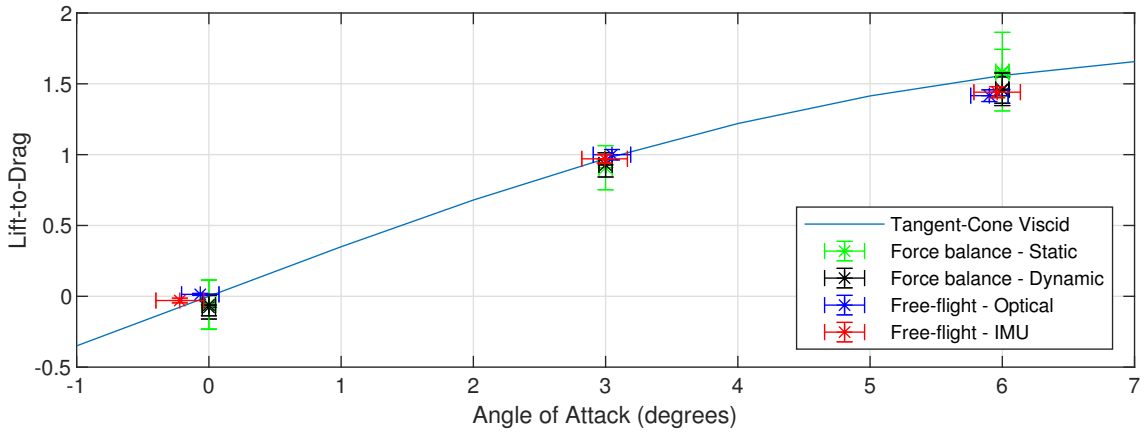

Fig. 5.13 Lift-to-drag ratio at Mach 5 condition. Individual tests plotted against tangent-cone numerical prediction

give uncertainties for both the facility and the measurement technique. For all cases, the static force balance calibration gives the highest uncertainties followed by the dynamic calibration. The uncertainties for free-flight are 50 % better or more for all of the measurement axis. It is also shown that the image tracking and IMU measurements give very similar uncertainties. A sensitivity analysis for the free-flight tests show the largest contribution to the uncertainties of the aerodynamic coefficients is the uncertainty of the measured accelerations. A shift from micro-electro-mechanical systems (MEMS) accelerometers to other forms of accelerometer may reduce these uncertainties further. For the force balance, the main contribution to the uncertainties is from the internal vibrations of the balance.

Other factors which must be taken to account are the ease of the experiments. Once a force balance experiment is setup and aligned with the freestream, it is very simple to

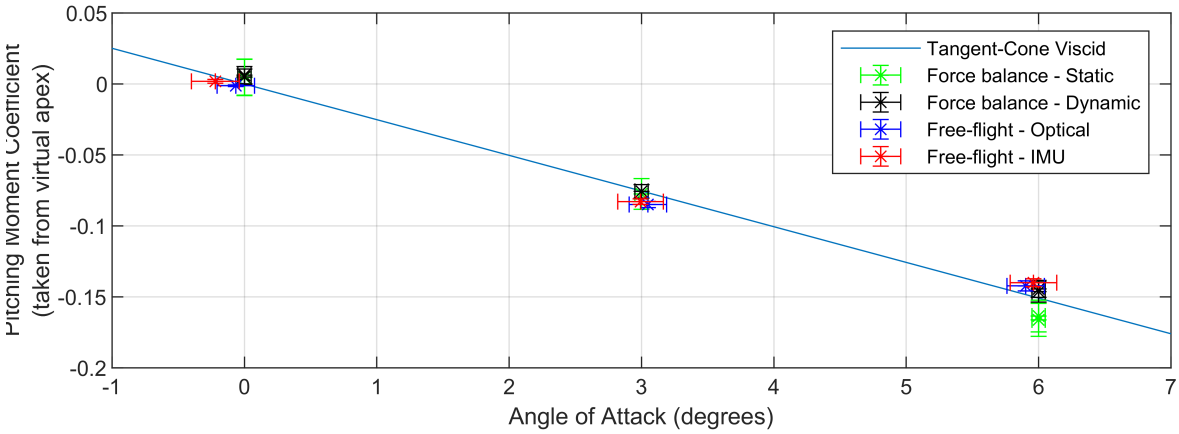

Fig. 5.14 Pitching moment coefficient (referenced from virtual apex of cone) at Mach 5 condition. Individual tests plotted against tangent-cone numerical prediction

Table 5.5 Force technique experimental uncertainties

Technique	C_L	L **(N)**	C_D	D **(N)**	C_M	M **(Nm)**
Force Balance - Static	$\pm$ 0.019	$\pm$ 2.74	$\pm$ 0.024	$\pm$ 3.46	$\pm$ 0.012	$\pm$ 0.42
Force Balance - Dynamic	$\pm$ 0.011	$\pm$ 1.59	$\pm$ 0.009	$\pm$ 1.27	$\pm$ 0.007	$\pm$ 0.27
Free-Flight - IMU	$\pm$ 0.004	$\pm$ 0.56	$\pm$ 0.003	$\pm$ 0.44	$\pm$ 0.003	$\pm$ 0.10
Free-Flight - Optical	$\pm$ 0.005	$\pm$ 0.73	$\pm$ 0.004	$\pm$ 0.53	$\pm$ 0.004	$\pm$ 0.13

adjust angle of attack on the traverse and so is quick to obtain a sweep of data with angle of attack. For free-flight, the model must be returned to the release mechanism at the start of each test which if the facility needs to be pumped to a vacuum prior to a test can be very time consuming. Another consideration for free-flight is the greater difficulty of testing at a specific angle of attack. For these experiments, the release has a variation of $\pm$ 0.2 $^\circ$ coupled with the potential for the model to pitch if the CoG is not at CoP which can make it more challenging to achieve the desired angle of attack. This is acceptable, however, if the experimenter is interested in general trends with respect to angle of attack and the uncertainty is not an issue. Another challenge for static free-flight is that the experimenter needs a prediction of CoP location prior to experiments so that the model can be designed to be ballasted suitably for static free-flight. This becomes more of an issue with complex geometries where CFD CoP predictions become much more difficult.

That is not to say that force balances do not pose their own problems. The uncertainties are much higher in these set of experiments and they are largely driven by the internal stress waves and harmonic structural oscillations not reaching equilibrium during the experimental test time. For a force balance - model structure to be suitable for use in hypersonic facilities with a static calibration, several natural frequency cycles must pass in the test time for

steady state forces to be measured [6]. For cantilever sting based force balances, creating a natural frequency that is high enough to achieve this is very difficult and therefore dynamic calibration is often required. Furthermore, dynamic characterisation of complex geometries is challenging due to the lack of flat edges providing a clean surface for an impulse hammer hit. As well as these issues, combining the discrete orthogonal hammer impulses into a GIRF for a complex geometry is challenging and there is no guarantee that for a complex model the balance response is linear.

5.6 Conclusion

The experimental measurement of forces and moments using two independent measurement techniques have been presented at the same freestream conditions for a 7 degree half-angle cone at a Mach 5 condition, providing to the authors knowledge, the first direct comparison of the two techniques in the same facility for the identical model geometries. It has been shown that all 3 methodologies (free-flight, static force balance and dynamic force balance) can provide accurate force and moment data but with varying uncertainties. As the force balance requires careful design of the string-model supporting structure to reduce the impact of internal vibrations from external aerodynamic forces imposing on the strain gauges, it is more susceptible to fluctuations about the mean data point than for the unconstrained free-flight methodologies which is ultimately reflected in the higher uncertainties for force balance data (both calibrations). These uncertainties may be reduced further if the force balance is designed optimally for the model being tested by increasing the natural frequency of the system so that the oscillations decay faster. Overall, it has been shown that the uncertainties for force measurement for the free-flight technique are half as much as the force balance in the University of Oxford High Density Tunnel demonstrating that free-flight is the preferred means at achieving high-quality, low-uncertainty force measurements in short duration facilities.

Chapter 6

The Measurement of Static Aerodynamic Coefficients of a Complex Body Using the Free-Flight Technique in Short Duration Hypersonic Flow

Preamble

The final research aim of the thesis was to apply the static free-flight technique to a complex geometry - one in which the centre of pressure is not constant with angle of attack. In this chapter, the static free-flight technique is applied to a finned cone and aerodynamic coefficients determined over a range of angles of attack. This Chapter validates the free-flight technique for complex geometries with the data compared to a numerical panel code simulation. This Chapter consists of a journal paper currently under review in the Journal of Spacecrafts and Rockets. The content and structure of this chapter represent 100 % of the main body of the original paper.

Authors of the original paper:

Hyslop, A., Doherty, L.J., McGilvray, M.

Author contribution:

- **Hyslop, A.** : Lead author, conceptualisation, data curation, formal analysis, and writing.
- Doherty, L.J. : Supervision as Senior Research Associate.
- McGilvray, M. : Supervision as Principal Investigator.

Associated Appendices:

Appendix C - Supplementary Free-Flight Manoeuvre Data

Abstract

The measurement of high quality force and moment coefficients in the hypersonic regime within short duration wind tunnels is challenging, particularly for complex geometries with control surfaces. In this study, the static free-flight force measurement technique has been applied to a finned 7 degree half-angle cone within the University of Oxford High Density Tunnel at a flight-representative Mach 7 condition. A quasi-static free-flight test is achieved by matching the locations of the centre of gravity and centre of pressure reducing the static margin of the body and hence the amount of pitching motion. This eliminates the influence of dynamic derivatives on the overall coefficient. Static free-flight becomes more difficult for complex bodies where the centre of pressure is a function of angle of attack. Longitudinal static force and moment coefficients were measured at the Mach 7 condition with the experimental data agreeing well with numerical predictions. Forces were obtained using both image tracking at 76,000 fps as well as the direct measurement of accelerations using an on-board inertial measurement unit. Uncertainties were at most $\pm$ 0.0075 for lift coefficient and $\pm$ 0.0051 for drag coefficient across all attitudes tested. The fins were also angled to allow the model to roll in free-flight so that roll coefficient could also be determined with a maximum experimental uncertainty of $\pm$ 0.0452.

6.1 Introduction

Methodologies that can obtain high quality force and moment measurements in hypersonic facilities for complex sub-scale models remain important for the development of flight vehicles. The optimal method of testing a geometry is to undergo a flight testing programme, but this is very expensive, so ground testing and computational fluid dynamics are often used to optimise the design before proceeding to this stage. However, full nose-to-tail computational simulations still have limitations when predicting forces as there are large uncertainties in the prediction of phenomena such as boundary layer transition for example [107] [91]. Therefore, there is still need for ground-based experiments to act as a validation to these simulations.

Force and moment measurements in many hypersonic facilities that produce flight representative flow conditions is difficult due to the short time durations they produce, ranging from milliseconds in shock facilities to tens of milliseconds in Ludwieg tubes. Due to the short time scales, conventional methods of measuring forces such as using a statically calibrated strain-gauge sting-mounted force balance is not the optimal method for flow durations of less than 100 ms [38] and other force measurement techniques can be used which result in lower experimental uncertainties. It is challenging to design a model that can sufficiently damp out the internal stress waves produced by the external aerodynamic forces within these short test times to provide steady, equilibrium force measurements. To overcome this, the stress-wave force measurement technique was designed and implemented by Sanderson and Simmons [84] and more recently applied by Mee et al. [62] and Doherty et al. [16] which uses a carefully calibrated impulse response to deconvolve the forces from the measured strain signals. Whilst shown to be successful in short duration facilities with tests times of 1 ms, it requires careful design of the mounting structure so that it does not interact with the flow field and influence the measured forces [79].

To overcome sting interference and mounting vibrational effects, the free-flight force measurement technique was created [6]. Rather than mounting the model rigidly, the model is released into the facility nozzle core flow and allowed to move unconstrained in six degrees-of-freedom. This requires the kinematics of the model to be measured, usually by optical methods or on-board inertial measurement units (IMU). The free-flight technique has successfully been applied at multiple facilities by Tanno et al. [97] at JAXA, Kennell et al. [39] and McQuellin et al. [59] at UNSW Canberra and Hyslop et al. [33] at the University of Oxford. In the experiments at UNSW and Oxford, low inertia models were free-flown which were allowed to pitch over a range of angles of attack. Due to the large degree of pitching motion of the model, the influence of dynamic derivatives is present which prompted the creation of the static free-flight technique [34]. For these experiments, the amount of pitching of the model was limited by matching the location of the centre of pressure and gravity, minimising the static margin to obtained purely static coefficients. This technique also produced uncertainties in aerodynamic coefficients below 3 %.

The static free-flight technique has been validated for simple geometries [34] with significantly smaller uncertainties than other force measurement techniques in the University of Oxford HDT (see Chapter 5). Following the groundwork of previous experiments, the static free-flight technique is applied to a complex geometry in this work at conditions representative of a true flight vehicle. Complications exist with more complex geometries as the centre of pressure is unlikely to remain constant with angle of attack and so careful adjustments to the ballasting between experiments is required to match the centre of gravity

to this location. The model used for these experiments is a 7 degree half-angle cone with 4 fins mounted at the base. As well as the measurement of longitudinal force and moment coefficients measured from image tracking and IMU measurements, the fins were angled and the model allowed to roll so that roll moment coefficients could be measured.

6.2 Static Free-Flight Technique

6.2.1 Aerodynamic Coefficients

The instantaneous aerodynamic coefficients in flight are summations of both static (time independent) and dynamic (time dependent) phenomena. Writing the aerodynamic coefficients in terms of their derivatives gives the following, where higher order terms have been neglected::

$$C_L = C_{L_0} + C_{L_\alpha}\alpha + C_{L_{\delta_e}}\delta_e + C_{L_v}\frac{v}{V} + C_{L_q}\frac{qc}{2V} + C_{L_{\dot{\alpha}}}\frac{\dot{\alpha}c}{2V} + ... \tag{6.1}$$

$$C_D = C_{D_0} + C_{D_\alpha}\alpha + C_{D_{\delta_e}}\delta_e + C_{D_v}\frac{v}{V} + C_{D_q}\frac{qc}{2V} + C_{D_{\dot{\alpha}}}\frac{\dot{\alpha}c}{2V} + ... \tag{6.2}$$

$$C_M = C_{M_0} + C_{M_\alpha}\alpha + C_{M_{\delta_e}}\delta_e + C_{M_v}\frac{v}{V} + C_{M_q}\frac{qc}{2V} + C_{M_{\dot{\alpha}}}\frac{\dot{\alpha}c}{2V} + ... \tag{6.3}$$

To measure purely static derivatives in wind tunnel facilities, the experimenter must remove the ability of the model to exhibit any dynamic behaviour with time. From equations 6.1 - 6.3, it can be seen that to remove any dynamic influence on the coefficients, two criteria must be fulfilled; the model must not be allowed to pitch and there must be minimal perturbations in the freestream velocity. The dependency on flow perturbations (or gusts in flight), C_{X_v}, can be assumed to be minimal in wind tunnel facility which generates constant freestream conditions and have small perturbations in the free-stream velocity during the test time. If the model is not allowed to pitch during the test and the angularity changes to the flow are uniform with respect to model position, the effects of C_{X_q} and $C_{X_{\dot{\alpha}}}$ may be negated. By fulfilling these conditions, a purely static condition is achieved and only the static coefficients are measured. This reduces Eq. 6.1 to (Equations 6.2 and 6.3 can also be rewritten in the same way):

$$C_L = C_{L_0} + C_{L_\alpha}\alpha + C_{L_{\delta_e}}\delta_e \tag{6.4}$$

For aerodynamic coefficients measured in wind tunnel facilities to be representative of those in flight, the conditions must be scaled so that similitude is achieved. Aerodynamic

coefficients are functions of both Mach number and Reynolds number, with Mach number similitude preserving compressibility effects (such as shock angles) and Reynolds number similitude preserving viscous effects (such as boundary layer thickness and skin friction). Therefore, matching both of these dimensionless groups and limiting the ability of the model to pitch allows for static aerodynamic coefficients to be measured.

6.2.2 Methodology of Static Free-Flight

For free-flight testing, the scaled model is free to move in six degrees of freedom so it is not possible to constrain the model from pitching through the use of rigid mounts to remove the influence of dynamic phenomena during a test. In free-flight, there are two ways of preventing pitching motion; the first is to have a model with sufficiently high inertia that during the test time the resultant pitching is minimal. This would likely result in a large, heavy model. Increasing the model's mass decreases the magnitude of the accelerations which would occur during the test, making it harder to measure the forces and increasing the uncertainty of the experiment.

The second method of minimising the pitching, which was used in these experiments, is to manipulate the aerodynamic pitching moment that acts on the body during the free-flight test. Consider the aerodynamic forces acting on a free body in free-flight; as the fluid passes over the body during a test, pressure and shear components are exerted on the surface of the body. Integrating the shear and pressure components over the body results in the overall aerodynamic force acting on the body. This integrated force can be considered to be a single force vector at the average integrated location, often referred to as the centre of pressure (CoP). The force vector is usually split into two orthogonal forces referred to as lift and drag. The final force that needs to be considered is the model's weight which can be considered to act as a single vector through the centre of gravity (CoG). The position of the CoG relative to the CoP determines the stability of the body in flight. If the CoG is fore of the CoP, the body is statically stable and will tend to pitch towards an equilibrium position if perturbed. If the CoG is aft of the CoP, the body is statically unstable and will pitch away from an equilibrium position which is often undesirable as it makes the body difficult to control. In both of these instances, the body will exhibit increasing pitch rates as the distance between the CoP and CoG is increased. If a model is designed so that the CoP is at the same position of the CoG, there will be no aerodynamic pitching moment and hence can be considered as a static free-flight test.

In practice, this requires: (1) a method of predicting the CoP location, (2) a model design that allows for fine tuning of the CoG location and (3) a setup that can accurately measure the CoG location before a test. It should be noted that in this static free-flight methodology, the

model design is independent of mass and moment of inertia and so the experimenter is not limited by material choice as they would be if scaling for dynamic experiments which require strict similitude criteria to be matched for mass and inertia to obtain flight representative dynamic derivatives.

6.3 Experimental Setup

6.3.1 Facility and Freestream Conditions

The free-flight experiments were conducted in the University of Oxford High Density Tunnel HDT, a heated Ludwieg tube that provides cold, high Reynolds number flow for steady plateaus of approximately 50 ms. The facility is rated for fill pressures of up to 275 bar which during a test is vented from a barrel through a quick-acting plug valve to a contoured converging/diverging nozzle with exit diameter of 350 mm. This provides a core flow of 280 mm at nozzle exit. The nozzles can be changed to provide a freestream Mach number of integers between 5 and 7. For further details on the HDT operation and measurement of freestream conditions, see McGilvray et al. [57] and Wylie et al. [108]. Figure 6.1 shows a schematic of the Oxford HDT.

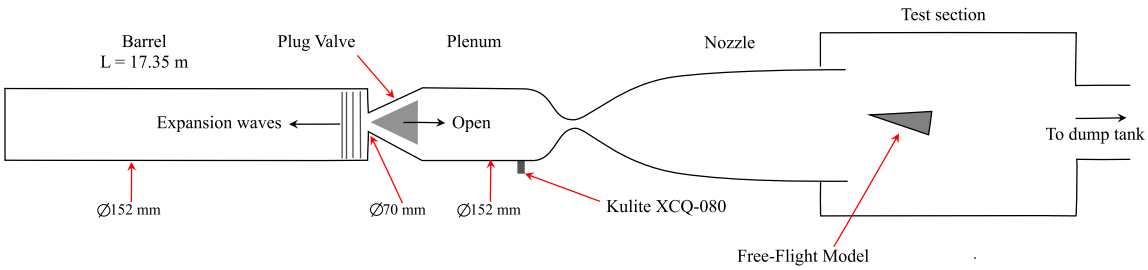

Fig. 6.1 Schematic of the University of Oxford HDT (adapted from Hillyer et al. [29].)

The freestream conditions used for the experiments were representative of a flight vehicle at an altitude of 35 km and Mach number of 7 [32]. To scale for these conditions, Reynolds and Mach number were matched between flight and tunnel, and it was assumed that full scale vehicle was 3 m in length, giving a scale factor of 1/12 for a 250 mm length wind tunnel model. This provided a model which is suitably sized for the core flow of the facility. The tunnel and flight freestream conditions are shown in Table 6.1 below.

The conditions obtained during a test were surveyed prior to the experiments using a rake instrumented with pressure transducers and thermocouples, providing freestream total pressure, Pitot pressure and total temperature traces. From these measurements, the Pitot-to-

Table 6.1 Mach 7 Flight vs scaled tunnel condition.

Measured Freestream Properties	**HDT Test Flow**	**Flight**
Total Pressure (kPa)	3348 ± 7	2313
Pitot Pressure (kPa)	49.9 ± 0.7	35.5
Total Temperature (K)	555 ± 15	2560
Calculated Freestream Properties		
Altitude (km)	35	35
Mach Number	7.05 ± 0.02	7
Velocity (ms^{-1})	1006 ± 14	2160
Density (kgm^{-3})	0.0532 ± 0.0018	0.0082
Static Pressure (Pa)	774 ± 15	559
Static Temperature (K)	50.8 ± 1.4	242
Dynamic Viscosity (μPas)	3.64 ± 0.10	15.2
Dynamic Pressure (kPa)	26.9 ± 0.6	19.1
Unit Reynolds Number ($10^6 m^{-1}$)	14.7 ± 0.7	1.16
Reynolds Number (10^6)	3.68 ± 0.16	3.48

nozzle-supply ratio was used to calculate Mach number, Keyes' Law to calculate dynamic viscosity [43] and isentropic relations to calculate the rest of the tunnel conditions. Equivalent flight conditions were calculated through US Standard Atmosphere [71] and viscosity using Sutherland's Law [94]. The uniformity of the core flow with respect to axial position was also measured with the rake. The core flow was determined to be of 280 mm diameter at nozzle exit reducing to 240 mm at 300 mm downstream. Uncertainties in the calculated freestream variables are determined using the Taylor Series Method through the propagation of uncertainties from the measured properties. Computation fluid dynamic (CFD) simulations of the nozzle conducted in Eilmer4 show agreement with the measured core flow diameter at nozzle exit and predict the angularity of the flow to remain within +/- 0.12 $^\circ$ within the core flow.

6.3.2 Test Infrastructure

The test infrastructure used to conduct free-flight experiments is shown in Figure 6.2 with the finned cone model in the test section prior to an experiment. The infrastructure can be split into three working functions; the release mechanism, protection of the model and optical setup aides. The infrastructure originates from Hyslop et al. [34] with some improvements.

The drop mechanism is used to release the model so that it is in the centre of the core flow when the facility is fired. A 25 mm Eclipse Magnetics electromagnet is used to hold the model in place. Prior to the facility firing, a TTL trigger is sent to a bespoke electronics

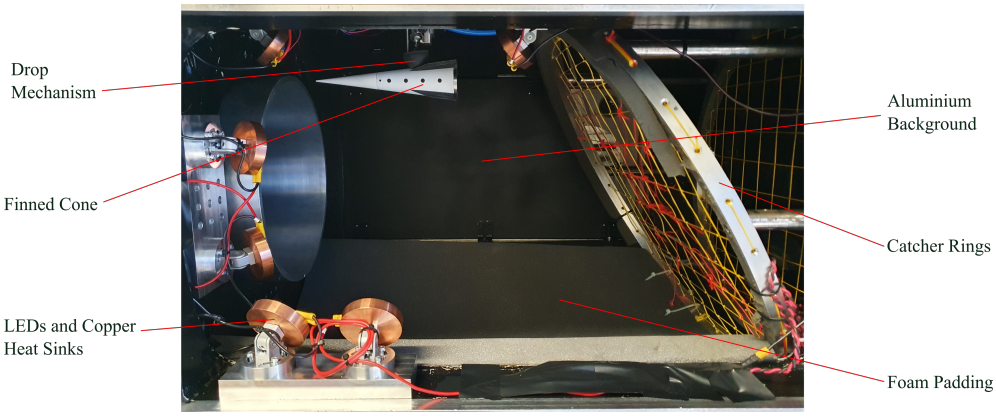

Fig. 6.2 Free-flight infrastructure in the HDT test section.

box which causes the electromagnet to release. This timing can be adjusted as the flow initiation is achieved by the motion of a fast-acting plug valve whose timings are well calibrated. The electronics box also activates two 100 psi solenoids that retract a 50 mm stroke length actuator. This removes the electromagnet from the core flow, preventing any shocks influencing the model during the test. The electromagnet is encased in a 3D printed holder which fits conformal to the shape of the finned cone model with different variations printed to set the angle of attack in two degree increments. A steel rod can be inserted into the holder which fixes the model position in yaw. The axial and roll location are fixed by painting a 'T' shape to the model which the conformal holder is designed to locate. The drop mechanism is mounted to a linear rail so that its axial position relative to the nozzle exit can be adjusted.

The model is protected after a free-flight experiment by two aluminium catcher rings. The rings are designed to be strung similar to a tennis racket using Dyneema cord which has a high tensile yield strength. The upstream ring is angled at 30 $^{\circ}$ to the vertical and is designed to deflect the model towards the floor of the test section on impact which is padded with triple layer density foam, providing a soft landing to protect the model. The second downstream ring lies parallel with the test section exit and provides a redundancy in case the first ring is breached to prevent the model entering the dump tank where it becomes difficult to retrieve.

Located within the tunnel were six Luminus PT-120-B-L11-EPG LEDs of 460 nm peak wavelength (blue light) with individual copper heat sinks. The position and rotation of these LEDs could be adjusted to provide sufficient and uniform lighting to the track the model at high frame-rates. This setup also allows for pressure-sensitive paint to be painted onto the model if required [102]. At the far side of the test section from the optical setup is a painted

black aluminium paint which provides a high contrast, uniform background against the white model to allow for improved edge detection for the image tracking algorithm.

6.3.3 Experimental Model

The experimental model shown in Figure 6.3 is a 7 degree half-angle cone of 250 mm length with four fins attached to the base of the model at cardinal positions. The fins were designed so that they did not interact with the bow shock from the nose tip of the cone calculated from a Taylor-Maccoll analysis of Mach 7 flow at zero degrees angle of attack. This results in fins of width 16.5 mm at the base which taper for a length of 83.3 mm (a third of the length of the body). The leading edges of the fins are angled at 15 degrees to keep the flow attached with a bluntness of 0.2 mm radius for machining reasons. The fins could be angled at $\pm 3^{\circ}$ but for the main body of the work were set to 0°. The fins were 3D printed so that they could be easily manufactured and replaced in the event of damage after free-flight. For the experiments, the model was tested with the fins orientated at 45 $^{\circ}$ to the horizontal.

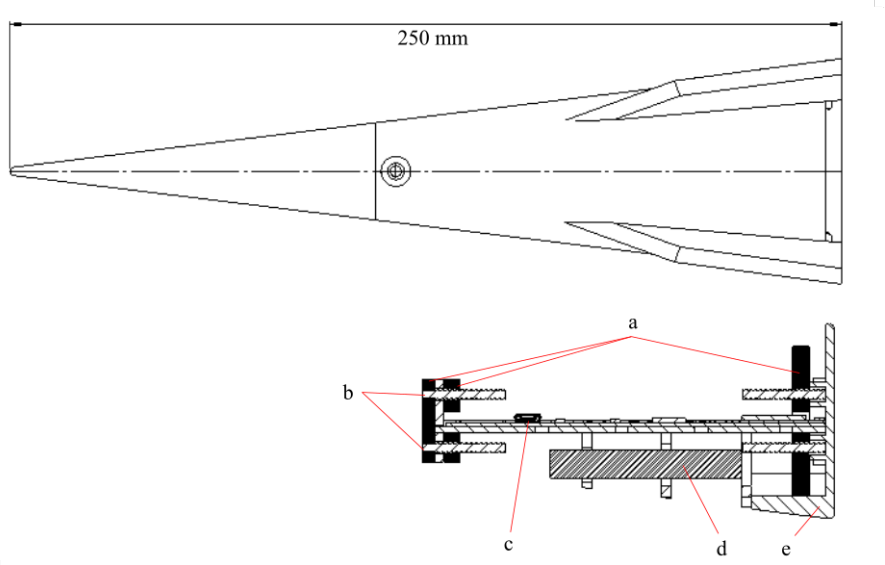

Fig. 6.3 Finned cone experimental model with co-ordinate system used in these experiments. Bottom shows the schematic of the internal instrumentation support (a - Tungsten ballast, b - threaded rod, c - DAQ, d - battery, e - 3D printed mount)

The body of the cone was machined from steel and could be split into two halves. This allows for easy access when instrumenting the model with on-board sensors and ballast. The base was also machined from steel and had notches which allowed for the fins to be bolted into place, ensuring sufficient rigidity in mounting. The two halves of the cone join to form a

male thread to which nose tips of different bluntnesses could be attached. For this work, a bluntness of 1.25 mm in radius was used. Internal to the model was an on-board DAQ which contained inertial measurement units. The DAQ was rigidly mounted to a 3D printed holder which was shaped to be conformal to the internal shape of the cone and remain fixed during a test. The external of the model was painted white to provide high contrast between the model and the black background of the test section to improve the accuracy of the edge tracking algorithm. After painting white, a laser cut stencil was used to paint black circles on the side of the cone and 'T' shapes at the top the cone with a positional tolerance of $\pm$ 0.2 mm.

Table 6.2 Model inertial and geometric properties

Length (mm)	250 ± 0.2
Cone Half-Angle ($^\circ$)	7 ± 0.03
Nominal Nose Radius (mm)	1.25 ± 0.1
Base Area (m^2)	$3.2\ \text{x}10^{-3} \pm 0.01$
Centre of gravity (mm)	70.7 ± 0.1
Mass (g)	832.323 ± 0.001
Pitching Moment of Inertia (kgm^2)	$2.91\ \text{x}10^{-3}$
Roll Moment of Inertia (kgm^2)	$0.30\ \text{x}10^{-3}$

An important aspect of static free-flight tests is that the centre of gravity (CoG) is in the same position as the centre of pressure (CoP) of the model. Prior to experiments, the COP was calculated using a panel method code with tangent cone pressure predictions to be 70.7 mm (from the base) at zero degrees angle of attack with a variation of $\pm$ 1 mm for the angles of attack of interest. To demonstrate the influence of static margin position and pitch rate, Figure 6.4 shows an analytical prediction of the rate the finned model would pitch from 6 $^\circ$ angle of attack with various static margins (difference between CoP and CoG) using the inertial properties in Table 6.2, the freestream conditions in Table 6.1 and aerodynamic coefficients from a panel method code. It is presented over 50 ms as this represents the test time of the HDT. It can be seen that a mismatch in CoG location to CoP of 1 mm can cause the model to pitch by over a degree in the test time. Therefore a lot of care must be token when ballasting the model and the CoG position must be changed between experiments if the angle of attack is changed if static free-flight is to be achieved with small changes of angle of attack over the test time (less than $\pm$ 0.5 $^\circ$).

The model was designed to feature ballasting which could place the CoG in this predicted location and the ability to adjust for experimental corrections. To achieve this, tungsten ballast could be placed at both the front and rear of the cone internal section and was adjustable using threaded rods and nuts. The ballasting tungsten can be seen in Figure 6.3 shaded black. The centre of gravity was measured using a moment balance, whereby the model was

suspended using two strings. The tension in the upstream string was measured using a load cell. This setup allowed the CoG to be determined to +/- 0.1 mm. The inertial properties of the model are shown in Table 6.2.

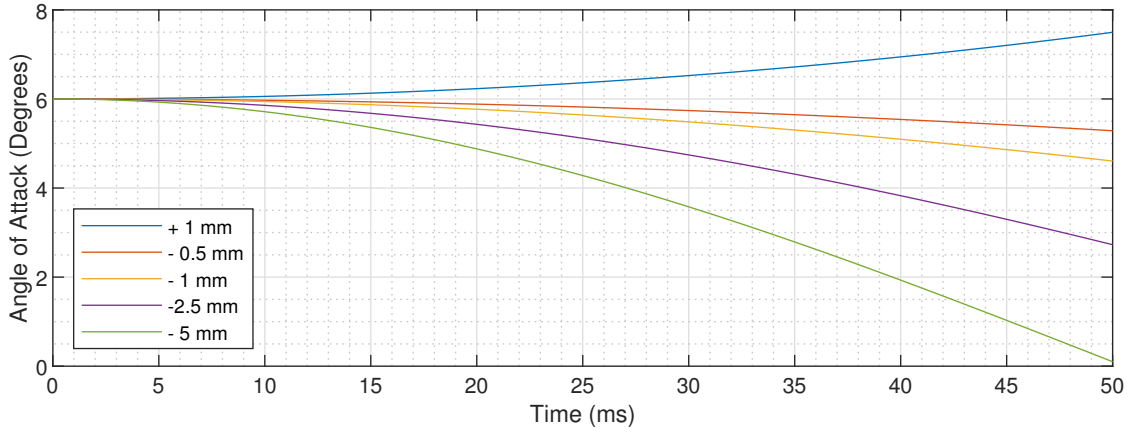

Fig. 6.4 The influence of static margin on pitch as predicted by an analytical model for the finned cone model

6.3.4 On-Board Data Acquisitions

The on-board inertial measurement board were designed and built by UNSW Canberra [42]. The board consisted of an integrated 3-axis accelerometer and 3-axis gyroscope, non-volatile memory, a Bluetooth radio module and a microcontroller, all integrated on a single printed circuit board of dimensions 114 mm x 12 mm. The IMU was a single chip containing both the accelerometer and gyroscope. The accelerometer had a full scale range of +/- 16 g and a data output rate of 4 kHz whilst the full scale range of the gyroscope was +/-2000 deg/s with a data output rate of 8 kHz. The board could be armed prior to testing to be triggered by the detection of sustained free-fall of the model release. A sampling rate of 8 kHz was used for this work which allowed for 320 samples to be obtained over the 40 ms of test time in free-flight. Non-linearity of the accelerometer and gyroscope axis is reported to be 0.1% and 0.5% respectively.

6.3.5 Optical Setup

The optical setup was designed to allow for longitudinal imaging of the model during free-flight at high frame rates to measure the model's linear and angular displacements. The camera was a monochrome Phantom TMX 7510 which allows imaging of uncropped frame rates of up to 76,000 fps at a resolution of 1 Mpx. The lens mounted to the camera was a

Tamron 24-70mm f2.8 lens set to a focal length of 50 mm and aperture of f2.8. The camera was positioned to face perpendicular to the longitudinal plane of motion so that the full test section was visible during a test. The camera was aligned with the test section using two plumblines suspended from known points on the test section. To allow for the images to be sufficiently exposed at 76,00 fps, six Luminus PT-120-B-L11-EPG LEDs were used to illuminate the test section, providing uniform lighting over the entire test area.

6.4 Data Processing

Forces and moments are presented in aerodynamic coefficient form, defined by the force or moment non-dimensionalised by the freestream dynamic pressure (Table 6.1) and a reference area (Table 6.2), plus an additional reference length (the length of the model) for moment coefficients. In free-flight, these equations can be written as follows:

$$C_L = \frac{m\ddot{z}}{\bar{q}S}, \quad C_D = \frac{m\ddot{x}}{\bar{q}S}, \quad C_M = \frac{I_{yy}\ddot{\theta}}{\bar{q}Sc} \tag{6.5}$$

For these experiments, forces are derived using two independent methods. One method is image tracking and the second is through on-board accelerometers and gyroscopes. The data reduction is discussed in more detail for both methodologies in this section.

6.4.1 Inertial Measurement Unit

Accelerometers and gyroscopes provide direct information on the accelerations and angular rates acting on a body. The complexity in the processing of the measured data lies in transforming frames of reference from the body's reference to the Global frame of reference. The Body frame of reference is defined relative to the model as +x towards the nose of the vehicle, +z towards the bottom of the vehicle with +y completing the orthogonal system. This is the frame of reference in which the IMU board is moving within. The Global or Earth frame of reference is defined as having the +z axis towards the ground, +x axis pointing upstream towards the facility nozzle and the +y axis orthogonal to both to form a right-hand coordinate system. This frame of reference is what all global force coefficients are defined relative to.

As the Body frame of reference in free-flight is constantly changing with respect to the Global frame of reference, transformations are required to turn the measured body accelerations into global accelerations and hence forces. To transform the data, first the body angular rates are transformed to Euler angular rates using Eq. 6.6, allowing the Euler angles to be determined via numerical integration of Euler-rates. Knowledge of the Euler angles

allows for the linear accelerations as measured by the IMU to be transformed to the Global frame of reference according to Eq. 6.7. Finally the aerodynamic coefficients can be obtained using Eq. 6.5.

The rotation matrix for the angular rates and accelerations (subscript E for Earth coordinates and B for body coordinates) are as follows (where c, s and t are cosine, sine and tangent functions respectively, p, q and r are body roll, pitch and yaw rates respectively and ϕ, θ and ψ are Euler angles):

$$\begin{bmatrix} \dot{\phi} \\ \dot{\theta} \\ \dot{\psi} \end{bmatrix} = \begin{bmatrix} 1 & s(\phi)t(\theta) & c(\phi)t(\theta) \\ 0 & c(\phi) & -s(\phi) \\ 0 & \dfrac{s(\phi)}{c(\theta)} & \dfrac{c(\phi)}{c(\theta)} \end{bmatrix} \begin{bmatrix} p \\ q \\ r \end{bmatrix} \tag{6.6}$$

$$\begin{bmatrix} \ddot{X} \\ \ddot{Y} \\ \ddot{Z} \end{bmatrix}_E = \begin{bmatrix} c(\psi)c(\theta) & c(\psi)s(\phi)s(\theta) - c(\phi)s(\psi) & s(\phi)s(\psi) + c(\phi)c(\psi)s(\theta) \\ c(\theta)s(\psi) & c(\phi)c(\psi) + s(\phi)s(\psi)s(\theta) & c(\phi)s(\psi)s(\theta) - c(\psi)s(\phi) \\ -s(\theta) & c(\theta)s(\phi) & c(\phi)c(\theta) \end{bmatrix} \begin{bmatrix} \ddot{X} \\ \ddot{Y} \\ \ddot{Z} \end{bmatrix}_B \tag{6.7}$$

Figure 6.5 shows a typical trace of the measured filtered linear accelerations for a test with the finned cone at -4 ° angle of attack. As seen in the figure, the model free-falls for approximately 130 ms before the onset of flow. During this time the model falls into the centre of the core flow of the tunnel. The tunnel takes 35 ms to start up before the steady plateau in freestream conditions are reached. It is during this steady plateau that the test time is taken. The filtered accelerations in the direction of lift and drag mimic the plateau in free stream stagnation pressure. The accelerations stay constant during the steady test time due to the minimal pitching exhibited by the model during a test. It can be seen, however, that there is a non negligible out of plane acceleration suggesting the model was initially slightly yawed with respect to the facility centre-line. With the current experimental setup and optical access, it is not easy to precisely align the model in yaw with the flow freestream. This acceleration will cause the measured drag coefficient to be slightly increased.

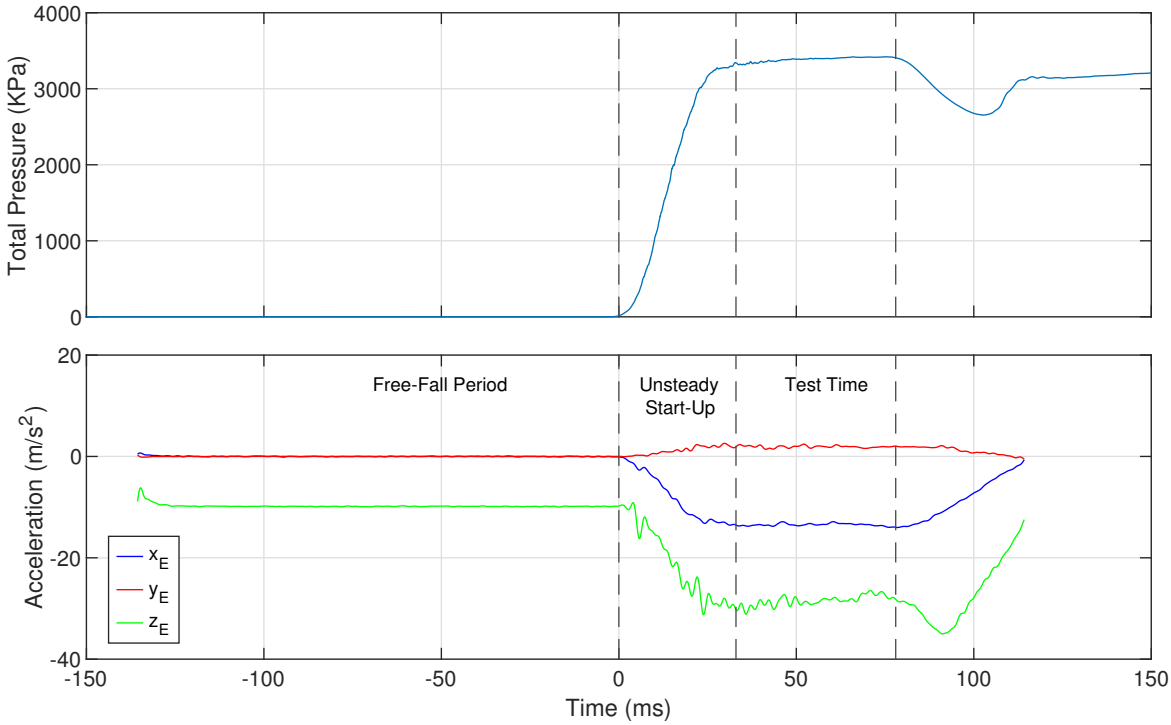

Fig. 6.5 Linear accelerations as measured by the IMU with freestream total pressure. The finned cone is at - 4 ° angle of attack for this test.

6.4.2 Optical Tracking

The second methodology used to obtain force coefficients in free flight is through optical tracking. Rather than directly measuring accelerations, optical tracking measures the model's displacement and angle of attack history and therefore requires double differentiation of the displacement data to obtain accelerations. It is highly desirable that the tracking data is as smooth and noise free as the differentiation process amplifies any noise in the data.

The algorithm used in this work is the same as used in Hyslop et al. [34]. It works by detecting the centre point of two circles of known position on the model. From these two centre points, the centre of gravity can be determined as the location is measured before an experiment. Detecting the centre of gravity for each frame gives a displacement history of the model in free-flight. For longitudinal tracking of the finned cone in free-flight (about pitch axis), four accurately located black circles are painted on the side of the model. Only two circles are required by the algorithm; the additional two circles are added for redundancy in the case of damage or non-uniform lighting. The methodology for image tracking is briefly summarised as follows:

1. Apply Gaussian filter to image and subtract from original (High pass filter).

2. Apply Canny filter to image so that only pixels detected as an edge are shown [9].
3. Apply Hough transform to find circles in the image after narrowing the search radius [30].
4. Detect pixels in the proximity of the circle located by the Hough transform.
5. Use sub-pixel detection on the original image using the methodology set out in von Gioi and Randall [99] at the location where pixels were detected by the Hough transform.
6. Fit a circle to the pixels using linear regression as set out in Laurence et al. [45] and use this equation to find the centre point of the circle.

After detecting the location of the two circles, a line is fitted between them for which the position of centre of gravity lies on. The distance of the centre of gravity is known relative to the circles and this process is repeated for each frame giving a time history of centre of gravity displacement. The physical distance between the two circles is also used as a reference to scale the image from pixels to metres. For the setup in this work, the scaling factor was 0.68 mm/pixel. Shown in Figure 6.6 is the image tracking algorithm overlaid on an example finned cone free-flight test. The red line indicates the location of the centre of gravity during the test time as detected and can be seen to remain in the core flow for the duration of the test time. Prior to testing, the spatial uniformity of the lens was measured and corrected for through the use of a uniform grid inserted into the tunnel using the Matlab camera calibrator algorithm.

To determine the aerodynamics coefficients, the displacement data is differentiated twice to give the accelerations and hence aerodynamic coefficients using Eq. 6.5. The intermediate velocity was numerically smoothed using a Gaussian filter before being differentiated into accelerations.

Angle of attack was determined using the edge of the cone and finding the relative angle to the horizontal. The edge is detected through the use of a Canny filter followed by sub-pixel detection to find the true edge. The model edge is the preferred method of detecting angle of attack (over the circles) as it is unaffected by model roll for axisymmetric geometries. Painting the model white gave strong contrast between the black background and the edge of the model.

The accuracy of the image tracking algorithm was calculated to be $\pm$ 4 μm in Hyslop et al. [34] which is small considering the pixel resolution was 0.68 mm/pixel. The analysis, however, did not take into account errors which result from misalignment of the optical equipment but gives an approximation of the uncertainty associated with the numerical algorithm.

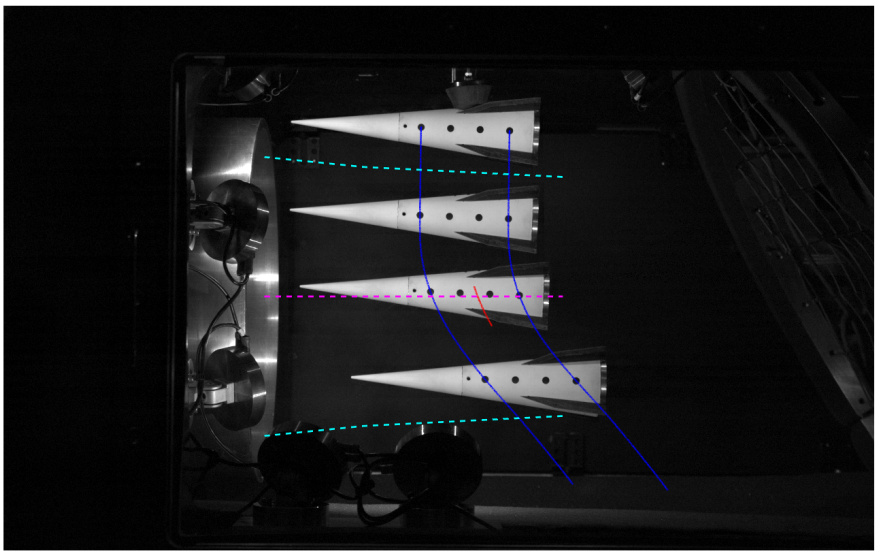

Fig. 6.6 Montage photo of image processing (Blue - detected circle centre points, Red - calculated centre of gravity, shown for test time, cyan - core flow location as acquired by a pitot survey, pink - nozzle centreline).

6.4.3 Freestream Alignment

The alignment between the tunnel freestream and model for sting mounted model is often corrected through the use of four radial pressure transducers which show that the model is aligned when all read the same value. In the current free-flight setup, there are no pressure transducers so the angle relative to the freestream is unknown. To resolve this issue, an alignment probe (four radial pressure transducers, north, east, south and west) was sting mounted to a two axis traverse and experiments were conducted to find the true zero angle of attack. This is at the point where the north and south pressure transducer read the same static pressure value. The optical cameras were used to calculate the angle of attack from their reference point and this offset was subsequently applied to all of the experimental data. The offset in angle of attack at Mach 7 was found to be +0.4 $\pm$ 0.05 $^\circ$ for this test campaign and was used as the 0 $^\circ$ reference for all experiments. The camera set up remained fixed between free-flight tests and alignment test. In an ideal setup with sufficient optical access, this process would also be conducted on the yaw plane too to guarantee full alignment with the freestream.

6.4.4 Comparison of IMU and Image Tracking

Figure 6.7 compares the image tracking and IMU results for the model kinematics for a single free-flight test at -4 ° angle of attack. The image tracking measures displacements directly so the accelerations are determined from differentiation and the IMU measures accelerations directly so the displacements are determined through integration. For the plots shown in Figure 6.7, the agreement between the two independent methodologies is excellent, demonstrating the either method can reliably be used to accurately measure static aerodynamic coefficients in free-flight experiments.

For both the horizontal and vertical acceleration, the agreement between the two independent methods is good. Importantly, the vertical acceleration during free-fall agree and measures at the value of gravitational acceleration in a vacuum. The IMU shows small vibrations superimposed on the signals which is the result of internal vibrations passing through the internal mounting structure that supports the IMU during the free-flight test. The agreement between the velocity and displacement data on both axes is also very good for the entire duration of the experiment. The trace for angle of attack appears to have less agreement between the data sets but the discrepancy between the two measurements remains within $\pm$ 0.1 ° during the experiment which is considered acceptable. This difference is expected to be a consequence of only optically tracking the model in 3 degrees of freedom - for this model small changes in yaw affect the detected pitch angle. It can also be seen in the 130 ms free-fall period, the model only pitches 0.15 °.

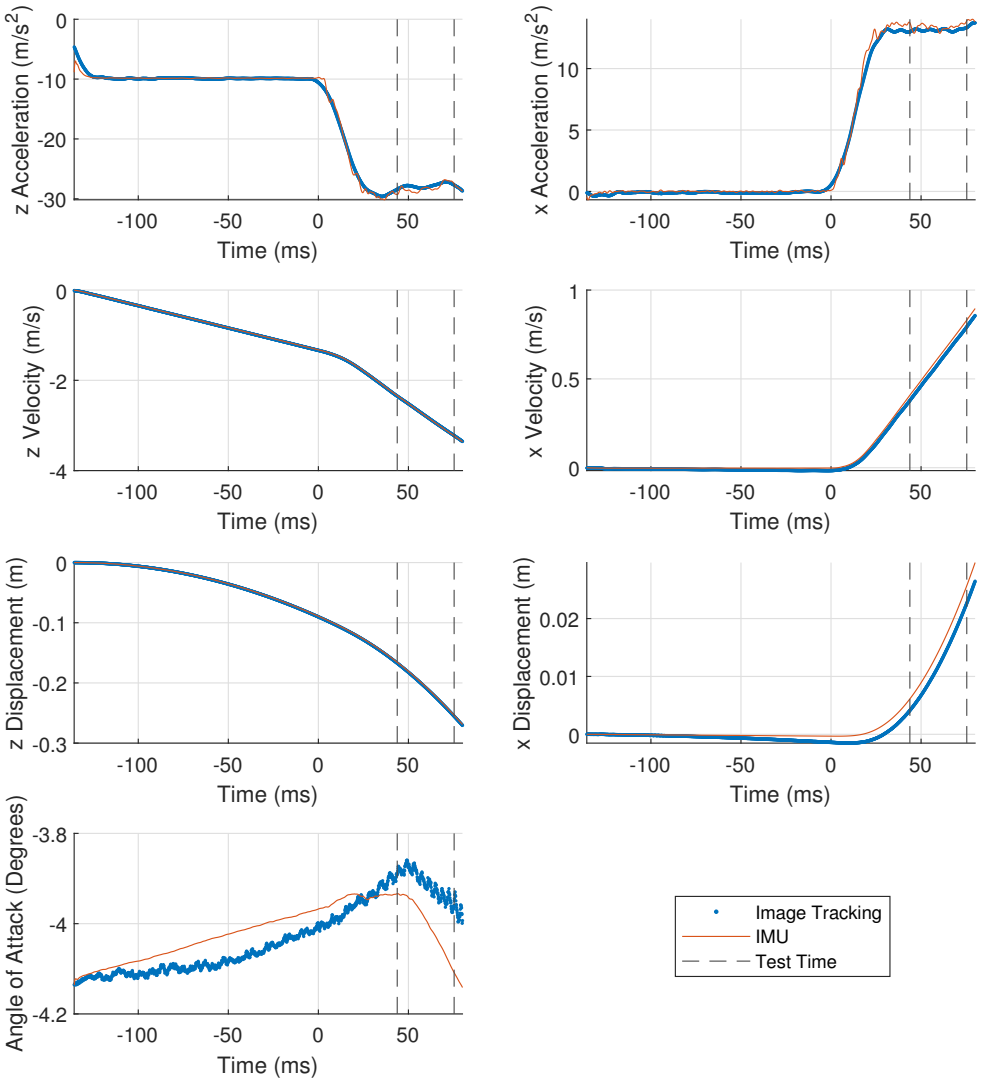

Fig. 6.7 Comparison of longitudinal motion as measured by image tracking and IMU data. Time = 0 is the point of flow initiation.

6.5 Experimental Results

This section presents the results from the free-flight experiments with the finned cone. In total 14 experiments were conducted ranging between -6 ° and 6 ° angle of attack so the half-angle of the cone was never exceeded. Lift, drag and pitching moment data are shown, as well as centre of pressure variation at the Mach 7 conditions. The experimental results are

shown for both the IMU data and optical tracking and presented against viscous tangent cone predictions from a numerical panel method simulations [34]. Uncertainties are shown as error bands around the data points as calculated using the Moffat's error propagation method [66] for freestream parameters, model properties, IMU and image tracking.

To produce numerical predictions of the finned cone in free-flight, tangent-cone numerical prediction was used for the body of the cone and shock-expansion calculations used to calculate the pressure distribution over the fins. For the subsequent plots, both the predictions for a cone with no fins and fins are presented.

6.5.1 Aerodynamic Coefficients

Figure 6.8 presents the measured variation in lift coefficient with angle-of-attack and a comparison with viscous tangent-cone calculations. It can be seen that the trend is generally linear and as expected, more lift is generated than for the cone without fins. The numerical prediction slightly over predicts the aerodynamic coefficients at the extremities but the general trend is in good agreement. The lift coefficient is zero at 0 $^\circ$ angle of attack which is expected for a body with symmetry about the yaw plane.

Drag coefficient variation with angle of attack is shown in Figure 6.9. The experimental data agrees well with the viscous numerical prediction and exhibits the expected parabolic shape. The fins increase the drag compared to the model with no fins as the frontal area of the cone is increased. It can be seen in the figure that at high angles of attack that the agreement between the drag coefficient for the IMU and image tracking gets worse (although remaining within experimental uncertainty). At high angles of attack, the cone was more likely to exhibit a small amount of roll. This resulted in measurement artefacts where the small angular roll would superimpose onto the translational motion measured by the image tracking algorithm, influencing the measured displacements and hence forces. As measured by the IMU for the high angle of attack tests, the model was exhibiting a slight clockwise roll at positive angles of attack. This influence could be removed by tracking the boundary of the model rather than using dots.

Figure 6.10 shows the variation of the lift-to-drag ratio with angle of attack. The overall agreement with the numerical prediction is good. The graph shows that the lift-to-drag ratio for a cone without fins is the same as for the cone with fins. This shows that adding extra control with fins does not sacrifice this parameter.

Figure 6.11 shows the variation of pitching moment against angle of attack as referenced from the nose of the cone. From this location, the gradient is negative showing that the vehicle is statically stable with the centre of gravity at this location, as expected. Furthermore, the trim angle of attack is 0 $^\circ$ which again is expected for this geometry. Figure 6.12 shows

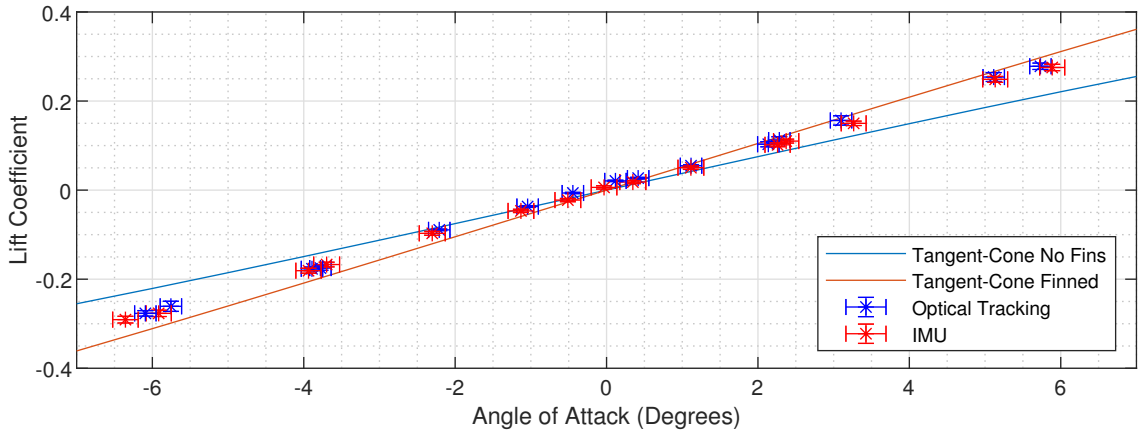

Fig. 6.8 Lift coefficient at Mach 7 condition. Individual tests plotted against tangent-cone numerical prediction

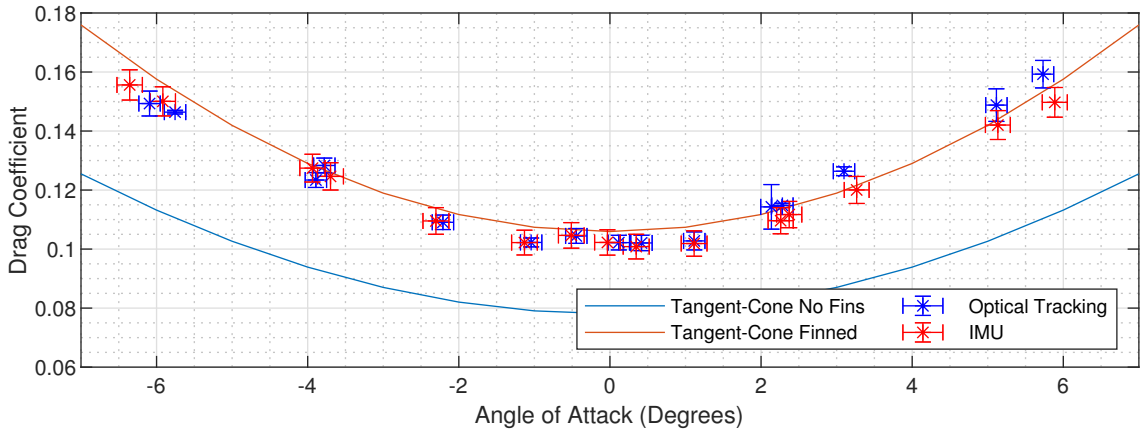

Fig. 6.9 Drag coefficient at Mach 7 condition. Individual tests plotted against tangent-cone numerical prediction

the variation of centre of pressure with angle of attack. Unlike for a cone with no fins, the numerical simulation predicts the centre of pressure to move with angle of attack by $\pm$ 0.7 mm within the tested range of angles of attack. If the CoG was kept in a constant position for all angles of attack, the change in static margin due to the shift in CoP can cause the vehicle to pitch more during a test making the static free-flight methodology more difficult to achieve. As a result, more shots are required when changing angle of attack to adjust the ballast of the model to be in the correct location so that the pitch remains at less than half a degree in the test time. The scatter of measured centre of pressure in the figure is due to the difficulty of resolving this measurement at small angles of attack, particularly as the angle approaches zero.

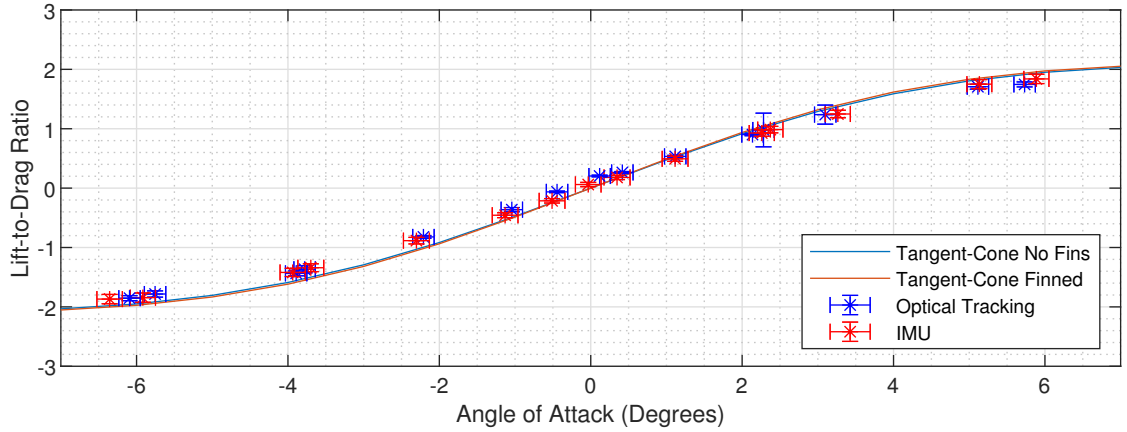

Fig. 6.10 Lift-to-drag ratio at Mach 7 condition. Individual tests plotted against tangent-cone numerical prediction

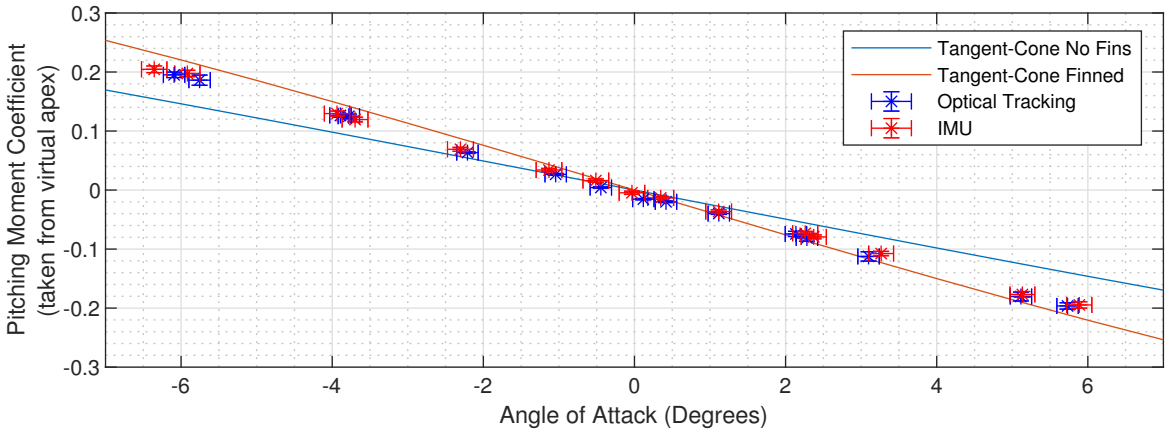

Fig. 6.11 Pitching moment coefficient at Mach 7 condition. Individual tests plotted against tangent-cone numerical prediction

6.5.2 Roll Moment Coefficient

A final set of experiments were conducted to examine the rolling moment coefficient of the model. The free-flight model was designed to allow for fins that had deflections of up to 3 °. Angling the fins in the same direction will produce a rolling moment upon flow initiation, causing the cone to spin. The equation of for roll moment coefficient is:

$$C_l = \frac{I_{xx}\ddot{\phi}}{\bar{q}Sc} \tag{6.8}$$

Figure 6.13 shows an example roll test where all the fins were angled at 3 °. Image tracking is not used for these tests as the model did not feature appropriate markings required to track roll. It can be seen that for the first two cone frames on the composite image that the

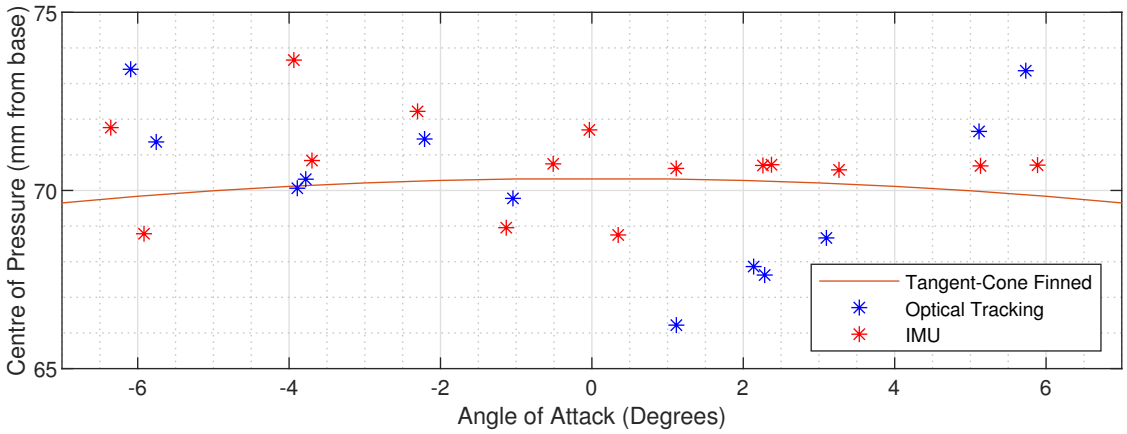

Fig. 6.12 Centre of Pressure Location (from cone base) at Mach 7 condition. Individual tests plotted against tangent-cone numerical prediction

tunnel is yet to have fired so the cone remains at 0 ° roll. After reaching the centreline of the core flow, the facility has fired and the cone begins to roll. By the end of the test time, the angular velocity has reached 2000 °/s, saturating the gyroscopes of the IMU.

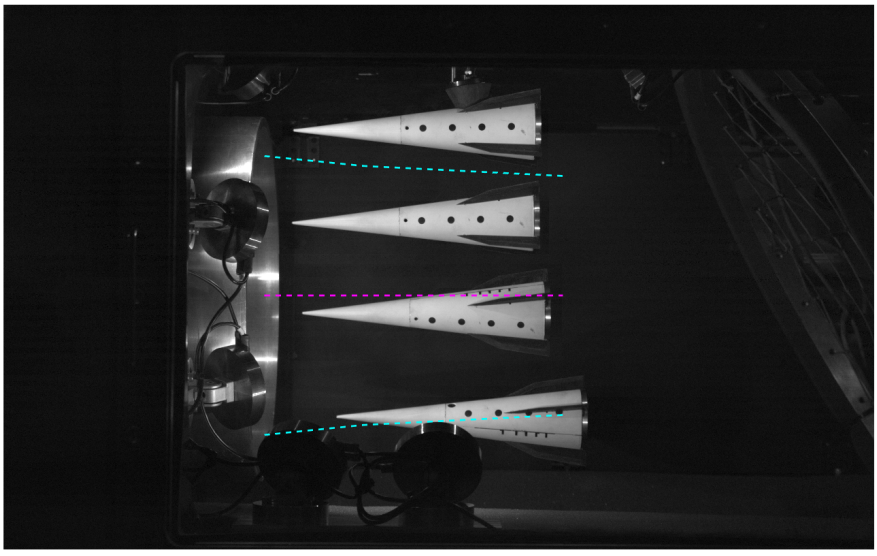

Fig. 6.13 Composite image of rolling finned cone (cyan - core flow location as acquired by a pitot survey, pink - nozzle centreline).

In total, 5 spin test were conducted in free-flight at zero degrees angle of attack. One with no fin deflections, 2 fins at ± 3 ° and 4 fins at ± 3 °. Figure 6.14 shows the measured transient roll coefficient for all 5 experiments with the test time overlaid. The signals contain some noise as the roll angular velocity is differentiated to obtain the acceleration to calculate the

roll coefficient. For the cases where four fins are deflected, the gyroscope saturates just after the end of the test time as seen in the figure. The results show good symmetry between the cases where the roll direction is opposite and in each test steady state is achieved within the available test flow duration. The maximum uncertainty was calculated to be $\pm$ 0.0452 using error propagation. As a percentage, this is a larger uncertainty than the force coefficients due to the requirement of differentiating the angular velocity measured by the IMU. These results show that it is possible to reliably measure roll coefficient in free-flight.

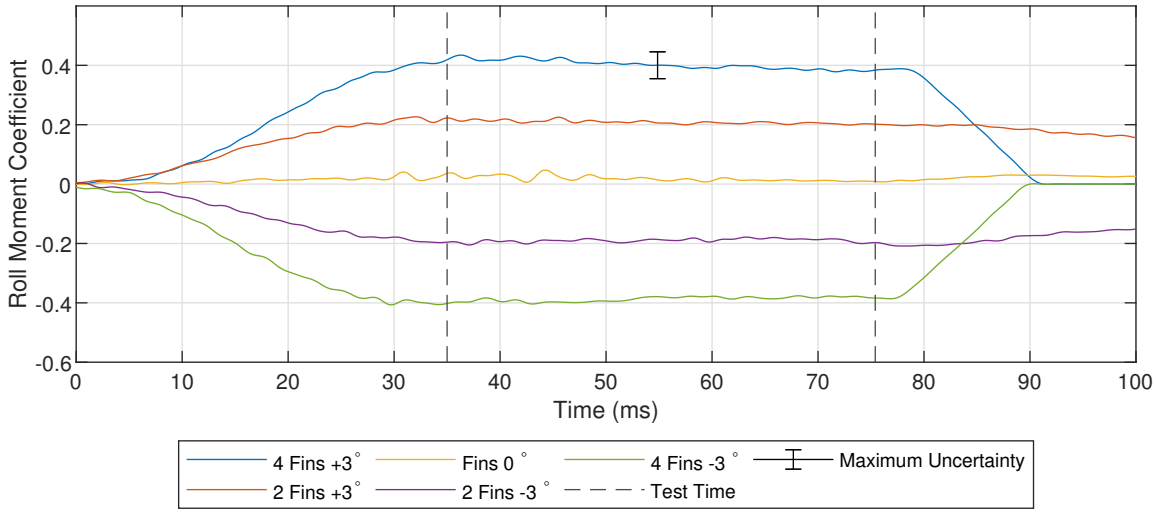

Fig. 6.14 Roll Coefficient at Mach 7 condition for various fin deflections

6.6 Conclusions

The static longitudinal and roll aerodynamic coefficients for a finned cone have been measured using the free-flight technique in the University of Oxford HDT. The finned cone adds the complexity of a varying centre of pressure position with angle of attack making it more challenging to achieve the quasi-static free-flight condition as the centre of gravity needs to be adjusted when a new angle of attack is tested. Nevertheless, high quality aerodynamic data were obtained Lift and drag coefficient exhibited the expected shapes with respect to angle of attack and agree well with the numerical predictions. However, care must be taken with image tracking if there is slight roll in an experiment, particularly for drag coefficient. Furthermore, the two independent methods of measuring accelerations, image tracking and an on-board IMU, show very good agreement in the experimental data, adding redundancy to the overall free-flight methodology. It has also been shown for the first time that the free-flight technique can be used to obtain high quality roll moment coefficient data. Overall,

the static free-flight technique has been validated for a complex body with non-constant centre of pressure with angle of attack which gives a high degree of confidence for obtaining static aerodynamic coefficients for any hypersonic vehicle geometry.

Chapter 7

Conclusion and Recommendations for Future Work

7.1 Conclusions

The overarching aim of this thesis was to develop and commission high quality force and moment measurement techniques to measure static aerodynamic coefficients in short duration hypersonic facilities with very low uncertainties at flight representative conditions. By identifying the static and dynamic derivatives that form the total aerodynamic coefficient, the dynamic derivatives could be eliminated within a free-flight test by limiting the pitching motion. This allowed only static derivatives to be measured similar to the commonly used force balance technique.

Chapter 4 presented the development and commissioning of the static free-flight technique and applied it to a 7 degree half-angle cone at a Mach 7 condition. By reducing the model's static margin and ability to pitch, constant forces were measured in the test-time, free from dynamic influence or sting effects. The use of a model with minimal static margin was shown to be effective at determining static aerodynamic coefficients with very low uncertainties (less than 3 %) that were validated against numerical panel-method simulations. Results are also presented within this chapter where the model is allowed to pitch (allowing for dynamic influence) and compared to the static results. The static method of measuring forces when compared to dynamic pitching tests gave less oscillations in the measured force data and therefore a more accurate measurement of the coefficient. Furthermore, divergence can be seen in the measured drag coefficient when the model is allowed to pitch resulting changes from the static values, hence justifying the use of the static free-flight methodology to obtain static coefficients. Overall this chapter achieved the thesis aim of developing and

commissioning high quality force and moment measurement technique within short duration hypersonic facilities that are representative of flight conditions.

Following from this work, experiments were conducted investigating a direct comparison between static free-flight and a sting-based force balance in Chapter 5. It was found that the free-flight technique had uncertainties half as much in magnitude than the force balance (stress-wave deconvolution) in the University of Oxford High Density Tunnel representing a large improvement in performance of the measurement technique. As the force balance requires careful design of the string-model supporting structure to reduce the impact of internal vibrations from external aerodynamic forces imposing on the strain gauges, it is more susceptible to fluctuations about the mean data point than for the unconstrained free-flight methodologies which is ultimately reflected in the higher uncertainties for force balance data (both calibrations).

Finally, the static free-flight technique was applied to a complex geometry which had a variation in position of centre of pressure with angle of attack. The results validated the technique and show that it can be applied to any configuration of hypersonic vehicle and successfully obtain aerodynamic coefficients. Expansion of the image tracking algorithm will be required for slim and slender geometries as the tracking of circles will be less appropriate. Overall, this thesis has shown the benefits of using the free-flight force measurement technique to obtain high quality aerodynamic coefficients with low uncertainties when compared to established techniques.

To summarise, this thesis has:

- Designed and commissioned the infrastructure for force measurement techniques required in the University of Oxford High Density Tunnel - free-flight and force balance (both static and dynamic calibration).
- Adapted the free-flight technique to measure only static aerodynamic coefficients and validated the methodology with a 7 degree half-angle cone at flight representative conditions.
- Shown that with the existing HDT infrastructure, the free-flight technique results in uncertainties half that of the force balance methodologies.
- Validated the static free-flight technique for a complex geometry - one in which the centre of pressure location is not constant with angle of attack.

7.2 Recommendations For Future Work

From the research conducted within this thesis, further research can be conducted to further improve force measurement techniques using the free-flight methodology. Future studies may include:

Free-Flight Model Capabilities

- Free-flight models instrumented with on-board pressure transducers. Having a model instrumented with four pressure transducers at cardinal locations allows for the vehicle orientation (pitch and yaw) to be known when flow is on. This will make on-board force measurement using the onboard DAQ truly isolated from image tracking (as it provides the initial reference) so both of the force measurement techniques in free-flight are independent. Furthermore, a gauge which measures pitot pressure during a test would help to fully define the freestream conditions during a test- in particular Mach number.
- Recording of accelerometer data prior to model release (pre-trigger). Information on the accelerometer readings before a model is released can be used to determine angle of attack, again making the IMU independent of image tracking.
- Ability to adjust location of IMU on DAQ. In an ideal setup, the IMU would be located at the location of the centre of gravity of the model. This is particularly important for the calculation of pitching moment where transformations are required if its not at this location (more important for dynamic tests). The ability to easily adjust the IMU as a satellite board would make this much easier to achieve.

Optical Improvements

- Top optical axis to HDT test section. This would allow cameras to visualise a free-flight model directly on the yaw axis, guaranteeing alignment with the freestream in yaw. This particularly benefits the drag measurement.
- Implementation of background orientated schlieren (BOS). There is potential for BOS to be included with the current infrastructure to obtain information on the shock structure of free-flying models. Traditional schlieren clashes with the current image tracking setup but BOS could be used with the same camera as the image tracking.
- The current work found the tracking of dots susceptible to model roll, in particular influencing the measurement of drag at high angles of attack. Using edge detection on

the outline of the model can allow for up to 6 degrees of freedom tracking of models in free-flight.

- Pressure sensitive paint - the use of pressure sensitive paint would be a further non-intrusive method of gaining more information from a free-flight test. With enough optical coverage of the model, it would be possible to predict the aerodynamic coefficients through the integrated pressure field.
- Infrared cameras - a further non-intrusive technique that has potential to be used in conjunction with free-flight models. Useful for studies on transition or effects of bluntness and heating on leading edges.

Scientific Studies

- Determining dynamic coefficients with a dynamically scaled model (scaling of mass and inertia). The recently developed Extended Ludwieg Mode offers up to 100 - 600 ms of test time which is sufficient to measure the dynamic damping derivatives.
- Experimentally determine the point at which the pitch rate causes large dynamic effects that influence the measured static coefficients.
- Free-flight of a complex geometry that is not a body of revolution. This is the final step in complexity for a static free-flight model.
- Base pressure studies - base pressure is known to influence a model that is sting mounted. An investigation with pressure sensors comparing free-flight to sting-mounted tests can give more information on this. The information would also be useful to inform numerical predications where base pressure is often difficult to predict.
- Shock impingement studies - the free-flight technique would allow for dynamic information on shock impingement to be obtained. This is particularly applicable in areas such as store separation.
- Vehicle manoeuvre studies - Control surface deflections would allow for manoeuvres to be investigated in free-flight. Provided the dynamic scaling is successfully achieved, it would give flight representative data on time periods of manoeuvres and their effectiveness.

References

[1] Acton, J. M. (2015). Hypersonic boost-glide weapons. *Science & Global Security*, 23(3):191–219.

[2] Anderson Jr, J. D. (2006). *Hypersonic and high-temperature gas dynamics*. American Institute of Aeronautics and Astronautics.

[3] Bailey, A. B. and Hiatt, J. (1971). Free-flight measurements of sphere drag at subsonic, transonic, supersonic, and hypersonic speeds for continuum, transition, and near-free-molecular flow conditions. Technical report.

[4] Baris, E., Britcher, C. P., and Altamirano, G. (2019). Wind tunnel testing of static and dynamic aerodynamic characteristics of a quadcopter. In *AIAA Aviation 2019 Forum*, page 2973.

[5] Barthelemy, R. (1989). The National Aero-Space Plane Program. In *Maintainablity of Aerospace Systems Symposium*, page 5053.

[6] Bernstein, L. and Pankhurst, R. C. (1975). Force measurements in short-duration hypersonic facilities. Technical report.

[7] Bowcutt, K. (2003). A perspective on the future of aerospace vehicle design. In *12th AIAA International Space Planes and Hypersonic Systems and Technologies*, page 6957.

[8] Calloway, R. L. (1981). Force and moment, flow-visualization, and boundary-layer tests on a shuttle orbiter model at Mach 6. Technical report.

[9] Canny, J. (1986). A Computational Approach to Edge Detection. *IEEE Transactions on Pattern Analysis and machine Intelligence*, PAMI-8(6):679–698.

[10] Chambers, J. (2015). *Modeling Flight NASA Latest Version: The Role of Dynamically Scaled Free Flight Models in Support of NASA Aerospace Programs.*, volume 3.

[11] Coleman, H. W. and Steele, W. G. (2018). *Experimentation, Validation, and Uncertainty Analysis for Engineers*. John Wiley & Sons.

[12] Cruz, C. I. and Sova, G. J. (1990). Improved tangent-cone method for the Aerodynamic Preliminary Analysis System (APAS) version of the hypersonic arbitrary-body program. Technical report.

[13] Di Benedetto, S., Di Donato, M. P., Rispoli, A., Cardone, S., Riehmer, J., Steelant, J., and Vecchione, L. (2017). HEXAFLY-INT Project: Design of a High Speed Flight Experiment. *Proceedings of ISHF*.

[14] Doherty, L. J. (2014). An experimental investigation of an airframe integrated three-dimensional scramjet engine at a Mach 10 flight condition.

[15] Doherty, L. J., Donaldson, N., and Owen, A. (2021). The Oxford Magnetic Suspension and Balance System: a Brief History & Development Status. In *AIAA Scitech 2021 Forum*, page 1870.

[16] Doherty, L. J., Smart, M. K., and Mee, D. (2015). Measurement of three-components of force on an airframe integrated scramjet at Mach 10. In *20th AIAA International Space Planes and Hypersonic Systems and Technologies Conference*, page 3523.

[17] Donaldson, N. L. and Ireland, P. (2017). A Panel Method Aerodynamic Preprocessor for Planetary Entry Trajectory Simulations. In *21st AIAA International Space Planes and Hypersonics Technologies Conference*, page 2379.

[18] Eckert, E. R. G. (1956). Engineering relations for heat transfer and friction in high-velocity laminar and turbulent boundary-layer flow over surfaces with constant pressure and temperature. *Transactions of the ASME*, 78(6):1273–1283.

[19] Eussel, W. R. (1980). *Aerodynamic Design Data Book, Volume-I, Orbiter Vehicle SIS-1*. National Technical Information Service.

[20] Ewald, B. F. R. (2000). Multi-component force balances for conventional and cryogenic wind tunnels. *Measurement Science and Technology*, 11(6):R81.

[21] Fisher, T. B., Quinn, M. K., and Smith, K. L. (2018). Free-flight testing of hypersonic edney shock interactions. *2018 Aerodynamic Measurement Technology and Ground Testing Conference*, (November).

[22] Friedl, D., Schramm, J. M., and Hannemann, K. (2015). Measurements By Means of Optical Tracking. *Proceedings of the 8th European Symposium on Aerothermodynamics for Space Vehicles*, (1).

[23] GEIGER, R. E. (1962). Experimental Lift and Drag of a Series of Glide Configurations at Mach Numbers 12.6 and 17.5. *Journal of the Aerospace Sciences*, 29(4):410–419.

[24] Grossir, G., Puorto, D., Ilich, Z., Paris, S., Chazot, O., Rumeau, S., Spel, M., and Annaloro, J. (2020). Aerodynamic characterization of space debris in the VKI Longshot hypersonic tunnel using a free-flight measurement technique. *Experiments in Fluids*, 61(7).

[25] Hannemann, K., Martinez Schramm, J., Laurence, S., and Karl, S. (2015). Shock tunnel free flight force measurements using a complex model configuration. In *Aerothermodynamics Conference ATD8, ATD8-89812, March 2015, Lisbon, Portugal*.

[26] Hermann, T., Mcgilvray, M., Hambidge, C., Doherty, L., and Buttsworth, D. (2019). Total Temperature Measurements in the Oxford High Density Tunnel. In *FAR Conference*.

[27] Hideyuki, T., Masatoshi, K., Tomoyuki, K., Kazuo, S., Katsuhiro, I., and Masahiro, T. (2009). Experimental and numerical studies to evaluate real-gas effects on generic models in the free-piston shock tunnel hiest. *European Space Agency, (Special Publication) ESA SP*, 659 SP(November 2008):3–6.

[28] Hideyuki, T., Tomoyuki, K., Kazuo, S., and Katsuhiro, I. (2017). Wind tunnel test comparison between JAXA-HIEST and ONERA-S4MA with HYFLEX lifting-body. *Eucass*, 34(4):1–6.

[29] Hillyer, J., Doherty, L., Estruch-samper, D., Barth, J., and Mcgilvray, M. (2022). HiSST : 2nd International Conference on High-Speed Vehicle Science & Technology Thermal Effects of Plume Impingement on a Hypersonic Vehicle. (September):1–13.

[30] Hough, P. V. C. (1962). Method and Means for Recognizing Complex Patterns.

[31] Hunt, J. and Rausch, V. (1998). Airbreathing hypersonic systems focus at NASA Langley Research Center. In *8th AIAA International Space Planes and Hypersonic Systems and Technologies Conference*, page 1641.

[32] Hunter, D. (2019). UK Hypersonic Glide Vehicle Concept and Performance Assessment. *RAeS Weapon Systems & Technology*.

[33] Hyslop, A., Doherty, L. J., McGilvray, M., Neely, A., McQuellin, L. P., Barth, J., and Mullen, G. (2021). Free-Flight Aerodynamic Testing of the Skylon Space Plane. *Journal of Spacecraft and Rockets*, pages 1–11.

[34] Hyslop, A. M., McGilvray, M., and Doherty, L. J. (2022). Free-Flight Aerodynamic Testing of a 7 Degree Half-Angle Cone. In *AIAA SCITECH 2022 Forum*, page 1324.

[35] Jessen, C. and Grönig, H. (1989). A new principle for a short-duration six component balance. *Experiments in fluids*, 8(3-4):231–233.

[36] Jones, T. V., Street, P., and Westby, M. (1992). Recent enhancements to the DRA shock tunnel. *Wind tunnels and wind tunnel test techniques*, page 30.

[37] Joshi, M. V. and Reddy, N. M. (1986). Aerodynamic force measurements over missile configurations in IISc shock tunnel at M= 5.5. *Experiments in Fluids*, 4(6):338–340.

[38] Juhany, K. A. and Darji, A. (2007). Force Measurement in a Ludwieg Tube Tunnel. *Journal of Spacecraft and Rockets*, 44(1):88–93.

[39] Kennell, C., Neely, A. J., Buttsworth, D. R., Choudhury, R., and Tahtali, M. (2016). Free Flight Testing in Hypersonic Flows: HEXAFLY-INT EFTV. In *54th AIAA Aerospace Sciences Meeting*, page 1152.

[40] Kennell, C., Neely, A. J., O'Byrne, S. B., and Buttsworth, D. (2015). Measurement of Vehicle Stability Coefficients in Hypersonic Wind Tunnels. In *20th AIAA International Space Planes and Hypersonic Systems and Technologies Conference*, page 3690.

[41] Kennell, C., Reimann, B., Choudhury, R., Buttsworth, D., and Neely, A. (2017). Subscale hypersonic free flight dynamics of HEXAFLY-INT EFTV+ ESM (multibody separation). In *7th European Conference for Aeronautics and Space Science*.

[42] Kennell C (2018). Study of Hypersonic Aerodynamics Using Free Flight Experiments. Technical report.

[43] Keyes, F. G. (1951). A Summary of Viscosity and Heat-Conduction Data for He, A, H2, O2, CO, CO2, H2O, and air. *Transactions of the ASME*, 73:589–596.

[44] Laitone, E. V. (1997). Wind tunnel tests of wings at Reynolds numbers below 70 000. *Experiments in fluids*, 23(5):405–409.

[45] Laurence, S. J. and Hornung, H. G. (2009). Image-Based Force and Moment Measurement in Hypersonic Facilities. *Experiments in Fluids*, 46(2):343–353.

[46] Laurence, S. J. and Karl, S. (2010). An improved visualization-based force-measurement technique for short-duration hypersonic facilities. *Experiments in Fluids*, 48(6):949–965.

[47] Leiser, D., Löhle, S., Zander, F., Buttsworth, D. R., Choudhury, R., and Fasoulas, S. (2022). Analysis of Reentry and Break-Up Forces from Impulse Facility Experiments and Numerical Rebuilding. *Journal of Spacecraft and Rockets*, pages 1–13.

[48] Lewis, H. O. and East, R. A. (1995). Measurement of free-flight dynamic stability derivatives of cones in a hypersonic gun tunnel. In *International Aerospace Planes and Hypersonics Technologies*.

[49] Liu, S. K. (1992). Numerical Simulation of Hypersonic Aerodynamics and the Computational Needs for the Design of an Aerospace Plane. Technical report.

[50] Longstaff, R. and Bond, A. (2011). The Skylon Project. In *17th AIAA International Space Planes and Hypersonic Systems and Technologies Conference*, page 2244.

[51] Lu, F. K. (2002). *Advanced hypersonic test facilities*, volume 198. AIAA.

[52] Lu, F. K. and Marren, D. E. (2002). Principles of hypersonic test facility development. *Progress in Astronautics and Aeronautics. Volume 198*, pages 17–27.

[53] Marineau, E. C. (2011). Force measurements in hypervelocity flows with an acceleration compensated piezoelectric balance. *Journal of spacecraft and rockets*, 48(4):697–700.

[54] Marineau, E. C., MacLean, M., Mundy, E. P., and Holden, M. S. (2012). Force measurements in hypervelocity flows with an acceleration compensated strain gage balance. *Journal of Spacecraft and Rockets*, 49(3):474–482.

[55] Martin, J. F. and Stevenson, L. M. (1962). *Instrumentation for force and pressure measurements in a hypersonic shock tunnel*. Number 113. Cornell Aeronautical Laboratory, Incorporated.

[56] Martinez, B., Bastide, M., and Wey, P. (2014). Free flight measurement technique in shock tunnel. (June):1–12.

[57] McGilvray, M., Doherty, L. J., Neely, A. J., Pearce, R., and Ireland, P. (2015). The Oxford High Density Tunnel. In *20th AIAA International Space Planes and Hypersonic Systems and Technologies Conference*, page 3548.

[58] McParlin, S., Bruce, R., Hepworth, A., and Rae, A. (2006). Low speed wind tunnel tests on the 1303 UCAV concept. In *24th AIAA Applied Aerodynamics Conference*, page 2985.

[59] McQuellin, L. P., Kennell, C. M., Neely, A. J., Sytsma, M. J., Silvester, T., Choudhury, R., and Buttsworth, D. R. (2020). Investigating endo-atmospheric separation of a hypersonic flyer-sustainer using wind tunnel based free-flight. *23rd AIAA International Space Planes and Hypersonic Systems and Technologies Conference, 2020*, pages 1–24.

[60] Meador, W. E. and Smart, M. K. (2005). Reference enthalpy method developed from solutions of the boundary-layer equations. *AIAA journal*, 43(1):135–139.

[61] Mee, D. J. (2003). Dynamic calibration of force balances for impulse hypersonic facilities. *Shock Waves*, 12(6):443–455.

[62] Mee, D. J., Daniel, W. J. T., and Simmons, J. M. (1996). Three-component force balance for flows of millisecond duration. *AIAA journal*, 34(3):590–595.

[63] Mehta, U. B., Aftosmis, M. J., Bowles, J. V., and Pandya, S. A. (2015). Skylon Aerodynamics and SABRE Plumes. In *20th AIAA International Space Planes and Hypersonic Systems and Technologies Conference*, page 3605.

[64] Mellinger, G. R. (1960). Design and Operation of the X-15 Hypersonic Research Airplane. Technical report, No. AGARD-288, Advisory Group for Aerospace Research and Development.

[65] Milhous, M., Levine, J., and Johannesen, B. (1971). Space shuttle: Basic hypersonic force data for Grumman delta wing orbiter configurations ROS-NB1 and ROS-WB1. Technical report.

[66] Moffat, R. J. (1988). Describing the uncertainties in experimental results. *Experimental thermal and fluid science*, 1(1):3–17.

[67] Mudford, N. R., O'Byrne, S., Neely, A., Buttsworth, D., and Balage, S. (2015). Hypersonic Wind-Tunnel Free-Flying Experiments with Onboard Instrumentation. *Journal of Spacecraft and Rockets*.

[68] Mutzman, R. and Murphy, S. (2011). X-51 Development: A Chief Engineer's Perspective. In *17th AIAA international space planes and hypersonic systems and technologies conference*, volume 13.

[69] Neely, A. J., West, I., Hruschka, R., Park, G., and Mudford, N. R. (2008). Determining aerodynamic coefficients from high speed video of a free-flying model in a shock tunnel.

[70] Newman, D. M. (2011). A technique for measurement of static and dynamic longitudinal aerodynamic derivatives using the DSTO water tunnel. Technical report.

[71] Oceanic, U. S. N., Administration, A., and Force, U. S. A. (1976). *US standard atmosphere, 1976*, volume 76. National Oceanic and Atmospheric Administration.

[72] Ocokoljić, G., Damljanović, D., Rašuo, B., and Isaković, J. (2014). Testing of a standard model in the VTI's large-subsonic wind-tunnel facility to establish users' confidence. *FME Transactions*, 42(3):212–218.

[73] Owen, A. and Owen, K. (2004). Magnetic suspension and balance testing in support of Hyper-X. In *12th AIAA International Space Planes and Hypersonic Systems and Technologies*, page 6958.

[74] Owen, A. K. and Owen, F. K. (2007). Hypersonic free flight measurement techniques. In *2007 22nd International Congress on Instrumentation in Aerospace Simulation Facilities*, pages 1–11. IEEE.

[75] Palermo, M. and Vos, R. (2020). Experimental aerodynamic analysis of a 4.6%-scale flying-v subsonic transport. In *AIAA Scitech 2020 Forum*, page 2228.

[76] Payne, F., Wyatt, G., Bogue, D., and Stoner, R. (2000). High Reynolds number studies of a Boeing 777-200 high lift configuration in the NASA ARC 12-ft pressure tunnel and NASA LaRC National Transonic Facility. In *18th Applied Aerodynamics Conference*, page 4220.

[77] Peebles, C. (2008). *Road to Mach 10: Lessons learned from the X-43A flight research program*. American Institute of Aeronautics and Astronautics, Inc.

[78] Phillips, W. and Cruz, C. (1993). Hypersonic Aerodynamic Characteristics for Langley Test Technique Demonstrator. In *11th Applied Aerodynamics Conference*, page 3443.

[79] Pick, G. S. (1971). Sting Effects in Hypersonic Base Pressure Measurements. Technical report, TR AL-85, Dec. 1971, Naval Ship Research and Development Center , Bethesda, Md.

[80] Pielke Jr, R. A. (1994). Data on and methodology for calculating space shuttle programme costs. *Space Policy*, 10(1):78–80.

[81] Robinson, M. J., Martinez Schramm, J., and Hannemann, K. (2011). Design and implementation of an internal stress wave force balance in a shock tunnel. *CEAS Space Journal*, 1(1):45–57.

[82] Rodden, W. P. and Giesing, J. P. (1970). Application of oscillatory aerodynamic theory to estimation of dynamic stability derivatives. *Journal of Aircraft*, 7(3):272–275.

[83] Sahoo, N., Suryavamshi, K., Reddy, K. P. J., and Mee, D. J. (2005). Dynamic force balances for short-duration hypersonic testing facilities. *Experiments in Fluids*, 38(5):606–614.

[84] Sanderson, S. R. and Simmons, J. M. (1991). Drag balance for hypervelocity impulse facilities. *AIAA journal*, 29(12):2185–2191.

[85] Schoenenberger, M., Brown, T. G., and Yates, L. (2017). Surface pressure ballistic range test of Mars 2020 capsule in support of MEDLI2. In *35th AIAA Applied Aerodynamics Conference*, page 4079.

[86] Seigel, A. E. (1959). Millisecond Measurement of Forces and Moments in Hypersonic Flow. *NOL Aeroballistic Research Facilities Dedication and Decennial, NOLR*, 1238:25–26.

[87] Spravka, J. J. and Jorris, T. R. (2015). Current hypersonic and space vehicle flight test instrumentation challenges. In *AIAA Flight Testing Conference*, page 3224.

[88] Starshak, W. C. and Laurence, S. J. (2018). Optical Free-Flight Measurements using GPU-Accelerated Computer Graphics. (September):1–14.

[89] Starshak, W. C. and Laurence, S. J. (2021). Computer-graphics-based optical tracking for hypersonic free-flight experiments. *AIAA Journal*, 59(12):4955–4968.

[90] Steelant, J., Villace, V., Marini, M., Pezzella, G., Reimann, B., Chernyshev, S. L., Gubanov, A. A., Talyzin, V. A., Voevodenko, N. V., and Kukshinov, N. V. (2016). Numerical and Experimental Research on Aerodynamics of High-Speed Passenger Vehicle within the HEXAFLY-INT Project'. In *30th Congress of the International Council of Aeronautical Sciences (ICAS)*, pages 25–30.

[91] Stetson, K. F. (1992). Hypersonic boundary-layer transition. In *Advances in Hypersonics*, pages 324–417. Springer.

[92] Storkmann, V., Olivier, H., and Gronig, H. (1998). Force measurements in hypersonic impulse facilities. *AIAA journal*, 36(3):342–348.

[93] Strawa, A. W., Chapman, G. T., Canning, T. N., and Arnold, J. O. (1991). Ballistic range and aerothermodynamic testing. *Journal of Aircraft*, 28(7):443–449.

[94] Sutherland, W. (1893). The Viscosity of Gases and Molecular Force. *The London, Edinburgh, and Dublin Philosophical Magazine and Journal of Science*, 36(223):507–531.

[95] Tanno, H., Komuro, T., Sato, K., Fujita, K., and Laurence, S. J. (2014). Free-flight measurement technique in the free-piston high-enthalpy shock tunnel. *Review of scientific instruments*, 85(4):45112.

[96] Tanno, H., Komuro, T., Sato, K., and Itoh, K. (2015). Free-flight aerodynamic test of elliptic cone in Shock Tunnel. In *20th AIAA International Space Planes and Hypersonic Systems and Technologies Conference*, page 3655.

[97] Tanno, H., Komuro, T., Sato, K., and Katsuhiro, I. (2018). Aerodynamic characteristics of Generic Test Models Under High-Temperature Real-Gas Condition in Free-Piston Shock Tunnel HIEST. In *HiSST: International Conference on High-Speed Vehicle Science Technology*, volume HiSST: Int, pages 1–11.

[98] Tanno, M. and Tanno, H. (2021). Aerodynamic characteristics of a free-flight scramjet vehicle in shock tunnel. *Experiments in Fluids*, 62(7):1–12.

[99] von Gioi, R. G. and Randall, G. (2017). A Sub-Pixel Edge Detector: an Implementation of the Canny/Devernay Algorithm. *IPOL Journal*, 7:347–372.

[100] Wang, Y., Liu, Y., Luo, C., and Jiang, Z. (2016). Force measurement using strain-gauge balance in a shock tunnel with long test duration. *Review of Scientific Instruments*, 87(5):55108.

[101] Wey, P., Seiler, F., Srulijes, J., Bastide, M., Martinez, B., and Gnemmi, P. (2012). Determination of aerodynamic coefficients from shock tunnel free flight trajectories. In *28th Aerodynamic Measurement Technology, Ground Testing, and Flight Testing Conference including the Aerospace T&E Days Forum*, page 3321.

[102] Wheeler, C., Hyslop, A., Vieira, J., Page, L. L., Quinn, M. K., and Nafiz, H. K. (2022). HiSST : 2nd International Conference on High-Speed Vehicle Science Technology Surface Pressure Measurements on a Free-Flying Cone at Mach 7 using Pressure Sensitive Paint. (September):1–19.

[103] Wilder, M. C., Bogdanoff, D. W., and Cornelison, C. J. (2015). Hypersonic testing capabilities at the NASA Ames ballistic ranges. In *53rd AIAA Aerospace Sciences Meeting*, page 1339.

[104] Wise, D. (2015). Experimental investigation of a three dimensional scramjet engine at hypervelocity conditions.

[105] Wolowicz, C. H., Bowman, J. S., and Gilbert, W. P. (1979). Similitude Requirements and Scaling Relationships as applied to Model Testing. Technical Report 1435, NASA.

[106] Wuilbercq, R. and Brown, R. E. (2015). Rapid Aero-Thermodynamic Analysis for Hypersonic Air Vehicles. In *Proceedings of the 8th European Symposium on Aerothermodynamics for Space Vehicles*.

[107] Wuilbercq, R., Pescetelli, F., Minisci, E., and Brown, R. E. (2014). Influence of Boundary Layer Transition on the Trajectory Optimisation of a Reusable Launch Vehicle. In *19th AIAA International Space Planes and Hypersonic Systems and Technologies Conference*, page 2362.

[108] Wylie, S., Doherty, L., and McGilvray, M. (2018). Commissioning of the Oxford High Density Tunnel (HDT) for Boundary Layer Instability Measurements at Mach 7. In *2018 Fluid Dynamics Conference*, page 3074.

[109] Yechout, T. R. (2003). *Introduction to aircraft flight mechanics*. Aiaa.

Appendix A

Free-Flight Aerodynamics of the Skylon Spaceplane

A.1 Abstract

The determination of aerodynamic coefficients for complex high speed vehicles still requires experimental measurement. This paper details the development of the free-flight measurement technique within the University of Oxford High Density Tunnel (HDT). In particular, a novel image processing technique is developed for calculating the position of the model from high speed video. This study focusses on the measurement of high Reynolds number experimental aerodynamic data for a subscale model of Reaction Engines' Skylon spaceplane. Testing was undertaken at a Mach 7 test condition replicating flight at an altitude of 63.5 km. Results for lift, drag and pitching moment coefficient were obtained over a range of angles of attack. Lift coefficient was nearly linear over the range of angles of attack tested and drag coefficient was parabolic in shape but sensitive to model yaw. The vehicle was also shown to be statically unstable, a common characteristic of canard configuration vehicles.

A.2 Introduction

Reusable single-stage-to-orbit (SSTO) spaceplanes have the potential to revolutionise the cost of orbital access. However, this requires a vehicle design that can perform over a range of flight regimes, as the vehicle takes off like a conventional aeroplane and accelerates from the subsonic regime to the hypersonic regime, carrying a payload to low Earth orbit (LEO) before returning to land.

Currently, there is little numerical or experimental aerodynamic performance data for spaceplanes, particularly at hypersonic Mach numbers. Furthermore, due to the length of spaceplanes, boundary layer transition is expected to occur on the vehicle which is difficult to predict computationally [107] [91]. In general, the creation of a high-fidelity, nose-to-tail numerical simulation of hypersonic vehicles is difficult and computationally expensive. Validation of such simulations requires high-quality experimental data.

A substantial amount of existing spaceplane research was conducted during the National Aero-Space Plane (NASP) programme (1986-1995). Phillips [78] conducted sting mounted aerodynamic tests for the Test Technique Demonstrator, a generic spaceplane geometry used in the development of NASP. Forces were measured using a six component strain-gauge balance at a range of hypersonic Mach numbers. In parallel, significant advancements were made in the development of computational models for spaceplanes during this period, however, there were high uncertainties in the laminar-turbulent transition location in the high Mach number regime [49]. The programme was ultimately terminated due to the increasing costs of achieving SSTO at the time.

Skylon, a SSTO spaceplane currently in development by Reaction Engines Ltd. (REL), utilises SABRE engines which harness state-of-the-art pre-cooler technology to enable the engine to remain air-breathing at altitudes up to 26 km at Mach 5, before transitioning to rocket mode [50]. Mehta *et al.* [63] conducted numerical simulations using NASA's Cart3D software to investigate the Skylon airframe aerodynamics for powered flight and assess the plume impingement from the SABRE engines on the aft fuselage for potential thermal-structural issues. The results showed that at Mach numbers above 8.5, the under-expanded plumes had a favourable effect on the aerodynamic coefficients causing divergence from in-house REL predications. Mehta provides the only source for information of trajectory points and aerodynamic coefficients of Skylon in open literature. However, there is a lack of experimental data that validate these numerical simulations.

This paper presents an experimental investigation of the aerodynamic performance of the Skylon vehicle through the development of the free-flight experimental technique in the Oxford High Density Tunnel (HDT), thereby creating an experimental aerodynamic coefficient database for Skylon at high Mach numbers which can be used to validate numerical data. Free-flight experiments require the model and flow conditions to be suitably scaled so that the dynamics and aerodynamics of the sub-scale model are representative of flight conditions. For spaceplanes, flight representative conditions are particularity important due to the sensitivity of aerodynamic coefficients to the position of boundary layer transition over the body of the vehicle. Aerodynamic data at a range of angles of attack was acquired using both image tracking on high speed videos and an on-board Inertial Measurement Unit (IMU).

This work represents the first experimental investigation of the aerodynamics of Skylon at high Mach number flight conditions. Section II of the paper describes the Free-flight technique as implemented in the HDT. Section III details the experimental set up, model design and the application of the scaling laws. Section IV discusses the data processing used to obtain aerodynamic coefficients. Section V presents the results of the experiments.

A.3 Free-Flight Technique and Scaling

There are many difficulties associated with measuring aerodynamic forces in hypersonic facilities. Conventional methods typically include the use of a sting to rigidly mount a sub-scale model with aerodynamic forces and moments measured through the use of a multicomponent force balance. The presence of the sting, however, results in undesirable drag and also produces unrealistic flow fields downstream of the model. Pick [79] showed that the interference effects of a sting is very influential at angles of attack of 15 degrees or greater for sharp cones in hypersonic flow. Additionally for sting mounted models, it is important that the dynamic response of the model and balance upon application of transient loads is shorter than the useful test time to allow for the measurement of quasi-static aerodynamic forces. This design criteria can often be difficult to achieve in short duration hypersonic facilities [38].

The free-flight technique discards the sting and allows the model to move unconstrained in the flow in six degrees of freedom [10]. A typical methodology of a free-flight test in short duration facilities is as follows: the model is released prior to arrival of the test flow, the flow is initiated over the model which allows it to move as it would in flight. Consequently, there is no external interference on the flow around the model, thus, it is more representative of real flight. This technique requires non-intrusive methods to measure accelerations, from which the aerodynamic forces may be derived. Measurement of acceleration can be achieved using two different methods: On-board accelerometers and gyroscopes, and image tracking of the vehicle's position from high speed videos. The free-flight technique has been successfully applied in short-duration hypersonic test facilities by several authors. Mudford [67] measured 6 degrees of freedom movement on a steel hemispherical-nosed cylinder using accelerometers and gyroscopes. This work was continued by Kennell *et al.* [40, 39] using ESA's HEAXFLY INT EFTV geometry. Tanno [97] also used accelerometers to measure 6 component motion of blunted cone, capsules and lifting bodies in a free piston shock tunnel. Laurence *et al.* [45] used image tracking with sub-pixel accuracy measuring 3 component motion on the NASA Orion vehicle.

The dynamic behaviour of models in free-flight is directly related to the model geometry, test flow properties and the model mass distribution. Therefore, it is important that all aspects of the vehicle of interest and flow properties are scaled appropriately so that the data obtained from the derived model during free-flight corresponds to the full-scale vehicle behaviour when in flight. Wolowicz [105] provides a thorough derivation and discussion on scaling; a brief summary is provided here. For free-flying models there are two methods available for scaling - Froude number scaling and Mach number scaling. Froude scaling allows for the preservation of gravitational effects acting on the model, thereby matching the kinematics of the model and maintaining angle of attack similitude. Mach scaling preserves the effects of compressibility within the flow. In this work, Mach scaling was used as all testing was conducted in the hypersonic regime where compressible effects dominate. Mach scaling requires that both the freestream Mach number and Reynolds number are matched between flight and the wind tunnel test. Matching Reynolds number preserves features such as boundary layer transition and viscous effects which are particularly important for geometries such as spaceplanes. All aspects of the vehicle's geometry are scaled by the desired factor, n, to give the model length, and the position of the centre of mass of the model for example. In practice, it is not always possible to scale all geometric aspects of the vehicle because features such as surface roughness would be required to be very fine and difficult to machine. To preserve the dynamic behaviour of the vehicle, the model's mass and moment of inertia must be scaled according to Eq. (A.1) and Eq. (A.2) where subscript m denotes the model, subscript v the full-scale vehicle and ρ_f is the fluid density.

$$\frac{m_m}{m_v} = n^3 \frac{\rho_{f,m}}{\rho_{f,v}} \tag{A.1}$$

$$\frac{I_m}{I_v} = n^5 \frac{\rho_{f,m}}{\rho_{f,v}} \tag{A.2}$$

Under the assumption of matched freestream Reynolds number and Mach number, taking ratios of Reynolds number gives:

$$\left(\frac{\rho_f T^{\frac{1}{2}}}{\mu} \right)_m = \left(\frac{\rho_f T^{\frac{1}{2}}}{\mu} \right)_v \tag{A.3}$$

If the model scale and vehicle trajectory point are defined, all properties on the right hand side of Eq. (A.3) are fixed. The left hand side therefore describes a test envelope that the facility must meet in order to achieve similitude. Once the facility conditions are chosen, Eq. (A.1) and Eq. (A.2) may be used to determine the required model mass and moment of inertia. This fully defines the model inertial specifications for dynamic similitude within

the limitations of Mach scaling. High temperature effects such as flow chemistry play a secondary role in aerodynamic experiments and as a consequence, stagnation enthalpies are not replicated in Mach scaling.

A.4 Experimental Setup

A.4.1 Facility and Test Infrastructure

The experiments were conducted in the University of Oxford High Density Tunnel located within the Oxford Thermofluids Institute. The facility was operated as a Ludwieg tube with a Mach 7 contoured nozzle with exit diameter 350 mm, producing a core flow of 280 mm at nozzle exit. The facility currently has a maximum operational total pressure of 50 bar (which can be upgraded to 275 bar). For further details on the HDT operation and measurement of freestream conditions, see McGilvray *et al.* [57] and Wylie *et al.* [108]. This facility was selected for these experiments because it offers sufficient steady flow duration ($\sim$ 50 ms) to allow the free-flight of low inertia models through a range of attitudes at flight representative conditions.

Shown in Fig. A.1, a catcher net and model drop mechanism were designed for the HDT. The catcher mechanism was designed to prevent the model from exiting the test section into the dump tank, from where it would be difficult to retrieve. The catcher mechanism was also designed to reduce the damage sustained by the model during a test. The catcher consisted of two aluminium rings with Dyneema cord of 1.5 mm diameter fed through 32 uniformly spaced holes. The upstream ring was held at a 30° inclination, with the purpose of deflecting the model towards the tunnel floor which was lined with multi-layer foam padding.

The drop mechanism was designed to release the model into the core flow prior to the arrival of test flow. The mechanism consisted of a 25 mm diameter electromagnet attached to a SMC pneumatic actuator of 50 mm stroke length. A bespoke electrical unit controls the timing of the solenoids. Upon receiving a TTL pulse from the tunnel, the box triggers the electromagnet to release the model and powers the solenoids to retract the actuator, pulling the electromagnet out of the oncoming flow. The TTL pulse timing may be varied with respect to the facility to achieve the desired time of model free-fall before flow onset. A 3D printed holder was used to house the electromagnet and set the initial angle of attack of the model. The holder shape was conformal to the Skylon model, setting and fixing the roll axis and a steel rod was connected to the holder to limit any rotations about the yaw axis. The printed holder is shaped to position the electromagnet directly above the centre of gravity of

the model to minimise any exerted rotational inertia on the model when it is released and hence provided a consistent and repeatable model release.

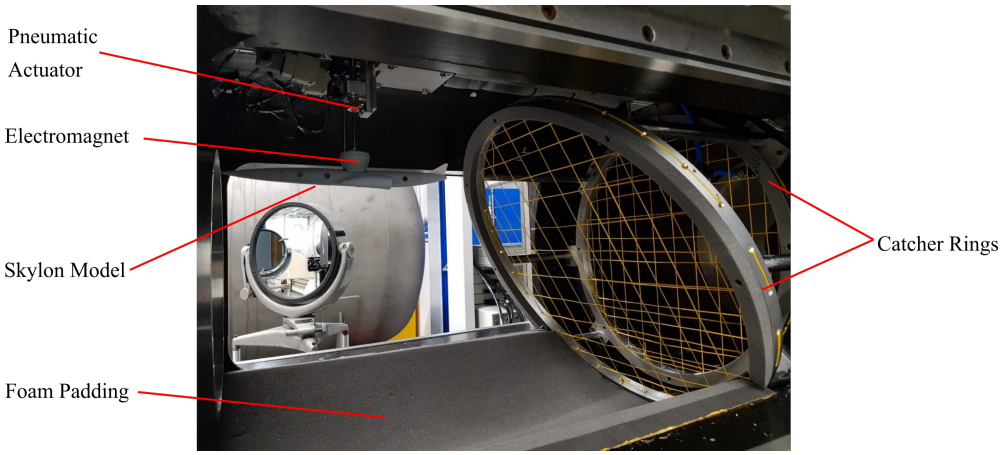

Fig. A.1 Free-flight drop mechanism and catcher rings in the HDT test section.

A.4.2 Test Condition and Model Scaling

Using the scaling laws set out in Section II, Figure A.2 plots the required unit Reynolds number to achieve similitude of flight conditions for a range of hypersonic vehicles over their trajectories for a given model length. The vehicle data corresponds to flight trajectory points assuming a model length of 337 mm, matching the length of model used in this work. Also plotted is the unit Reynolds number capability of the HDT for each nozzle. It can be seen from Figure A.2 that dynamic similitude of spaceplanes requires large unit Reynolds numbers that are in excess of the capability of the HDT. This is a direct consequence of the significant length (on order of 80m) of this class of vehicle in comparison with the other vehicles presented.

For Skylon, similitude can only be achieved at Mach 7 at the upper operational limit of HDT. Figure A.3 presents the variation in required flow total pressure with model length assuming Mach 7 flow and a Reynolds number of 32.3×10^6 as used by Mehta *et al.* [63] (equivalent to 42 km altitude). The variation in required model mass, calculated according to Eq. (A.1) is also plotted. A model length of 337 mm was chosen, corresponding to a scale of 1:240. This scale was selected so that the model would have room to manoeuvre in the core flow during the course of a test. At this scale, a total pressure of 208 bar is required to ensure similitude. Although the HDT is capable of achieving this condition, the use of free-flight at such high forces was deemed to be too risky to the tunnel infrastructure. Consequently, a

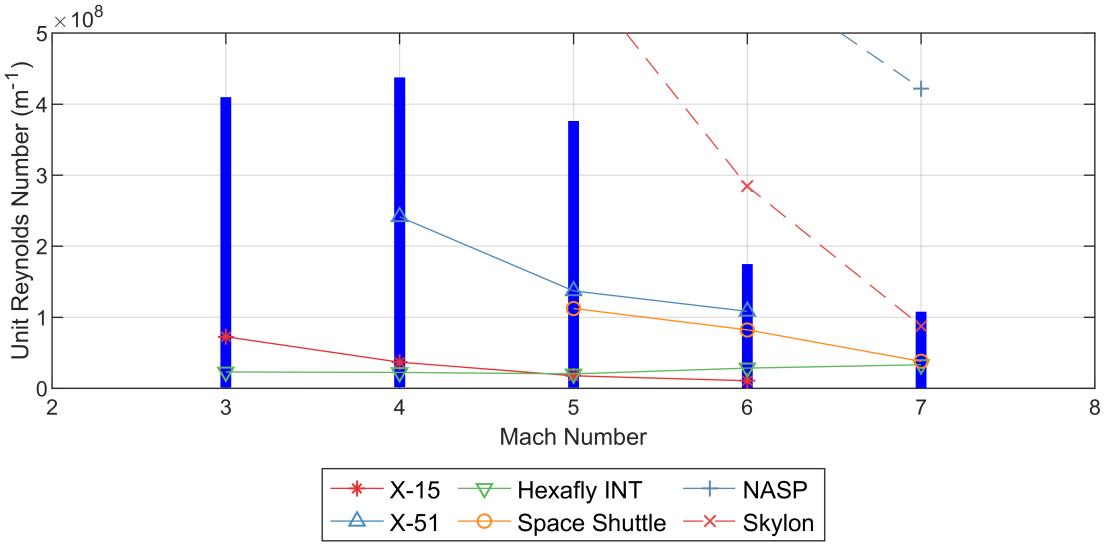

Fig. A.2 Unit Reynolds number capability (blue bars) of HDT facility compared with similitude requirements of various hypersonic vehicles assuming a model length of 337 mm. Trajectory points for the vehicles are taken from [64], [68], [13], [19], [5] and [63].

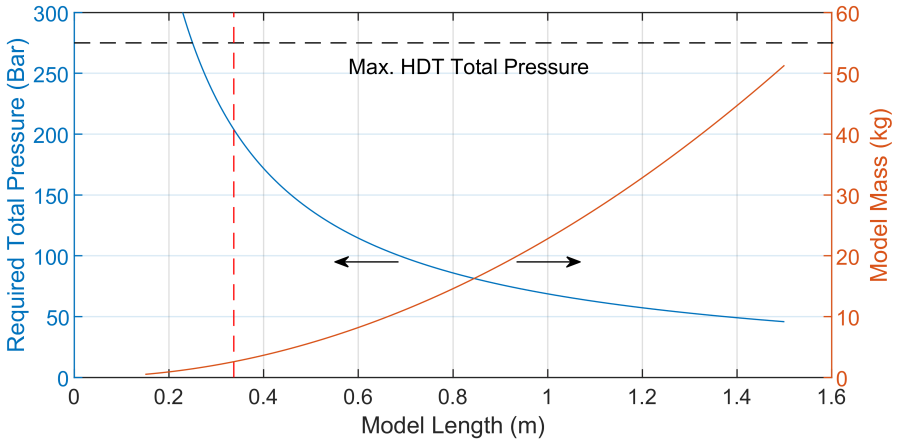

Fig. A.3 Mach scaling applied to Skylon for an altitude of 42 km to match Reynolds number and mass (Mach 7, T_0 = 537 K). Red dashed line represents model length used in this work

reduced total pressure of 14 bar was chosen for this work, corresponding to an altitude of 63.5 km.

Table A.1 compares the nominal test condition with an equivalent flight condition. Flight conditions are derived by matching the Reynolds number of the 14 bar tunnel condition at Mach 7. Viscosity was calculated using Keyes' Law [43] for tunnel conditions and Sutherland's Law [94] for flight. Equivalent flight conditions were calculated through US

Standard Atmosphere [71]. Flight total temperature was calculated using isentropic relations with a ratio of specific heats (γ) of 1.4.

Table A.2 compares the scaled inertial properties for similitude and the test model properties for the Mach 7 test condition. The vehicle mass includes the fuel load and is taken from the Mach 7, 42 km altitude condition. Moment of inertia was predicted using CAD software for the model. The position of the centre of gravity was well matched to the full-size vehicle and therefore the model gives insight into vehicle longitudinal stability. However, a lighter model was used for ease of manufacture and to prevent damage to the HDT in this proof-of-concept campaign. Consequently, model rotational and linear motion during the test will be greater than flight but the magnitude of measured aerodynamic forces are unaffected by the mass mis-match.

Table A.1 Flight vs scaled tunnel condition.

	HDT Test Flow	**Flight**
Altitude (km)	63.5	63.5
Mach Number	7	7
Velocity (ms^{-1})	989.6	2181
Density (kgm^{-3})	0.022	0.00018
Static Pressure (Pa)	317.4	12.53
Total Pressure (kPa)	1331	51.88
Static Temperature (K)	49.7	241.5
Total Temperature (K)	537	2608
Dynamic Viscosity (μPas)	3.56	0.16
Unit Reynolds Number ($10^6 m^{-1}$)	6.26	0.025
Reynolds Number (10^6)	2.1	2.1

Table A.2 Scaling applied to the inertial properties of Skylon.

	Full Scale	**Scaled**	**Model**	**Mismatch Error**
Length	81.3 m	337 mm	337 ± 0.1 mm	0 %
Mass	2.43x10^5 kg	2.03 kg	0.219 ± 0.001 kg	89.2 %
$\mathbf{X}_{cg}$	43.84 m	181.3 mm	181 ± 1 mm	0.2 %
$\mathbf{Z}_{cg}$	-0.26 m	-1 mm	-1 ± 1 mm	0 %
$\mathbf{I}_{yy}$	1.77x10^7 kgm^2	2.43x10^6 gmm^2	1.07x10^6 gmm^2	127.1 %

A.4.3 Model Design

The experimental model was geometrically scaled from the full-size vehicle, with the exception of the wings, canards and tail, which were thickened to 0.2 mm at the trailing edge to maintain sufficient rigidity. The engines were designed as if in rocket/reentry mode, i.e. closed to the oncoming flow. This increases the overall drag compared with the vehicle in air-breathing mode. Due to the small model scale, no engine plume effects were accounted for in these experiments. The model was designed to be suitable for rapid prototyping using a Polyjet Objet 30 3D printer. The vehicle was subdivided into 4 sections: nose, tail, fuselage and wings, thereby allowing for delicate features to be replaced in the case of damage during a test. Dividing the model also allowed for cavities to be created that accommodated ballast (used to locate the centre of mass) and the on-board Data Acquisition module (DAQ) and battery. The model was also designed so that the inertial measurement unit (IMU) on the DAQ was located at the centre of mass of the model to within +/- 0.1 mm. A bespoke metal plate was machined to fit the top of the model to allow compatibility with the drop mechanism electromagnet. Figure A.4 shows a photograph of the final assembly. The black circles visible on the side are for image tracking of the model during free-flight.

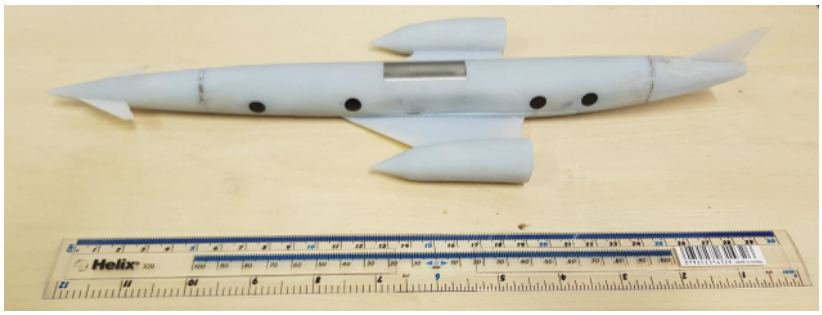

Fig. A.4 Skylon scale model.

A.4.4 On-board Data Acquisition System

The on-board inertial measurement instrument (hereby referred to as the DAQ) consisted of an integrated 3-axis accelerometer and 3-axis gyroscope, non-volatile memory, a Bluetooth radio module and a microcontroller. These components were integrated on a single printed circuit board with planform dimensions of $\sim$ 114 mm x 12 mm. This measurement system has successfully demonstrated the ability to collect accurate acceleration and angular velocity data necessary for hypersonic wind tunnel model aerodynamics [39, 59]. The IMU was a single chip device with an accelerometer full scale range of +/- 16 g and a data output rate of 4 kHz. The full scale range of the gyroscope was +/-2000 deg/s with a data output rate of

8 kHz. Non-linearity of the accelerometer and gyroscope axis is reported to be 0.1% and 0.5% respectively. For this work a sample rate of 8 kHz was used which allowed for $\sim$ 320 samples over the 40 ms duration of the experiment. Triggering of the instrument was achieved by detection of sustained free-fall upon model release.

A.4.5 Optical Setup

For this work, the flow field was imaged using schlieren and the model movement by direct imaging using two high speed cameras. For the schlieren, a conventional Z-type setup with horizontal knife edge was used to visualise the density gradients in flow field around the Skylon model. The light was emitted continuously from a Luminous PT-120-TE green LED as the camera's detector is particularly sensitive to this wavelength region. The flow was imaged with a FASTCAM AX200 high-speed camera set to a frame rate of 6400 fps with 1,024 x 1,024 pixel resolution at a focal length of 130 mm which fully encapsulated the test time of the flow. The camera was set to have a 200 frame pre-trigger and was activated by a TTL pulse from the facility prior to the test. The schlieren mirrors were of 300 mm diameter and had a focal length of 1660 mm.

A FASTCAM UX100 high-speed camera with a 30 mm lens recorded the model movement directly for image tracking purposes. The camera faced directly through the test section windows, imaging the longitudinal plane of motion of the model. A frame rate of 4000 fps was used giving a resolution 1,280 x 1,024 pixels. Two LED bike lights were used to front light the model, producing sufficient light for the model to be well exposed. To fully capture the free-fall of the model, a pre-trigger of 800 frames was used and a total of 2180 frames recorded. A discussion of the image tracking technique is discussed in Section IV B.

The two cameras were positioned as such that both systems could operate concurrently during a test with neither system obstructing the field of view of the cameras.

A.5 Data Analysis

Two non-intrusive techniques, on-board sensors and image tracking, were used to measure the kinematics of the model. The data reduction methods for both techniques are discussed below. Ultimately, the calculated linear and angular accelerations are used to calculate the aerodynamic coefficients according to Eq. (A.4), where the freestream dynamic pressure is calculated from the variables in Table A.1, the mass and moment of inertia are taken from Table A.2 and a reference area of S = 6.11x10^{-3} m^2 was used. The reference length used in the calculation of pitching moment was the model length. Calculation of the uncertainties is detailed in Appendix 1.

$$C_L = \frac{m\ddot{z}}{qS}, \quad C_D = \frac{m\ddot{x}}{qS}, \quad C_M = \frac{I_{yy}\ddot{\theta}}{qSc} \tag{A.4}$$

A.5.1 Processing IMU Data

Aerodynamic coefficients are conventionally measured relative to the oncoming flow, known as the stability axis. For wind tunnel experiments, this coincides with the Earth or Inertial frame which is defined as having the +z axis towards the ground, +x axis pointing upstream towards the facility nozzle and the +y axis orthogonal to both forming a right-hand coordinate system. During an experiment, the model and therefore IMU, rotate relative to the Earth frame of reference. Shown in Figure 5, the IMU data is thus recorded in a body fixed coordinate frame.

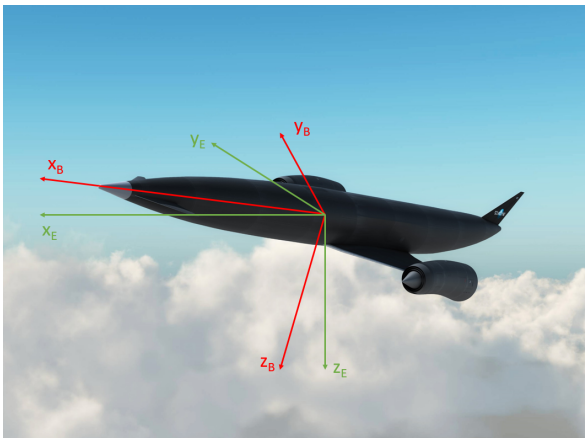

Fig. A.5 Co-ordinate frames of reference (B is Body and E is Earth).

To convert the raw IMU data to aerodynamic coefficients, the following steps were taken. First, the data received from the on-board IMU was filtered using a 6^{th} order low pass Butterworth filter. The body-axis angular rates are then transformed to Euler-angle

rates in the Earth axis through Eq. (A.5). This allows for the Euler angles to be determined through numerical integration of Euler-rates. Using these Euler angles, the measured linear accelerations are transformed from the body axes to the Earth axes using Eq. (A.6) so that lift and drag forces can be calculated.

The rotation matrix for the angular rates and accelerations are as follows (where c, s and t are cosine, sine and tangent functions respectively):

$$\begin{bmatrix} \dot{\phi} \\ \dot{\theta} \\ \dot{\psi} \end{bmatrix} = \begin{bmatrix} 1 & s(\phi)t(\theta) & c(\phi)t(\theta) \\ 0 & c(\phi) & -s(\phi) \\ 0 & \dfrac{s(\phi)}{c(\theta)} & \dfrac{c(\phi)}{c(\theta)} \end{bmatrix} \begin{bmatrix} p \\ q \\ r \end{bmatrix} \tag{A.5}$$

$$\begin{bmatrix} \ddot{X} \\ \ddot{Y} \\ \ddot{Z} \end{bmatrix}_E = \begin{bmatrix} c(\psi)c(\theta) & c(\psi)s(\phi)s(\theta) - c(\phi)s(\psi) & s(\phi)s(\psi) + c(\phi)c(\psi)s(\theta) \\ c(\theta)s(\psi) & c(\phi)c(\psi) + s(\phi)s(\psi)s(\theta) & c(\phi)s(\psi)s(\theta) - c(\psi)s(\phi) \\ -s(\theta) & c(\theta)s(\phi) & c(\phi)c(\theta) \end{bmatrix} \begin{bmatrix} \ddot{X} \\ \ddot{Y} \\ \ddot{z} \end{bmatrix} \tag{A.6}$$

Example filtered acceleration data in the Earth axes are presented in Fig. A.6. As seen, the model free-falls for 120 ms before the onset of test flow, positioning the model at the nozzle centreline at flow start up. The facility has an approximately 40 ms start-up time in which the total pressure rises before reaching a plateau where the test time is taken. As seen in the figure the facility is timed so that only one plateau is produced, as after this time the model has moved out of the core flow and it reduces the likelihood of damage to the model.

A.5.2 Image Processing

Optical tracking to determine the model displacement used four black circles of known location, painted on the side of the model (Figure A.4). Although only two circles are needed for data processing, additional circles provided redundancy in the event of low image contrast (a possible consequence of non-uniform lighting). The algorithm to determine the centre point of each circle for each video frame was as follows:

1. Apply Gaussian filter to image and subtract from original (High pass filter).
2. Apply Canny filter to image so that only pixels detected as an edge are shown [9].
3. Apply Hough transform to find circles in the image after narrowing the search radius [30].
4. Detect pixels in the proximity of the circle located by the Hough transform.

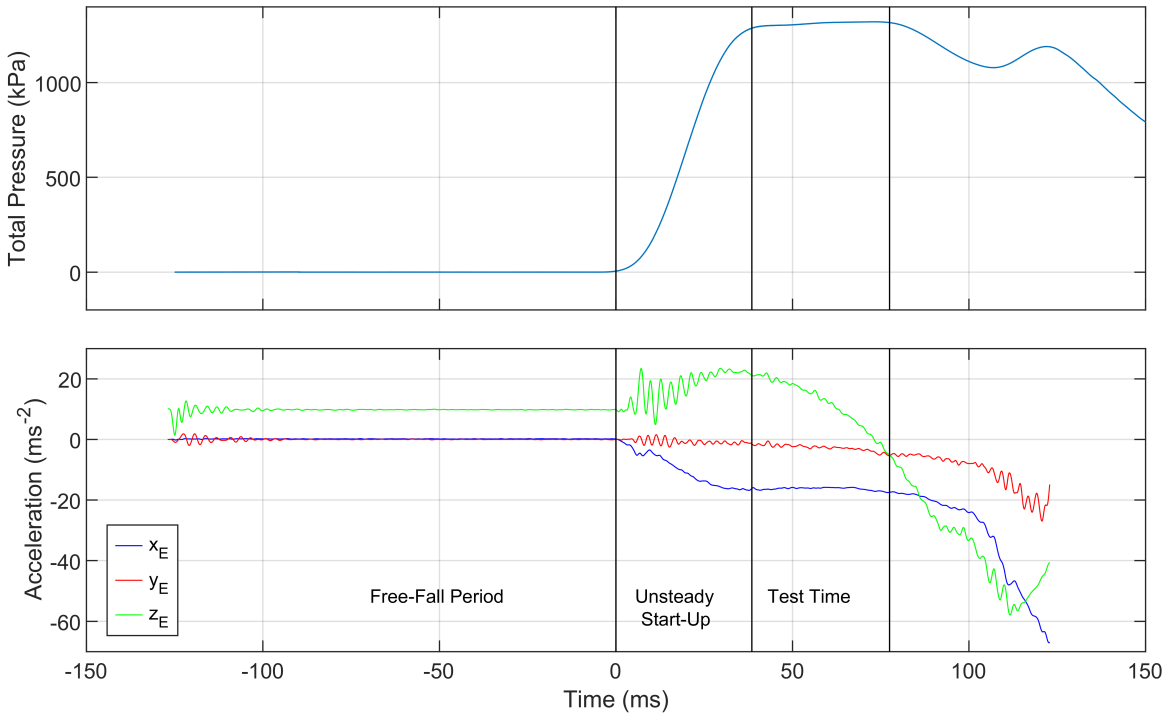

Fig. A.6 Example filtered accelerometer accelerations in the Earth frame of reference with HDT total pressure.

5. Use subpixel detection on the original image, at the location pixels were detected. Subpixel methodology set out in von Gioi [99].

6. Fit a circle to the pixels using linear regression as set out in Laurence *et al.* [45] and use this equation to find the centre point of the circle.

The centre of gravity and angle-of-attack are inferred by drawing a straight line between the centres of any two circles. Centre of gravity was measured prior to the test and was known relative to the circle locations. This process was repeated on each frame until the displacement (in pixels) of the centre of gravity and angle-of-attack history was obtained. As the distance between circles was known, the spatial resolution of the images can be found (0.54 mm/pixel) and used to determine actual displacement. The displacement of the model was differentiated twice to give accelerations and hence aerodynamic coefficients (Eq. (A.4)). The raw displacement data and intermediate velocity required smoothing before differentiation. Figure A.7 shows an example of the image tracking for a test for which the model was close to the trim angle of attack. Prior to testing, the spatial uniformity of the lens was measured and corrected for through the use of a uniform grid inserted into the tunnel.

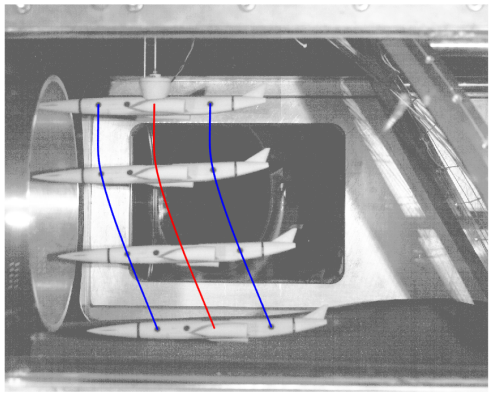

Fig. A.7 Montage photo of image processing (Blue - detected circle centre points, Red - calculated centre of mass).

The performance of the algorithm was analysed by calculating the position of centre of gravity for 250 frames where the model was held stationary. The standard deviation of centre of gravity position for this test was calculated to be 41 μm. This is a very small standard deviation considering the spatial resolution of the pixels (0.54 mm/pixel) and the relative size of circles (radius of approximately 9.5 pixels) detected in relation to the rest of the frame (1,280 x 1,024 pixels.). This analysis does not take into account errors which come from misalignment of the optical equipment but gives an approximation of the uncertainty associated with the numerical algorithm.

A.6 Results

The results from the free-flight experiments are presented in this section. Lift, drag and pitching moment coefficients are calculated from the IMU data for four independent tests. Coefficients calculated from image tracking are also presented for a single shot. Finally, schlieren imagery is shown at the end of the section.

A.6.1 IMU Data

In total, four Skylon free-flight tests were conducted at the Mach 7 test condition. Figures A.8 and A.9 present lift and drag coefficient versus angle of attack measured by the accelerometers. Uncertainties are shown as shaded bands around the data points as calculated in Appendix 1 using the Taylor Series Method determining the propagation of uncertainties in freestream parameters, model properties and the IMU. Out of plane motion such as yaw was not included

in the calculation of uncertainties. Data is also taken from Mehta *et al.* [63] and plotted on the figures.

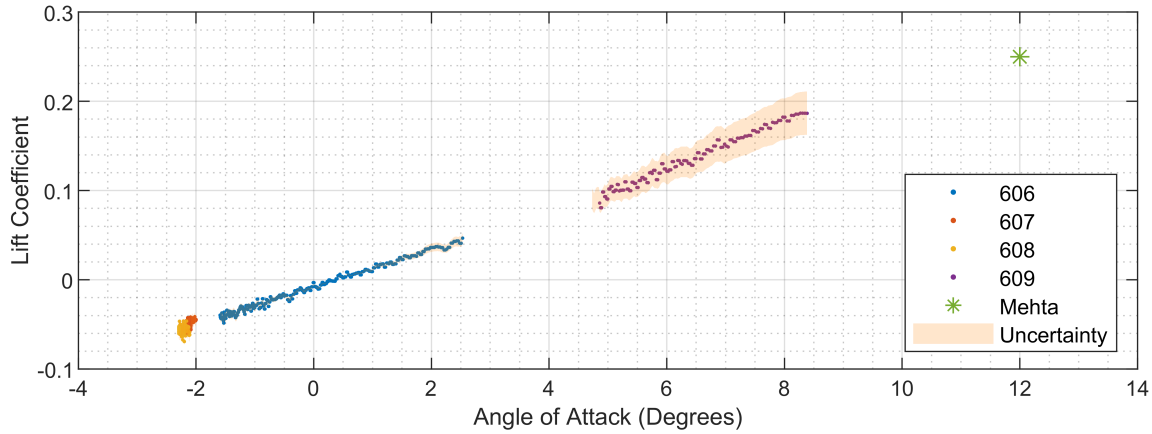

Fig. A.8 Lift coefficient variation with angle of attack derived from the IMU data.

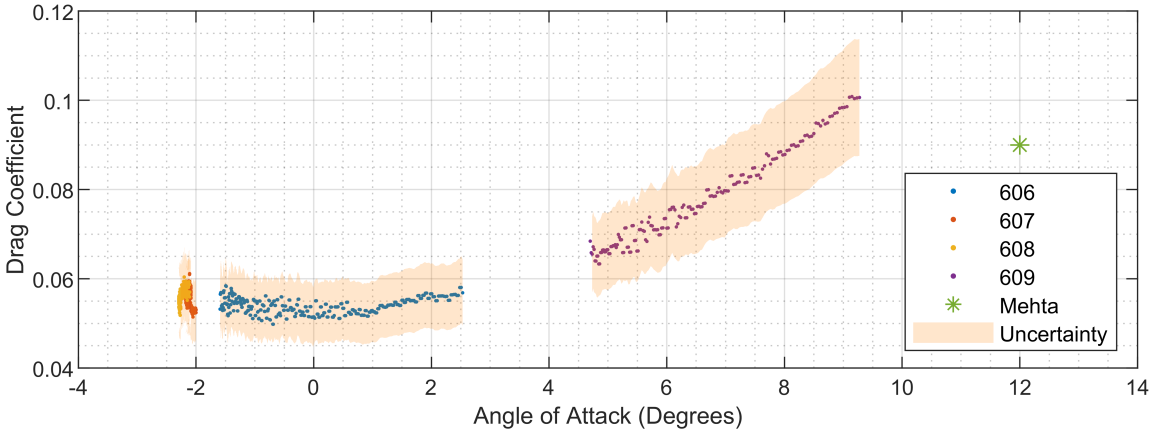

Fig. A.9 Drag coefficient variation with angle of attack derived from the IMU data.

Lift coefficient, shown in Fig. A.8, gives a linear trend with angle of attack, however, there is a slight increase in the gradient between shots 606 and 609. The lift coefficient is zero at approximately 0.27 ° angle of attack if a linear fit is chosen for the data. Extrapolating a linear fit to the data gives a lift coefficient of 0.26 $\pm$ 0.03 at 12 ° angle of attack. This compares well with the data from Mehta which is 0.25 at the same angle of attack.

The data for drag coefficient is noisier than the data for lift coefficient. This is due to the sensitivity of model drag with respect to out-of-plane rotations such as yaw. The trend in drag coefficient was quadratic with a minimum occurring at 0.05 °. Extrapolating the trend in drag coefficient to alpha = 12 ° gives $C_D = 0.133 \pm 0.017$; a result that is significantly higher than that of Mehta. This difference is seen because in the current work the model has sealed engine intakes, which inherently increase the drag. Furthermore, these tests were conducted at a Reynolds number over an order of magnitude lower than Mehta which increases the expected drag.

Shots 607 and 608 exhibit minimal pitching during the run with both being at a similar angle of attack. This suggests that the trim angle of attack is in the region of -2 to -2.4 °. This is further supported by Fig. A.10 which presents the variation in pitching moment with angle of attack and has the zero pitching coefficient at a similar angle of attack. This data is inherently noisy due to the differentiation of the pitch rate data from the gyroscope to calculate angular acceleration for the pitching moment coefficient. In Fig. A.10 the data is smoothed using a moving average filter. The data exhibits a general positive linear trend which implies static instability of the Skylon model. This agrees with motion seen in the footage for the tests in which the model pitches away from trim angle of attack when perturbed from equilibrium. Static instability is a common characteristic of vehicles with canards as increasing lift is generated near the front of the vehicle as angle of attack increases, which in turn increases the moment causing the vehicle to pitch (for a fixed canard angle). The small scale of the current model prevent the canards from being actively controlled as they would be on the real vehicle. Thus, the static instability could not be corrected during the test flow, resulting in the model sweeping through large range of angle of attack on some tests.

Figure A.11 presents the lift-to-drag ratio for data recorded by the IMU. Initially the data increases linearly but the gradient decreases at higher angles of attack, eventually beginning to plateau at approximately 9 ° angle of attack. Testing at higher angles-of-attack was avoided due to the large lift generated and hence acceleration of the model to the top of the test section (which was not padded).

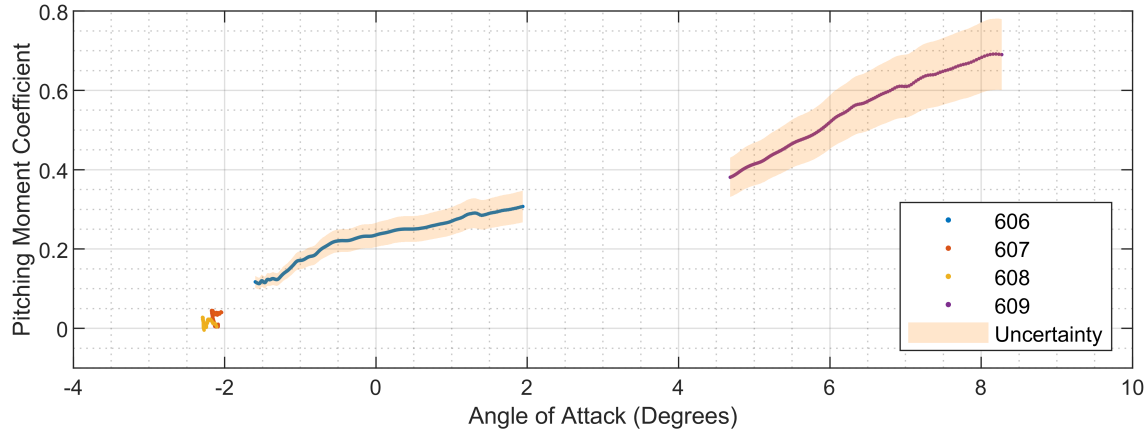

Fig. A.10 Pitching Moment coefficient variation with angle of attack derived from the IMU data.

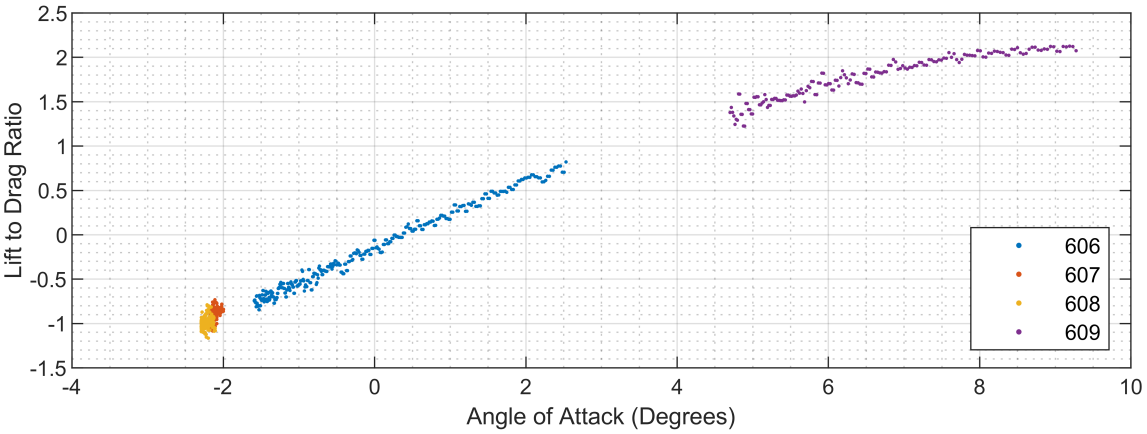

Fig. A.11 Lift to Drag Ratio Lift variation with angle of attack derived from the IMU data.

A.6.2 IMU vs Image Processing

Figure A.12 shows the aerodynamic coefficients from both methods, converted from their respective accelerations. The aerodynamic coefficients as measured through image processing show more scatter (approximately 5 times) due to the process of differentiation amplifying noise, even with smoothing. For lift coefficient there is an offset observed between the two methods which is attributed to the uncertainty in initial angle of attack of the model when released. As the calculation of angle of attack from angular velocities recorded by the gyroscopes requires knowledge of the initial conditions, any uncertainty in this value causes an offset in the whole entire set. Drag coefficient for image processing shows even greater scatter but overall compares well with the IMU data. Overall, it is still very useful to have both methods to measure coefficients as it gives some degree of validation to the results.

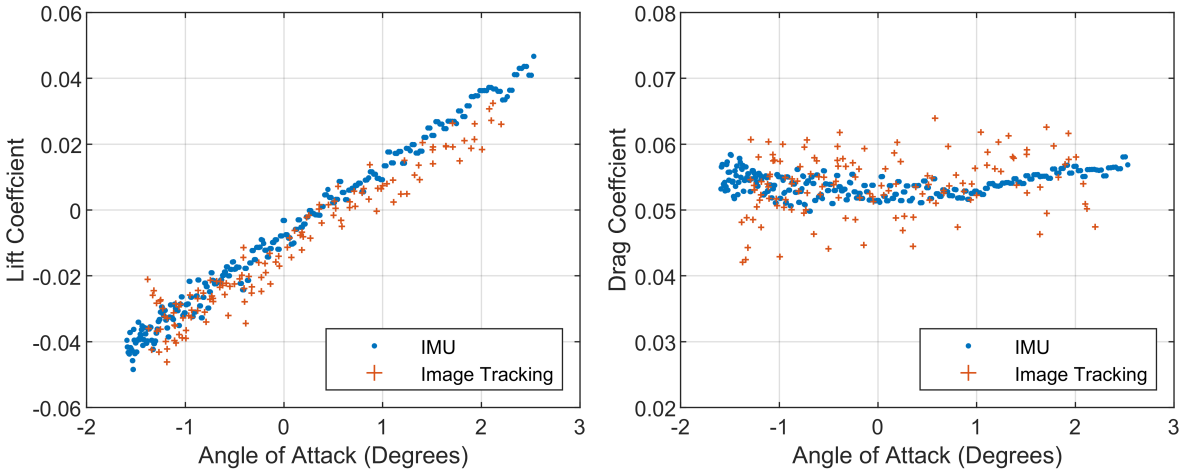

(a) (b)

Fig. A.12 Comparison of lift (a) and drag (b) coefficient as measured by image tracking and on-board sensors for shot 606

A.6.3 Flow Visualisation

Schlieren was used to visualise the flow field around the model as it moved. Expansion and shock waves can clearly be seen throughout the course of a test. Unfortunately, the whole Skylon vehicle cannot be seen in one frame due to the limitation of mirror size at the facility and elliptical field of view. Figure A.13 shows a series of images from a Skylon free-flight test and the model trajectory as determined derived by the IMU. As the test progresses and the model begins to pitch, the bow shock moves closer to the underside of the model.

A.7 Conclusion

The experimental measurement of lift, drag and pitching moment have been presented for the Reaction Engines Skylon spaceplane for 4 independent shots at a Mach 7 test condition. Whilst the mass scaling requirements were not met in this campaign and the test conditions represented a higher altitude than the flight trajectory point, the results still gave useful insight into aerodynamic coefficients of the Skylon vehicle, which can be validated against numerical simulations. Lift and drag coefficient exhibited the expected shapes with respect to angle of attack and the gradient of pitching moment coefficient showed the vehicle to be statically unstable, which was clear from the test videos. This instability is an expected feature of the vehicle due to the lack of active control on the model with respect to the canards. Further research could be conducted to investigate what angle of attack of the

canards is required to trim the vehicle and counteract the nose-up moment produced in these series of tests. To determine the dominant factor for the disagreement of drag coefficient against Mehta's numerical simulations, future experiments could be conducted at a higher Reynolds number or having flow-through inlets on the model. Coupling image tracking with on-board accelerations allows for independent validation of the model accelerations during a test. To conclude, the new infrastructure designed for free-flight experiments has allowed for successful tests in the Oxford High Density Tunnel with consistent data measured across different tests.

A.8 Acknowledgments

The authors would like to acknowledge Dr. Chris Kennell for his advice on kick-starting free-flight experiments at the University of Oxford. We are also grateful for the tireless work of Mr C. Hambidge and Dr. T. Hermann in the operation of the HDT.

A.9 Appendix A.1: Aerodynamic Coefficient Uncertainty

For a comprehensive understanding of experimental results, quantification of experimental uncertainties is required. With regards to free-flight, there are many sources of uncertainty such as; flow conditions, model geometric and inertial properties, experimental setup and

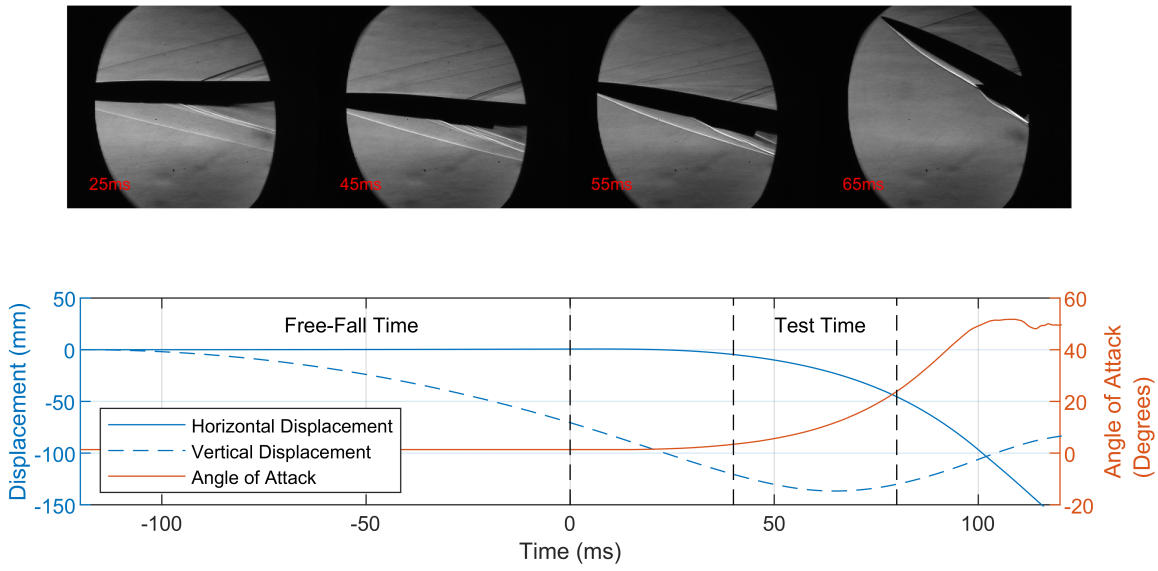

Fig. A.13 Schlieren images and model trajectory determined from IMU for shot 609

orientation of the model in the flow. For the following analysis, the Taylor Series Method (TSM) will be used to determine the propagation of uncertainties. The assumption is also made that roll and yaw is negligible during a test to simplify the analysis. The following equation describes the propagation of the uncertainties in the measured variables into the overall uncertainty of the desired output (for a full derivation see Coleman [11]):

$$U_r = \left[\sum_{i=1}^{J} \left(\frac{\partial r}{\partial X_i} \right)^2 U_i^2 \right]^{\frac{1}{2}} \tag{A.7}$$

As discussed, the main outcome of the free-flight technique is the measurement of aerodynamic coefficients. Application of Equation A.7 to Equation A.4 for lift coefficient yields (the same analysis can be completed for drag and pitching moment):

$$U_{C_L}^2 = \left(\frac{\partial C_L}{\partial m} \right)^2 U_m^2 + \left(\frac{\partial C_L}{\partial \ddot{z}} \right)^2 U_{\ddot{z}}^2 + \left(\frac{\partial C_L}{\partial \rho_\infty} \right)^2 U_{\rho_\infty}^2 + \left(\frac{\partial C_L}{\partial U_\infty} \right)^2 U_{U_\infty}^2 + \left(\frac{\partial C_L}{\partial S} \right)^2 U_S^2 \tag{A.8}$$

However, the variables ρ_∞ and U_∞ are not measured directly in the tunnel. Both variables are derived properties from isentropic relations through the use of other measured variables. Therefore, these two variables require their own uncertainty analysis which propagate back to the lift coefficient uncertainty. The isentropic relations for freestream velocity and freestream density are as follows (the uncertainty in Mach number and total temperature have been obtained in previous studies):

$$U_\infty = M \sqrt{\frac{\gamma R T_0}{\left(1 + \frac{\gamma - 1}{2} M^2 \right)}} \tag{A.9}$$

$$\rho_\infty = \frac{P_0}{R T_0} \left(1 + \frac{\gamma - 1}{2} M^2 \right)^{-\frac{1}{\gamma - 1}} \tag{A.10}$$

Equation A.9 shows that the freestream velocity is a function of total temperature and Mach number whereas density in Equation A.10 is a function of the aforementioned as well as total pressure. The application of Equation A.7 to these isentropic relations yields:

$$U_{U_\infty}^2 = \left(\frac{\partial U_\infty}{\partial M} \right)^2 U_M^2 + \left(\frac{\partial U_\infty}{\partial T_0} \right)^2 U_{T_0}^2 \tag{A.11}$$

$$U_{\rho_\infty}^2 = \left(\frac{\partial \rho_\infty}{\partial M} \right)^2 U_M^2 + \left(\frac{\partial \rho_\infty}{\partial T_0} \right)^2 U_{T_0}^2 + \left(\frac{\partial \rho_\infty}{\partial P_0} \right)^2 U_{P_0}^2 \tag{A.12}$$

The relevant partial differential equations which can be substituted into Equations A.8, A.11 and A.12 can be found at the end of this appendix. This uncertainty analysis can be extended further with knowledge of the static and pitot pressure transducers used to determine the uncertainty in freestream Mach number in the HDT. Substitution of the partial derivatives in the appendix and dividing through by the variable of interest gives the following equations for which the uncertainties are calculated from:

$$\left(\frac{U_{U_\infty}}{U_\infty}\right)^2 = \left(\frac{1}{\left(1+\frac{\gamma-1}{2}M^2\right)}\right)^2 \left(\frac{U_M}{M}\right)^2 + \frac{1}{4}\left(\frac{U_{T_0}}{T_0}\right)^2 \tag{A.13}$$

$$\left(\frac{U_{\rho_\infty}}{\rho_\infty}\right)^2 = \left(\frac{M^2}{\left(1+\frac{\gamma-1}{2}M^2\right)}\right)^2 \left(\frac{U_M}{M}\right)^2 + \left(\frac{U_{T_0}}{T_0}\right)^2 + \left(\frac{U_{P_0}}{P_0}\right)^2 \tag{A.14}$$

$$\left(\frac{U_{C_L}}{C_L}\right)^2 = \left(\frac{U_m}{m}\right)^2 + \left(\frac{U_{\ddot{z}}}{\ddot{z}}\right)^2 + \left(\frac{U_{\rho_\infty}}{\rho_\infty}\right)^2 + 4\left(\frac{U_{U_\infty}}{U_\infty}\right)^2 + \left(\frac{U_S}{S}\right)^2 \tag{A.15}$$

Table A.3 summarises the uncertainty values used for this analysis as well as those calculated in Equations A.13 and A.14. Mach number and total temperature uncertainties are obtained from other test campaigns in the HDT as currently in the free-flight setup, these two variables are not measured. The uncertainty in stagnation pressure is calculated from the uncertainty in the pressure transducer used to measure it.

Table A.3 Uncertainties in freestream variables

Variable	Uncertainty (%)
Mach Number	± 5
Total Temperature	± 8.7
Total Pressure	± 1.25
Freestream Velocity	± 4.37
Freestream Density	± 8.80

It can be seen that the major source of uncertainty in the freestream variables originates from the uncertainty in total temperature which propagates through to give a large uncertainty in freestream density. The HDT has a very strong transient increase in total temperature during the first plateau of a shot due to unsteady compression in the plenum upstream of the nozzle throat and as all free-flight testing occurs during this first plateau, it results in a large uncertainty in total temperature. For more details on total temperature in the HDT see Herman *et al.* [26].

Table A.4 Uncertainties in model variables

Variable	Uncertainty
Acceleration	$\pm$ 0.05 (ms^{-2})
Angular Velocity	$\pm$ 0.005 $(degs^{-1})$
Mass	$\pm$ $5x10^{-4}(kg)$
Reference Area	$\pm$ $1.6x10^{-4}(m^2)$

With the information contained in Tables A.3 and A.4 it is possible to calculate the uncertainty in the aerodynamic coefficients. A similar analysis to the above can be conducted to derive analogous equations for the uncertainty in drag and pitching moment coefficient. Therefore, the overall uncertainties in lift, drag and pitching moment coefficient are shown in the following table:

Table A.5 Uncertainties in aerodynamic coefficients

Variable	Maximum Uncertainty (%)
Lift Coefficient	$\pm$ 12.4
Drag Coefficient	$\pm$ 12.5
Pitching Moment Coefficient	$\pm$ 12.7

The following presents the partial derivatives calculated as part of the uncertainty analysis. Starting with lift coefficient:

$$\frac{\partial C_L}{\partial m} = \frac{\ddot{z}}{\frac{1}{2}\rho_\infty U_\infty^2 S} = \frac{C_L}{m} \tag{A.16}$$

$$\frac{\partial C_L}{\ddot{z}} = \frac{m}{\frac{1}{2}\rho_\infty U_\infty^2 S} = \frac{C_L}{\ddot{z}} \tag{A.17}$$

$$\frac{\partial C_L}{\partial \rho_\infty} = -\frac{m\ddot{z}}{\frac{1}{2}\rho_\infty^2 U_\infty^2 S} = -\frac{C_L}{\rho_\infty} \tag{A.18}$$

$$\frac{\partial C_L}{\partial U_\infty} = -\frac{m\ddot{z}}{\frac{1}{4}\rho_\infty U_\infty^3 S} = -\frac{2C_L}{U_\infty} \tag{A.19}$$

$$\frac{\partial C_L}{\partial S} = -\frac{m\ddot{z}}{\frac{1}{2}\rho_\infty U_\infty^2 S^2} = -\frac{C_L}{S} \tag{A.20}$$

$$\frac{\partial \rho_\infty}{\partial P_0} = \frac{1}{RT_0}\left(1+\frac{\gamma-1}{2}M^2\right)^{-\frac{1}{\gamma-1}} = \frac{\rho_\infty}{P_0} \tag{A.21}$$

Appendix B

Supplementary Experimental Data

Further to the experiments in Chapter 4, free-flight experiments with the 7 degree half angle cone were also conducted at a Mach 6 condition. This appendix contains the freestream conditions that the experiments were conducted at (Table B.1) and the measured aerodynamic coefficients plotted against numerical predictions (Figures B.1 - B.5).

Table B.1 Mach 6 Flight vs scaled tunnel condition.

Measured Freestream Properties	**HDT Test Flow**	**Flight**
Total Pressure (kPa)	1968 ± 7	882.4
Pitot Pressure (kPa)	55.4 ± 0.7	24.8
Total Temperature (K)	500 ± 15	1943
Calculated Freestream Properties		
Altitude (km)	35	35
Mach Number	6.07 ± 0.02	6
Velocity (ms^{-1})	941 ± 14	1851.7
Density (kgm^{-3})	0.067 ± 0.002	0.0082
Static Pressure (Pa)	1154 ± 22	558.9
Static Temperature (K)	59.7 ± 1.8	237.1
Dynamic Viscosity (μPas)	4.3 ± 0.1	15.3
Dynamic Pressure (kPa)	29.8 ± 0.6	34.3
Unit Reynolds Number ($10^6 m^{-1}$)	15.9 ± 0.7	1.0
Reynolds Number (10^6)	3.98 ± 0.19	3.98

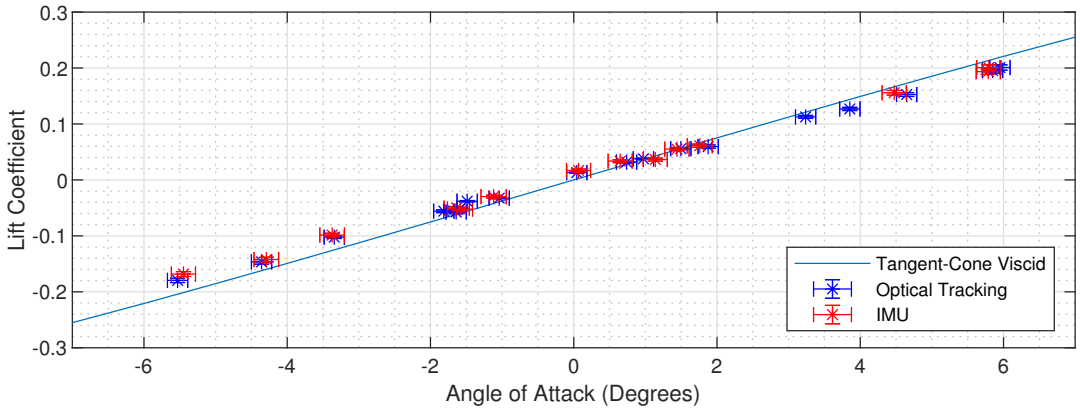

Fig. B.1 Lift coefficient at Mach 6 condition. Individual tests plotted against tangent-cone numerical prediction

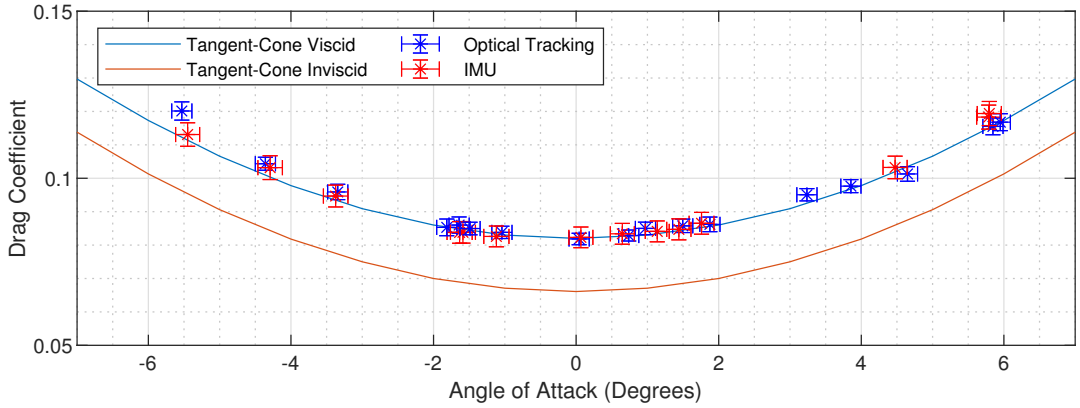

Fig. B.2 Drag coefficient at Mach 6 condition. Individual tests plotted against tangent-cone numerical prediction

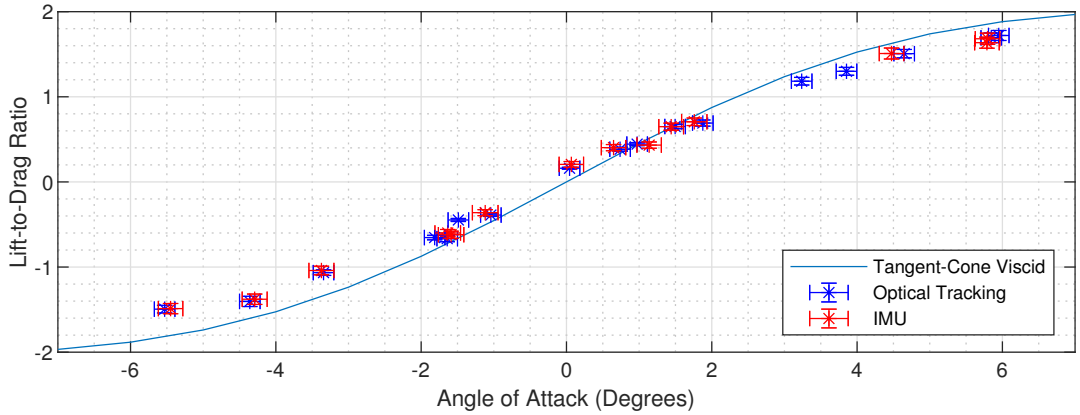

Fig. B.3 Lift to drag ratio at Mach 6 condition. Individual tests plotted against tangent-cone numerical prediction

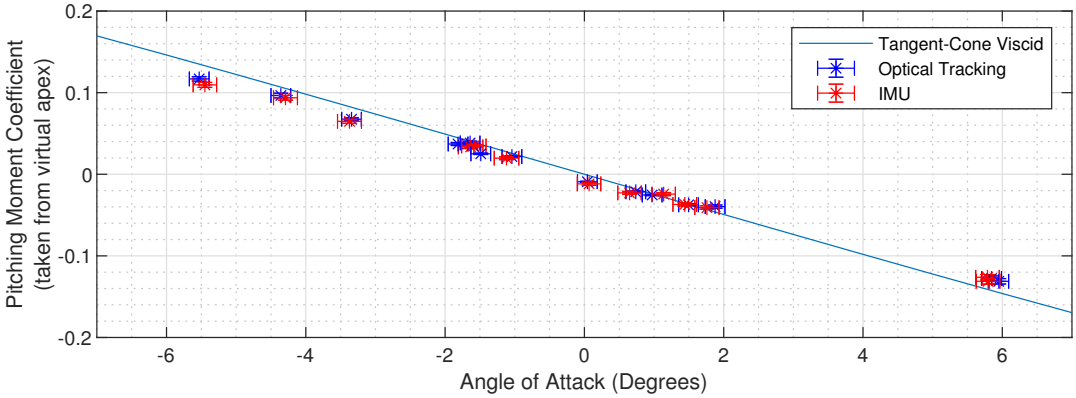

Fig. B.4 Pitching moment coefficient at Mach 7 condition. Individual tests plotted against tangent-cone numerical prediction

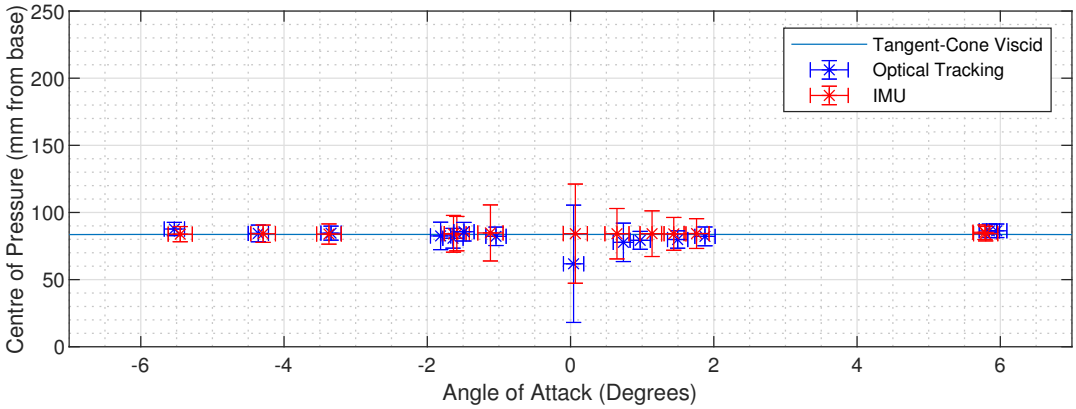

Fig. B.5 Centre of pressure at Mach 6 condition. Individual tests plotted against tangent-cone numerical prediction

Appendix C

Supplementary Free-Flight Manoeuvre Data

The free-flight experiments in Chapter 6 used a 7 degree half angle cone with fins to measure the static longitudinal aerodynamic coefficients and roll moment coefficients. Further manoeuvres to those in the Chapter were conducted and are discussed in this Appendix. The model, test section infrastructure and freestream conditions are the same as those in the Chapter.

C.1 Banking Manoeuvre

A single test was conducted that allowed the finned cone to bank on the yaw axis. To achieve this banking manoeuvre, the model was orientated so that the fins lay on the cardinal positions with the north and south fins angled at 3 ° as shown in Figure C.1.

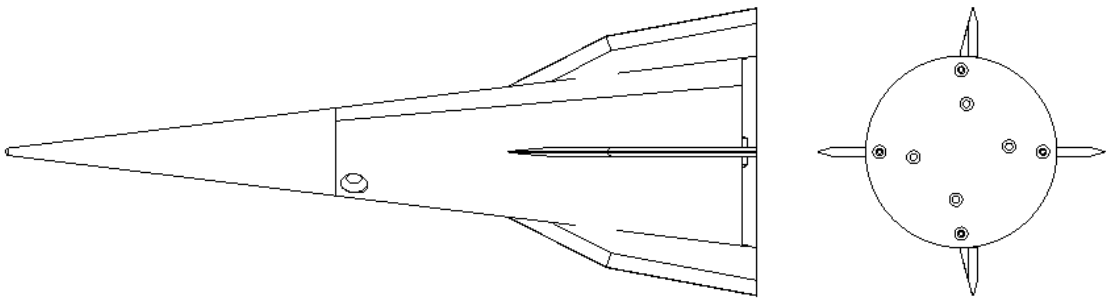

Fig. C.1 Orientation of Fins for banked manoeuvre experiments

Unlike the static experiments in Chapter 6, the centre of gravity of the cone was moved to 96.6 mm from the base so that the model was statically stable. This allowed the electromagnet to be positioned above the centre of gravity and not interfere with the fins. Only IMU data is presented for this experiment as the image tracking in its current form is unable to measure yaw. Figure C.2 shows a composite image of the banked cone test.

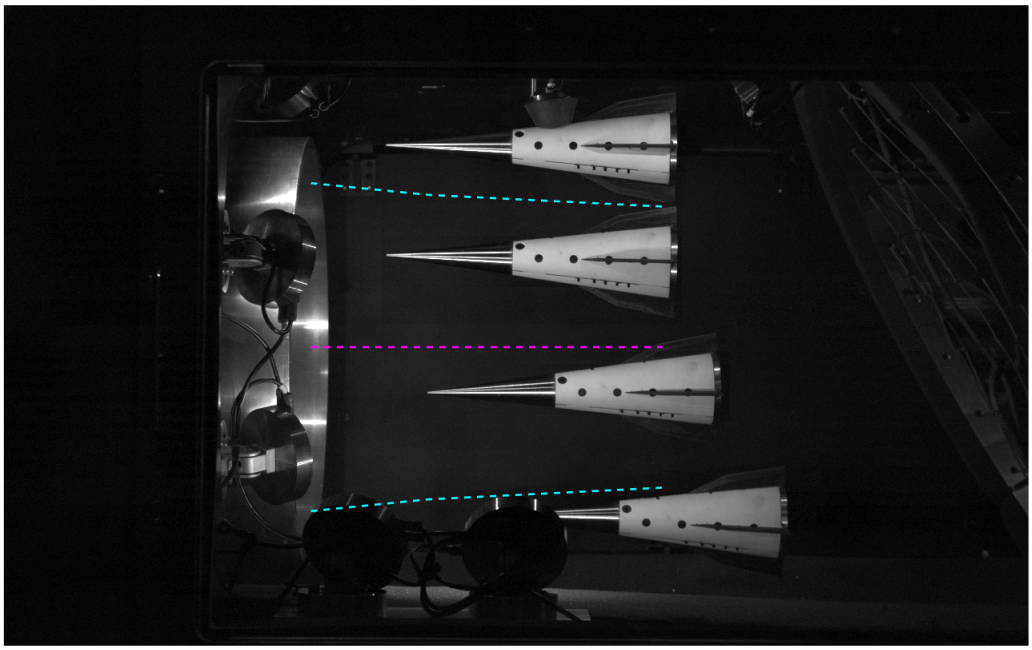

Fig. C.2 Composite image of banking finned cone (cyan - core flow location as acquired by a pitot survey, pink - nozzle centreline).

Figure C.3 shows the global angular displacements as measured by the IMU. As the model is statically stable, the figure shows that when flow begins at time 0 ms, the model begins to pitch towards the trim angle of attack of 0 ° which it then overshoots and then begins to pitch back to the trim angle. The centre of gravity location was not marked on the model unlike the static experiments which is why the model pitches when released from the electromagnet. A similar trend can be seen in the yaw data. The fins are angled at 3 ° so upon flow arrival the model yaws towards -3 °, overshoots and then yaws back towards this angle. Due to the mass and inertia of the model, this dynamic behaviour of the model in both yaw and pitch is not resolved in the test time, however, it shows that with increased test time, the capability of free-flight to research vehicle manoeuvres is possible. Roll is also seen in Figure C.3 which is most likely a result of yaw-roll coupling. As the model yaws, one of the fins becomes shadowed to the freestream which results in a roll moment being generated.

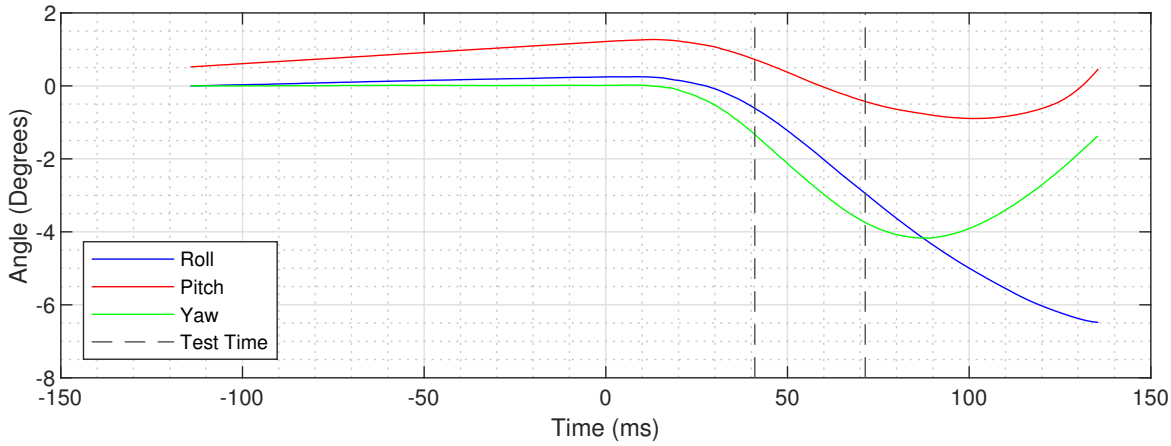

Fig. C.3 Global angular displacements as measured by the onboard IMU. Time at 0 ms is defined by the initiation of flow in the facility.

C.2 Shock Impingement

A single experiment was conducted with the cone model (with no fins) with a 10 ° wedge installed downstream of the nozzle to generate a shock that impinges on the model upon flow initiation. The centre of gravity position of the model was the same as in Chapter 3 so that the static margin was minimised and the shock impinging on the model would have a large influence on the resulting pitching motion of the model by shifting its centre of pressure.

Figure C.4 shows a composite image of a free-flight test with shock impingement. The wedge used to generate the shock can be seen suspended above the centre line of the nozzle. IMU measurements were not taken due to the high impact speed of the cone resulting from the shock. As seen in Figure C.4, the shock causes the model to become statically unstable and pitch downwards and therefore accelerate towards the floor due to higher pressures generated by the shock on the top surface of the cone. This high acceleration results in the model not entirely being in the core flow during the test time. As the nose tip is not in the core flow, it is not possible to determine aerodynamic coefficients that are only caused by the influence of the shock impingement during the test time. However, this experiment shows that the HDT has the ability to conduct shock impingement tests on model stability in free-flight with adjustments to the current infrastructure. These changes include moving the wedge higher so that the model can be released higher and stay in the core flow longer, and adjusting the release timings used in the experiments.

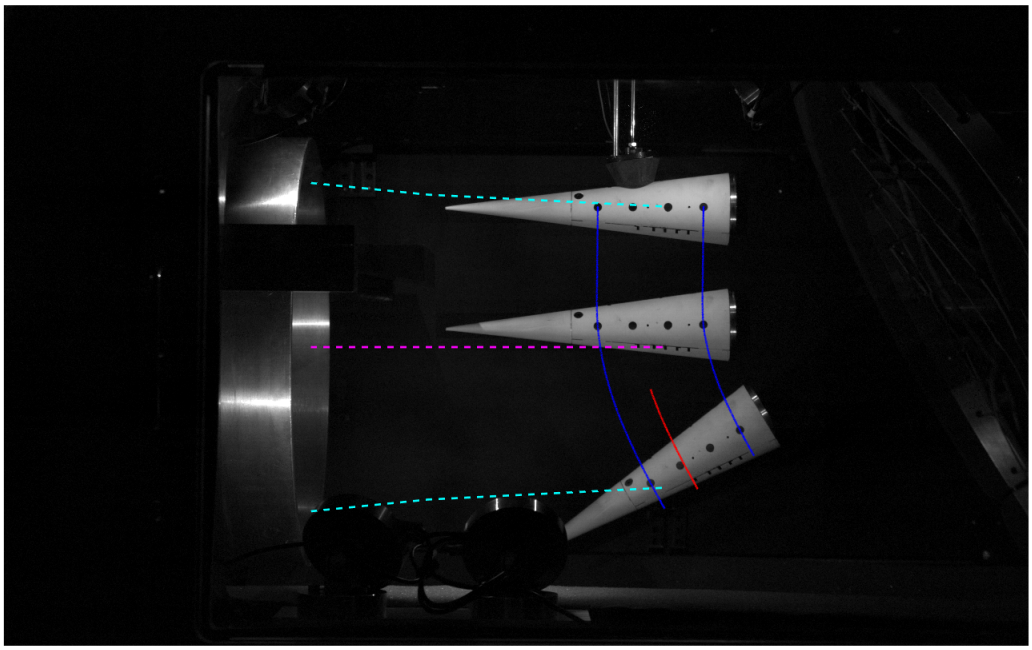

Fig. C.4 Composite image of shock impinged cone (Blue - detected circle centre points, Red - calculated centre of gravity, shown for test time, cyan - core flow location as acquired by a pitot survey, pink - nozzle centreline).